



**HAL**  
open science

# Imaging of fractured rock properties from flow and heat transport : field experiments and inverse modelling

Maria V. Klepikova

► **To cite this version:**

— Maria V. Klepikova. Imaging of fractured rock properties from flow and heat transport : field experiments and inverse modelling. Hydrology. Université Rennes 1, 2013. English. NNT : . tel-00865302

**HAL Id: tel-00865302**

**<https://theses.hal.science/tel-00865302>**

Submitted on 24 Sep 2013

**HAL** is a multi-disciplinary open access archive for the deposit and dissemination of scientific research documents, whether they are published or not. The documents may come from teaching and research institutions in France or abroad, or from public or private research centers.

L'archive ouverte pluridisciplinaire **HAL**, est destinée au dépôt et à la diffusion de documents scientifiques de niveau recherche, publiés ou non, émanant des établissements d'enseignement et de recherche français ou étrangers, des laboratoires publics ou privés.



**THÈSE / UNIVERSITÉ DE RENNES 1**  
*sous le sceau de l'Université Européenne de Bretagne*

pour le grade de

**DOCTEUR DE L'UNIVERSITÉ DE RENNES 1**

*Mention : Sciences de la Terre*

**École doctorale sciences de la matière**

présentée par

**Maria Klepikova**

préparée à l'unité de recherche UMR6118, GR  
Géosciences Rennes  
UFR Sciences et Propriétés de la matière

---

**Imaging of fractured  
rock properties from  
flow and heat transport:  
field experiments and  
inverse modelling**

---

**Thèse soutenue à Rennes  
le 16 Mai 2013**

devant le jury composé de :

**Alain Dassargues**

professeur, l'université de Liège (Belgique)/  
*rapporteur*

**Philippe Ackerer**

Directeur de Recherche, CNRS/ *rapporteur*

**Kerry Gallagher**

professeur, l'université de Rennes 1/  
*examineur*

**Laurent Guillou-Frottier**

géophysicien, BRGM / *examineur*

**Ralf Brauchler**

senior scientist, l'université de Zurich (Swiss)/  
*examineur*

**Olivier Bour**

professeur, l'université de Rennes 1/ *directeur  
de thèse*

**Tanguy Le Borgne**

physicien adjoint, l'université de Rennes 1/  
*directeur de thèse*

**John Selker**

professeur, Oregon State University (États-  
Unis d'Amérique)/ *invité*



## **Acknowledgements**

This thesis was funded by the European Commission through FP7 projects ITN project, IMVUL project (Grant Agreement 212298).



## Abstract

The accurate characterization of distribution of hydraulic properties and connectivity distribution is essential to predict flow and transport in fractured media. Classical approaches were developed for homogeneous aquifers and result in smooth tomograms that often do not match true heterogeneity distribution of fractured media. The main goal of this thesis is to develop new inverse approaches specifically for imaging hydraulic and transport properties in fractured media at the field-scale. To attain this objective new *in situ* measurement methods as well as new inverse modelling frameworks are proposed.

We first propose flow tomography (i.e., sequential cross-borehole flowmeter tests) as a new approach for characterizing fracture connectivity and transmissivities. Based on a discrete fracture network approach, we present a general method to invert flow tomography data. From synthetic case studies, we show that the tomographic approach reduces significantly the uncertainty on the parameter estimation. Flow tomography approach provides detailed characterization on fracture networks without the necessity of using packers. We then study the contribution of temperature measurements for quantifying flow in fractured media. The advantage of using temperature data is that temperature profiles can be obtained more easily and continuously in space, compared to flowmeter profiles. Using a numerical model of flow and heat transfer at the borehole scale, a method to invert temperature measurements to derive borehole flow velocities was proposed. We then couple the two previously proposed approach in a new experimental approach which we call temperature tomography. This experiment consists of sequential borehole temperature logging under cross-borehole flow conditions. The full inverse framework is then

presented to interpret temperature tomography experiments. Application of the temperature tomography approach to Stanger Brune field site showed encouraging results for the identification of general connectivity patterns and transmissivities of the main flowpaths. Finally, we explore the interest of using push-pull thermal tracer tests. Through field experiments and numerical modelling, we demonstrate that conducting push-pull heat tracer tests provide important constraints on the effective transport behavior.

## Résumé

La caractérisation de l'agencement spatial des propriétés hydrauliques est essentielle pour prédire les écoulements et le transport des solutés dans les milieux hétérogènes. Les méthodes de tomographie hydraulique, principalement développées pour estimer les propriétés des milieux poreux, n'ont qu'une faible résolution spatiale qui ne reflète pas la vraie hétérogénéité des distributions de fractures des milieux fracturés. Le principal objectif de cette thèse est de développer une nouvelle méthode d'inversion spécifique pour imager les propriétés hydrauliques et de transport des milieux fracturés à l'échelle du site. Pour atteindre ces objectifs, des expériences *in situ* ainsi qu'une nouvelle approche de modélisation inverse sont proposées, notamment en utilisant la température comme marqueur des écoulements.

Nous proposons tout d'abord la tomographie d'écoulement basée sur des tests séquentiels de débitmétrie entre puits, comme une nouvelle approche pour caractériser la connectivité des fractures ainsi que leur transmissivité. À partir de simulations numériques reproduisant des cas d'études synthétiques, nous montrons que l'approche par tomographie réduit significativement l'incertitude sur les paramètres estimés, et fournit une caractérisation détaillée du réseau de fracture sans requérir à l'utilisation d'obturateurs hydrauliques. Nous montrons ensuite comment les mesures de température peuvent être utilisées pour quantifier les écoulements dans les milieux fracturés. Le grand intérêt d'utiliser la température est d'obtenir facilement et de façon continue en puits des profils de température. En utilisant un modèle numérique d'écoulement et de transfert de chaleur à l'échelle du puits, une méthode d'inversion pour estimer les vitesses d'écoulement dans

le puits à partir des données de température est proposée. Nous couplons ensuite les deux approches présentées précédemment dans une nouvelle approche expérimentale consistant en des enregistrements séquentiels de température dans un puits dans des conditions de pompage entre puits. L'application de cette approche de tomographie en température sur le site de Stang er Brune montre des résultats encourageants pour l'identification du réseau global de connectivité et des zones d'écoulement principales. Enfin, nous discutons de l'intérêt d'utiliser la chaleur comme traceur par rapport à l'utilisation de traceurs classiques. Nous montrons que réaliser des tests de traçage thermiques en milieu fracturé fournit des contraintes supplémentaires importantes sur les propriétés de transport du milieu.

## Remerciements

Je remercie tout d'abord mes directeurs de thèse Tanguy Le Borgne et Olivier Bour, qui m'ont permis d'effectuer cette thèse dans les meilleures conditions, aussi bien qu'humaines que scientifiques et techniques. Je remercie également Jean Raynald de Dreuzy, qui m'a beaucoup appris sur les modèles inverses.

Une grande partie de ma thèse a été consacrée aux expériences de terrain. J'ai beaucoup aimé les journées ensoleillées passées à Stang er Brune. Je tiens à remercier Rebecca et Nicolas pour leur contribution indispensable au bon déroulement de ces expériences. J'ai par ailleurs beaucoup apprécié la possibilité de travailler avec d'autres équipes, et notamment avec Vicor Bense, Tom Read, Caroline Dorn, Andreas Englert, Peter Kang et Niklas Linde.

Je souhaite également remercier les membres du jury de ma thèse: Kerry Gallagher, Alain Dassargues, Ralf Brauchler, John Selker, Laurent Guillou-Frottier et Philippe Ackerer, qui ont pris le temps de lire et de juger cette thèse et pour leurs remarques constructives.

Durant ces quatre années passées à Géosciences, j'ai beaucoup apprécié la bonne ambiance dans notre équipe et je tiens à remercier toutes les personnes pour tous nos échanges scientifiques et quotidiens. Notamment, merci à Pietro pour avoir partager son toit à mon arrivée en France. Merci à Morgane pour m'avoir proposé la collocation. Merci à mes collègues de bureau - Sarah, Jérémy et Régis. Et merci à vous tous : Nico, Clément, Antoine, Virginie, Joaquin, Pascal et Jérôme. Un grand merci aussi à Catherine Barbedor.

Enfin, merci à toute ma famille. Merci beaucoup à mes parents et grand-parents qui ont toujours été présents et qui m'ont permis d'arriver jusque là. Merci beaucoup à Thibault, Seva et Alice pour votre soutien, vos encouragements et vos conseils.

Et enfin merci à Thibault pour avoir corrigé mon français!

---

# Contents

<b>Contents</b>	<b>xi</b>
<b>List of Figures</b>	<b>xv</b>
<b>Nomenclature</b>	<b>xxi</b>
<b>1 General introduction</b>	<b>3</b>
1.1 Flow in fractured media . . . . .	3
1.1.1 Single fracture . . . . .	3
1.1.2 Fracture networks . . . . .	5
1.2 Transport in fractured media . . . . .	9
1.3 Flow and transport modeling in fractured media . . . . .	13
1.4 Imaging of hydraulic and transport properties of fractured media .	16
1.4.1 Hydraulic tomography . . . . .	16
1.4.2 Flowmeter tests . . . . .	20
1.4.2.1 Single-borehole flowmeter test . . . . .	20
1.4.2.2 Cross- borehole flowmeter test . . . . .	20
1.4.3 Temperature . . . . .	22
1.4.3.1 Heat tracer test . . . . .	26
1.5 Approaches proposed in thesis . . . . .	28
<b>2 Inverse framework for flow tomography experiment</b>	<b>31</b>
2.1 Introduction . . . . .	31

## CONTENTS

---

2.2	Paper: Inverse modelling of flow tomography experiments in fractured media (Klepikova et al., submitted for possible publication in Water Resources Research) . . . . .	32
2.3	Conclusions . . . . .	68
<b>3</b>	<b>Ploemeur field site</b>	<b>69</b>
3.1	Introduction . . . . .	69
3.2	Site localization . . . . .	70
3.3	Hydrogeological context . . . . .	71
3.4	Stanger Brune site . . . . .	74
3.4.1	Analysis of thermal properties . . . . .	80
3.5	Conclusions . . . . .	82
<b>4</b>	<b>Using borehole temperature profiles to estimate borehole flow velocities</b>	<b>83</b>
4.1	Introduction . . . . .	83
4.2	Paper: A methodology for using borehole temperature-depth profiles under ambient, single and cross-borehole pumping conditions to estimate fracture hydraulic properties (Klepikova et al., Journal of Hydrology, 2011) . . . . .	84
4.3	Conclusions . . . . .	93
<b>5</b>	<b>Temperature tomography experiment in fractured media</b>	<b>95</b>
5.1	Introduction . . . . .	95
5.2	Paper: Temperature tomography experiment in fractured media (Klepikova et al., in preparation) . . . . .	95
5.3	Conclusions . . . . .	131
<b>6</b>	<b>Heat and solute transport in fractured media</b>	<b>133</b>
6.1	Introduction . . . . .	133
6.2	Heat transport: numerical modeling . . . . .	136
6.2.1	Sensitivity analysis . . . . .	140
6.2.1.1	Sensitivity of temperature recovery to push time	140

6.2.1.2	Sensitivity of temperature recovery to flow rate and geometry . . . . .	142
6.2.1.3	Sensitivity of temperature recovery to the fracture aperture . . . . .	145
6.3	Heat transport: push-pull heat tracer tests . . . . .	151
6.4	Discussion and Conclusions . . . . .	158
<b>7</b>	<b>Conclusions and perspectives</b>	<b>161</b>
7.1	Conclusions . . . . .	161
7.2	Perspectives . . . . .	165
7.2.1	Tomography approaches . . . . .	165
7.2.2	Temperature and flow heterogeneity . . . . .	166
7.2.3	Heat as a tracer . . . . .	167
 <b>Appendix 1. Paper: Inferring transport characteristics in a frac- tured rock aquifer by combining single-hole ground-penetrating radar reflection monitoring and tracer test data (Dorn et al., Water Resources Research, 2012)</b>		 <b>169</b>
 <b>Appendix 2. Paper: Characterizing groundwater flow and heat transport in fractured rock using Fiber-Optic Distributed Tem- perature Sensing (Read et al., Geophysical Research Letters, ac- cepted)</b>		 <b>189</b>
 <b>References</b>		 <b>213</b>

## CONTENTS

---

# List of Figures

1.1	Example of self-affine fracture aperture (a) and dimensionless hydraulic flow norm computed with this aperture (b) (from Neuville et al. [2010]). . . . .	4
1.2	Fracture map from one of the Stripa mine tunnel, showing H-zone, which produces 80 % of the total flow (from Olsson [1992]). . . . .	5
1.3	Fracture distribution at Mirror Lake site, transmissive fractures are shown with a bold line, from Day-Lewis et al. [2000] (a). Distribution of hydraulic conductivity measured in one borehole at Mirror Lake site, from Hsieh [1998] (b). . . . .	6
1.4	Permeability data from different fractured field sites plotted against measurement scale. (from Illman [2006]). . . . .	6
1.5	Example of flow in fractured network from Le Goc et al. [2010]. (a) Synthetic fracture network. (b) Flows computed with a constant sub-horizontal hydraulic gradient of direction given by the arrow. All fractures have the same transmissivity. The grey color is proportional to the logarithm of flow normalized by the total flow entering the domain. (c) Simplified fracture structure carrying 70% of the flow. (d) Sketch of the possible main flow channels. . . . .	7
1.6	(a) Example of a constant-length ( $l = 1$ ) fault network at the percolation threshold; (b) the infinite cluster of the network presented in (a); (c) fault networks at the percolation threshold in the case of power law fault lengths distribution ( $N(l) = \alpha l^{-a}$ , $a = 1.5$ ); (d) largest cluster of the network presented in (c). From Bour and Davy [1997]. . . . .	9

## LIST OF FIGURES

---

1.7	Photographies of tracer propagation through homogeneous (a) and heterogeneous (b) media from Levy and Berkowitz [2003]. . . . .	10
1.8	Push-pull tracer tests showing a very long time for tracer recovery from Becker and Shapiro [2003] (a) and Haggerty et al. [2001](b). Different conceptual models are used: Becker and Shapiro [2003] fitted their tracer test BTCs using a multichannel model, while Haggerty et al. [2001] explain the data with a double porosity model.	12
1.9	Example of application of stochastic continuum approach to hydraulic tomography data. Hydraulic conductivity $K$ tomogram ( $m/d$ ) obtained from the inversion of two cross-hole tests from Illman et al. [2009]. . . . .	14
1.10	An example of the application of a stochastic discrete fracture network (DFN) approach to borehole flow rates data measured during extraction pumping, from Frampton and Cvetkovic [2010]. One DFN realization colored by transmissivity and the corresponding pressure field (drawdown). . . . .	15
1.11	Schematic cross-sectional view of hydraulic tomography experiment [Butler et al., 1999]. . . . .	17
1.12	Example of imaging of permeability field with hydraulic tomography in laboratory experiment, from [Sharmeen et al., 2012]. Pumping locations are shown by red points and observation locations are shown by black points. . . . .	19
1.13	The principle of single- and cross-borehole flowmeter test. Flowing fracture corresponds to inflow point during single-borehole pumping test. During cross-borehole pumping hydraulic heads change only in flowpath connected to pumping well. . . . .	21
1.14	Application of borehole temperature profiles, from Anderson [2005]	23
1.15	Range of hydraulic conductivities and hydraulic gradients where GWF can induces GST perturbations. The red zone indicates the range of minimum Darcy fluxes (from Ferguson [2006] . . . . .	24

## LIST OF FIGURES

---

1.16	Borehole temperature profiles that are typical for fractured media: (a) temperature profile affected by flow in small-scale fractures with either warmer or cooler origins, from Ge [1998], (b) steady-state (bold lines) and transient (thin curves) temperature profiles affected by hot fluid flow in a large-scale fracture. Hot fluid flow provides a constant temperature boundary condition, from Saar [2011], (c) temperature logs collected in open and lined borehole. Rose arrows indicate ambient borehole flow, blue arrows indicate interpreted flow zones, from Pehme et al. [2010]. . . . .	25
1.17	Temperature field computed for a realistic fracture geometry(a) at a matrix permeability of (b) $10^{-11} \text{ m}^2$ , (c) $10^{-13} \text{ m}^2$ , (d) $10^{-15} \text{ m}^2$ . The temperature field for the high matrix permeability case ( $10^{-11} \text{ m}^2$ ) is after 50 days; all other fields are after 100 days. From Geiger and Emmanuel [2010] . . . . .	27
1.18	Schema of flow and temperature measurements during cross-borehole pumping test. Two scales of investigation are shown. Small-scale study considers borehole-matrix thermal exchange. Large-scale investigations concerns to flowpaths connecting the pair of 'pumping-observation' boreholes. Hot water movement in fractures is controlled by fracture-matrix thermal exchange. . . . .	29
3.1	Ploemeur site localization. Ploemeur main pumping site and Stanger Brune experimental site. . . . .	70
3.2	a) Geological context of the Ploemeur area within South Brittany. b) Synthetic geological map of Ploemeur area, c) Schematic 3D diagram of Ploemeur aquifer geology showing the regional contact dipping toward the north and the $N20$ dextral normal fault. This schematic diagram of the pumping area is not scaled but corresponds roughly to the area within the white square on b (from Ruelleu et al. [2010]). . . . .	72

## LIST OF FIGURES

---

3.3	a) Simplified north-south geological cross-section. Dashed lines mark foliation. b) Photograph showing aspects of contact zone between granite and overlying micaschists, marked by granite and pegmatite dykes. c) Borehole cores of micaschists, granite, and breccias encountered within the water supply zone. Core diameter is 8 cm (from Ruelleu et al. [2010]). . . . .	73
3.4	Estimates of transmissivity at borehole scale, cross borehole scale and site scale (from Le Borgne et al. [2007]). . . . .	73
3.5	Stanger Brune field site. . . . .	74
3.6	Flowmeter and caliper logs in B1. (a) Ambient vertical velocity (positive values correspond to upward flow), (b) vertical velocity measured while pumping in the cased part of the well at a rate of 19 l/min. The steady state drawdown observed was 55 cm, (c) vertical velocity measured while pumping in the cased part of the well at a rate of 82 l/min. The steady state drawdown observed was 6.76 m and (d) caliper log. . . . .	76
3.7	Flowmeter and caliper logs in B2. (a) Ambient vertical velocity (positive values correspond to upward flow), (b) vertical velocity measured while pumping in the cased part of the well at a rate of 42 l/min. The steady state drawdown observed was 21 cm, (c) vertical velocity measured while pumping in the cased part of the well at a rate of 140 l/min. The steady state drawdown observed was 1.9 m and (d) caliper log. . . . .	77
3.8	Flowmeter and caliper logs in B3. (a) Ambient vertical velocity (positive values correspond to upward flow), (b) vertical velocity measured while pumping in the cased part of the well at a rate of 19 l/min. The steady state drawdown observed was 3 cm, (c) vertical velocity measured while pumping in the cased part of the well at a rate of 145 l/min. The steady state drawdown observed was 63 cm and (d) caliper log. . . . .	78

---

## LIST OF FIGURES

3.9	Extracts of the migrated multioffset single-hole GPR sections of B1 and B2 with superimposed interpretations of tracer pathways from Dorn et al. [2012]. Red circles indicate the tracer injection points, while red and blue arrowheads locate saline and unaffected groundwater inflow into the pumping borehole, respectively. Light red regions highlight fractures through which the injected tracer is interpreted to move, whereas blue regions highlight reflections from other boreholes. Light blue letters refer to transmissive fractures identified in the boreholes using optical logs and flowmeter tests with corresponding blue lines indicating their corresponding dips [Le Borgne et al., 2007]. (d) Dip angles corresponding to the axis aspect ratio $r : z$ of 2 : 1 [Dorn et al., 2012](Appendix1). . . . .	79
3.10	Optical images of B1-2 (50.9 <i>m</i> depth) and B1-4 (78.7 <i>m</i> depth) fractures [Le Borgne et al., 2007]. . . . .	80
3.11	Thermal properties of rock samples from B1 borehole at the Stanger Brune field site. . . . .	81
6.1	Temperature field for an example of model geometry with a fracture with 2 <i>mm</i> aperture. . . . .	137
6.2	A. Model geometry and parameters used for model validation. Two dimensional, single planar fracture system, numerical temperature solution shown at 3 days (compare to Molson et al. [2007]). B. Comparison of the numerical model (COMSOL) against the analytical model (SFRAC-H, Molson et al. [2007]) for a single fracture system (A). . . . .	139
6.3	Simulated temperature distribution during pulse tracer injection in a single fracture with aperture fixed to $b = 15$ <i>mm</i> for injection with the rate $Q = 3.5$ <i>L/min</i> and during the fixed time $t_{inj} = 1000$ <i>s</i> . The tracer is pushed with water of the ambient temperature. The temperature is given at different times $t = 1500, 6000, 11000$ <i>s</i> . . . . .	142

## LIST OF FIGURES

---

6.4	Simulated heat breakthrough curves during push-pull tracer test in a single fracture with aperture fixed to $b = 15 \text{ mm}$ for injection with the fixed pumping rate $Q = 3.5 \text{ L/min}$ and during the fixed time $t_{inj} = 1000 \text{ s}$ , while pushing time is varied as $t_{push} = 500, 1000, 10000 \text{ s}$ . . . . .	143
6.5	Simulated heat breakthrough curves during push-pull tracer test in a single fracture aperture $b = 15 \text{ mm}$ and various pumping rate ( $Q = 3.5, 35$ and $70 \text{ L/min}$ . The injection time $t_{inj} = t_{push} = 1000 \text{ s}$ . The temperature of injected water is constant $T_{inj} = 33^\circ\text{C}$ . . .	145
6.6	Simulated temperature breakthrough curves during push-pull tracer test. Fracture aperture varies from $1 \cdot 10^{-3} \text{ m}$ up to $50 \cdot 10^{-3} \text{ m}$ , flow rate $Q$ is given by $3.5 \text{ L/min}$ and for all experiments injection time is given by $17 \text{ min}$ . Here $T_D = (T - T_{zero})/(T_{inj} - T_{zero})$ . . .	147
6.7	Spatial profiles of temperature and concentration of a conservative tracer at the end of injection period ( $t = 1000 \text{ s}$ ). Position of thermal front is shown by black line. . . . .	148
6.8	Movement of the thermal front in the fracture for $b = 5 \text{ mm}$ and $b = 15 \text{ mm}$ fracture apertures, shown on a log-log plot . . . . .	150
6.9	Tracer test experimental schema. Push-pull tracer in B1-2 fracture isolated with packers. . . . .	152
6.10	Temperature and concentration breakthrough curves measured in between packers for Test 2. . . . .	153
6.11	Temperature breakthrough curves for push-pull heat tracer tests in B1 – 2 fracture. . . . .	154
6.12	Breakthrough curves for push-pull heat tracer tests in B1 – 2 fracture. Here temperature is normalized so that its integral, over injection and pushing time, is 1. . . . .	156
6.13	Measured breakthrough curves and model fit (fracture aperture $b = 27 \text{ mm}$ ) for radial convergent tracer tests between B1 – 2 fracture and B2 borehole. . . . .	157

## LIST OF FIGURES

---

6.14	(A) Temperature breakthrough curves for a single 20 mm aperture fracture (red line) and for two 20 mm aperture fractures separated by 20 mm distance. The total flow rate for both experiments $Q$ is given by 3.5 L/min (for the case with two fractures the flow rate in each fracture is reduced to half the rate that was seen for the single-fracture case $Q_1 = Q_2 = 1.75$ L/min) and for all experiments injection time is given by 17 min. (B) Temperature distribution for two 20 mm aperture fractures separated by 20 mm distance at different times. . . . .	160
7.1	Illustration of the inverse modelling methods for imaging of fracture hydraulic properties developed during the thesis. In Chapter 2, we propose an inverse model approach for inverting flow tomography data. In Chapter 4, we propose a framework to invert temperature measurements to derive borehole flow velocities. In Chapter 5, we couple the approaches developed in the two previous chapters to interpret experimental data set to image fracture hydraulic properties at the site scale. . . . .	163
7.2	An example of fracture network and its conceptualization with a model. For this fracture network, model simplicity does not allow to represent fr1-2 as an independent flowpath. . . . .	165
7.3	Temperature anomalies at large scale. In November 2009, pumping took place in PSR3 borehole and in April 2010 temperature was measured under ambient flow conditions. . . . .	167

## LIST OF FIGURES

---

Speak in French when you can't  
think of the English for a thing –  
turn out your toes as you walk –  
and remember who you are!

Lewis Carroll



# Chapter 1

## General introduction

This chapter presents the background relevant to the imaging of fractured rock properties. It starts with a discussion about the influence of the media heterogeneities on flow and transport patterns. Then different modeling approaches are described. Furthermore, existing methods of imaging of fractured media are presented. Based on this background, the approaches proposed in the thesis are introduced in the last section.

### 1.1 Flow in fractured media

In fractured media flow is generally focused along a few preferred pathways. This phenomenon is referred to as flow channeling. It is recognized that flow channeling, arising on all scales, significantly complicates flow and transport prediction. The issue is to properly describe heterogeneous characteristics of fractured media. Throughout this section, flow within individual fractures and within multifracture networks is discussed.

#### 1.1.1 Single fracture

At the fracture scale, flow patterns are influenced by the fracture aperture variability and the roughness of the facing aperture surfaces. For a laminar flow in sufficiently open fractures, the cubic law provides a good estimates of the flow

## 1. GENERAL INTRODUCTION

---

rate  $q$  per a unit fracture length [e.g. Moreno et al., 1988]

$$q = -\frac{d^3}{6\eta}\nabla P, \quad (1.1)$$

The geometrical heterogeneity of the fracture walls results in variable hydraulic behavior of fractures [e.g. Berkowitz, 2002; Meheust and Schmittbuhl, 2001; Tsang and Neretnieks, 1998]. Numerous studies demonstrate that due to heterogeneous characteristics of the fracture aperture, flow channeling occurs [e.g. Moreno et al., 1990; Tsang and Neretnieks, 1998]. An example from Neuville et al. [2010] of a fracture aperture is shown in 1.1 a. The hydraulic flow computed inside this morphology, shown in 1.1 b, exhibits a strong channeling as previously described by Meheust and Schmittbuhl [2001]. Moreover, this study demonstrates that depending on the orientation of the hydraulic gradient (relative to heterogeneities in wall roughness), flow can be either enhanced or inhibited in comparison to a parallel wall fracture.

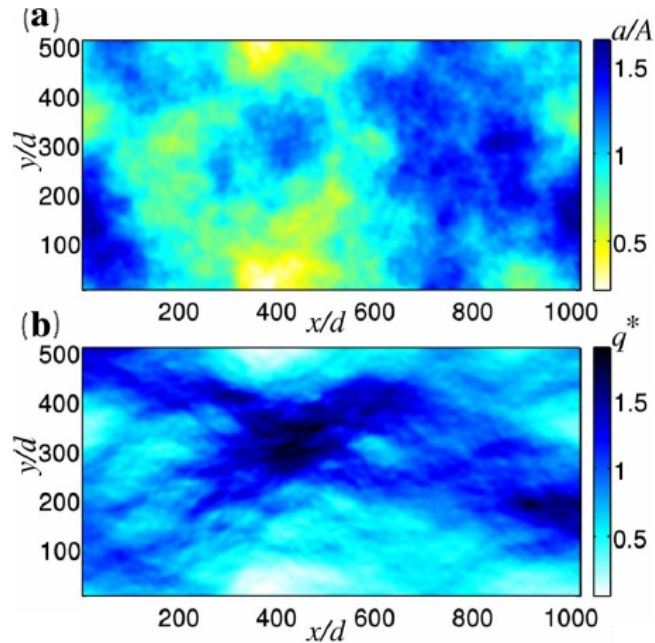


Figure 1.1: Example of self-affine fracture aperture (a) and dimensionless hydraulic flow norm computed with this aperture (b) (from Neuville et al. [2010]).

### 1.1.2 Fracture networks

In addition to flow in individual fractures being organized in channels, flow channeling or preferential flowpaths in fracture networks has been demonstrated by numerous field observations [Tsang and Neretnieks, 1998]. For example, in a fractured granitic rock at Stripa mine, 80 % of the total flow arrived in one of the tunnel is produced by a single fracture [Olsson, 1992] (Figure 1.2). At the Mirror Lake site, the major part of flow was shown to be channelized in a few fractures (Figure 1.3a). Hsieh [1998] demonstrates that at the Mirror Lake site high degree of heterogeneity arises from a large variability of hydraulic permeability at the fracture network scale (Figure 1.3b). Several other studies show that fractured rocks are generally characterized by spatial variability of permeability on all scales [Clauser, 1992; Hsieh, 1998] (Figure 1.4). The causes of this variability and permeability scaling are still debated [e.g. Illman, 2006].

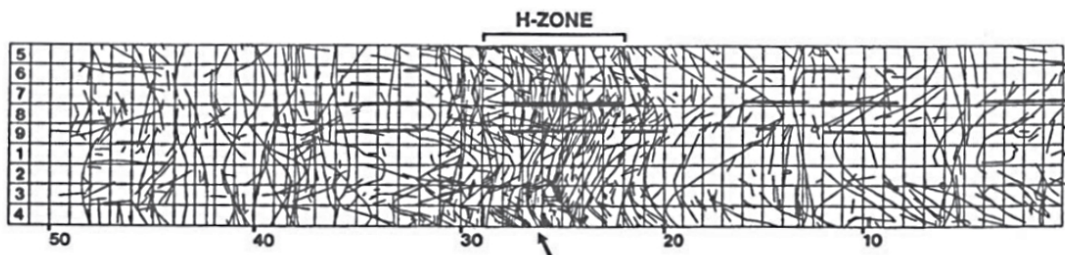


Figure 1.2: Fracture map from one of the Stripa mine tunnel, showing H-zone, which produces 80 % of the total flow (from Olsson [1992]).

# 1. GENERAL INTRODUCTION

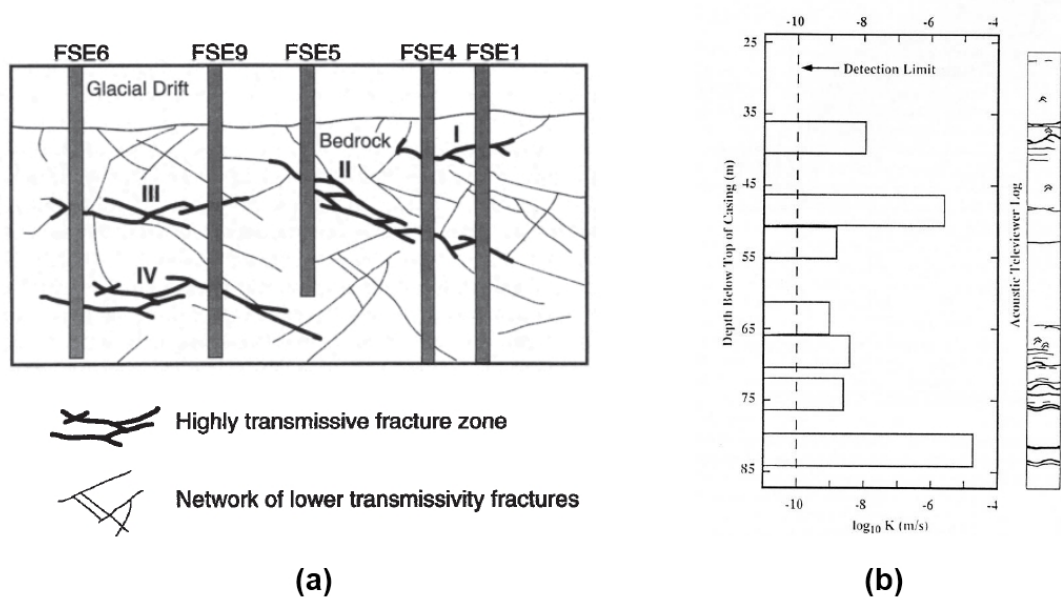


Figure 1.3: Fracture distribution at Mirror Lake site, transmissive fractures are shown with a bold line, from Day-Lewis et al. [2000] (a). Distribution of hydraulic conductivity measured in one borehole at Mirror Lake site, from Hsieh [1998] (b).

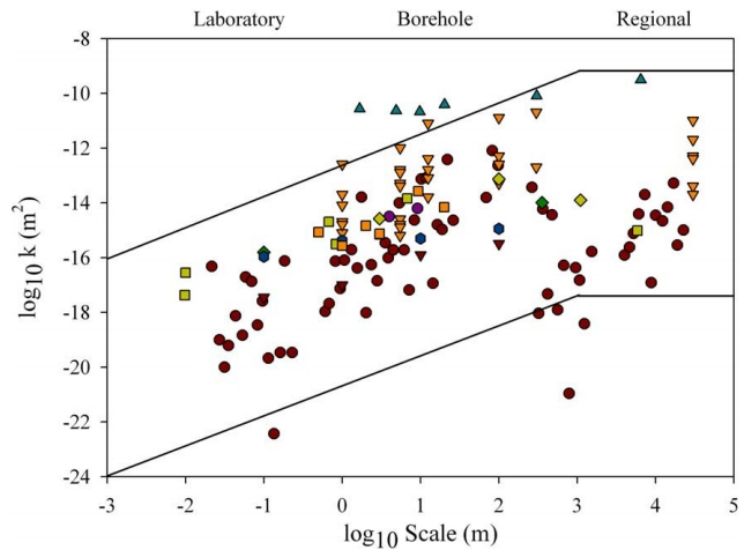


Figure 1.4: Permeability data from different fractured field sites plotted against measurement scale. (from Illman [2006]).

The experimental evidence of flow channeling stimulated a series of numerical and theoretical studies. Figure 1.5 presents an example of channeled flow obtained on a synthetic 2D fracture network, where a total flow is carried only by a few among all generated fractures (Figure 1.5). This is explained by the fact that the key characteristic controlling fluid flow at the network scale is the connectivity of fractures [Bour and Davy, 1997]. Fracture connectivity, in turn, depends on geometrical properties of fracture network. The influence of geometrical fracture network characteristics such as fracture density, fracture length distribution, distribution of fracture orientations and apertures on fracture-network connectivity and on the permeability scaling is the subject of numerous experimental and numerical studies [e.g. Berkowitz, 2002; Berkowitz et al., 2000; Bour and Davy, 1998; Darcel et al., 2003; de Dreuzy et al., 2001; Margolin et al., 1998].

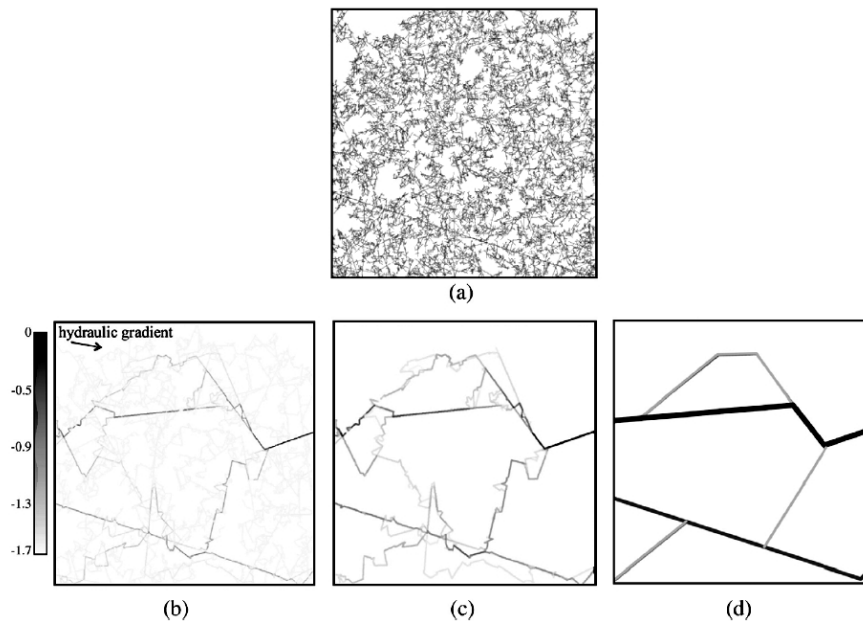


Figure 1.5: Example of flow in fractured network from Le Goc et al. [2010]. (a) Synthetic fracture network. (b) Flows computed with a constant sub-horizontal hydraulic gradient of direction given by the arrow. All fractures have the same transmissivity. The grey color is proportional to the logarithm of flow normalized by the total flow entering the domain. (c) Simplified fracture structure carrying 70% of the flow. (d) Sketch of the possible main flow channels.

## 1. GENERAL INTRODUCTION

---

In order to characterize fracture network connectivity, percolation theory was shown to be an efficient approach [Stauffer and Aharony, 1985]. Thus, for infinitely large systems, consisting of a uniformly distributed cracks of constant length, there exists a critical density of elements  $p_C$  (the percolation threshold) below which systems are not connected, and above which systems are always connected whatever the scale of investigation. For a widely scattered length distribution systems ( $N(l) = \alpha l^{-a}$ ), the challenge is to find a parameter of percolation that is a right measure of network connectivity, i.e., that does not depend on scale at connectivity threshold [Berkowitz et al., 2000; Bour and Davy, 1997, 1998; Darcel et al., 2003]. Thus, Bour and Davy [1997] demonstrate that for widely scattered length distribution systems even for a low density of elements there always exists a scale for which the percolation threshold is reached (Figure 1.6). These studies demonstrate that while channeling in single-fractures is due to heterogeneity of the fracture aperture, flow channeling at the field-scale is controlled by distribution of fracture conductivities and by connectivity of fractures [Berkowitz, 2002].

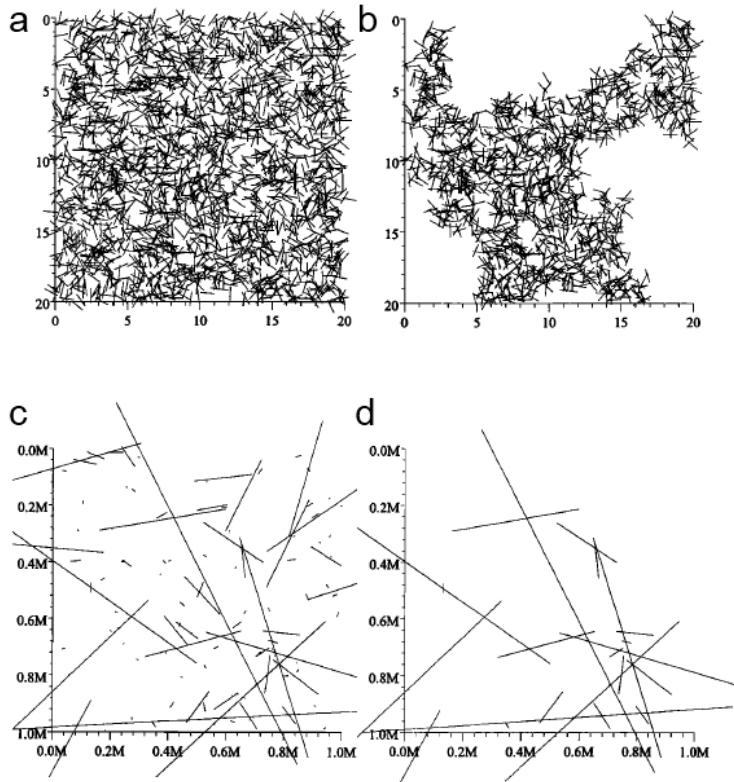


Figure 1.6: (a) Example of a constant-length ( $l = 1$ ) fault network at the percolation threshold; (b) the infinite cluster of the network presented in (a); (c) fault networks at the percolation threshold in the case of power law fault lengths distribution ( $N(l) = \alpha l^{-a}$ ,  $a = 1.5$ ); (d) largest cluster of the network presented in (c). From Bour and Davy [1997].

## 1.2 Transport in fractured media

Flow heterogeneities in fractured media influence transport behavior by inducing a broad range of transport rates. The coexistence of high velocity flow paths and immobile zones complicates the prediction of transport pattern. A basic transport model which can be used to describe the tracer migration in homogeneous media is the advection-dispersion model accounting for advection of the solute in the fracture plane and hydrodynamic dispersion. The equation is given by

## 1. GENERAL INTRODUCTION

---

$$\frac{\partial C}{\partial t} = -\nabla \cdot (Cv) + \nabla \cdot [D\nabla C] \quad (1.2)$$

where  $C$  is concentration,  $t$  is time,  $D$  is the hydrodynamic dispersion tensor and  $v$  is average fluid velocity.

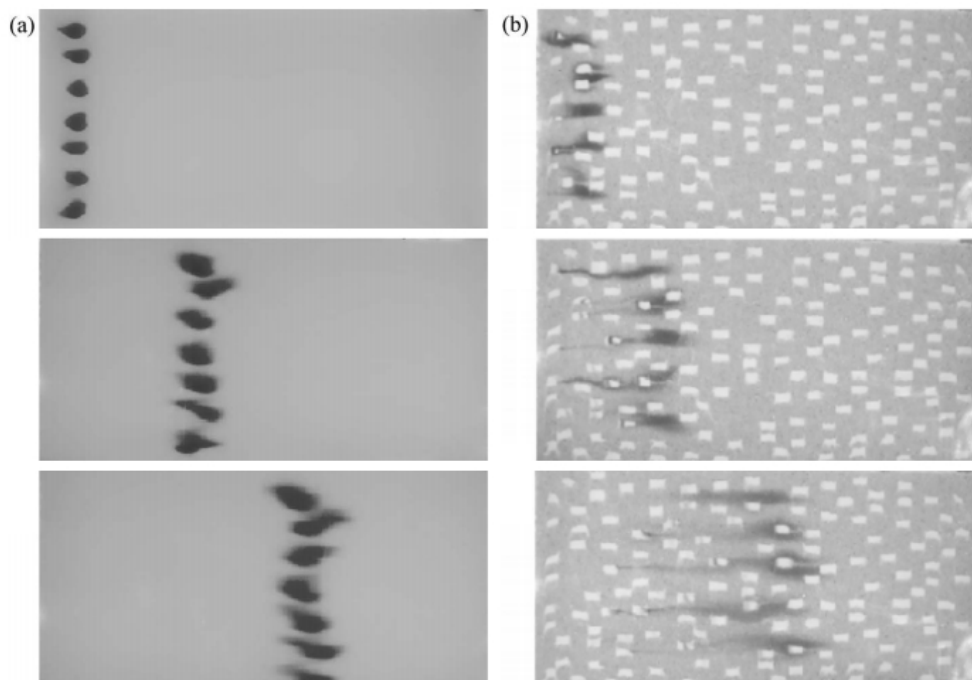


Figure 1.7: Photographies of tracer propagation through homogeneous (a) and heterogeneous (b) media from Levy and Berkowitz [2003].

The experimental results from Levy and Berkowitz [2003], shown in Figure 1.7, demonstrate the difference in transport behavior in homogeneous and heterogeneous media. Figure 1.7a, corresponding to homogeneous media, shows tracer plume that disperses uniformly around average tracer velocity. In contrast, irregular shapes of tracer plume in heterogeneous media reflect mass spreading related to preferential flowpaths (Figure 1.7b). As a consequence, the classical advection-dispersion theory cannot effectively describe transport in heterogeneous media. The investigation of processes involving in transport in fractured media is a subject of numerous studies [e.g. Becker and Shapiro, 2003; Bodin et al., 2003a; Gelhar and Welty, 1992]. Additional processes involved in transport in fractured

media have been well identified and one can synthesize them as follows [Bodin et al., 2003a]:

- Dispersion at fracture scale related to fracture roughness and fracture aperture variability [Detwiler et al., 2000].
- Dispersion at the scale of a fracture network due to transport in different flowpaths [Moreno and Neretnieks, 1993].
- Diffusion of the solute in the fracture plane and in the rock matrix [Novakowski and Lapcevic, 1994].
- Physico-chemical reactions between the solute and the solid material of the matrix and the fracture walls [Smellie and Karlsson, 1999].

The principal equations describing these processes for a single fracture are described in Bodin et al. [2003b].

Solute transport in groundwater flow systems can be studied through the use of tracer migration experiments. Tracer tests generally involve the injection of solutes into one or more injection wells, and monitoring of tracer returns in fluids produced from offset observation wells (cross-borehole) or the injection well itself (push-pull) wells. Due to different transport mechanisms, mentioned above, tracer breakthrough curves (of concentration versus time) in fractures often exhibit 'anomalous' behavior including fast initial arrival times, long tails and multiple concentration peaks. Numerous studies explain breakthrough tailing by molecular diffusion of tracer into the porous matrix [Neretnieks, 1980; Novakowski and Lapcevic, 1994], while other researchers attribute such a behavior to dispersion mechanisms [Becker and Shapiro, 2003]. Multimodal curves can be explained by the channeling effects in relatively independent flowpaths [Park et al., 1997].

In order to understand and interpret tracer test data, modelling approaches are generally applied. Parameters of the model are adjusted to obtain a best fit to breakthrough curve. For such a fitting to be meaningful, the model must account for all important mechanisms that influence flow and transport patterns. However, in general the same breakthrough curve can be fitted with different conceptual models and simple tracer test data do not allow us to determine which

## 1. GENERAL INTRODUCTION

mechanism is dominant [Sanchez-Vila and Carrera, 2004]. Figure 1.8 demonstrates an example of fitting models to the tracer test data. Both tests were conducted in fractured aquifers under push-pull configuration and show a very long time for tracer recovery. Two different models, a multichannel model and a double porosity model, provide good fits to data. In the field, a better understanding of the transport behavior could be obtained by performing tracer tests under different flow and transport conditions (varying tracer velocities, pumping conditions, and distances) [Becker and Shapiro, 2000, 2003]. Moreover, different types of data, such as solute and heat tracer test data, can be used to better constraint flow and transport model. Key questions, that we want to explore in this thesis, are therefore to know if these data taken together offer complementary information and how to incorporate the different types of data in the model.

In the next section we present existing numerical approaches.

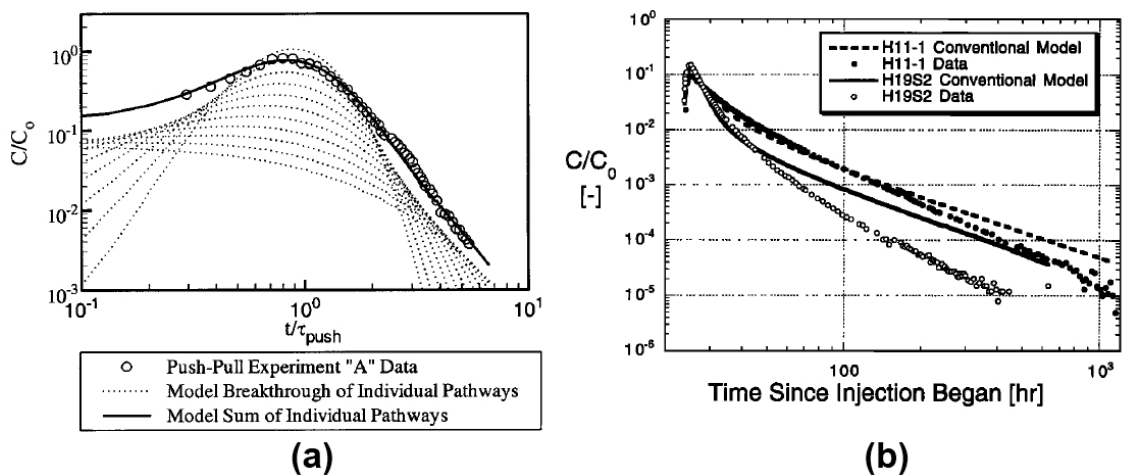


Figure 1.8: Push-pull tracer tests showing a very long time for tracer recovery from Becker and Shapiro [2003] (a) and Haggerty et al. [2001](b). Different conceptual models are used: Becker and Shapiro [2003] fitted their tracer test BTCs using a multichannel model, while Haggerty et al. [2001] explain the data with a double porosity model.

### 1.3 Flow and transport modeling in fractured media

In general, fractured aquifers are accessible to the direct observation only in boreholes. Nevertheless, often just a limited number of fractures intersecting the borehole form a connected flow paths at site scale [e.g. Le Borgne et al., 2006b]. In order to predict flow and transport in the region between boreholes, physical models that account for heterogeneous character of fractured media should be applied. A major challenge for modeling fractured media is the adequate description of heterogeneities at different scales. In order to model flow and transport in fractured media, two large classes of approaches were developed: continuum approaches and discrete fracture models. In either case, deterministic or stochastic frameworks can be considered. In contrast to deterministic concept, stochastic models provide a range of values rather than a unique solution. Furthermore, the 'hybrid' approach was proposed as a combination of stochastic continuum approach with known deterministic fractures [Berkowitz, 2002; de Dreuzy, 1999].

Continuum approaches (Figure 1.9), including equivalent porous continuum concept, dual porosity model, dual permeability model [Ando et al., 2003; Hao et al., 2008; Illman et al., 2009; Y.W.Tsang et al., 1996], aim to describe the averaged hydraulic behavior of the system, while their simplicity allows us to constrain the model with the available set of data. Nevertheless, Long et al. [1982] demonstrate that the application of a continuum approach is credible only for high density fracture networks with uniform aperture distribution and nonuniform orientation distribution.

## 1. GENERAL INTRODUCTION

---

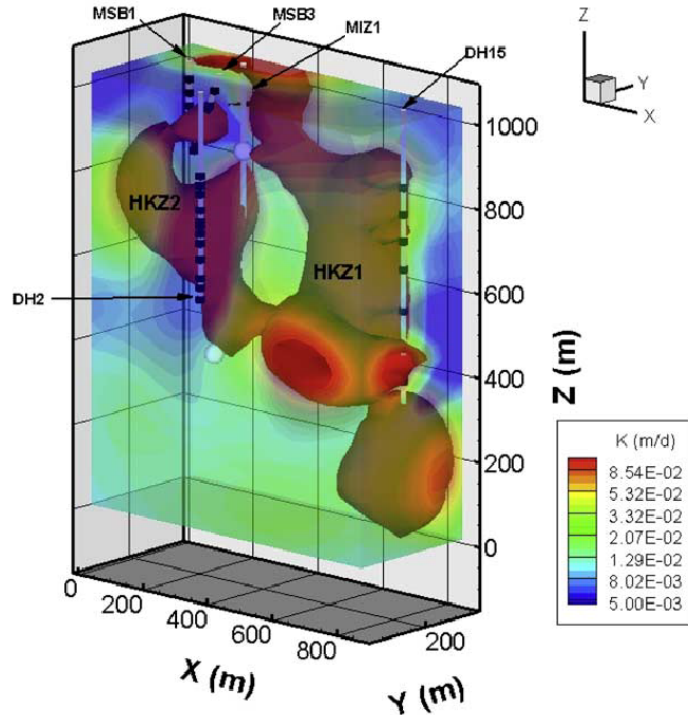


Figure 1.9: Example of application of stochastic continuum approach to hydraulic tomography data. Hydraulic conductivity  $K$  tomogram ( $m/d$ ) obtained from the inversion of two cross-hole tests from Illman et al. [2009].

Instead of capturing the effect of heterogeneity on hydraulic properties, the discrete approach represents heterogeneity (as fractures) themselves based on *in situ* measurements [Cacas et al., 1990; Frampton and Cvetkovic, 2010; Le Goc et al., 2010] (Figure 1.10). The advantage of the discrete fracture approach is that it can account explicitly for the effects of individual fractures on fluid flow and solute transport. However, the discrete fracture approach demands detailed field data including fracture geometries and spatial distribution, that limits its practical application. For a detailed overview of different numerical approaches, see de Dreuzy [1999].

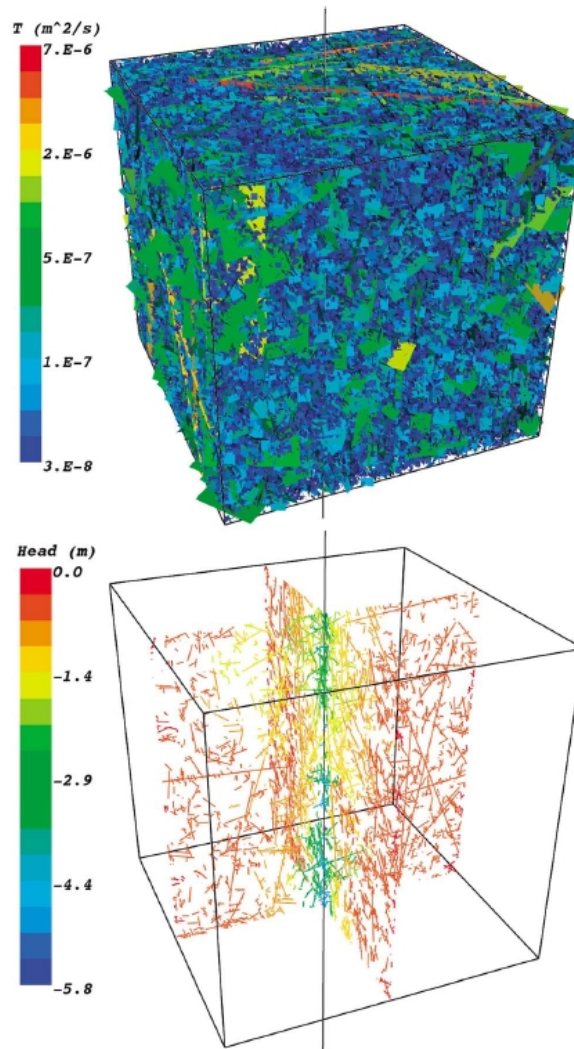


Figure 1.10: An example of the application of a stochastic discrete fracture network (DFN) approach to borehole flow rates data measured during extraction pumping, from Frampton and Cvetkovic [2010]. One DFN realization colored by transmissivity and the corresponding pressure field (drawdown).

Numerous applications demonstrate that both the continuum and discrete fracture models can capture the main flow and transport patterns [e.g. Cacas et al., 1990; Hao et al., 2008; Illman et al., 2009]. To date, images of fractured hydraulic properties obtained with continuum approaches are characterized by a high smoothness and low resolution (Figure 1.9). On the other hand, available

## 1. GENERAL INTRODUCTION

---

data content are generally limited, resulting in high uncertainties in individual fracture characterization with DFN models [e.g. Le Goc et al., 2010]. The choice of the most suitable conceptual model for characterization of fractured media is still highly debated [Neuman, 2005]. On the basis of these models, a wide variety of experimental methods has been reported in the literature. In the next part we discuss the existing field methods for imaging of fractured media in between boreholes.

### 1.4 Imaging of hydraulic and transport properties of fractured media

For realistic modelling of flow knowledge about the spatial characteristics of hydraulic parameters is required. Different hydraulic and tracer tests measurements have been proposed for imaging of fracture hydraulic properties and their connectivity. Geophysical surveys may also image fractured media by providing fracture geometry [Rubin and Hubbard, 2005]. An example showing the advantage of using geophysical methods is shown in Chapter 3. The combination of tracer test data with geophysical imaging is investigated in Dorn et al. [2012] (Appendix A). However, in this section we focus on hydraulic and tracer test data based approaches.

#### 1.4.1 Hydraulic tomography

Hydraulic tomography was proposed recently as a field method for imaging of hydraulic conductivity between boreholes [Butler et al., 1999; Yeh and Liu, 2000]. A classical pumping test consists of pumping in a well while monitoring water levels in the other wells, assuming aquifer homogeneity. Application of the tomography principle to cross-hole pumping test allows us to gain more information on the spatial distribution of hydraulic properties. The idea of tomography is to change successively the source and monitoring wells. By using packers, the well is divided into a small intervals, and then water is pumped from (or injected into) the aquifer through these isolated intervals. The hydraulic head responses are then monitored in others intervals (Figure 1.12). By sequentially changing

the pumping and observation intervals many hydraulic head data sets can be obtained. The joint inversion of the series of such cross-pumping tests produces then the images of hydraulic conductivity and specific storage (if transient heads are used). Several researchers proposed the inverse models to interpret such data sets [e.g Day-Lewis et al., 2000; Illman et al., 2008, 2009; Yeh and Liu, 2000].

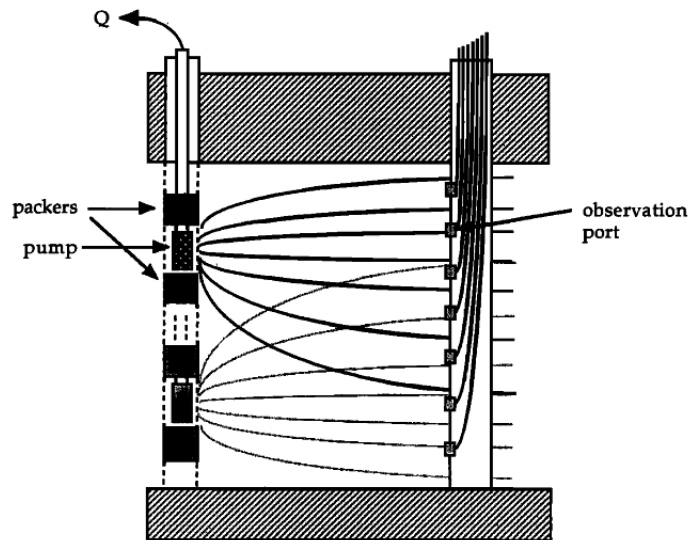


Figure 1.11: Schematic cross-sectional view of hydraulic tomography experiment [Butler et al., 1999].

The sequential successive linear estimator (SSLE) was proposed by Yeh and Liu [2000] to analyze steady state head data from a hydraulic tomography survey. SSLE is an iterative geostatistical inverse method for estimating the distribution of hydraulic parameters, that uses head data sets sequentially. This is the extension of SLE (successive linear estimator) approach, that uses a linear estimator successively to seek mean parameter fields conditioned on available data. Zhu and Yeh [2005] extended the method for interpreting data from transient hydraulic tomography to estimate three-dimensional hydraulic conductivity and specific storage fields of aquifers. The application of this algorithm to synthetic fractured media demonstrated the feasibility of hydraulic tomography to detect the fracture zone distribution and obtaining their general connectivity pattern [Hao et al., 2008]. Results of this study also demonstrate that characterization of fracture

## 1. GENERAL INTRODUCTION

---

connectivity became more successful with the increasing number of observation wells. Illman et al. [2009] applied SSLE algorithm on a fractured granite field site to characterize fracture distribution, connectivity and their hydraulic parameters ( $K$  and  $S$ ). The estimated 3-D conductivity field presented on Figure 1.9 reveals two fast flow pathways. Nevertheless, due to the high smoothness of the inferred tomograms it seems difficult to delineate individual fractures pattern. Recently, Sharmeen et al. [2012] demonstrated from the controlled laboratory conditions that conducting a larger number of pumping tests can significantly improve imaging of fracture patterns and their connectivity. Thus, although promising, hydraulic tomography does not still allow fine resolution imaging on field site scale.

On the other hand, application of hydraulic tomography is associated with a technical difficulty: obtaining a 3D characterization with hydraulic tomography requires isolation of all fractures with a packer system. This operation involves a large amount of equipment and is practically impossible in many cases, in particular when boreholes are screened. Moreover, to ensure the effective location of measurement intervals, the identification of flowing fractures is required a priori.

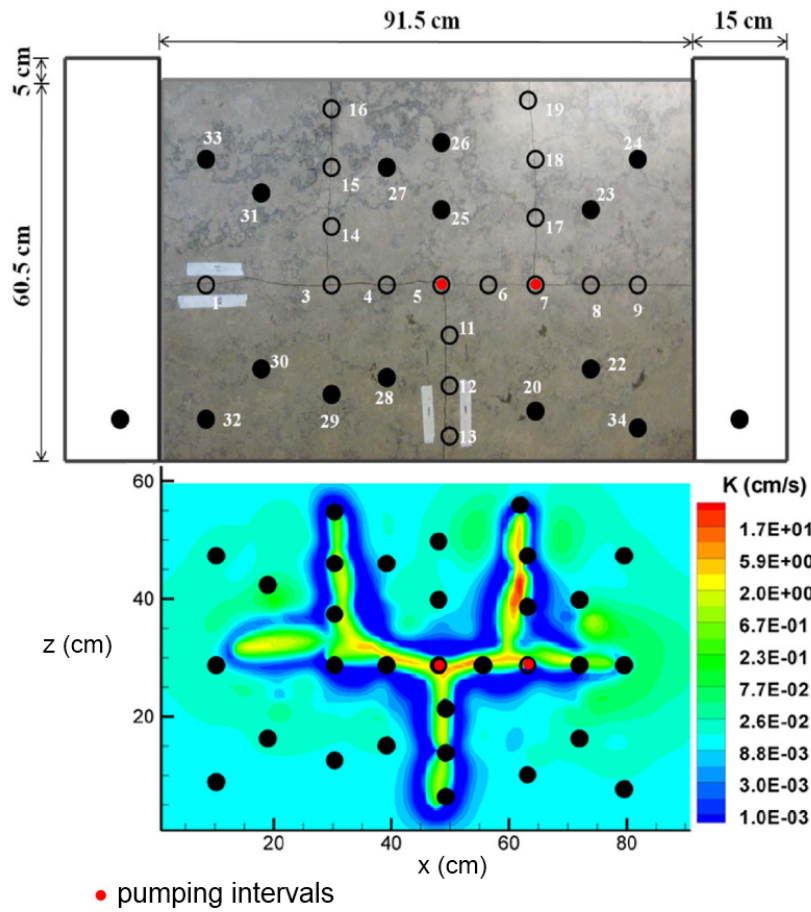


Figure 1.12: Example of imaging of permeability field with hydraulic tomography in laboratory experiment, from [Sharmeen et al., 2012]. Pumping locations are shown by red points and observation locations are shown by black points.

## 1. GENERAL INTRODUCTION

---

### 1.4.2 Flowmeter tests

An alternative field method, that does not require the use of packers, is flowmeter test. This section describes single- and cross-borehole flowmeter tests.

#### 1.4.2.1 Single-borehole flowmeter test

High-resolution borehole flow logs are used to identify the flowing fractures intersecting boreholes [Molz et al., 1989; Paillet, 1998]. Under ambient conditions, differences in hydraulic heads between large-scale flow paths that connect to a borehole generally create ambient vertical flow within the borehole [Paillet, 1998]. These differences in hydraulic head are due to the global flow direction: downwards in recharge areas and upwards in discharge areas. To estimate the hydraulic heads and local transmissivities locally to the borehole, single-borehole flowmeter tests need to be performed under two different flow conditions, usually ambient and pumping conditions (Figure 1.13). Flowing fractures can be then characterized by inspection of the pairs of ambient and pumping flow profiles [Paillet, 1998, 2000]. The most commonly used devices for such logging are the heat-pulse flowmeter [Hess, 1986], electromagnetic flowmeter and impeller flowmeter (applicable for a big discharge rates). The possible sources of errors related to flow measurements and corrections to be applied are discussed in [Paillet, 2004].

#### 1.4.2.2 Cross- borehole flowmeter test

Cross-borehole flowmeter tests are performed by turning on a pump in one of the wells, while drawdown and changes in the vertical velocity ( $s, v$ ) are monitored in observation boreholes. An example of flow pattern for a couple of boreholes under ambient conditions and cross-borehole pumping is shown in Figure 1.13. When pumping in one of the wells, hydraulic heads change only in the flow paths connected to the pumping well. Thus flow variation can be related to fracture connections in the region between and around the pumped and observation boreholes. While single-borehole flow logs are used to provide information about the properties of the individual fracture segments surrounding the borehole, cross-borehole flowmeter tests provide information on the properties of the flow zones that connect borehole pairs [Le Borgne et al., 2006a,b, 2007; Paillet, 1998].

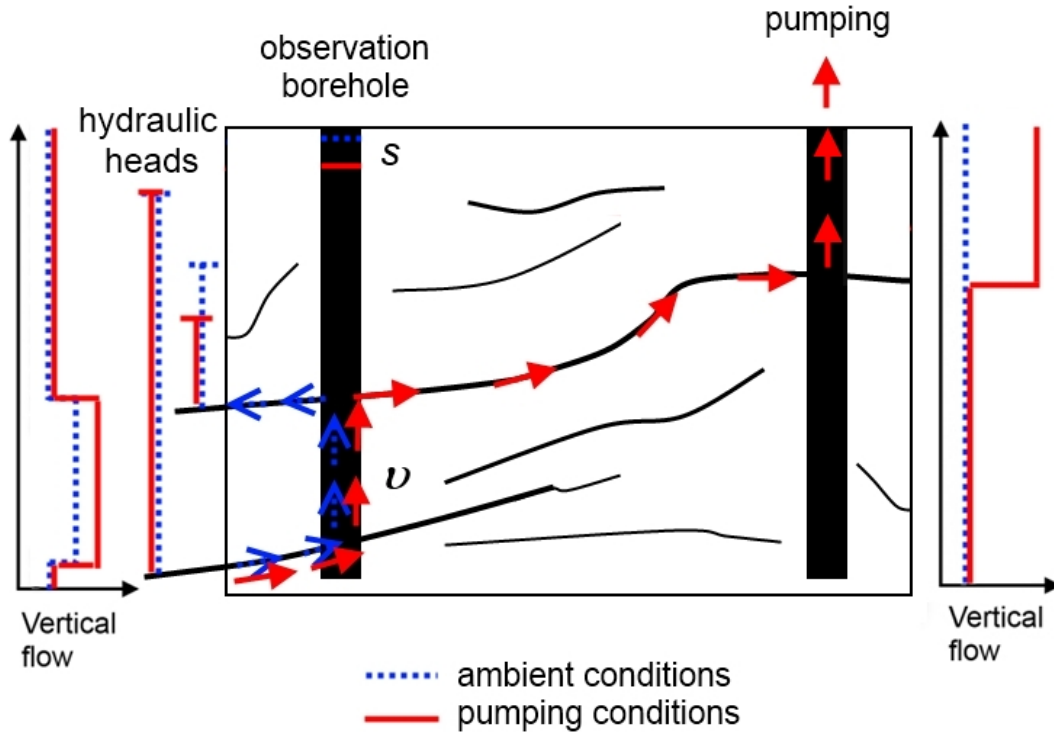


Figure 1.13: The principle of single- and cross-borehole flowmeter test. Flowing fracture corresponds to inflow point during single-borehole pumping test. During cross-borehole pumping hydraulic heads change only in flowpath connected to pumping well.

A forward modeling approach for simulating borehole flow was proposed to quantify the hydraulic properties of the large-scale flow zones [Le Borgne et al., 2007; Paillet, 1998; Williams and Paillet, 2002]. In the recent study of Paillet et al. [2012] the cross-borehole flow method is used to characterize fracture connections between two boreholes. By matching the results of transient cross-borehole pumping tests with a modeled flow they estimated fracture hydraulic properties of the 200-m deep Melechov boreholes, Czech Republic.

However, the many degrees of freedom imply that matching of the cross-borehole flowmeter data with a forward model that incorporates flowpath geometry and hydraulic properties as well as borehole flow does not have a simple nor

## 1. GENERAL INTRODUCTION

---

a unique solution. If multiple connections exist between boreholes, it is difficult to determine exactly fracture connection pattern in between the borehole pair [Le Borgne et al., 2007]. As yet, there have been no inverse methods developed for interpreting cross-borehole flowmeter tests. This is a subject of the Chapter 2.

### 1.4.3 Temperature

As we have seen qualitatively from the previous sections, characterization of flow and transport patterns from hydraulic heads or tracer tests data in fractured media is a strongly under-constrained inverse problem. The coupling of several types of data that are directly but differently sensitive to groundwater flow is a possible way to reduce the associated uncertainty [e.g. Jardani and Revil, 2009]. Recent studies demonstrate an increasing interest for using temperature data [Anderson, 2005; Saar, 2011], as geothermal heat can be seen as a natural tracer of ground water flow. The advantage of temperature measurements is that temperature can be measured easily and very accurately, continuously in space and time [Gosselin and Mareschal, 2003]. New Fiber optic methods now open the possibility to monitor in time the evolution of temperature profiles [Henderson et al., 2009; Selker et al., 2006]. The natural (conductive) geothermal gradient depends on the heat flux, the thermal conductivity of rocks and radioactive heat sources. Borehole temperature profiles are commonly measured to estimate the heat flux Jaupart et al. [2009]. Methods have been developed to estimate ground surface temperature histories and climate change [e.g. Ferguson, 2006; Freifeld et al., 2008; Rolandone et al., 2003]. For these applications one generally investigates depths where the temperature gradients are not influenced by groundwater flow.

Other applications focus on the region where the temperature gradients are disturbed. Even small deviations from a linear, conductive temperature-depth profile can represent significant advective heat transfer and indicate groundwater flow. Figure 1.14 presents the typical borehole temperature-depth profiles. Within the first ten meters, temperature is influenced by seasonal temperature variations of the land surface. Below this depth, within the geothermal zone, the

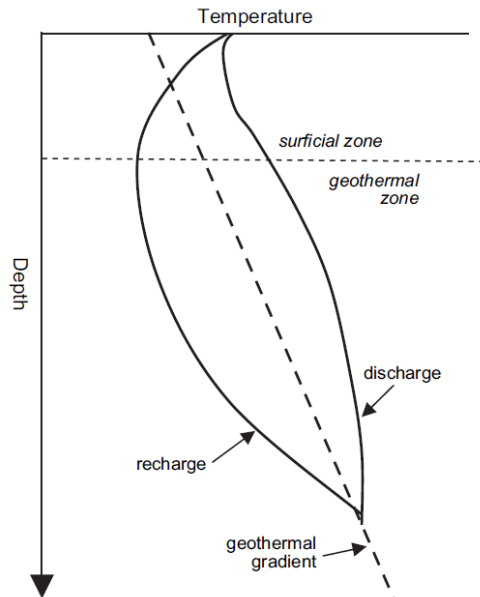


Figure 1.14: Application of borehole temperature profiles, from Anderson [2005]

temperature profile is expected to be approximately linear except when perturbed by ground water flow, changes in thermal conductivity or by the vertical flow in the borehole itself. The range of hydrogeological parameters where groundwater flow can perturbate subsurface temperature regime was shown by Ferguson [2006] (Figure 1.15). Ground water flow perturbs the geothermal gradient by downward infiltration of relatively cool water or by upward flow of relatively warm water, causing concave upward profiles in recharge areas and convex upward profiles in discharge areas (Figure 1.14). Several studies have intended to use temperature anomalies to quantify regional groundwater flow velocities [Cartwright, 1979; Marechal and Perrochet, 2001; Sorey, 1971]. This fact has been used by Bredehoeft and Papadopoulos [1965] for describing vertical steady flow of groundwater and heat through an isotropic and homogeneous media. Type curves were presented that can be matched with the temperature profile in a well to obtain the rate of regional vertical steady state ground water flow. Ge [1998] established a similar model and type curves for estimating regional flow velocities in fracture zones.

The simplest use of borehole temperature profiles in heterogenous media is

## 1. GENERAL INTRODUCTION

---

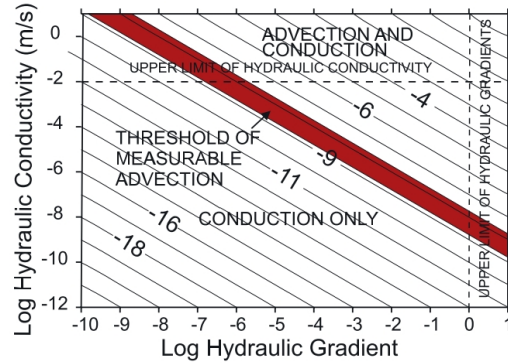


Figure 1.15: Range of hydraulic conductivities and hydraulic gradients where GWF can induces GST perturbations. The red zone indicates the range of minimum Darcy fluxes (from Ferguson [2006])

to detect the inflow zone locations. In particular, [Drury and Lewis, 1983] found that well temperature profiles in fractured rocks often show abrupt temperature changes which are caused by water of warmer or colder origins. Two types of phenomena can be observed in fractured rocks. The first type corresponds to localized abrupt temperature changes, which are controlled by fractured zones ranging from several meters to several hundred meters [Ge, 1998] (Figure 1.16a). Second pattern, shown in Figure 1.16b, is provided by large-scale fractures that conduct flow of hotter or colder temperature than the ambient temperature at a given depth. In this case sub horizontal flowing fracture distorts the linear geothermal profile by providing a fixed temperature boundary condition. Moreover, temperature profiles measured by Pehme et al. [2010] within static water columns of sealed boreholes demonstrated, that the ambient vertical flow in the borehole itself results in significant perturbations of temperature profile in between the flowing fractures (Figure 1.16c).

Borehole temperature profile in fractured media, resulting in the combination of diffusion and advection processes, is a complex signal containing a lot of information about underlying processes. Yet, relatively few methods exist for using temperature to image spatial distribution of hydraulic properties. In the next section we discuss the possible constraints that temperature data can provide on the transport behavior.

# 1. General Introduction

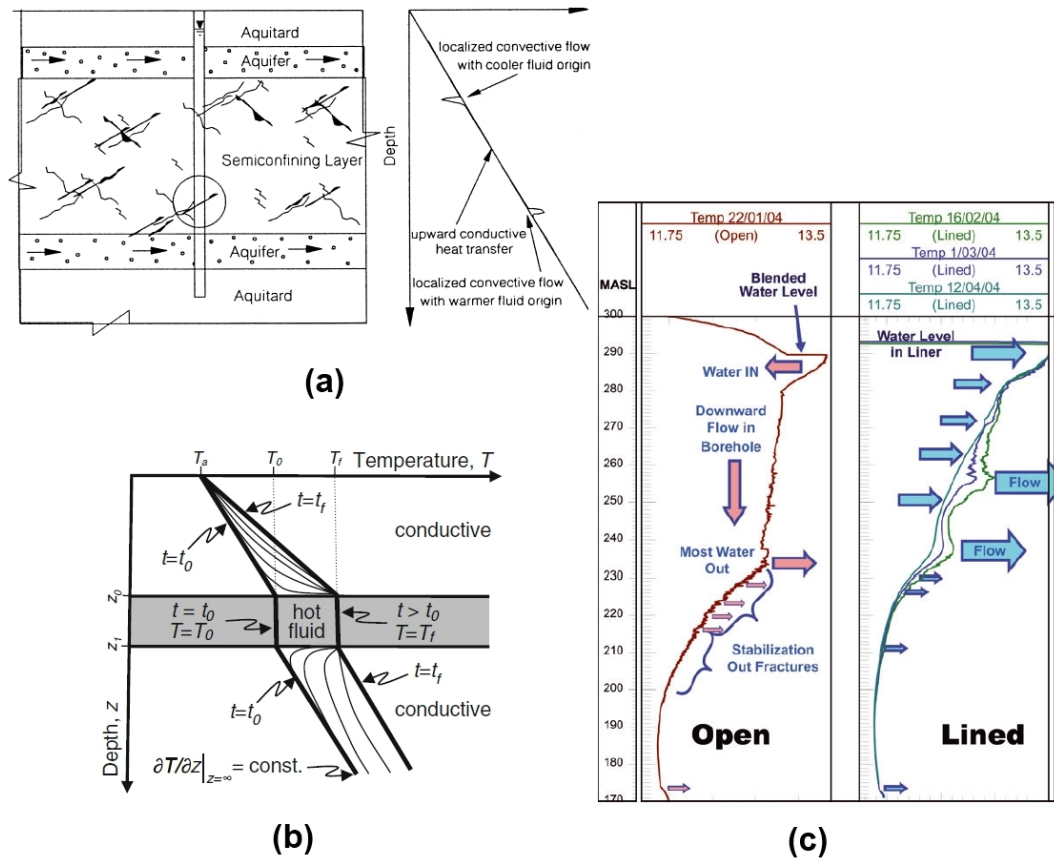


Figure 1.16: Borehole temperature profiles that are typical for fractured media: (a) temperature profile affected by flow in small-scale fractures with either warmer or cooler origins, from Ge [1998], (b) steady-state (bold lines) and transient (thin curves) temperature profiles affected by hot fluid flow in a large-scale fracture. Hot fluid flow provides a constant temperature boundary condition, from Saar [2011], (c) temperature logs collected in open and lined borehole. Rose arrows indicate ambient borehole flow, blue arrows indicate interpreted flow zones, from Pehme et al. [2010].

## 1. GENERAL INTRODUCTION

---

### 1.4.3.1 Heat tracer test

Using thermal tracer tests for characterizing fracture properties may provide more constraints compared to classical tracer tests. The fundamental difference between solute and heat transport is that heat diffusion in rocks is large compared to molecular diffusion of solutes, implying that fracture-matrix exchange is much more significant for heat than for solute tracers. Several theoretical and numerical studies investigated the movement of fluid of contrast temperature through fractures. Thus, Lauwerier [1955] proposed an analytical solution for injection of hot fluid into a confined layer. By using this model Bodvarsson and Tsang [1982] presented type curves that can be used to predict the time of thermal breakthrough during interwell heat tracer tests through fractures. These theoretical works as well as numerical studies of hydrothermal coupling at different scales [Geiger and Emmanuel, 2010; Kolditz, 1995; Molson et al., 2007; Neuville et al., 2010] show that heat transfer from rocks to fluids through the available fracture-matrix interface area results in high thermal retardations and significantly attenuates thermal signals. An example of heat transport simulations in two-dimensional realistic fracture networks (Figure 1.17) show how the change in fracture-matrix interface area influences the heterogeneity of the temperature field. Thus, at high matrix permeability, poorly connected fractures can contribute to the heat transport, resulting in heterogeneous heat distribution in the whole matrix block (Figure 1.17 a). In contrast, for a lower matrix permeability (Figure 1.17 b and c) heat transport occurs mainly through fractures that form a fully connected pathway between the inflow and outflow boundaries, that results in highly non-Fourier behavior, characterized by early breakthrough and long tailing [Geiger and Emmanuel, 2010].

The desire for obtaining test results quickly thus promoted the idea of using 'push-pull' heat tracer tests [Kocabas, 2005; Kocabas and Horne, 1990]. Numerical simulations of Pruess and Doughty [2010] demonstrated that 'push-pull' heat tracer tests are strongly sensitive to changes in fracture-matrix interface area, while insensitive to changes in effective fracture aperture. Recently, Jung and Pruess [2012] proposed an analytical solution for 'push-pull' tracer test including a quiescent period. This solution implies that the effect of fracture aperture on

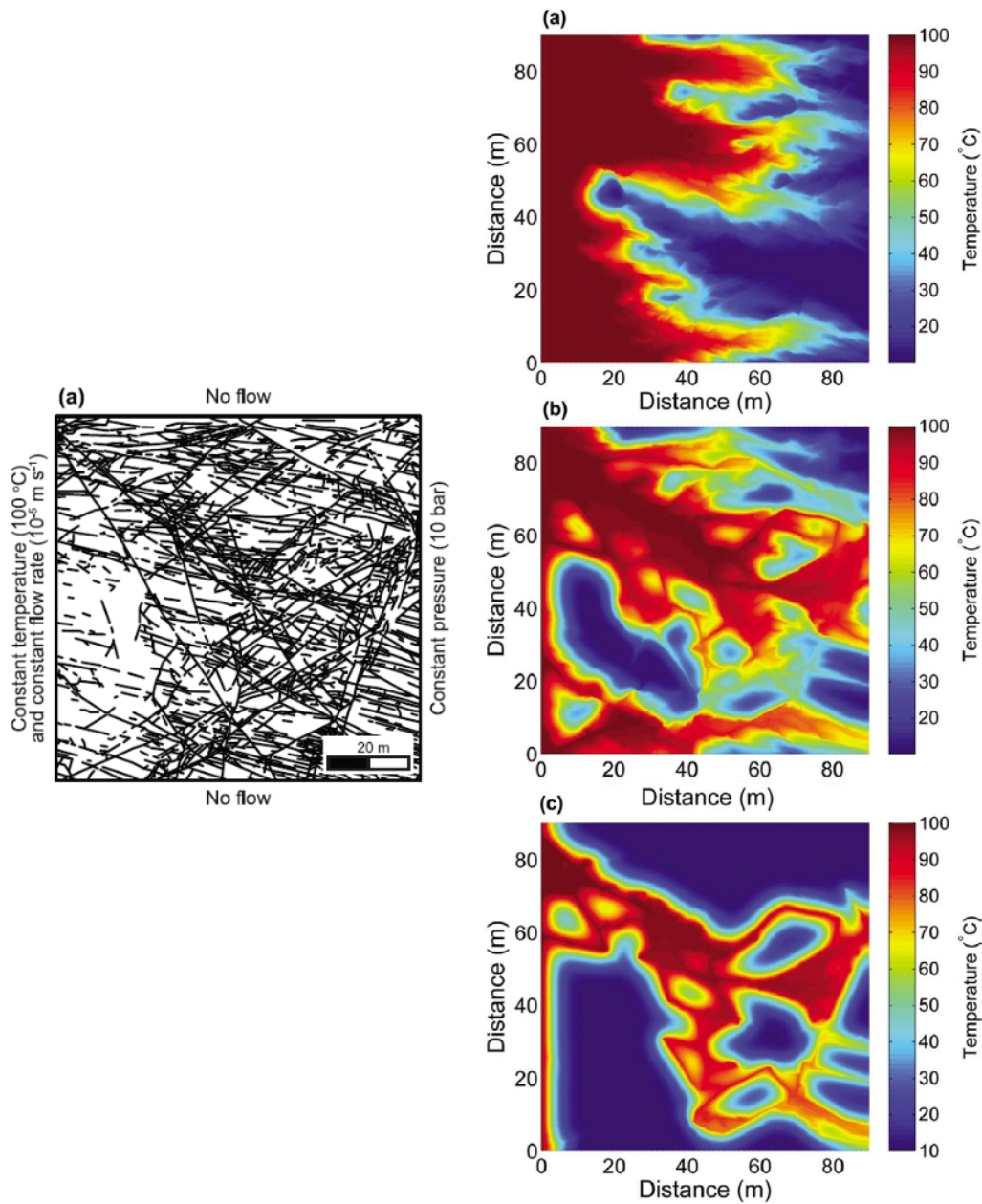


Figure 1.17: Temperature field computed for a realistic fracture geometry(a) at a matrix permeability of (b)  $10^{\hat{A}L\hat{S}11} m^2$ , (c)  $10^{\hat{A}L\hat{S}13} m^2$ , (d)  $10^{\hat{A}L\hat{S}15} m^2$ . The temperature field for the high matrix permeability case ( $10^{\hat{A}L\hat{S}11} m^2$ ) is after 50 days; all other fields are after 100 days. From Geiger and Emmanuel [2010]

## 1. GENERAL INTRODUCTION

---

temperature signal during push-pull tracer tests is weak. However, by applying different flow velocities for injection and withdrawal the sensitivity of thermal breakthrough curves to the fracture aperture can be increased [Jung and Pruess, 2013]. It was also demonstrated that while flow rate influence both the cooling rate during injection and the heating rate during pumping. As a result these effects are compensated at the fracture inlet.

Thus, the question of what information can be extracted from heat tracer tests and what parameters are likely to be difficult to determine should to be addressed. Moreover, it is necessary to verify and validate the models by heat tracer tests in real fractures networks in their natural environment i.e. by in situ experiments.

### 1.5 Approaches proposed in thesis

Fractures may act as flow conduits or barriers thereby forming extremely heterogeneous media. The prediction of flow and transport in such a heterogeneous media presents a challenge. Direct characterization of heterogeneities is possible only through the boreholes or using geophysical methods. And, as we have shown in previous sections, fine resolution imaging of fracture hydraulic properties in between the boreholes is currently not possible. In this thesis we are focusing on developing new methods for imaging the hydraulic and transport properties of transmissive fractures at the field-scale. For this purpose we performed new experiments that were conducted at the fractured crystalline Ploemur field site, where a comprehensive database including geological, geophysical and hydraulic data is available. The detailed description of the site is given in Chapter 3. We propose four complementary approaches that involve new field measurements as well as new inverse modeling frameworks. These approaches constitute the four chapters of the thesis.

As discussed in this chapter, traditional inversion methods have been developed for porous aquifers whose hydraulic properties vary smoothly in space. Our objective is to develop new inversion methods that are adapted for fractured media. We then propose an inverse model framework for interpreting cross-borehole data providing an inverse solution to fracture connectivity and transmissivities.

## 1. General Introduction

As we have shown, temperature data can be used to deduce flow patterns. We then demonstrate in the second chapter, that temperature gradient anomalies can be inverted to estimate vertical borehole flow velocities (Figure 1.18). This borehole-scale study allows the inference of properties of fractures intersecting the borehole.

Based on this finding, we propose a new temperature tomography approach in the third chapter, in which temperature profiles are measured under combinations of pumping conditions by successively changing pumping and observation boreholes. Thus, these results provide new insights on how to include temperature profiles in inverse problem for imaging heterogeneous fracture properties at the site-scale. As discussed in this section, the characterization of transport fracture properties from tracer tests is a strongly under-constrained inverse problem. In the last section of the thesis we discuss the advantages of using heat tracer test data to provide new constraints on transport in fractured media.

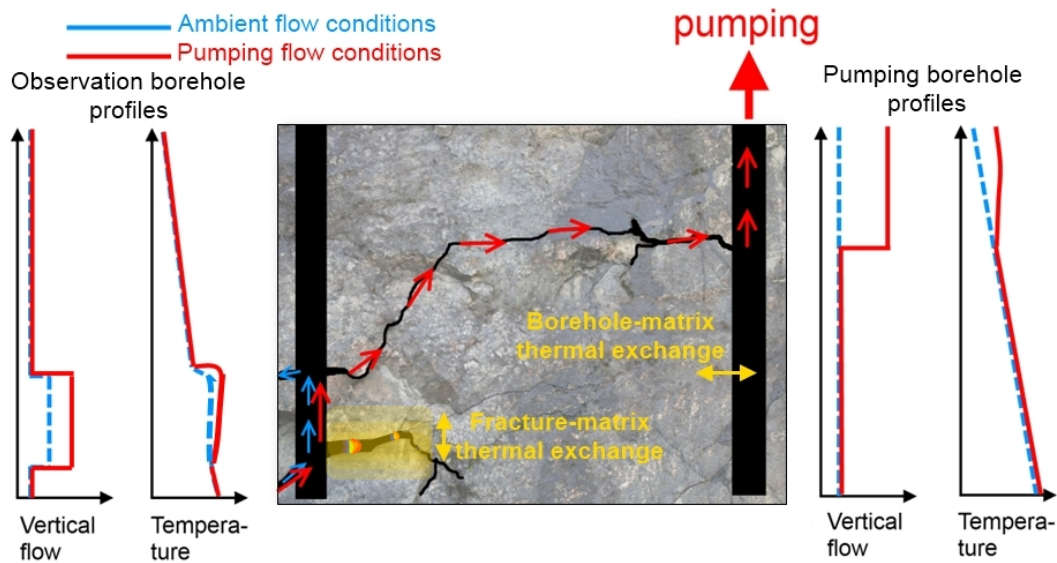


Figure 1.18: Schema of flow and temperature measurements during cross-borehole pumping test. Two scales of investigation are shown. Small-scale study considers borehole-matrix thermal exchange. Large-scale investigations concerns to flowpaths connecting the pair of 'pumping-observation' boreholes. Hot water movement in fractures is controlled by fracture-matrix thermal exchange.

## 1. GENERAL INTRODUCTION

---

# Chapter 2

## Inverse framework for flow tomography experiment

### 2.1 Introduction

As discussed in Chapter 1, the cross-borehole flowmeter test is a promising method to delineate hydraulic heterogeneities [Le Borgne et al., 2006b; Paillet, 1998]. The principle of this approach is to monitor vertical borehole flows induced by differences in fracture hydraulic heads. These differences in heads are either driven by ambient conditions or by pumping in neighboring boreholes. Pumping in one of the wells modifies hydraulic heads in large-scale flow paths, which in turn change vertical flow between the fractures intersecting the observation borehole [Le Borgne et al., 2006a]. These flow variations provide information on the connectivity and hydraulic properties of the fracture zones that connect borehole pairs [e.g., Le Borgne et al., 2007; Paillet, 1998, 2000; Paillet et al., 2012]. However, due to many degrees of freedom, the interpretation of cross-borehole flowmeter test data is not straightforward. As yet, no inverse method has been proposed to interpret such a data set.

In this paper we investigate the utility of using the cross-borehole flowmeter test in a tomographic approach, where the roles of pumping and observation wells are successively exchanged. We demonstrate that this new method, referred to as flow tomography, provides detailed characterization of fracture networks

## 2. INVERSE FRAMEWORK FOR FLOW TOMOGRAPHY EXPERIMENT

---

without the necessity of using packers. We propose a general method to invert flow tomography data based on a discrete fracture network approach.

### 2.2 Paper: Inverse modelling of flow tomography experiments in fractured media (Klepikova et al., submitted for possible publication in Water Resources Research)

# <sup>1</sup> Inverse modelling of flow tomography experiments in <sup>2</sup> fractured media

Maria V. Klepikova<sup>1</sup>, Tanguy Le Borgne<sup>1</sup>, Olivier Bour<sup>1</sup>, and Jean-Raynald  
de Dreuzy<sup>1,2</sup>

---

Corresponding author: M. V. Klepikova, Géosciences Rennes, OSUR, UMR CNRS 6118, University of Rennes 1, Rennes, France. (maria.klepikova@univ-rennes1.fr)

<sup>1</sup>Géosciences Rennes, OSUR, UMR CNRS  
6118, University of Rennes 1, Rennes,  
France.

<sup>2</sup>Institute of Environmental Analysis and  
Water Studies, CSIC, Barcelona, Spain.

**Abstract.**

The accurate characterization of the location, hydraulic properties and connectivity of major fracture zones is essential to model flow and solute transport in fractured media. Cross-borehole flowmeter tests, which consist of measuring changes in vertical borehole flows when pumping a neighboring borehole, were shown to be an efficient technique to provide information on the properties of the flow zones that connect borehole pairs [Paillet, 1998; Le Borgne *et al.*, 2006b]. The interpretation of such experiments may, however, be quite uncertain when multiple connections exist. In this study, we explore the potential of flow tomography (i.e., sequential cross-borehole flowmeter tests) for characterizing aquifer heterogeneity. We propose a framework for inverting flow and drawdown data to infer fracture connectivity and transmissivities. We demonstrate that successively exchanging the roles of pumping and observation boreholes improves the quality of available information and reduces the under-determination of the problem. The inverse method is validated for several synthetic flow scenarios. It is shown to provide a good estimation of connectivity patterns and transmissivities of main flowpaths. It also allows the estimation of the transmissivity of fractures that connect the flowpaths but do not cross the boreholes, although the associated uncertainty may be high for some geometries.

## 1. Introduction

23 Fractured aquifers are characterized by strong heterogeneities at multiple scales [e.g.  
24 *Bonnet et al.*, 2001]. However, flow generally takes place in a limited number of dominant  
25 fracture zones [*Tsang and Neretnieks*, 1998]. The identification of these dominant flow  
26 paths, their connectivity patterns and their hydraulic properties is critical as they control  
27 the transfer of fluids as well as the transport of solutes in the subsurface [*Dorn et al.*,  
28 2011; *Illman et al.*, 2009].

29 Recent developments show that applying hydraulic tomography (HT) to cross-hole  
30 pumping test is a promising approach to delineate hydraulic heterogeneities [*Yeh et al.*,  
31 2000; *Sharmeen et al.*, 2012]. The principle of such tomography is to change successively  
32 the pumping and monitoring wells to image the properties of the medium [*Butler et al.*,  
33 1999]. Thus, *Hao et al.* [2008] demonstrated the feasibility of hydraulic tomography to  
34 detect high hydraulic conductivity fracture zones and obtain their general connectivity  
35 pattern. Using this method, *Illman et al.* [2009] were able to successfully identify and  
36 characterize transmissive flow paths in a fractured granite where all transmissive frac-  
37 tures were isolated with a packer system. However, isolation of fractures with a packer  
38 system involves a large amount of equipments and is practically impossible in many cases,  
39 in particular when boreholes are screened. Moreover, to ensure the effective location of  
40 measurement intervals, the identification of flowing fractures is required a priori.

41 An alternative method that does not require the use of packers is the cross-borehole  
42 flowmeter test approach [*Paillet*, 1998; *Le Borgne et al.*, 2006b]. The principle of this  
43 approach is to monitor vertical borehole flows induced by differences in fracture hydraulic

heads. These differences in heads are either driven by ambient conditions or by pumping  
in neighboring boreholes. Pumping in one of the wells induces hydraulic head variations in  
large-scale flow paths, which in turn drives vertical flow variations between the fractures  
intersecting the observation borehole [*Le Borgne et al.*, 2006a]. These flow variations can  
be interpreted to estimate the connectivity and hydraulic properties of the fracture zones  
that connect borehole pairs [e.g., *Paillet*, 1998, 2000; *Le Borgne et al.*, 2007; *Paillet et al.*,  
2012]. Nevertheless, due to the many degrees of freedom, matching the cross-borehole  
flowmeter data with a forward model that incorporates flowpath geometry and hydraulic  
properties as well as borehole is unlikely to have a simple nor a unique solution. As yet,  
no inverse methods have been developed for interpreting cross-borehole flowmeter tests.  
This is the objective of the present study.

We investigate the interest of using the cross-borehole flowmeter test principle in a  
tomographic approach, where the pumping and observation wells are successively changed.  
We hypothesize that such tomography approach based on flowmeter measurements should  
reduce the uncertainty and non uniqueness of the solution with respect to classical cross-  
borehole flowmeter tests. Furthermore, it should provide the same level of characterization  
as 3D hydraulic tomography without the necessity of using packers. We therefore develop  
an inverse modeling framework for flow tomography experiments using a discrete fracture  
conceptual model of flow and connectivity.

In the first part of this paper we detail the principle of the cross-borehole flowmeter  
test. In the second section we present a simple conceptual model of flow and connectivity  
for fractured media. In the third section, we describe the numerical flow model and  
we develop an inverse problem approach for flow tomography. In the final part of the

67 manuscript we focus on a sensitivity analysis and discuss the uncertainties of the method  
68 for different flow scenarios.

## 2. Principle of Cross-Borehole Flowmeter Tests

69 An example of flow pattern for two boreholes under ambient, single-borehole and cross-  
70 borehole pumping conditions is shown in Figure 1. Under ambient condition, differences  
71 in hydraulic heads between the different flow paths that connect to a borehole generally  
72 create ambient vertical flow within the borehole [Paillet, 1998]. During pumping in one of  
73 the wells, hydraulic head changes occur only in the flow paths connected to the pumping  
74 well. By inspection of the pairs of ambient and pumping flow profiles, main flow zones  
75 intersecting the borehole pair can be detected and characterized from changes in the  
76 measured vertical flow [Paillet, 1998; Le Borgne et al., 2007]. During cross-borehole  
77 flowmeter tests the drawdown and the variations in vertical velocity ( $s, v$ ) are monitored  
78 in observation boreholes. The drawdown  $s$  depends on the overall transmissivity of all  
79 connected fractures. The magnitude of the velocity  $v$  is controlled by the difference  
80 in hydraulic heads induced by pumping. This difference in hydraulic heads, in turn,  
81 depends on the transmissivities of the connecting fractures. Cross-borehole flowmeter  
82 tests can be used to determine which of the fracture zones in the observation well are  
83 connected to the pumping well and to infer fracture hydraulic properties through type  
84 curves matching [Hess, 1986; Molz et al., 1989; Paillet, 1998]. Nevertheless, if multiple  
85 connections exist between boreholes, the connectivity patterns may be less easy to identify  
86 as different combinations of fracture connectivity and transmissivity may provide similar  
87 cross borehole flow responses [Le Borgne et al., 2007]. In the following, we investigate this  
88 uncertainty and its potential reduction by use of the tomography approach.

### 3. Conceptual Model of Flow and Connectivity

89 Appropriate inverse models to interpret hydraulic tomography data sets are still under  
90 debate [e.g., *Day-Lewis et al.*, 2000; *Yeh et al.*, 2000; *Illman et al.*, 2008, 2009; *Brauchler*  
91 *et al.*, 2011; *Castanga et al.*, 2011]. Classical approaches assign averaged properties to  
92 bulk regions of the aquifer and results in smooth tomograms that do not match the sharp  
93 variations of fracture patterns [*Day-Lewis et al.*, 2005; *Illman et al.*, 2009]. In the case  
94 of fractured media, discrete fracture network models may be more appropriate since flow  
95 is highly localized in fractures with hydraulic apertures of a few millimeters to at most a  
96 centimeter [*Olsson*, 1992; *Wellman and Poeter*, 2005]. However, detailed characterization  
97 of fracture network geometry including information on location, orientation, length and  
98 spacing of fractures is generally not possible without using additional geophysical surveys  
99 [e.g. *Day-Lewis et al.*, 2003; *Dorn et al.*, 2012]. Furthermore, a large number of adjustable  
100 parameters would be required to express the complexity of real fracture geometry (Figure  
101 2A). However, the data available in the field are typically insufficient to provide such a  
102 degree of complexity. Drastic simplification is required to produce a tractable numerical  
103 model.

104 Considering a pumping and a observation borehole, several main flowpaths can in gen-  
105 eral be detected in each borehole with single-borehole flowmeter measurements (Figure  
106 2A). Considering the case where each borehole is intersected by two main fractures, the  
107 typical fracture connections that are possible can be synthesized through (Figure 2B): 1)  
108 a single fracture connecting the pumping and observation boreholes and one disconnected  
109 fracture in each borehole; 2) two pumping borehole fractures connecting one observation  
110 borehole fracture; 3) two fractures connecting both boreholes without any interconnec-

111 tion between them; 4) two fractures connecting both boreholes with an interconnection  
112 between them through a fracture that does not intersect the boreholes. Furthermore, we  
113 believe that more complex cases with a large number of fractures in the interval between  
114 the boreholes can be approximated by juxtaposition of these basic kinds of connections.

115 Here we propose a simplified discrete fracture network approach that highlights such  
116 connectivity structures. This conceptual model attempts to reproduce fracture network  
117 connectivity without taking fracture geometry (length, orientation, dip) into account. In  
118 this simplified fracture network model (Figure 2C), the observation and pumping bore-  
119 holes are both intersected by two horizontal fractures of transmissivity  $T_B$ . These fractures  
120 are connected by a vertical fracture equally distanced from both boreholes. To control  
121 connectivity between the boreholes different values of transmissivity are attributed to  
122 the different sections of the vertical connecting fractures ( $T_1$ ,  $T_2$  and  $T_3$  in Figure 2C).  
123 The upper ( $T_1$ ) and/or lower ( $T_3$ ) sections of the vertical fracture ensure the connectivity  
124 between both boreholes, while the inter connection ( $T_2$ ) section controls the interconnec-  
125 tion of the upper- and lower- fractures. The different combinations of these parameters  
126 ( $T_1$ ,  $T_2$  and  $T_3$ ) allow this case to be split into the four kinds of fracture connections  
127 described in Figure 2B. Thus this approach allows all the principal types of connections  
128 to be differentiated (Figure 2B) while introducing an order of complexity that matches  
129 the information content of the data. In applying this simplified model to a real fracture  
130 systems, it is important to recognize that the approach does not model fracture network  
131 geometry. Despite this simplification, we aim to asses both the structure of preferential  
132 flowpaths and its hydraulic properties, whereas existing continuous approaches provide  
133 only the mean property of media.

134 The flow tomography approach proposed in this study consists of the following steps:

135 • Detection of fracture zones intersecting the observation and pumping boreholes and  
 136 definition of local transmissivities of these fractures ( $T_B$ ) through interpretation of ambient  
 137 and steady pumping flow profiles [*Paillet, 2000; Sawdey et al., 2012*].

138 • Definition of the fracture connectivity model. Once the local fracture transmissivities  
 139 have been determined, the number of parameters is equal to the number of possible  
 140 connecting fractures.

141 • Estimation of the transmissivities of connecting fractures between the pumping and  
 142 observation boreholes through inversion of cross-borehole flow profiles.

143 The first two steps correspond to preliminary investigations and in this study we are  
 144 focusing on the inverse problem of the last step.

#### 4. Direct Flow Modeling

145 We study the hydraulic responses of connected fractures under cross-borehole pumping  
 146 conditions, by developing a 3-D numerical model (with 2-D flow in each fracture) that  
 147 simulates flow in the simplified fracture network (Figure 3). The model considers cylin-  
 148 drical boreholes that are intersected by the fractures. The rock matrix between fractures  
 149 is impermeable but the approach can be easily extended to fractured/porous rock. We  
 150 assume a Darcy flow in the fractures, and the volume flow rate per unit fracture length  
 151 on the fracture is given by

$$u = -\frac{k}{\mu}d\nabla p, \quad (1)$$

where  $k$  describes the fracture permeability ( $m^2$ ),  $d$  is the fracture aperture ( $m$ ). Each fracture is characterized by a value of transmissivity  $T$ , which is given by

$$T = d \frac{k \rho g}{\mu}. \quad (2)$$

152 In the following synthetic flow models, the fracture aperture is fixed at  $d = 1 \cdot 10^{-3} m$ . We  
 153 apply zero-head boundary conditions on the edges of fractures and no-flux boundary on  
 154 the faces of the rock matrix. Under these conditions, no ambient flow takes place in the  
 155 boreholes. Hence, the model results can be compared to field data, with the ambient flow  
 156 profile subtracted from the pumping profiles [Paillet, 1998]. Furthermore, we simulate  
 157 here steady-state flow profiles, which are relevant for fracture media where quasi-steady  
 158 state conditions are quickly attained, due to low storativity and relatively large trans-  
 159 missivity [Le Borgne et al., 2007]. However, the approach can be further extended to  
 160 simulate and invert transient responses. The partial differential equations are solved with  
 161 the finite element code Comsol Multiphysics 4.2a with a fine tetrahedral meshing. Various  
 162 tests were performed to get a mesh-independent result. The code was also benchmarked  
 163 against analytical solutions for ground water flow and an existing hydraulic model for  
 164 cross-borehole flow analysis [Paillet, 1998].

165 The rectangular domain  $L_x = 200 m$ ,  $L_y = 200 m$ ,  $L_z = 100 m$  dimensions are set to be  
 166 much larger than the radius of influence of the pumping tests. Two boreholes separated  
 167 by  $7 m$  are each intersected by a pair of fractures. Pumping in one of the wells induces  
 168 radial flow through connected fractures. The borehole radius is set at  $0.05 m$  and the  
 169 pumping rate is fixed at  $Q = 2.5 \cdot 10^{-3} m^3/s$ . To test the model we let the transmissivities  
 170 of the fracture connections vary in a reasonable range given by  $T_n \simeq [10^{-6} m^2/s, 10^{-3}$   
 171  $m^2/s]$  for  $n = 1, 2$  and  $3$ . For illustration purposes, the transmissivities of the fractures

172 intersecting the borehole are set equal and fixed at an intermediate value  $T_B = 5 \cdot 10^{-4}$   
 173  $m^2/s$ . Nevertheless, they can in general be different and should be determined from  
 174 the single-borehole profiles [Paillet, 1998; Le Borgne et al., 2006a]. An example of flow  
 175 simulation is given in Figure 3, for the case where the upper-connection section is the  
 176 most permeable ( $T_1 = 10^{-3} m^2/s$ ,  $T_2 = 10^{-6} m^2/s$  and  $T_3 = 10^{-6} m^2/s$ ). The inverse  
 177 model consists of adjusting the transmissivities of the connecting fracture to match the  
 178 vertical flow velocities and borehole drawdowns. The transmissivities of the connecting  
 179 fractures ( $T_1$ ,  $T_2$  and  $T_3$ ) are the only fitted parameters. The inverse method for this task  
 180 is discussed in the following section.

## 5. Inverse Model Description

To estimate the fracture transmissivities from the cross-borehole flow profiles and draw-down measurements in an inverse problem approach we couple the direct flow model with an optimization algorithm. We adopt a quasi-Newton algorithm which is effective for solving nonlinear optimization problems [e.g., Yeh, 1986; Cheng and Yeh, 1992; Tarantola, 2004]. A Sequential Quadratic Programming (SQP) constrained algorithm [Mayer et al., 1999] with quasi-Newton approximations to the Hessian matrix (i.e., of the second-order partial derivatives of the misfit function) provides a superior rate of convergence when compared to the classical gradient methods [Tarantola, 2004; Hill and Tiedeman, 2007]. The misfit function,  $FO$ , which evaluates the difference between flow model simulations and observations and includes the data misfit of drawdown data ( $FO_{drawdown}$ ) and velocity data ( $FO_{velocity}$ ), is given by

$$FO = FO_{drawdown} + FO_{velocity} = \frac{1}{\sigma_v^2} \frac{1}{N_v} \sum_0^{N_v} (v_{obs} - v_{mod})^2 + \frac{1}{\sigma_s^2} \frac{1}{N_s} \sum_0^{N_s} (s_{obs} - s_{mod})^2 \quad (3)$$

181 where  $v_{obs}$  and  $s_{obs}$  are the flowmeter and drawdown observations,  $\sigma_v$  and  $\sigma_s$  are data errors  
182 for flow and drawdown respectively,  $N_v$  and  $N_s$  are the numbers of observations for flow  
183 and drawdown respectively,  $v_{mod}$  and  $s_{mod}$  are the velocity and drawdown predicted by  
184 the model. As demonstrated in Section 6.3.1, for the case with two fractures (Figure 2B)  
185 the objective function thus defined has several local minima (Figure 7). The number of  
186 local minima tends to increase with the number of fractures. Because the result provided  
187 by the quasi-Newton method is not necessarily the absolute minimum of the objective  
188 function, we improve this direct-search method by using the global search algorithm from  
189 the MATLAB optimization toolbox to generate a number of random starting points [Urgay  
190 *et al.*, 2007]. A local solver is then used to find the optima in the basins of attraction of  
191 the starting points. In the next section, we show that this simple improvement is well  
192 adapted to the fracture models studied here. As the objective function (Equation 3) is  
193 normalized to the data errors, data errors influence the value of the objective function.  
194 The convergence criteria is reached when the objective function value equals one, thereby  
195 defining the selection of acceptable solutions.

## 6. Results

196 A series of numerical simulations is first performed to study the sensitivity of obser-  
197 vation borehole drawdown and vertical flow velocity ( $s, v$ ) with respect to parameters.  
198 These results are then used to discuss the uncertainties in parameter estimation related  
199 to measurement errors. Finally, to validate our inverse approach, the flow tomography  
200 inversion is performed for different synthetic fracture network geometries.

## 6.1. Sensitivity Analysis

201 We investigate the sensitivity of drawdown and vertical flow velocity in observation  
 202 borehole  $(s, v)$  with respect to the log-transformed transmissivities of connecting fractures.  
 203 To do so, we simulate flow in the simplified fracture network (Figure 2C) with fixed  
 204 transmissivity of the fractures intersecting the borehole ( $T_B = 5 \cdot 10^{-4} \text{ m}^2/\text{s}$ ) and varying  
 205 the connecting fracture transmissivities  $(T_1, T_2, T_3)$ . Drawdown and vertical borehole  
 206 velocities were obtained for all the combinations of transmissivities of connecting fractures  
 207 changing in the interval  $T_n \simeq [10^{-6} \text{ m}^2/\text{s}, 10^{-3} \text{ m}^2/\text{s}]$  for  $n = 1, 2$  and  $3$  with a step  
 208  $\log T = 0.2$  (Figure 2C).

### 6.1.1. Sensitivity of Drawdown to Connecting Fracture Transmissivity

210 Drawdown values obtained for the different fracture transmissivities are presented in  
 211 Figure 4A as orthogonal slice planes along the  $\log T_1$ ,  $\log T_2$  and  $\log T_3$  directions. The  
 212 drawdown in the observation well is found to be strongly sensitive to the upper and lower  
 213 connection transmissivities ( $T_1$  and  $T_3$ ) and not very sensitive to the inter connection frac-  
 214 ture transmissivity  $T_2$ . Figure 4B presents a slice with a fixed value of inter connection  
 215 transmissivity  $\log T_2 = -3$ . An increase in upper ( $T_1$ ) or lower ( $T_3$ ) connection transmis-  
 216 sivity results in an increase in drawdown. Due to the symmetry of the system, the upper  
 217 ( $T_1$ ) and lower ( $T_3$ ) connection transmissivities have equal effects on the drawdown in the  
 218 observation well, as shown by the symmetry of the drawdown map in Figure 4B.

### 6.1.2. Sensitivity of Flow Velocity to Connecting Fracture Transmissivity

220 The influence of fracture transmissivities on vertical borehole velocity is shown in the  
 221 3D matrices in Figure 5A. A 2D slice with a fixed inter fracture transmissivity  $\log T_2 = -6$   
 222 is shown in Figure 5B. The upflow is maximum when the upper connection transmissivity

223  $T_1$  is largest and the lower connection transmissivity  $T_3$  is smallest. The distribution of  
224 hydraulic head for this configuration is shown in Figure 3. Conversely the downflow is  
225 maximum when the upper connection transmissivity  $T_1$  is smallest and the lower con-  
226 nection transmissivity  $T_3$  is largest. When the difference in hydraulic heads between the  
227 upper and lower connections decreases, the value of absolute velocity decreases. Hence,  
228 the difference between the upper ( $T_1$ ) and lower ( $T_3$ ) connections transmissivities controls  
229 the absolute velocity value. The direction of the vertical velocity is towards the largest  
230 transmissivity connection.

231 The effect of the inter connection transmissivity  $T_2$  can be understood from the slice  
232 with the fixed transmissivity of the lower connection  $\log T_3 = -6$  (Figure 4C). An increase  
233 of fracture inter connection transmissivity  $T_2$  leads to a decrease in the absolute value  
234 of vertical velocity since it corresponds to a decrease in the difference in hydraulic heads  
235 between the upper and lower connections.

### 236 6.1.3. Synthesis of the Sensitivity Analysis

237 The results of the sensitivity analysis can be summarized as follows:

238 A. The observed well drawdown increases with the upper( $T_1$ ) or lower( $T_3$ ) connection  
239 transmissivity and is insensitive to the inter connection transmissivity  $T_2$ .

240 B. The magnitude of the vertical borehole flow velocity increases with the difference  
241 between the upper ( $T_1$ ) and lower ( $T_3$ ) connection transmissivities and decreases with the  
242 inter connection transmissivity  $T_2$ .

243 C. The direction of the vertical borehole flow velocity is towards the largest connection  
244 transmissivity.

245 These conclusions constitute the major constraints provided by flow and borehole draw-  
246 down measurements.

## 6.2. Uncertainty Analysis

247 To evaluate the capacity of flow tomography experiments to provide reliable estimates of  
248 fracture transmissivity, we perform an uncertainty analysis on the basis of the previously  
249 obtained results (Figures 4A and 5A). The uncertainty is determined for each pair of  
250 observations as the standard deviation of the parameters that provide similar solutions  
251 within the range of error ( $\sigma = (\sigma_s, \sigma_v)$ ). Figure 6 presents the estimated uncertainties  
252 for a measurement uncertainty  $\sigma = (0.01 \text{ m}, 2 \cdot 10^{-3} \text{ m/s})$ , which correspond to typical  
253 measurement errors [Klepikova et al., 2011]. The white areas correspond to precluded  
254 couples  $(s, v)$  for the range of transmissivity values considered here.

255 According to Figures 6A and 6C the uncertainty associated with the upper ( $T_1$ ) and  
256 lower ( $T_3$ ) connection transmissivities is smaller when flow is directed towards these con-  
257 nections in the observation well. This result can be understood from the sensitivity analy-  
258 sis (Section 6.1.3). The fracture zone towards which the flow is directed in the observation  
259 well corresponds to the largest transmissivity connection (conclusion C). This connection  
260 is thus the one that controls drawdown in the observation well (conclusion A). Hence, its  
261 value is well determined. Conversely, the uncertainty for the connection that produces  
262 the flow in the observation well increases as the magnitude of borehole flow decreases. For  
263 small borehole flows, similar velocities can be produced by different combinations of the  
264 interconnection transmissivity  $T_2$  and the smallest values of  $T_1$  and  $T_3$  (conclusion B).

265 The uncertainty pattern for fracture inter connection transmissivity  $T_2$  in Figure 6B  
266 shows higher uncertainty for smaller borehole flow velocities in the observation well. This

267 uncertainty decreases with the increase in amplitude of the vertical velocity. According  
268 to conclusion B, the borehole flow velocities are small when the fracture connection trans-  
269 missivities  $T_1$  and  $T_3$  are close to each other. Furthermore, in the latter case, they are not  
270 very sensitive to the fracture inter connection transmissivity  $T_2$ . Thus, for zero vertical  
271 velocity the uncertainty about the  $T_2$  parameter is maximum. Hence, in the case of equal  
272 upper( $T_1$ ) and lower( $T_3$ ) connection transmissivity it is difficult to distinguish between  
273 the third and fourth kinds of fracture connection on Figure 2B.

274 The added value of the flow velocity data is determined by conducting the same study  
275 without taking into account vertical borehole velocity. Hence, in this case only the first  
276 constraint applies (conclusion A). The observation borehole drawdown is found to be  
277 almost insensitive to the interconnection transmissivity  $T_2$ . Moreover, the uncertainty  
278 about the  $T_1$  and  $T_3$  parameters is found to be higher and ranges from 0.3 to 0.9, which is  
279 the maximum uncertainty for the range of transmissivities tested. Thus, uncertainty can  
280 be significantly reduced by using velocity data.

### 6.3. Inverse Modeling of Multiple Connection Fracture Networks

#### 281 6.3.1. Simple Synthetic Cases

282 We first apply the inverse approach to the simple synthetic cases 1 and 4 of Figure 2B.  
283 For synthetic case 1, the parameter set is  $(\log T_1, \log T_2, \log T_3) = (-6, -6, -3)$ , which  
284 provides the largest possible vertical velocity  $v = -0.021$  m/s and a drawdown  $s = 0.5$   
285 m (Figures 4 and 5). For synthetic case 4, the parameter set is  $(\log T_1, \log T_2, \log T_3) =$   
286  $(-4.6, -4.6, -4.6)$ , which provides a zero vertical velocity and a drawdown  $s = 0.27$  m.  
287 To underline the interest of combining drawdown and flow data we present the misfit of

288 each data type separately,  $FO_{drawdown}$  and  $FO_{velocity}$ , and the sum of the two misfits,  
 289 which corresponds to the global objective (equation 3).

290 The objective functions for synthetic case 1 are shown in Figure 7 as a function of the  
 291 log-transformed parameters. For a fixed upper connection transmissivity  $\log T_1 = -6$ ,  
 292 the drawdown misfit ( $FO_{drawdown}$ , Figure 7a) displays few local minima. This is due to  
 293 the insensitivity of the drawdown to the inter connection transmissivity  $T_2$ . For a fixed  
 294 inter-connection transmissivity  $\log T_2 = -6$ , the drawdown misfit  $FO_{drawdown}$  (Figure  
 295 7d) also presents several local minima since different combinations of  $T_1$  and  $T_3$  can give  
 296 similar drawdowns. The velocity misfit on the other hand shows only one global minimum  
 297 (Figures 7b and e). Hence the global objective function presents one global minimum as  
 298 well (Figures 7c and f).

299 The objective functions for synthetic case 4 are shown in Figure 8 as a function of the  
 300 log-transformed parameters for a fixed inter connection  $\log T_2 = -4.6$ . As in the previous  
 301 case, the drawdown misfit  $FO_{drawdown}$  possesses several local minima (Figure 8a). In this  
 302 case, the velocity misfit  $FO_{velocity}$  also has a number of local minima lying on a diagonal  
 303 (Figure 8b). This is explained by the fact that zero borehole flow velocity results from  
 304 equivalent values of upper- and lower- connections (Figure 5). However, the sum of both  
 305 misfits provides a convex function with a global minimum (Figure 8c). Note that we do  
 306 not present here the misfit as a function of  $\log T_2$  since both drawdown and velocity are  
 307 insensitive to this parameter in this case (Figure 6B).

308 In both cases the objective functions are convex and possess a global minimum. Hence,  
 309 the global minima are found successfully by the applied optimization algorithm (Section  
 310 5) in both cases. Thus, the inverse method proposed seems to be sufficiently robust to

311 identify the main fracture connectivities and transmissivities. In the following we test  
312 the capacity of the flow tomography inversion to identify fracture flow patterns in more  
313 complex structures.

### 314 **6.3.2. Complex Synthetic Cases**

315 In this section we test the inverse approach for a synthetic example with more com-  
316 plex fracture network geometry. The cross-section of model geometry is presented in  
317 Figure 9 A (pumping and observation boreholes can be reversed). The pair of 'pump-  
318 ing - observation' boreholes is intersected by six fractures of transmissivity  $T_B$  form-  
319 ing two zones of constant vertical flow in each borehole. The system is parameterized  
320 by five fracture connection transmissivities  $T_i$ , with  $1 \leq i \leq 5$ . To confirm our hy-  
321 pothesis that parameters are better determined for large velocities (Section 6.2), we  
322 investigate here two generic cases, which provide two extreme cases of possible cross-  
323 borehole flow observations (large flow velocity and zero flow velocity). Firstly, we allow  
324 only one flowpaths between the boreholes ('Test 5', Figure 9B). In the second case, we  
325 consider three independent main flow paths ('Test 6', Figure 9B). The corresponding pa-  
326 rameter sets are  $(\log T_1, \log T_2, \log T_3, \log T_4, \log T_5) = (-6, -6, -3, -6, -6)$  ('Test 5') and  
327  $(\log T_1, \log T_2, \log T_3, \log T_4, \log T_5) = (-3, -6, -3, -6, -3)$  ('Test 6'). For these examples,  
328 the borehole radius is fixed at  $0.1 \text{ m}$  and the pumping rate is fixed at  $Q = 1 \cdot 10^{-2} \text{ m}^3/\text{s}$ .  
329 As before, the transmissivity of the horizontal fractures is set at  $T_B = 5 \cdot 10^{-4} \text{ m}^2/\text{s}$ .

330 To probe the interest of performing a tomography experiment, we inverse the 'pumping  
331 - observation' points for each cross-borehole pumping test. Moreover, we also perform a  
332 joint inversion of both 'pumping - observation' pumping tests. Observations for the two  
333 pumping tests consist of four vertical velocities and two drawdowns in the observation

334 borehole. A set of 50 random starting points is generated for each configuration to search  
335 for the minimum in the basins of attraction of the starting points. The minimum of the  
336 objective function provides the 'true' parameter set for all tested cases, including 'Test  
337 5' and 'Test 6' for each pair of pumping and observation boreholes and for both jointly  
338 inverted. Hence, this validates our methodology, and shows that the information content  
339 of the data is sufficient to drive the inverse algorithm to the solution. Below we perform  
340 the uncertainty analysis for both cases.

#### 341 **6.3.2.1. Complex Synthetic Case, 'Test 5'**

342 The distribution of hydraulic heads in the fracture network for 'Test 5' is shown in  
343 Figure 10A. In this case only one of the fracture connections is significantly permeable  
344 (Figure 10B). During pumping in one of the wells, the hydraulic head changes in the cen-  
345 tral connected fracture zone, cause large borehole flow velocities in both borehole sections  
346 below and above this flowpath in the observation well. The uncertainties in parameter  
347 estimation for 'Test 5' are shown on Figure 10. Figures 10 C and D present results of  
348 the inversion for each pumping test. High uncertainty about the  $T_3$  and  $T_4$  parameters  
349 are obtained when pumping from the 'right' borehole, as well as about the  $T_2$  and  $T_3$   
350 parameters when pumping from the 'left' borehole. This is explained by the fact that  
351 different combinations of fracture connection transmissivities can provide similar veloci-  
352 ties and drawdowns. For instance, during pumping from the 'right' borehole, the set of  
353 parameters  $(-6, -6, -6, -3, -6)$  gives the same observation values as a 'true' parameter  
354 set  $(-6, -6, -3, -6, -6)$ . Similarly during pumping from the 'left' borehole the set of  
355 parameters  $(-6, -6, -3, -6, -6)$  and  $(-6, -3, -6, -6, -6)$  give identical observation val-  
356 ues (Figure 9A). However, joint inversion of the two pumping tests (Figure 10C) leads

357 to a much lower uncertainty. This demonstrates the interest of performing tomography  
358 experiments.

### 359 **6.3.2.2. Complex Synthetic Case, 'Test 6'**

360 The distribution of heads and flow velocities for the second synthetic case is shown  
361 in Figures 11A and B. For 'Test 6' the drawdown is large and the velocity is close to  
362 zero. As for synthetic case 4 (Figure 2B), zero velocity is caused by equal transmissivity  
363 flowpaths. The sensitivity analysis performed for synthetic case 4 suggests that estima-  
364 tion of inter connection transmissivities in this case is uncertain. Figure 11C, D and E  
365 shows the uncertainties in parameter estimation for 'Test 6'. As expected, the inversion  
366 results show that small observed velocities do not provide a strong constraint for the inter  
367 connection fracture transmissivities ( $T_2$  and  $T_4$ ). In this case, the joint inversion of both  
368 pairs of pumping and observation wells, do not improve the estimations significantly, and  
369 estimated transmissivities of inter connection fracture vary over more than one order of  
370 magnitude. Nevertheless, despite this high uncertainty, the inverse model algorithm does  
371 converge to the 'true' parameter values for the global optimum.

## 7. Conclusions

372 The flow tomography approach is proposed to characterize the connectivity and trans-  
373 missivity of preferential permeable flow paths in fractured aquifers. We explore the po-  
374 tential of this approach for simplified synthetic fracture network models and quantify the  
375 sensitivity of drawdown and borehole flow velocities to the transmissivity of the connecting  
376 flowpaths. Flow tomography is expected to be most effective if cross-borehole pumping  
377 induces large changes in vertical borehole velocities. The uncertainty of the transmissivity  
378 estimates increases for small borehole flow velocities. The uncertainty about the trans-

379 missivity of fractures that connect the main flowpath but not the boreholes is generally  
380 higher.

381 An inverse model approach is developed to estimate log-transformed transmissivity  
382 values of hydraulically active fractures between the pumping and observation wells by  
383 inverting cross-borehole flow and water level data. While the misfit functions for draw-  
384 down data alone are characterized by multiple minima, the global objective function for  
385 drawdown and flow velocity is convex and possesses a global minimum. Thus, the inverse  
386 model is shown to converge to the 'true' parameter values in all tested cases. Our anal-  
387 ysis also demonstrates that the inversion of pumping and observation points significantly  
388 reduces the uncertainty about parameter estimation. These conclusions are confirmed for  
389 more complex connectivity patterns.

390 Flow tomography appears to be a promising approach for identification of general con-  
391 nectivity patterns and transmissivities of the main flowpaths. Even though the chosen  
392 fracture network geometry has been simplified here, the general methodology may be  
393 applied to other fracture network geometries. Hence, the results of this investigation en-  
394 courage the application of flow tomography to natural fractured aquifers. Furthermore, a  
395 possible extension of this inverse approach consists of using transient flow data to estimate  
396 both transmissivities and specific storage of the main flowing fractures.

397 **Acknowledgments.** This work was supported by the European Marie Curie network  
398 IMVUL (Grant Agreement 212298), by the National Research Observatory H+ and by  
399 the European Interreg IV project CLIMAWAT.

## References

- 400 Bonnet, E., O. Bour, N.E. Odling, P. Davy, I. Main, P. Cowie, and B. Berkowitz (2001),  
401 Scaling of fracture systems in geological media, *Rev. Geophys.*, *39*(3), 347–383.
- 402 Brauchler, R., R. Hu, P. Dietrich, and M. Sauter (2011), , *Water Resour. Res.*, *47*,  
403 W03503
- 404 Brauchler, R., R. Hu, P. Dietrich, and M. Sauter (2011), A field assessment of high-  
405 resolution aquifer characterization based on hydraulic travel time and hydraulic attenu-  
406 ation tomography, *Water Resour. Res.*, *47*(11), W03503, doi:10.1029/2010WR009635.
- 407 Butler, J.J., McElwee, C.D., Bohling, G.C. (1999), Pumping tests in networks of multilevel  
408 sampling wells: motivation and methodology, *Water Resour. Res.*, *35*(11), 3553–3560.
- 409 Castagna, M., M. W. Becker, and A. Bellin (2011), Joint estimation of transmissiv-  
410 ity and storativity in a bedrock fracture, *Water Resour. Res.*, *47*, W09504, doi:  
411 10.1029/2010WR009262.
- 412 Cheng, J.-M. and W. W.-G. Yeh (1992), A proposed quasi-Newton method for parameter  
413 identification in a flow and transport system, *Advances in Water Resources*, *15*(4),  
414 239–249.
- 415 Day-Lewis, F. D., P. A. Hsieh, and S. M. Gorelick (2000), Identifying fracture-zone ge-  
416 ometry using simulated annealing and hydraulic-connection data, *Water Resour. Res.*,  
417 *36*(7), 1707–1721, doi:10.1029/2000WR900073.
- 418 Day-Lewis, F. D., J. W. Lane Jr., J. M. Harris and S. M. Gorelick (2003), Time-lapse  
419 imaging of saline-tracer transport in fractured rock using difference-attenuation radar  
420 tomography, *Water Resour. Res.*, *39*(10), 1290, doi:10.1029/2002WR001722.

- 421 Day-Lewis, F. D., K. Singha, and A. M. Binley (2005), Applying petrophysical models  
422 to radar travel time and electrical resistivity tomograms: Resolution-dependent limita-  
423 tions, *J. Geophys. Res.*, *110*, B08206, doi10.1029/2004JB003569.
- 424 Dorn C., N. Linde, T. Le Borgne, O. Bour, and L. Baron (2011), Single-hole GPR  
425 reflection imaging of solute transport in a granitic aquifer, *Geophys. Res. Lett.*, *38*,  
426 doi10.1029/2011GL047152.
- 427 Dorn C., N. Linde, T. Le Borgne, O. Bour, and M. Klepikova (2012), Infer-  
428 ring transport characteristics in a fractured rock aquifer by combining single-hole  
429 GPR reflection monitoring and tracer test data, *Water Resour. Res.*, *48*, W11521,  
430 doi10.1029/2011WR011739.
- 431 Hao Y., T. C. Yeh, J. Xiang, W. A. Illman, K. Ando, K. C. Hsu and C. H. Lee (2008),  
432 Hydraulic tomography for detecting fracture zone connectivity, *Ground Water*, *46*(2),  
433 183–192, doi10.1111/j.1745-6584.2007.00388.x.
- 434 Hess, A. E. (1986), Identifying hydraulically conductive fractures with a slow velocity  
435 borehole flowmeter, *Can. Geotechn.*, *23*, 69–78.
- 436 Hill, M.C. and Tiedeman, C.R., 2007, Effective groundwater model calibration: With  
437 analysis of data, sensitivities, predictions, and uncertainty: Wiley and Sons, New York,  
438 New York
- 439 Hill, M.C. and Tiedeman, C.R. (2007), Effective groundwater model calibration: With  
440 analysis of data, sensitivities, predictions, and uncertainty, *Wiley and Sons, New York*,  
441 *New York*, 383–390.
- 442 Illman, W. A., A. J. Craig, and X. Liu (2008), Practical issues in imaging hydraulic  
443 conductivity through hydraulic tomography, *Ground Water*, *46*(1), 120–132.

- 444 Illman, W. A., X. Liu, S. Takeuchi, T.-C. J. Yeh, K. Ando, and H. Saegusa (2009), Hy-  
445 draulic tomography in fractured granite: Mizunami Underground Research site, Japan,  
446 *Water Resour. Res.*, *45*, W01406, doi10.1029/2007WR006715.
- 447 Klepikova, M., T. Le Borgne., O. Bour, P. Davy (2011), A methodology for using  
448 temperature-depth profiles under ambient, single and cross-borehole pumping condi-  
449 tions to estimate fracture hydraulic properties, *Journal of Hydrology*, *407*(1-4), 145–152,  
450 doi10.1016/j.jhydrol.2011.07.018.
- 451 Le Borgne, T., Paillet, F.L., Bour, O., Caudal, J.-P. (2006), Cross-borehole flowmeter tests  
452 for transient heads in heterogeneous aquifers, *Ground Water*, *44*, doi10.1111/j.1745-  
453 6584.2005.00150.x.
- 454 Le Borgne, T., Bour, O., Paillet, F.L., Caudal, J.-P. (2006), Assessment of pref-  
455 erential flow path connectivity and hydraulic properties at single-borehole and  
456 cross-borehole scales in a fractured aquifer, *Journal of Hydrology*, *328*, 347–359,  
457 doi10.1016/j.jhydrol.2005.12.029.
- 458 Le Borgne, T., O. Bour, M.S. Riley, P. Gouze, P.A. Pezard, A. Belghoul, G. Lods,  
459 R. Le Provost, R. B. Gresswell, P. A. Ellis, E. Isakov, and B. J. Last (2007),  
460 Comparison of alternative methodologies for identifying and characterizing preferen-  
461 tial flow paths in heterogeneous aquifers, *Journal of Hydrology*, *345*(3-4), 134–148,  
462 doi10.1016/j.jhydro1.2007.07.007.
- 463 Le Goc, R., J. -R. de Dreuzy and P. Davy (2010), An inverse problem method-  
464 ology to identify flow channels in fractured media using synthetic steady-state  
465 head and geometrical data, *Advances in Water Resources*, *33*(3-4), 782–800,  
466 doi10.1016/j.advwatres.2010.04.011.

- 467 Li, W., Englert, A., Cirpka, O.A., Vereecken, H. (2008), Three-Dimensional Geostatistical  
468 Inversion of Flowmeter and Pumping Test Data, *Groundwater*, 46(2), 193–201.
- 469 Mayer, A. S., and C. Huang (1999), Development and application of a coupled-process  
470 parameter inversion model based on the maximum likelihood estimation method, *Ad-  
471 vances in Water Resources*, 22(8), 841–853.
- 472 Molz, F.J., R.H. Morin, A.E. Hess, J.G.Melville and O. Guven (1989). The impeller  
473 meter for measuring aquifer permeability variations: evaluation and comparison with  
474 other tests, *Water Resources Research*, 25(7), 1677–1683.
- 475 Olsson, O., (1992). Site characterization and validation, Final Report, Stripa Project  
476 92-22, Conterra AB, Uppsala, Sweden
- 477 Paillet, F. L. (1998), Flow modeling and permeability estimation using borehole flow logs  
478 in heterogeneous fractured formations *Water Resource Research*, 34(5), 997–1010.
- 479 Paillet, F. L. (2000), A field technique for estimating aquifer parameters using flow log  
480 data, *Ground Water*, 38(4), 510–521.
- 481 Paillet, F. L., J. H. Williams, J. Urik, J. Lukes, M. Kobr and S. Mares (2012), Cross-  
482 borehole flow analysis to characterize fracture connections in the Melechov Granite,  
483 Bohemian-Moravian Highland, Czech Republic, *Hydrogeology Journal*, 20(1), 143–154,  
484 doi10.1007/s10040-011-0787-1.
- 485 Sawdey, J.R., and A.S. Reeve (2012), Automated inverse computer modeling of borehole  
486 flow data in heterogeneous aquifers, *Computers and Geosciences*, 46, 219–228.
- 487 Schuster G. T. (1996), Resolution limits for crosswell migration and travelttime tomogra-  
488 phy, *Geophys. J. Int.*, 127, 427–440.

- 489 Sharmeen, R., W. A. Illman, S. J. Berg, T.-C. J. Yeh, Y.-J. Park, E. A. Sudicky, and  
490 K. Ando (2012), Transient hydraulic tomography in a fractured dolostone: Laboratory  
491 rock block experiments, *Water Resour. Res.*, *48*, W10532, doi10.1029/2012WR012216.
- 492 Tarantola, A. (2004), Inverse Problem Theory and Model Parameter Estimation, *SIAM*.
- 493 Tsang, C.F., and I. Neretnieks (1998), Flow channeling in heterogeneous fractured rocks,  
494 *Rev. Geophys.*, *36*, 275-298.
- 495 Wellman, T. P. and E. P. Poeter (2005), Estimating spatially variable representative  
496 elementary scales in fractured architecture using hydraulic head observations, *Water*  
497 *Resour. Res.*, *41*, W03001, doi10.1029/2004WR003287.
- 498 Williams, J.H., and F.L. Paillet. (2002), Using flowmeter pulse tests to define hydraulic  
499 connections in the subsurface: A fractured shale example, *Journal of Hydrology*, *265*(1-  
500 4), 100–117.
- 501 Yeh, W. W. -G. (1986), Review of parameter identification procedures in groundwater  
502 hydrology: the inverse problem, *Water Resour. Res.*, *22*(2), 95–108.
- 503 Yeh, T.-C. J., and S. Liu (2000), Hydraulic tomography: Development of a new aquifer  
504 test method, *Water Resour. Res.*, *36*(8), 2095–2105, doi10.1029/2000WR900114.
- 505 Ugray, Zsolt, Leon Lasdon, Plummer, J. C., Glover, F., Kelly, J., and R. Marti (2007),  
506 Scatter Search and Local NLP Solvers: A Multistart Framework for Global Optimiza-  
507 tion, *INFORMS Journal on Computing*, *19*(3), 328–340.

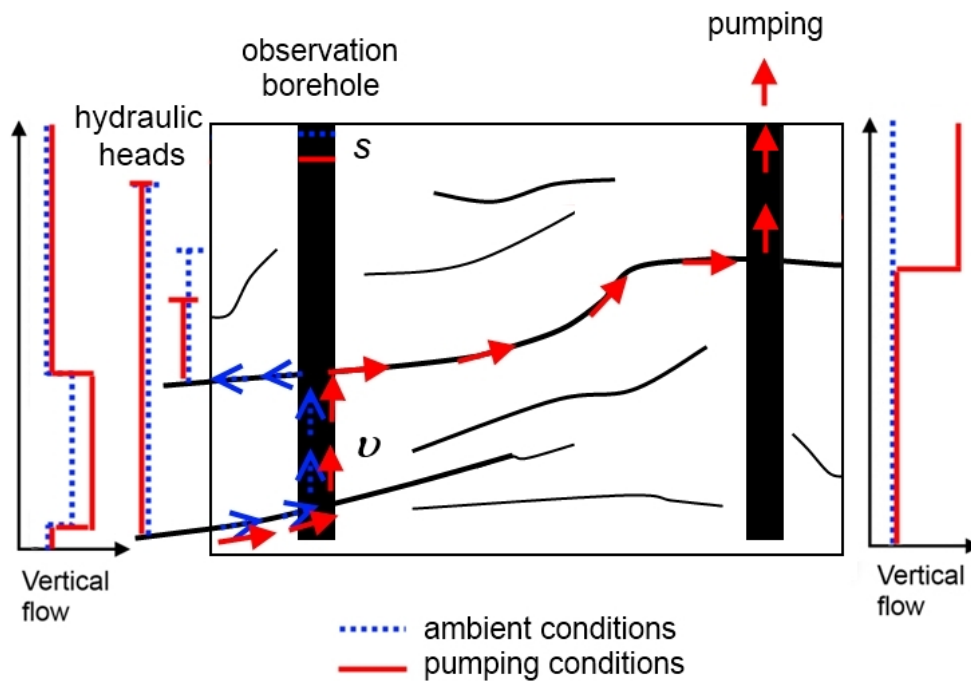


**Figure 1.** Flow pattern, hydraulic head difference between fractures and flow profiles for a pair of pumping and observation boreholes connected by one main flowpath under ambient (blue dotted line) and pumping (red line) flow conditions.

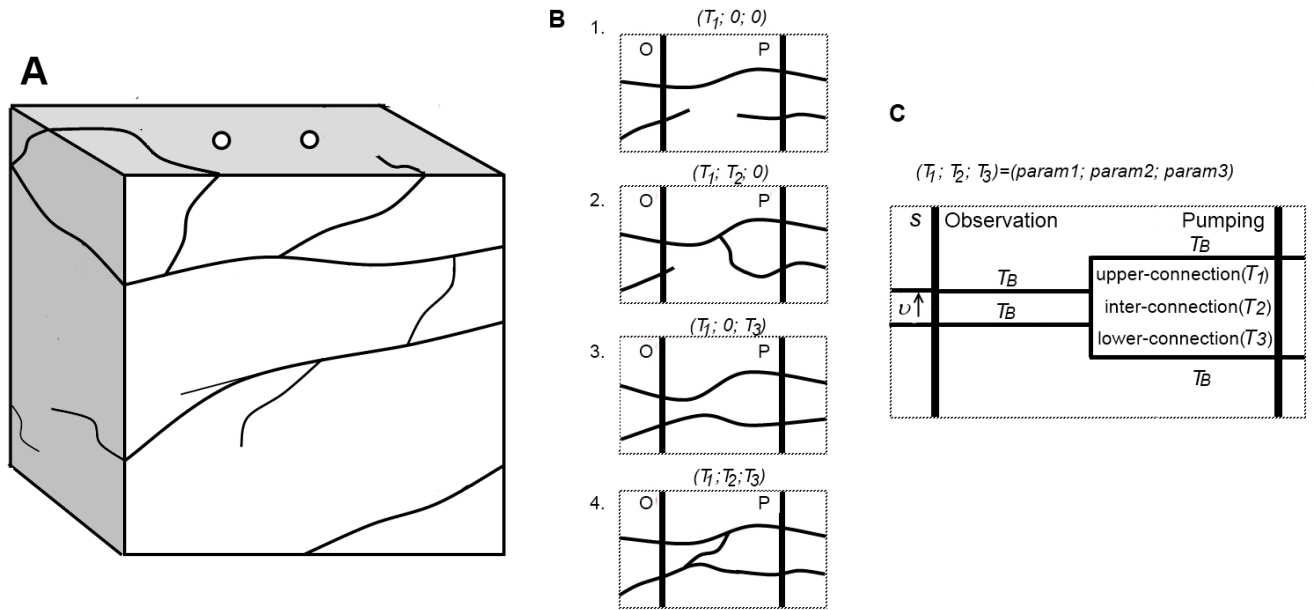


**Figure 2.** (A) Example of fracture network intersected by two boreholes. (B) Cross-sections of synthetic model: the observation and pumping boreholes are both intersected by two flowing horizontal fractures of equal transmissivity ( $T_B$ ). These fractures are connected by a vertical fracture consisting of three sections with  $T_1$ ,  $T_2$  and  $T_3$  transmissivities. (C) Basic connections that could be modeled by different combinations of connection transmissivities  $T_1$ ,  $T_2$  and  $T_3$ .

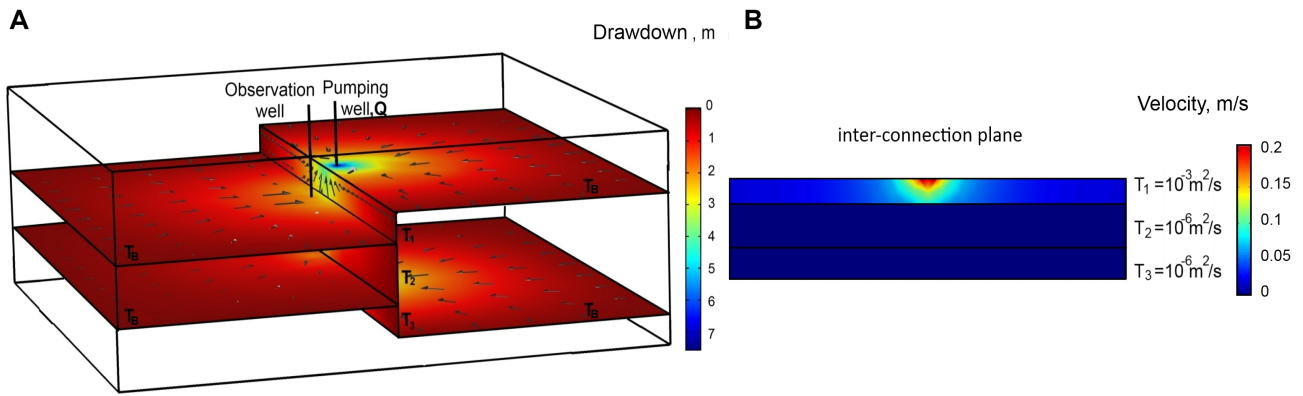


**Figure 3.** (A) Drawdown  $s$  (color scale) and flow velocity field  $v$  (arrows) in an example of flow model geometry. For this example the borehole radius is  $0.05\text{ m}$ , the pumping rate is  $Q = 2.5 \cdot 10^{-3}\text{ m}^3/\text{s}$ . The transmissivities of fractures are given by  $T_B = 5 \cdot 10^{-4}\text{ m}^2/\text{s}$ ,  $T_1 = 10^{-3}\text{ m}^2/\text{s}$ ,  $T_2 = 10^{-6}\text{ m}^2/\text{s}$  and  $T_3 = 10^{-6}\text{ m}^2/\text{s}$ . (B) Distribution of the flow velocity  $v$  in the inter connection plane.

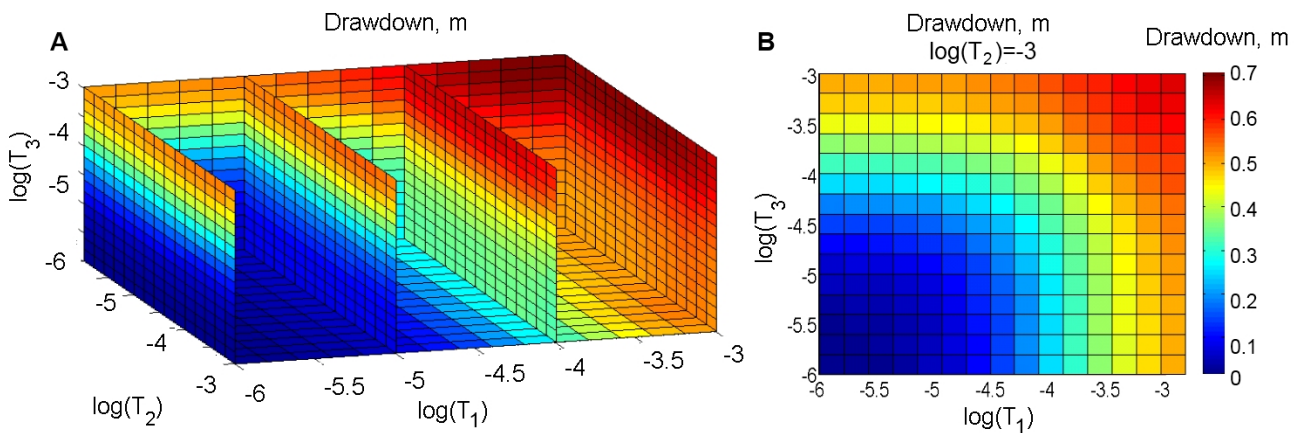


**Figure 4.** (A) Model computation of drawdown  $s$  in the observation borehole as a function of the log-transformed transmissivities of the vertical fractures  $\log T_1$ ,  $\log T_2$  and  $\log T_3$ . (B) Model computation of drawdown  $s$  in the observation borehole with fixed inter connection fracture transmissivity  $\log T_2 = -3$ .

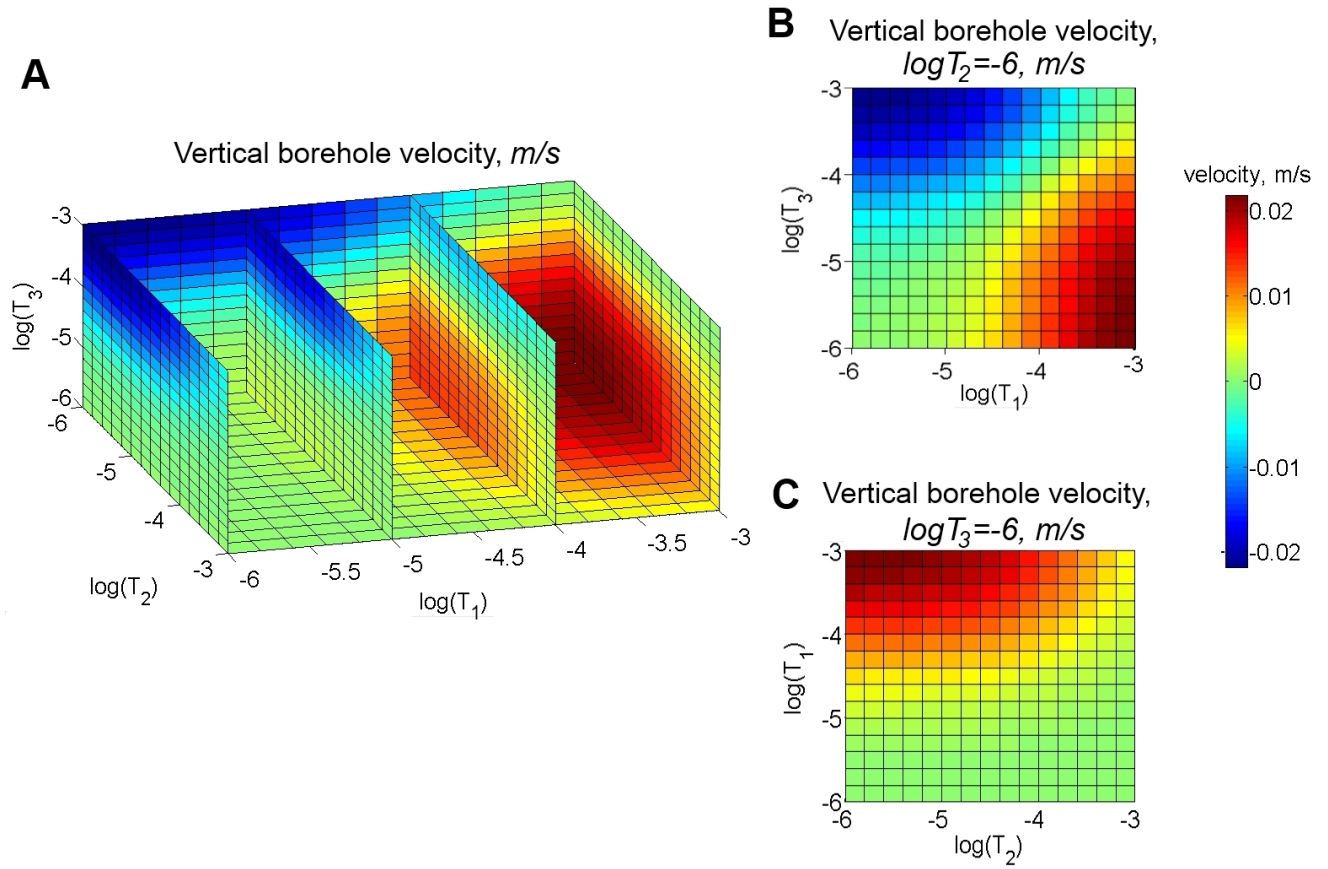


**Figure 5.** (A) Model computation of vertical flow velocities  $v$  in observation borehole as a function of log-transformed transmissivities of vertical fractures  $\log T_1$ ,  $\log T_2$  and  $\log T_3$ . (B) Model computation of vertical flow velocities  $v$  in the observation borehole with fixed inter connection fracture transmissivity  $\log T_2 = -6$ . (C) Model computation of vertical flow velocities  $v$  in the observation borehole with fixed inter connection fracture transmissivity  $\log T_3 = -6$ .

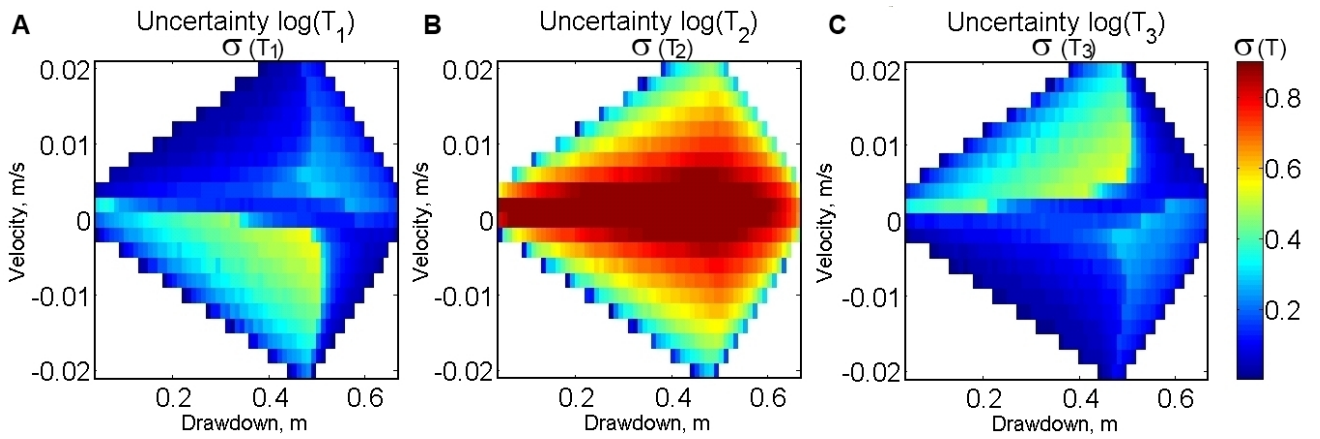


**Figure 6.** Uncertainty analysis of the flow model. The range of allowable drawdown and vertical borehole velocity observations ( $s, v$ ) for the synthetic case presented on Figure 2B and the estimated uncertainties about  $\log T_1$  (A),  $\log T_2$  (B),  $\log T_3$  (C) for measurement errors  $(\sigma_s, \sigma_v) = (0.01 \text{ m}, 2 \cdot 10^{-3} \text{ m/s})$ .

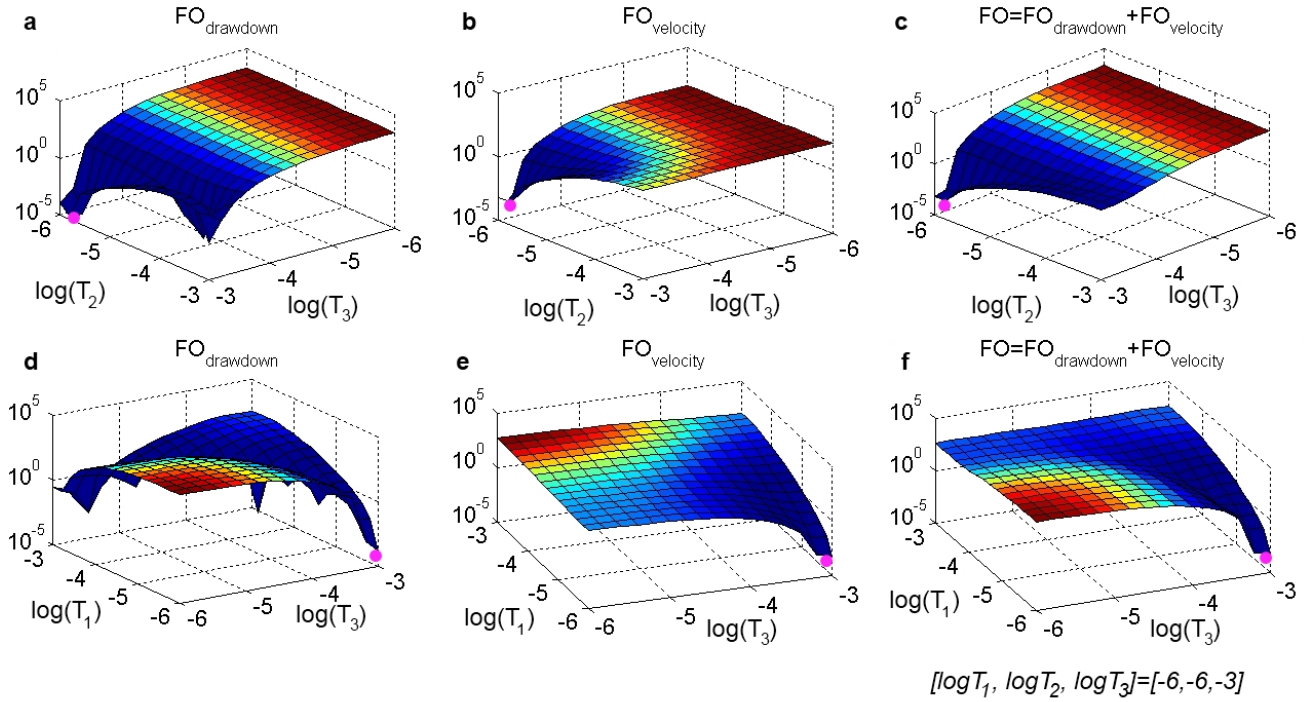


**Figure 7.** The objective function for the simple synthetic case  $(\log T_1, \log T_2, \log T_3) = (-6, -6, -3)$  (Figure 2) for the drawdown (a), velocity (b) and the sum of both (c) with respect to the log-transformed inter and lower connection transmissivities ( $\log T_2$  and  $\log T_3$ ) and with respect to the log-transformed upper- and lower- connection transmissivities ( $\log T_1$  and  $\log T_3$ ) (d, e, f).

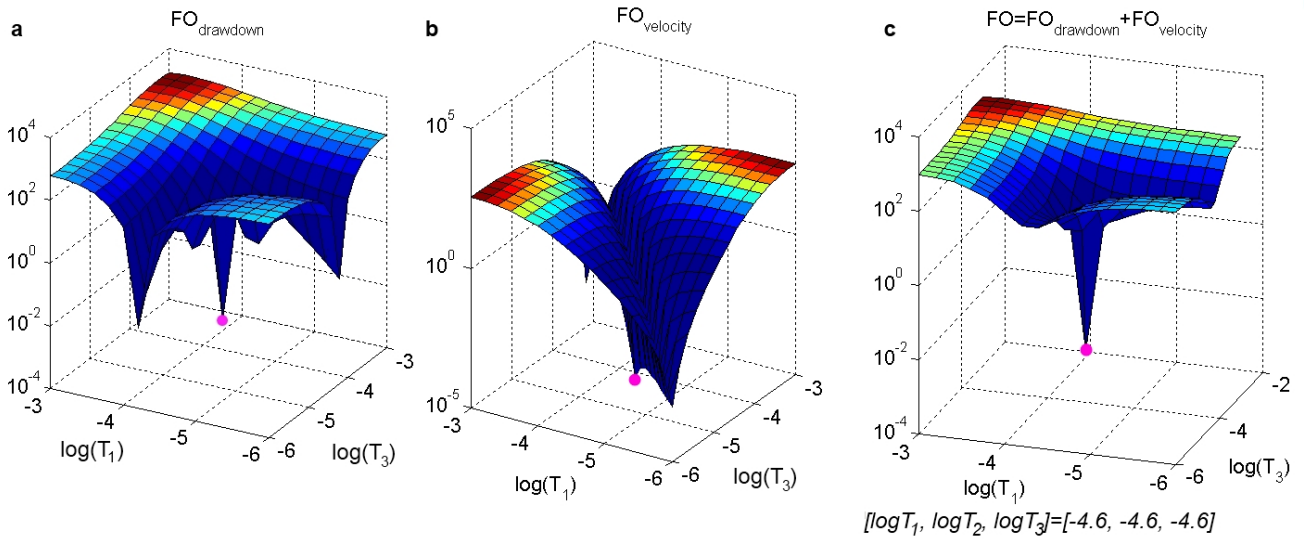


**Figure 8.** The objective function for the simple synthetic case  $(\log T_1, \log T_2, \log T_3) = (-4.6, -4.6, -4.6)$  (Figure 2) for the drawdown (a), velocity (b) and the sum of both (c) with respect to the log-transformed upper and lower connection transmissivities ( $\log T_1$  and  $\log T_3$ ).

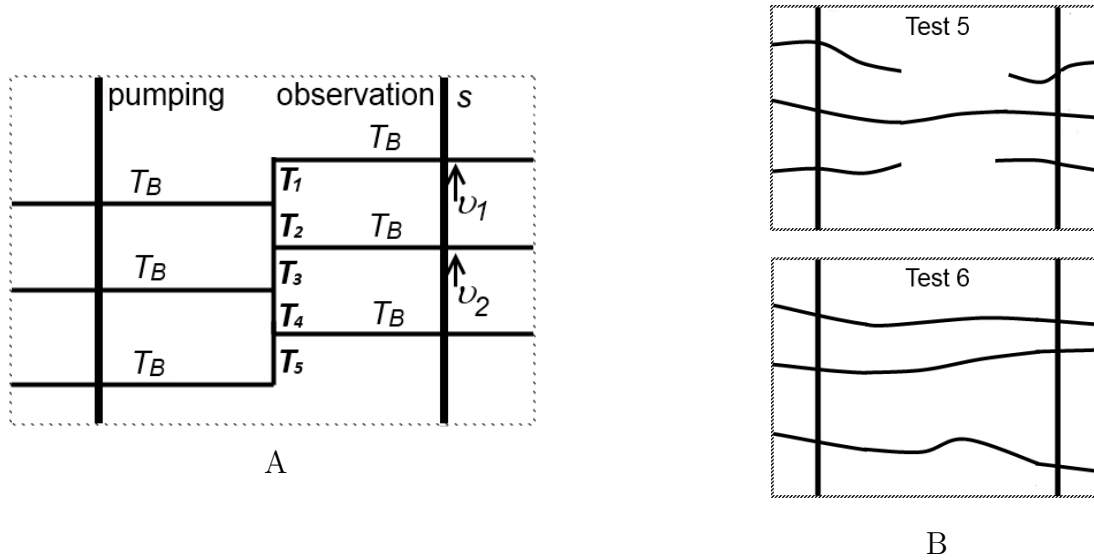


**Figure 9.** Sketch of the synthetic flow model (A) Cross-sections of the synthetic flow model. The model comprises six horizontal fractures of transmissivity  $T_B$  and five vertical fractures of  $T_1, T_2, T_3, T_4$  and  $T_5$  transmissivity. (B) Configurations of synthetic tests : 'Test 5' ( $\log T_1, \log T_2, \log T_3, \log T_4, \log T_5$ )= $(-6,-6,-3,-6,-6)$  and 'Test 6' ( $\log T_1, \log T_2, \log T_3, \log T_4, \log T_5$ )= $(-3,-6,-3,-6,-3)$ .

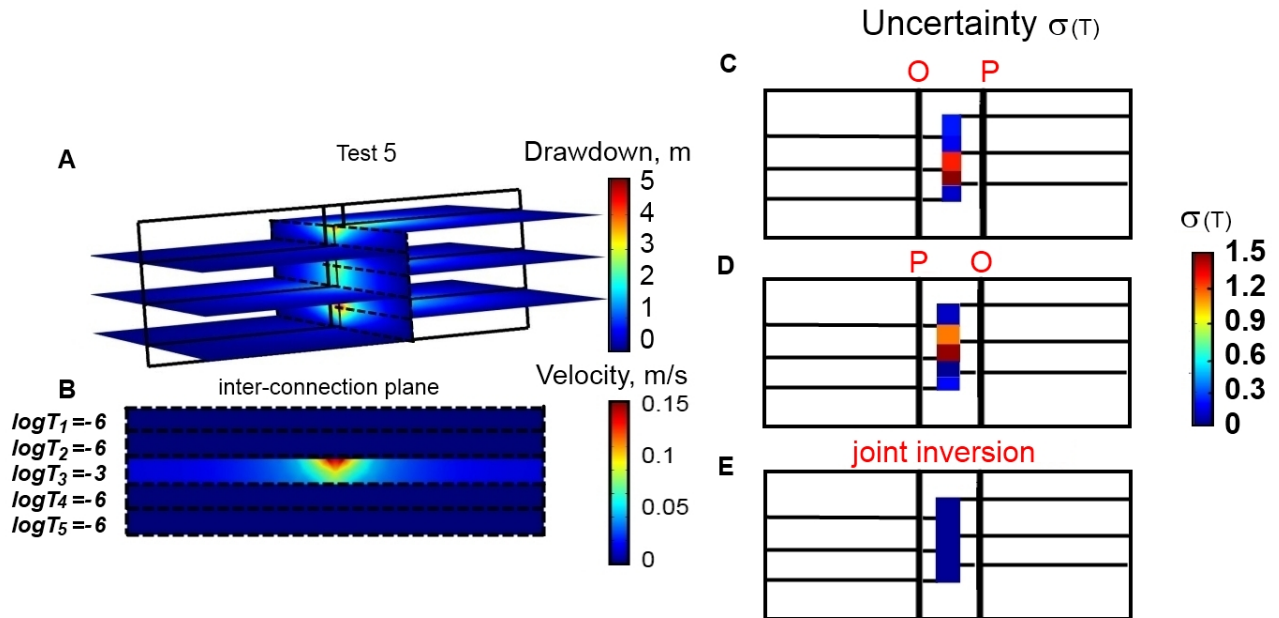


**Figure 10.** Modeling results for 'Test 5'. (A) Drawdown distribution for 'Test 5' during pumping from the right borehole. (B) Fracture velocities in the interconnection plane. The uncertainty about the estimated log-transformed  $T_1, T_2, T_3, T_4$  and  $T_5$  transmissivities during pumping from the left borehole (C), during pumping from the right borehole (D) and joint inversion of both pumping tests (E).

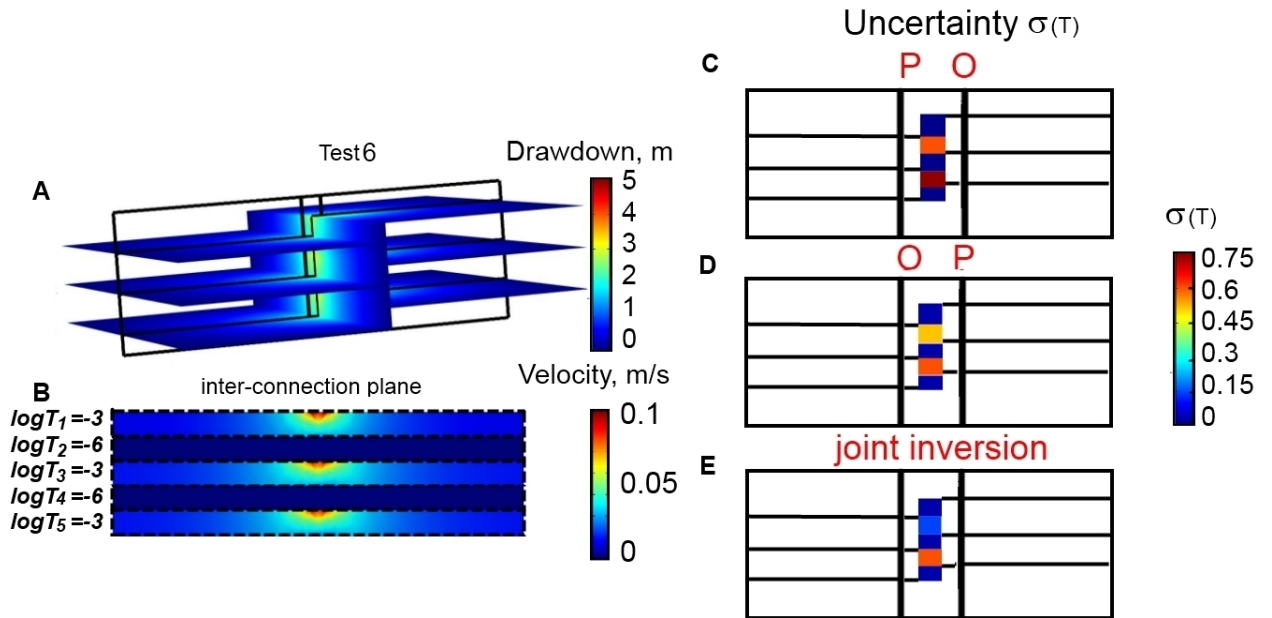


**Figure 11.** Modeling results for 'Test 6'. (A) Drawdown distribution for 'Test 6' during pumping from the right borehole. (B) Fracture velocities in the interconnection plane. Uncertainty about the estimated log-transformed  $T_1, T_2, T_3, T_4$  and  $T_5$  transmissivities during pumping from the left borehole (C), during pumping from the right borehole (D) and joint inversion of both pumping tests (E).

### 2.3 Conclusions

To summarize, in this chapter we propose flow tomography (i.e., sequential cross-borehole flowmeter tests) as a new approach for characterizing fracture connectivity and transmissivity. We propose a framework for inverting flow and drawdown data to infer fracture connectivity and transmissivities. We show that the tomographic approach reduces significantly the uncertainty on the inference of connectivity patterns and hydraulic parameters. The proposed approach is validated for different synthetic flow scenarios.

We have quantified the associated uncertainty about parameter estimation for a range of simplified fracture network geometries. Finally, the flow tomography approach was shown to provide a good estimation of connectivity patterns and transmissivities of main flowpaths. It also allows the estimation of the transmissivity of fractures that connect the flowpaths but do not cross the boreholes, although the associated uncertainty was found to be higher for some geometries. Furthermore, in Chapter 4 we apply the proposed inverse modelling framework at the fractured field site.

# Chapter 3

## Ploemeur field site

All the methods proposed in the thesis were tested at the experimental Stang er Brune site, located near the main Ploemeur pumping site, in similar geological conditions. The site consists of 4 boreholes that were also subject to many other types of data acquisition, including geological logging of continuous core, borehole geophysics, flowmetering, straddle packer tests [Le Borgne et al., 2007], geophysical surveys [Dorn et al., 2012], temperature measurements, including fiber optic measurements [Read et al.] and temperature profiles measured within static water columns of sealed boreholes. We first describe the main pumping Ploemeur site and then present some data from these other methods. The objective of this chapter is to explain the suitability of Stang er Brune site for the methods proposed in the thesis.

### 3.1 Introduction

The Ploemeur aquifer is a fractured crystalline bedrock aquifer, which has been exploited for public water supply since 1991. The main particularity of the aquifer is to be very transmissive (on the order of  $10^{-3} \text{ m}^2/\text{s}$ ) even at large scale due to the good fracture network connectivity [Le Borgne et al., 2006a]. This large-scale connectivity is related to the existence of a sub-horizontal contact between the intrusive granite and the overlying mica-schist [Leray et al., 2012; Ruelleu et al., 2010; Touchard, 1999]. Such high values of transmissivities imply hydraulic

### 3. PLOEMEUR FIELD SITE

---

conductivity much larger than the ones usually measured in crystalline rocks [Clauser, 1992; Hsieh, 1998].

#### 3.2 Site localization

The Ploemeur site is located on the south coast of Brittany near the city of Lorient (Figure 3.1). This bedrock aquifer was discovered in 1991 when the city of Ploemeur wanted to complement surface water supply. Despite the crystalline nature of the rocks, it was decided to explore for an underground water supply. The site has subsequently been developed and exploited at an average rate of about 2000  $L/min$  to provide the main water supply for a town of 20,000 inhabitants. Despite the low permeability of the lithologies encountered this confined aquifer has provided very valuable water resources.

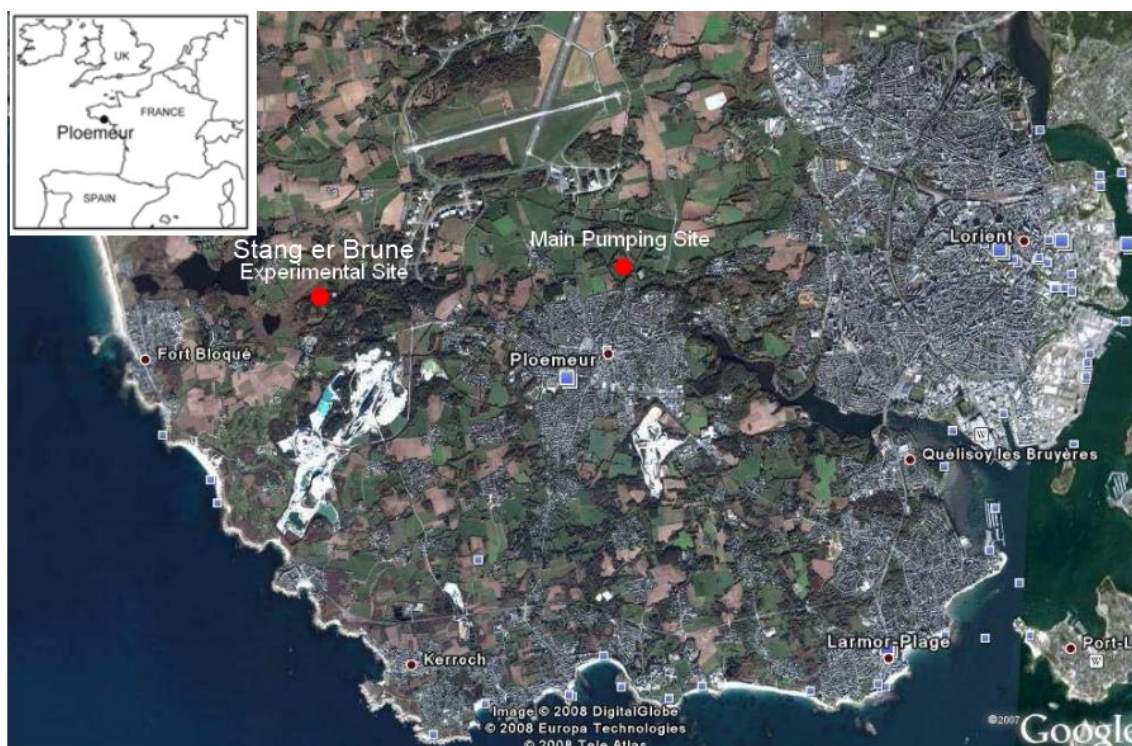


Figure 3.1: Ploemeur site localization. Ploemeur main pumping site and Stang er Brune experimental site.

The Ploemeur field site belongs to the Observatory for Environmental Research H+, a network of hydrogeological sites. As such, it is one of the main sites in France for research on flow and transport in fractured media. Research addresses pumping test interpretation, fine-scale interwell connectivity [Le Borgne et al., 2006a,b], hydraulic characterization, transport properties, chemical reactivity, recharge estimation, hydro-mechanical coupling, modeling strategies [Leray et al., 2012], risk assessment and uncertainty quantification. The main pumping site consists of forty boreholes which are equipped for piezometric and geochemical monitoring. A number of geophysical experiments (seismic, electric imaging, borehole geophysics) along with imaging, cores, and thin-section analyses have been performed on the site. Several characterization techniques (single-borehole and cross-borehole flowmeter tests, pumping tests, tracer tests) are used on distinct scales of investigations. The surface deformation in response to hydrologic variations is monitored using high resolution tiltmeters.

### 3.3 Hydrogeological context

A geological description of the Ploemeur site can be found in Ruelleu et al. [2010]. At the local scale, the pumping site is located at the intersection of two main structures: a contact between Late Hercynian granite, the Ploemeur granite, and its overlying micaschist dipping about  $30^\circ$  to the north, and a dextral normal fault zone striking north  $20^\circ$  and dipping  $70^\circ$  to the east. The contact zone at the granite roof consists of alternating deformed granitic sheets and enclaves of micaschists, pegmatite and aplite dykes, as well as quartz veins (Figure 3.2, 3.3 from Ruelleu et al. [2010], ). The main deformation zones are characterized by intense deformation and by fault breccias or gouge zones associated or not associated with fractured pegmatite (Figure 3.2, c). The most permeable fractures are presented by crush zones, sub horizontal fractures in pegmatite zones and by vertical fractures in micaschists [Ruelleu et al., 2010].

### 3. PLOEMEUR FIELD SITE

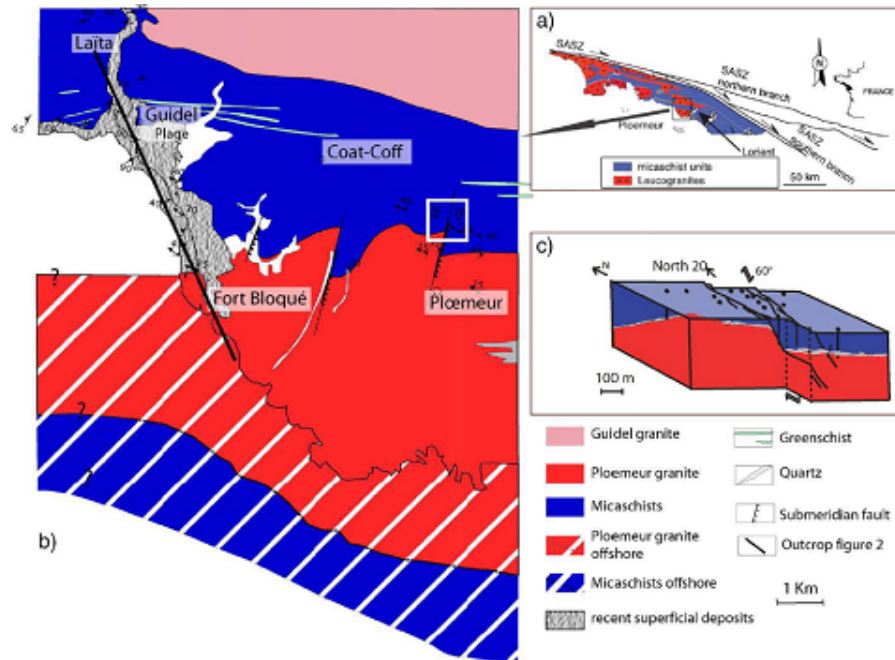


Figure 3.2: a) Geological context of the Ploemeur area within South Brittany. b) Synthetic geological map of Ploemeur area, c) Schematic 3D diagram of Ploemeur aquifer geology showing the regional contact dipping toward the north and the  $N20$  dextral normal fault. This schematic diagram of the pumping area is not scaled but corresponds roughly to the area within the white square on b (from Ruelleu et al. [2010]).

At the local scale, the hydrogeology of the area is marked by highly heterogeneous terrains [Le Borgne et al., 2006a, 2007], as expected for crystalline basement [Clauser, 1992]. Total air lift flows measured at the end of each drilling varied from 10 to about  $100 \text{ m}^3/h$ . The most productive boreholes are marked by great water inflows localized within the contact zone between granite and micaschists [Ruelleu et al., 2010; Touchard, 1999]. Thus, the most permeable feature is found at the interface between the granitic intrusion and the overlying micaschists. Water supply from the pumping well is sustained by the good large scale connectivity of transmissive fractures, which ensure the large scale transmissivity of the site [Le Borgne et al., 2006b] (Figure 3.4).

Since 1991, the aquifer is exploited at a rate of about  $106 \text{ m}^3$  per year which is

### 3. Ploemeur field site

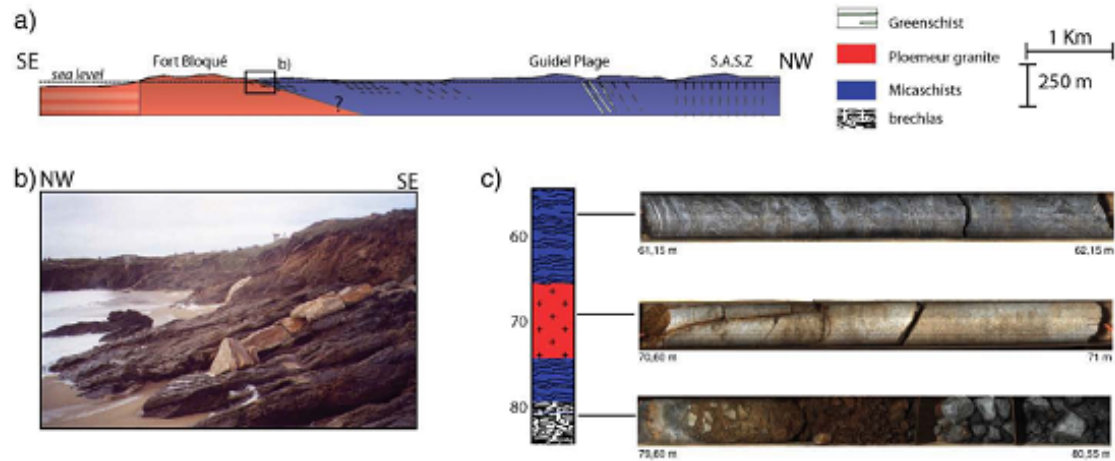


Figure 3.3: a) Simplified north-south geological cross-section. Dashed lines mark foliation. b) Photograph showing aspects of contact zone between granite and overlying micaschists, marked by granite and pegmatite dykes. c) Borehole cores of micaschists, granite, and breccias encountered within the water supply zone. Core diameter is 8 cm (from Ruelleu et al. [2010]).

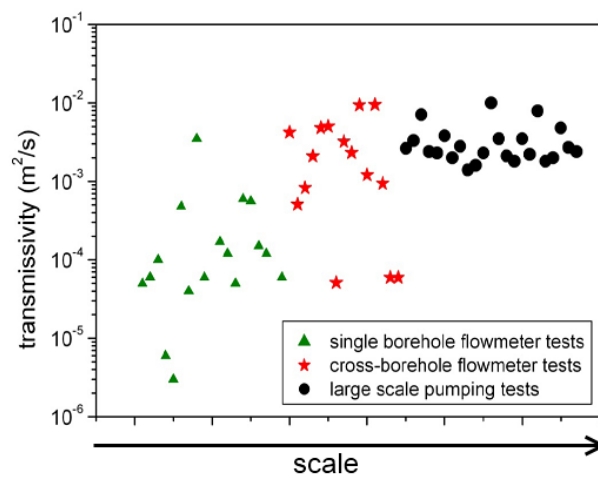


Figure 3.4: Estimates of transmissivity at borehole scale, cross borehole scale and site scale (from Le Borgne et al. [2007]).

much higher than other water supplies in crystalline rocks of the region. It implies a good recharge of the aquifer that cannot be achieved through a sub-vertical

### 3. PLOEMEUR FIELD SITE

---

fracture only. Such a recharge area may be compatible with a horizontal or gently dipping permeable reservoir in order to drain over a sufficient surface [Leray et al., 2013; Ruelleu et al., 2010]. The geometrical arrangement that combines vertical faults with a very permeable sub-horizontal interface may explain the exceptional water resources at the Ploemeur site [Ruelleu et al., 2010].

### 3.4 Stang er Brune site

The Stang er Brune experimental site consists of 4 unscreened boreholes: B1 borehole (83 *m* deep), B2 and B3 boreholes (100 *m* deep) and F22 borehole (70 *m* deep). B1, B2 and B3 form a triangle within the radius of 10 *m* and F22 is 30 *m* from this triangle (Figure 3.5). The boreholes B1, B2 and B3 were drilled by the University of Birmingham during the European project ALIANCE in collaboration with the University of Montpellier. The objective was to develop an experimental site in fractured rock. The upper part of the boreholes is in mica-schists, while below 30 – 40 *m* is granite. All boreholes are open below 24 *m*. Several studies were conducted at the site in order to characterize connected fracture networks.

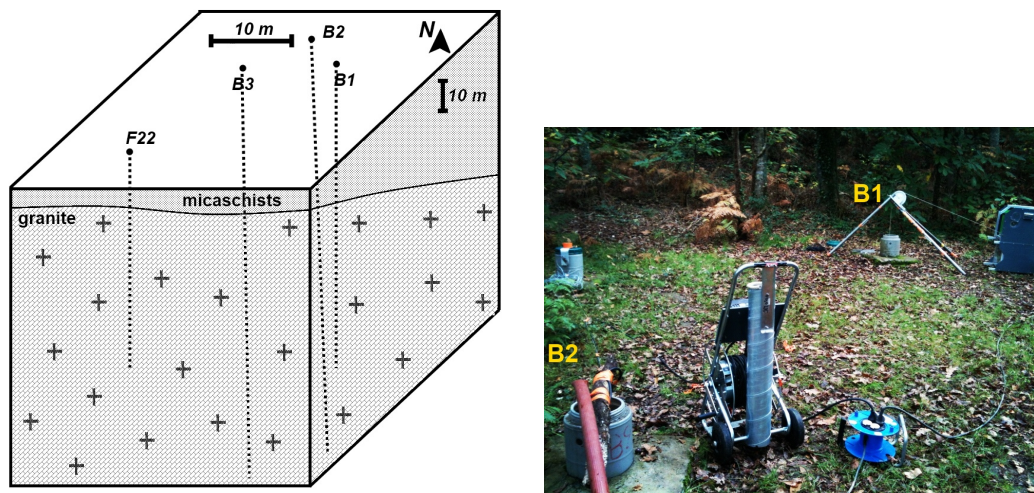


Figure 3.5: Stang er Brune field site.

Le Borgne et al. [2007] used borehole geophysical measurements along with single- and cross-borehole flowmeter tests in order to characterize flowing fractures that intersect the boreholes and identify those that are hydraulically connected. Each borehole was found to be intersected by 3 – 5 flowing fractures with overall hydraulic transmissivities on the order of  $10^{-3} \text{ m}^2/\text{s}$  over the borehole length. The cluster of fracture connected all over the site is composed of several of these fractures Le Borgne et al. [2007].

Vertical borehole flow velocities, measured at all boreholes under the ambient and pumping conditions, and caliper logs are presented in Figure 3.6 (B1), Figure 3.7 (B2) and (Figure 3.8 (B3)). For each borehole we measured an ambient vertical upward flow of  $0.2 - 5 \text{ L}/\text{min}$ . Pumping flowmeter profiles were measured for 2 different flowrates using heat-pulse flowmeter and impeller flowmeter [Le Borgne et al., 2007; Paillet, 2004]. Using flow model, presented in Chapter 2, we interpret these data to infer transmissivities of fractures intersecting the borehole. Results are presented in Table 3.11. Moreover, step-drawdown single packer tests, performed for some borehole intervals in the site [Le Borgne et al., 2007], were also interpreted in terms of fracture transmissivity and reported in Table 3.11. Step-drawdown tests were analyzed by applying Bierschenk & Wilson method based on Jacob’s equation [Clark, 1977]. Finally, all estimations are in a relatively good agreement.

### 3. PLOEMEUR FIELD SITE

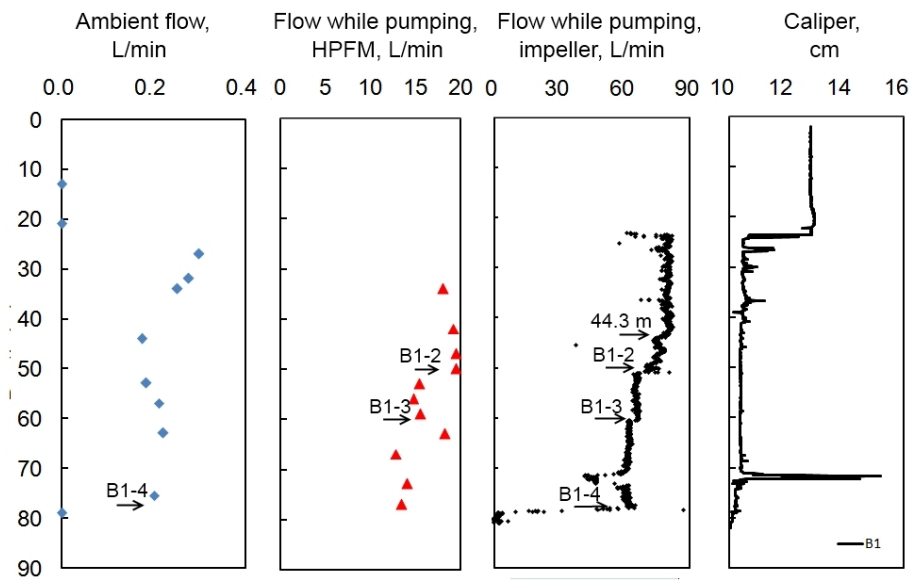


Figure 3.6: Flowmeter and caliper logs in B1. (a) Ambient vertical velocity (positive values correspond to upward flow), (b) vertical velocity measured while pumping in the cased part of the well at a rate of 19  $l/min$ . The steady state drawdown observed was 55  $cm$ , (c) vertical velocity measured while pumping in the cased part of the well at a rate of 82  $l/min$ . The steady state drawdown observed was 6.76  $m$  and (d) caliper log.

### 3. Ploemeur field site

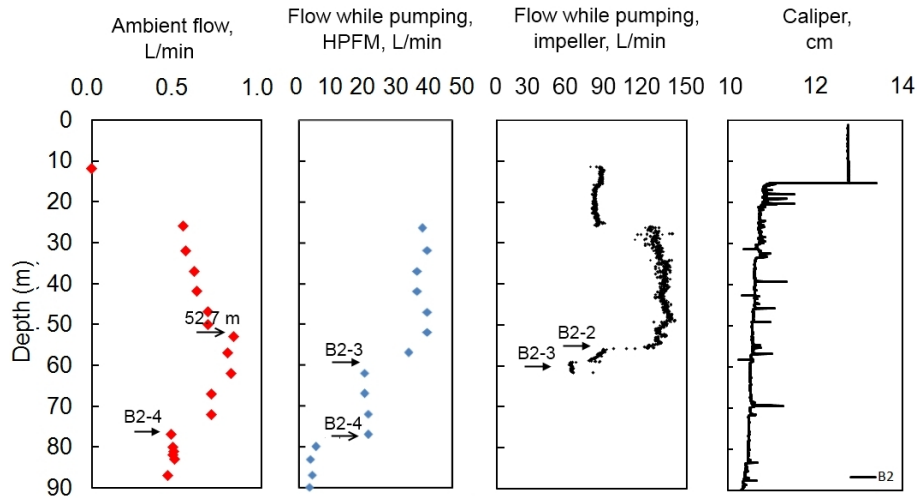


Figure 3.7: Flowmeter and caliper logs in B2. (a) Ambient vertical velocity (positive values correspond to upward flow), (b) vertical velocity measured while pumping in the cased part of the well at a rate of  $42 \text{ l/min}$ . The steady state drawdown observed was  $21 \text{ cm}$ , (c) vertical velocity measured while pumping in the cased part of the well at a rate of  $140 \text{ l/min}$ . The steady state drawdown observed was  $1.9 \text{ m}$  and (d) caliper log.

### 3. PLOEMEUR FIELD SITE

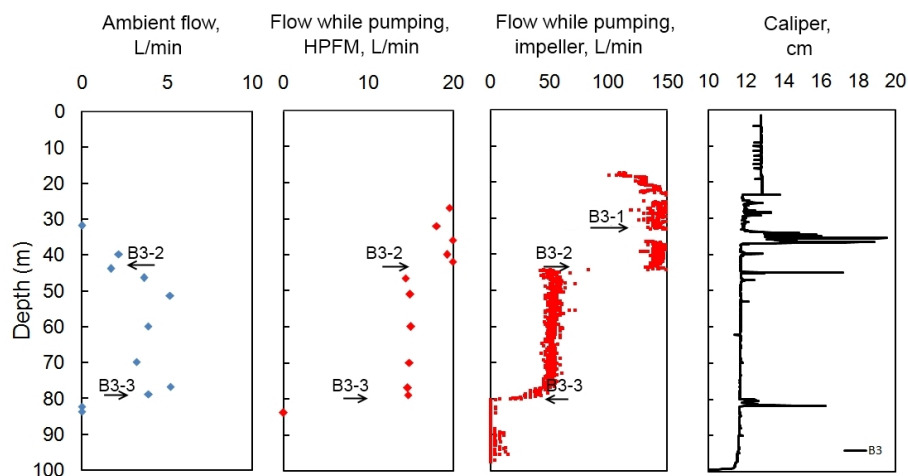


Figure 3.8: Flowmeter and caliper logs in B3. (a) Ambient vertical velocity (positive values correspond to upward flow), (b) vertical velocity measured while pumping in the cased part of the well at a rate of  $19 \text{ l/min}$ . The steady state drawdown observed was  $3 \text{ cm}$ , (c) vertical velocity measured while pumping in the cased part of the well at a rate of  $145 \text{ l/min}$ . The steady state drawdown observed was  $63 \text{ cm}$  and (d) caliper log.

Table 3.1: Estimation of transmissivities of fractures intersecting B1, B2 and B3 boreholes.

Fracture	from HPFM, $m^2/s$	from impeller, $m^2/s$	from step-drawdown, $m^2/s$
$T_{B1-2}$	$1.3e-4$	$4.4e-5$	$1.7e-4$
$T_{B1-3}$	$6.3e-5$	$1.1e-5$	$3e-5$
$T_{B1-4}$	$4.2e-4$	$1.6e-4$	$3e-5$
$T_{B2-2+B2-3}$	$1.8e-3$	$8.5e-4$	$1.5e-3$
$T_{B2-4}$	$1.5e-3$	$6.5e-4$	$1.4e-3$
$T_{B3-1}$	$7e-4$	$2e-4$	
$T_{B3-2}$	$2.45e-3$	$1.6e-3$	$7e-3$
$T_{B3-3}$	$3.85e-3$	$1e-3$	

Dorn et al. [2012] used tracer test data combined with single-hole ground-penetrating radar (GPR) reflection monitoring data between B1 and B2 boreholes (Appendix 1). Using GPR data the evolution of tracer plumes during five tracer

### 3. Ploemeur field site

experiments were provided at radial distances 2 – 10 m from the boreholes. For all experiments, multiple transport paths were found to carry the tracer between the injection fracture and the pumping borehole (Figure 3.9).

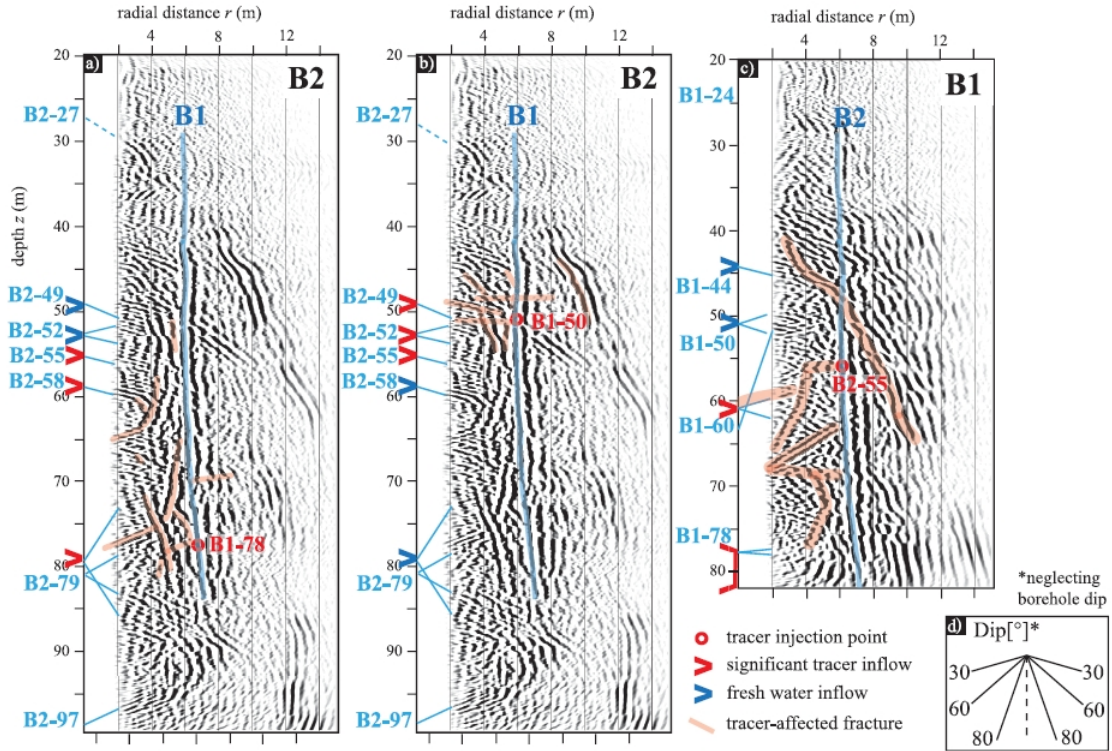


Figure 3.9: Extracts of the migrated multioffset single-hole GPR sections of B1 and B2 with superimposed interpretations of tracer pathways from Dorn et al. [2012]. Red circles indicate the tracer injection points, while red and blue arrowheads locate saline and unaffected groundwater inflow into the pumping borehole, respectively. Light red regions highlight fractures through which the injected tracer is interpreted to move, whereas blue regions highlight reflections from other boreholes. Light blue letters refer to transmissive fractures identified in the boreholes using optical logs and flowmeter tests with corresponding blue lines indicating their corresponding dips [Le Borgne et al., 2007]. (d) Dip angles corresponding to the axis aspect ratio  $r : z$  of 2 : 1 [Dorn et al., 2012] (Appendix 1).

During the period during which this thesis was developed several tracer tests were conducted, including heat tracer tests described in Chapter 6 and Appendix 2 [Read et al.] and solute tracer tests described in Appendix 1 Dorn et al. [2012].

### 3. PLOEMEUR FIELD SITE

---

These tracer tests were mainly conducted with injection taking place in B1-2 (50.9 *m* depth) and B1-4 (78.7 *m* depth) fractures [Le Borgne et al., 2007]. Figure 3.10 shows the optical images of these fractures, obtained by Montpellier University.

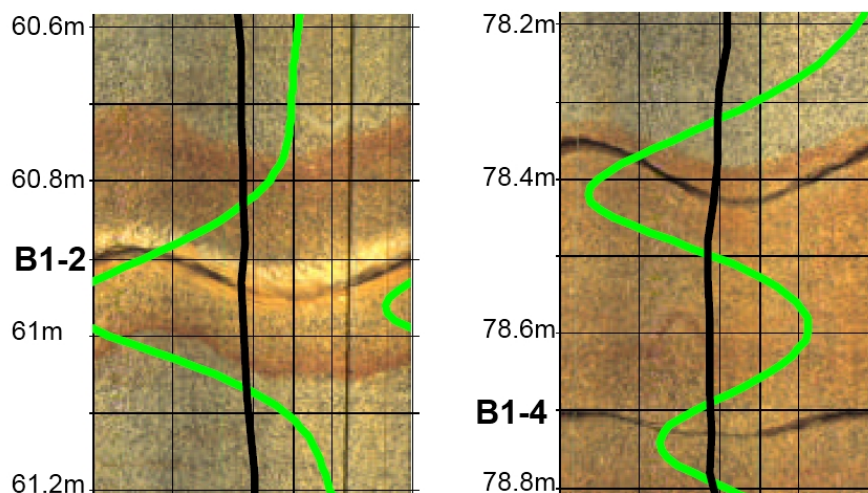


Figure 3.10: Optical images of B1-2 (50.9 *m* depth) and B1-4 (78.7 *m* depth) fractures [Le Borgne et al., 2007].

#### 3.4.1 Analysis of thermal properties

In this thesis temperature data were used to characterize fracture hydraulic properties. In order to reduce uncertainty we performed laboratory measurements of the specific heat, thermal diffusivity and bulk density of the rock. The B1 borehole at the Stang er Brune field site have been fully cored. Thus, thermal analysis were conducted on the core samples. 10 samples were chosen, including 3 samples in mica-schists and 7 samples in granite. Table 3.11 synthesizes the obtained results. According to this analysis the mean bulk density, thermal diffusivity, specific heat and thermal conductivity can be given as followings:  $\rho_m = 2520 \text{ kg/m}^3$ ,  $\rho_g = 2470 \text{ kg/m}^3$ ,  $\alpha_m = 1.4 \cdot 10^{-6} \text{ m}^2/\text{s}$ ,  $\alpha_g = 1.8 \cdot 10^{-6} \text{ m}^2/\text{s}$ ,  $c_m = c_g = 738 \text{ J/kgK}$ ,  $\lambda_m = 2.59 \text{ W/mK}$ ,  $\lambda_g = 3.31 \text{ W/mK}$ .

### 3. Ploemeur field site

---

<b>Sample</b>	<b>Density g/cm<sup>3</sup></b>	<b>Thermal Diffusivity mm<sup>2</sup>/s</b>	<b>Specific Heat J/(g·K)</b>	<b>Thermal Conductivity W/(m·K)</b>
mica-schists	2.586	0.943	0.710	1.731
mica-schists	2.410	1.885	0.753	3.422
granite	2.551	2.282	0.698	4.061
granite	2.437	1.798	0.732	3.210
granite	2.592	1.442	0.778	2.908
granite	2.533	1.728	0.726	3.178
granite	2.456	1.821	0.743	3.321
granite	2.394	1.904	0.773	3.521
granite	2.311	1.799	0.717	2.980
mica-schists	2.563	1.365	0.750	2.626

Figure 3.11: Thermal properties of rock samples from B1 borehole at the Stanger Brune field site.

## 3.5 Conclusions

Stanger Brune experimental site, located in the vicinity of the sub-horizontal contact between Ploemeur granite and the overlying micaschist, is characterized by a high transmissivity provided by a connected fracture network. High values of transmissivities imply hydraulic conductivity much larger than the ones usually measured in crystalline rocks [Clauser, 1992; Hsieh, 1998]. Moreover, rapid transfer times on the site allow conduction of relatively short and easy tracer test experiments. This has motivated scientific investigations on this site over the last ten years. A number of experimental studies have been conducted on the site to provide relevant data designed to characterize, quantify, and model flow and transport within this complex, heterogeneous aquifer. This comprehensive database, including geological, geophysical and hydraulic data, establish the hydrogeologic context for the methods proposed in the thesis.

# Chapter 4

## Using borehole temperature profiles to estimate borehole flow velocities

### 4.1 Introduction

Temperature data can be seen as a natural tracer of ground water flow [Anderson, 2005]. The potential advantage of temperature data, compared to direct measurements of flow or drawdown measurements, is that it can be measured easily and accurately in time and in space. Currently, relatively few methods exist for using temperature to characterize fracture hydraulic properties. To investigate this topic, we started with studying temperature profiles at the borehole scale.

In this chapter we show that borehole temperature-depth profiles are strongly related to vertical flow in the boreholes. Using a numerical model of flow and heat transfer at the borehole scale, we present a new methodology to derive precise and continuous flowmeter profiles from borehole temperature profiles.

#### 4. USING BOREHOLE TEMPERATURE-DEPTH PROFILES TO ESTIMATE BOREHOLE FLOW VELOCITIES

---

4.2 Paper: A methodology for using borehole temperature-depth profiles under ambient, single and cross-borehole pumping conditions to estimate fracture hydraulic properties (Klepikova et al., *Journal of Hydrology*, 2011)



# A methodology for using borehole temperature-depth profiles under ambient, single and cross-borehole pumping conditions to estimate fracture hydraulic properties

Maria V. Klepikova<sup>\*</sup>, Tanguy Le Borgne, Olivier Bour, Philippe Davy

Geosciences Rennes, UMR 6118, CNRS, University of Rennes 1, Rennes, France

## ARTICLE INFO

### Article history:

Received 3 January 2011  
 Received in revised form 6 April 2011  
 Accepted 13 July 2011  
 Available online 23 July 2011  
 This manuscript was handled by Philippe Baveye, Editor-in-Chief, with the assistance of D.P. Ahlfeld, Associate Editor

### Keywords:

Temperature  
 Vertical flow  
 Fracture  
 Borehole velocity  
 Flowmeter

## SUMMARY

Temperature profiles in the subsurface are known to be sensitive to groundwater flow. Here we show that they are also strongly related to vertical flow in the boreholes themselves. Based on a numerical model of flow and heat transfer at the borehole scale, we propose a method to invert temperature measurements to derive borehole flow velocities. This method is applied to an experimental site in fractured crystalline rocks. Vertical flow velocities deduced from the inversion of temperature measurements are compared with direct heat-pulse flowmeter measurements showing a good agreement over two orders of magnitudes. Applying this methodology under ambient, single and cross-borehole pumping conditions allows us to estimate fracture hydraulic head and local transmissivity, as well as inter-borehole fracture connectivity. Thus, these results provide new insights on how to include temperature profiles in inverse problems for estimating hydraulic fracture properties.

© 2011 Elsevier B.V. All rights reserved.

## 1. Introduction

In heterogeneous and fractured rocks, borehole temperature profiles often show temperature changes which are caused by water of warmer or colder origins flowing from permeable flow zones (Drury and Lewis, 1983; Ge, 1998; Pehme et al., 2010, 1995; Bense et al., 2008). Several studies use temperature anomalies to quantify vertical or horizontal groundwater flow velocities (Stallman, 1965; Anderson, 2005; Bredehoeft and Papadopoulos, 1965; Marechal and Perrochet, 2001; Land and Paull, 2001; Sorey, 1971; Cartwright, 1979; Arriaga and Leap, 2006; Bense and Kooi, 2004; Fairley and Nicholson, 2006). Most of these studies assume that water in the borehole is stagnant, and, thus, the temperature profile in the well is representative of the temperature in the aquifer. In open or screened boreholes, differences in hydraulic head between large-scale flow paths that connect to a borehole generally create ambient vertical flow within the borehole (e.g. Paillet, 1998). These differences in hydraulic head are in general due to regional flow conditions: downward flow in recharge areas and upward flow in discharge areas. The resulting vertical flow within the borehole significantly disturbs the temperature profile (Borner and Berthold, 2009; Chatelier et al., 2011). Examples of flow and temperature profiles in a fractured rock borehole are given in Fig. 1 from the

Ploemeur site, Brittany, France (Le Borgne et al., 2007). One borehole is not affected by vertical flow (see the F13 temperature profile in Fig. 1) and presents a classical temperature evolution with depth according to the geothermal gradient. The other borehole is clearly affected by vertical flow and presents strong temperature anomalies (arrows in Fig. 1).

The estimation of borehole vertical flow in itself is of interest as it can be used to derive large scale hydraulic connections (e.g. Le Borgne et al., 2007; Szekely and Galsa, 2006). Under a single-borehole configuration (Fig. 2B), the estimation of vertical flow can be used to estimate the local transmissivities and the hydraulic head differences driving the flow through the borehole. Under a cross-borehole set up (Fig. 2C), it can be used to characterize hydraulic connections and estimate their hydraulic properties (Paillet, 1998; Le Borgne et al., 2007). Temperature profiles display a strong correlation with vertical borehole velocity profiles. The objective of the present study is to demonstrate that temperature profiles can be inverted to deduce the vertical borehole velocity profiles, thus converting the temperature probe into a high resolution flowmeter. The advantage of temperature measurements compared with classical flowmeters is that they can be obtained easily and very accurately (Gosselin and Mareschal, 2003; Jaupart et al., 1982; Pehme et al., 2010) and continuously in space with new fiber optic methods (Selker et al., 2006; Henderson et al., 2009).

The relationship between vertical borehole flow and temperature profiles is investigated in the first part of the paper using a

<sup>\*</sup> Corresponding author.

E-mail address: [maria.klepikova@univ-rennes1.fr](mailto:maria.klepikova@univ-rennes1.fr) (M.V. Klepikova).

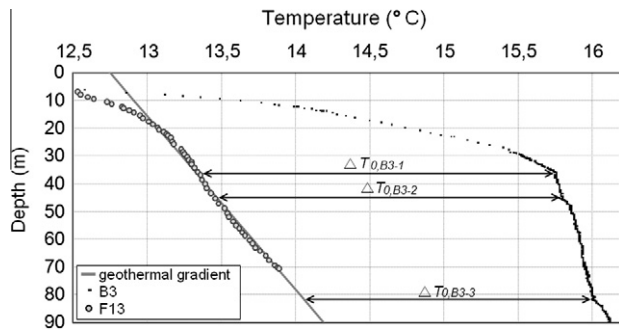


**Fig. 1.** Examples of borehole temperature profiles affected and unaffected by borehole flow. The black points represents borehole temperature profile collected in B3 under ambient condition. The F13 profile which is not affected by vertical flow is shown on the figure by gray circles. The gray line represents the geothermal gradient.

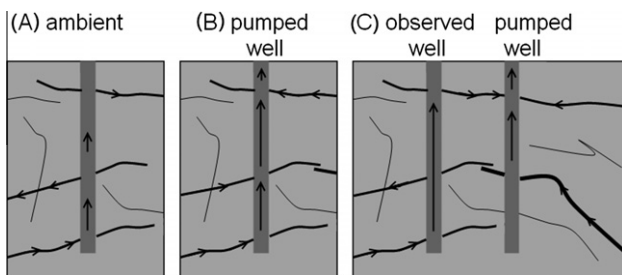


**Fig. 2.** Illustration of different hydraulic conditions. (A) Ambient vertical flow in the borehole. (B) Single borehole flowmeter test. (C) Cross-borehole flowmeter test.

flow and heat transfer numerical model at the borehole scale. In the second part of the manuscript, the flow velocities inverted from temperature anomalies are compared with direct velocity measurements obtained from a precise heat-pulse borehole flowmeter. In the third part, we focus on the interpretation of temperature profiles under single and cross-borehole pumping conditions to estimate hydraulic properties and heads of local fractures and characterize flow paths in-between boreholes. In the last part, the main sources of uncertainties related to the estimation of velocities from temperature profiles are discussed.

## 2. Heat and flow distribution at the borehole scale

A few analytical solutions exist for modeling flow and heat transfer at the borehole scale. The early works of Bredehoeft and Papadopoulos (1965) have focused on relating flow in the formation to temperature measured in the borehole, assuming that the borehole temperature is representative of the formation temperature. Thus, these are not relevant when considering vertical flow in the borehole itself. Other studies have considered the propagation of temperature anomalies in the rock formation by borehole flow (Drury and Lewis, 1983; Ramey, 1962; Chekhaluk, 1965; Becker and Davis, 2003) under transient conditions. In these analytical solutions, the temperature evolves constantly with time as the surrounding rock is progressively influenced by the temperature in the borehole. As we will show in the following, when heat exchange with the soil surface is taken into account, the temperature anomaly propagates in the rock until the flux of heat is dissipated through the soil surface. Thus, under this condition, temperature profiles can be assumed to be representative of steady state.

To study flow and heat transfer under such conditions, we develop a numerical model that simulates heat and flow at the borehole scale using COMSOL Multiphysics. We assume a constant vertical laminar flow in the borehole. Here we do not model the

fracture geometry (which is unknown) outside the borehole. Under this assumption, the system has an axial symmetry around the borehole axis. We assume that the rock matrix has homogenous and isotropic thermal properties. In our model, the rock matrix is impermeable but the approach can be easily extended to fractured/porous rock. We do not model heat exchange between the fracture and the rock formation. The validity of these assumptions are tested a posteriori by comparing the flow velocities estimated from the temperature profile to those measured directly in the borehole.

We consider a section of cylindrical borehole with radius  $r_0$  in between a flowing fracture and the soil surface (Fig. 3A). Due to the axial-symmetry we model a 2D domain, bounded by the borehole axis, at radial distance  $r = 0$ , and a radial distance  $r = R_0$ . We consider here upflow to allow comparisons with our experimental results, but downflow can also be modeled in a similar fashion.

Considering heat conduction in the rock and heat convection in the borehole, the heat transfer equation under steady state condition is given by

$$\nabla \cdot (\alpha_i \nabla T) - v \nabla T = 0, \quad (1)$$

where  $T$  is temperature,  $i = \{Fluid, Rock\}$ ,  $\alpha_i = k_i / \rho_i C_i$  is the thermal diffusivity,  $k_i$  is the thermal conductivity,  $C_i$  is the heat capacity, and  $\rho_i$  is the density. Flow velocity  $v$  in the borehole is assumed to follow a parabolic velocity profile given by,

$$v(r) = \begin{cases} -\frac{v_{max}}{r_0^2} \cdot r^2 + v_{max}, & \text{if } r \leq r_0 \\ 0, & \text{if } r > r_0 \end{cases} \quad (2)$$

where  $r$  is the radial position with respect to the borehole center,  $r_0$  is the borehole radius and  $v_{max}$  is the velocity in the center of the borehole. Note that the flow is considered to be zero outside the borehole, so that heat transfer in the rock occurs only through diffusion.

We consider a section of the borehole in between a flowing fracture and the soil surface (Fig. 3A). The rock temperature at the outer boundary at distance  $r = R_0$  away from the borehole is taken as the geothermal gradient

$$T_{Rock}|_{r=R_0} = T_0 + \gamma z, \quad (3)$$

where  $\gamma$  is the geothermal gradient and  $T_0$  is a fixed temperature at the soil surface  $T_{Rock}|_{z=0} = T_0$ . The boundary condition at the lower boundary is taken as a geothermal heat flux  $Q|_{z=H} = -k_{Rock} \gamma$ . The borehole water temperature at the bottom of the section ( $z = H$ ) is set to  $T_{BH}|_{z=H} = T_0 + \gamma H + \Delta T_0$ , where  $\Delta T_0$  describes the contrast between the water temperature measured in the borehole at this depth and the expected geothermal temperature at the same depth. At the bottom of each modeled section we impose the borehole flow as the sum of all fractures inflows and outflows below the modeled section. The inflow temperature (here bottom temperature for each section) is taken from the measured temperature profile. Note that this temperature may be the result of a mixing of inflows from several fractures located below the considered section. The radial boundary distance  $R_0$  is determined so that it is larger than the radial distance for transferring the heat flux produced by the borehole temperature anomaly to the surface, denoted  $R$ . An example of heat distribution and heat flow lines is given in Fig. 4. The radius of influence  $R$  of the borehole temperature anomaly is defined as the minimum radial distance below which heat flow lines originating from the borehole attain the upper horizontal boundary. The radius of influence  $R$  depends on the borehole length, on the temperature anomaly and on the flow velocity. The estimated radius of influence for a 100 m deep fracture is plotted as a function of flow velocity in Fig. 4. The vertical boundary  $r = R_0$  for our numerical model is chosen to be larger than  $R$ , that allows us to treat the problem under steady state conditions.

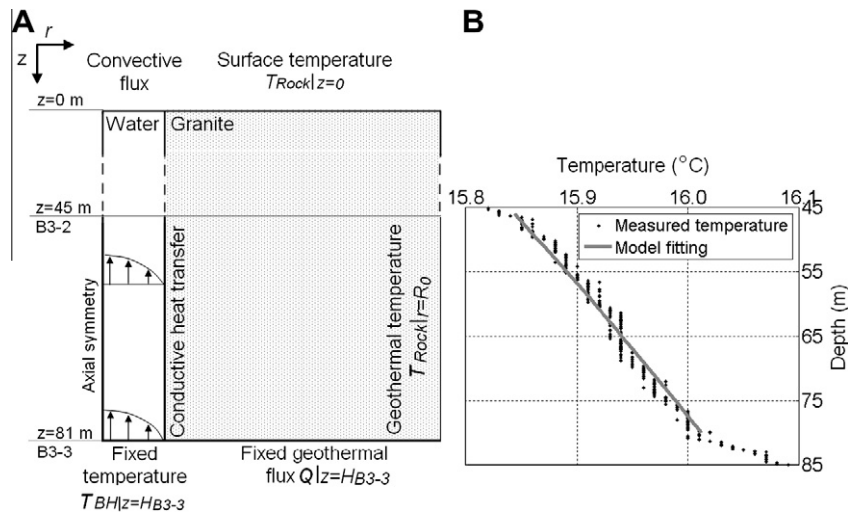


**Fig. 3.** Illustration of the flow and temperature propagation simulation. (A) Heat transfer model boundary conditions for Section 3 (in-between B3-3 and B3-2 fractures). (B) Borehole temperature profile collected in B3. The gray line represents the fitted numerical model for Section 3.

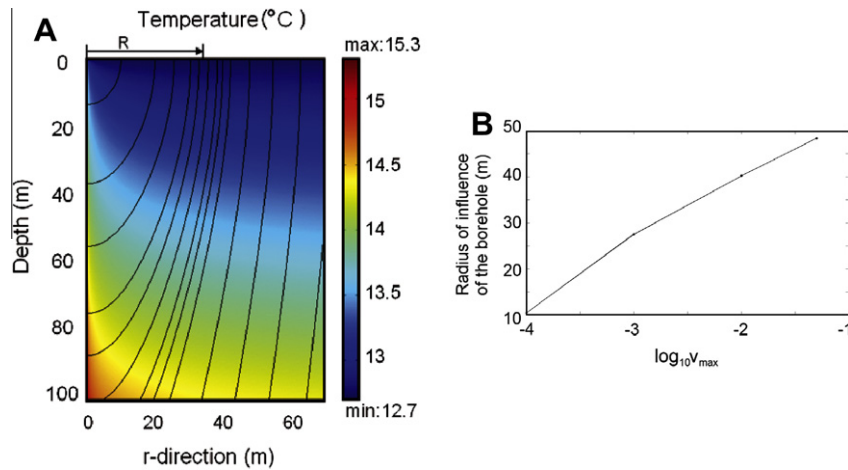


**Fig. 4.** (A) Simulated temperature distribution and streamlines for a velocity  $v_{max} = 0.01$  and a temperature anomaly  $\Delta T_0 = 1$  °C. The borehole wall is located at radial position  $r = 0$ . The radius of the influence of the borehole  $R$ , shown with the arrow, characterizes the radial distance at the surface that dissipates the heat created by the borehole temperature anomaly. (B) Dependence of the radius of influence of the borehole  $R$  with respect to the vertical flow velocity. Here for a temperature anomaly  $\Delta T_0 = 1$  °C.

Examples of numerically obtained temperature profiles for different velocities are given in Fig. 5. The flow velocity in the borehole is varying from  $v_{max} = 1 \times 10^{-4}$  m/s to  $v_{max} = 1 \times 10^{-2}$  m/s, a typical range of borehole flow velocities observed in fractured formations under ambient conditions (Paillet, 1998). For this example, the section length is  $H = 50$  m, the value of the geothermal gradient is  $\gamma = 0.016$  °C/m, the rock thermal conductivity  $k_{Rock} = 2.5$  W/m °C, the water thermal properties  $k_{Fluid} = 0.59$  W/m °C and  $C_{Fluid} = 4189$  J/kg °C (Incropera and DeWitt, 1996), and the temperature anomaly is  $\Delta T_0 = 1$  °C. The temperature anomaly  $\Delta T$  is advected upwards in the borehole with the flow velocity  $v_{max}$  and attenuates as heat dissipates in the rock. The temperature profiles are found to be very sensitive to borehole flow velocities. For a small borehole flow the temperature equilibrates quickly with the rock temperature. Thus, a large temperature gradient is observed close to the inflow zone (Fig. 5). An increase of the flow velocity implies that the water flowing in the borehole has less time to exchange heat with the borehole wall and hence it implies a smaller temperature gradient. For each borehole section of constant flow, the flow velocity can be estimated by matching the measured temperature profile with the numerically simulated temperature profile. The flow velocity is the only fitted parameter. Thus, the fitting procedure consists in

adjusting the vertical flow velocity to match the measured temperature gradient. Uncertainties related to this method are discussed in the last section of this article.

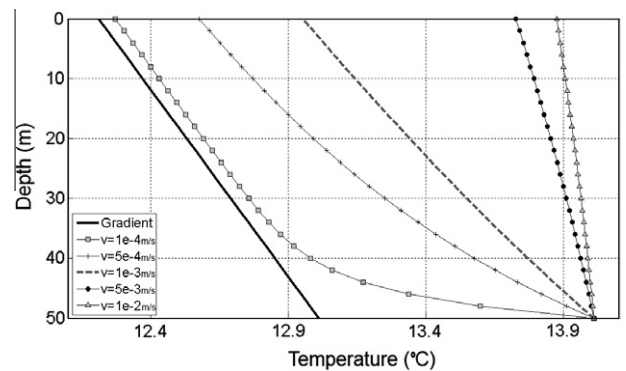


**Fig. 5.** Simulated temperature profile at the center of the borehole for different flow velocities and a temperature anomaly  $\Delta T_0 = 1$  °C. The inflowing zone is located at depth 50 m. The geothermal gradient is represented by color in this figure legend, the reader is referred to the web version of this article.)

### 3. Comparison of temperature-derived flow velocities with flowmeter measurements

In order to test the possibility to use temperature profiles to estimate vertical borehole flow velocities, we measured both borehole temperature and vertical flow using a heat-pulse flowmeter at the Ploemur experimental site (Le Borgne et al., 2007). In the example of Fig. 1, the temperature profile shows abrupt changes at 37, 45 and 81 m, which correspond to the three most permeable fracture zones located at  $37.5 \pm 0.5$ ,  $45 \pm 1$  and  $80.4 \pm 0.5$  m. In the section in between the B3-3 and B3-2 zones, and in the section in between the B3-2 and B3-1 zones, the temperature gradient is much smaller than the geothermal gradient (Fig. 1). This indicates an important upflow since the flowing water does not have time to exchange much heat with the borehole wall (Fig. 5). On the other hand, the temperature gradient above zone B3-1 is much steeper, indicating a small borehole flow that allows for significant heat exchange between the borehole water and the rock.

Borehole flow velocities were measured in ambient conditions using a heat-pulse flowmeter with an accuracy of  $\pm 2 \times 10^{-3}$  m/s (Paillet, 1998). At this site, the deep confined fractures have a higher hydraulic head than the shallow fractures leading to ambient vertical up flow in boreholes. The measured borehole flow velocities for the different borehole sections (from the top to the bottom of the borehole) are  $5.8 \times 10^{-3}$ ,  $3.2 \times 10^{-2}$  and  $4.7 \times 10^{-2}$  m/s, which confirms the qualitative interpretation of the temperature profiles. Note that obtaining these precise estimations requires time-consuming repeated heat-pulse flowmeter measurements at discrete positions in the borehole. This motivates the development of a method for estimating precisely vertical borehole flow velocities from temperature profiles. Note that the section below B3-3 is particular. The temperature gradient is relatively steep with warmer water than in the section above. This seems to indicate that another fracture is present below fracture B3-3 and that it is producing a small flow. However, no fracture was detected in this zone from flowmeter measurements (Le Borgne et al., 2006a). This highlights the potential of temperature profiles for detecting fractures producing a flow which is not detectable by high precision flowmeters. A similar conclusion was drawn by Pehme et al. (2010).

In order to estimate the flow velocities from the temperature profiles, we simulate flow and temperature propagation from each transmissive fracture up to the surface. We do this for both inflowing and outflowing fractures. The flow and temperature at the bottom of the section are fixed as those measured just above the fracture which is at the bottom of the section. We fit the simulated temperature profile to the measured temperature profile only in the section of constant flow in between the considered fracture and the next flowing fracture located above. By doing so, we assume that the heat flux in the rock that may come from lower fractures is negligible compared to the geothermal heat flux. We tested this assumption by including several fractures in a single model. The flow velocity of the model is adjusted so that the simulated profile matches the measured temperature profile in a given borehole section. Fig. 3 represents the best fit obtained for one of the section of B3 borehole in-between the B3-3 and B3-2 fractures. We perform a similar fitting procedure for each section of constant flow located in-between two transmissive fractures.

The parameters of the model were chosen as follows. We used the value of  $k_{Rock} = 2.72 \pm 0.14$  W/m °C for thermal conductivity which corresponds to the mean thermal conductivity measured over Hercynian granites in Brittany Jolivet et al. (1988). The heat capacity of the granite is  $C_{Rock} = 775$  J/kg °C. The values for water properties are  $k_{Fluid} = 0.59$  W/m °C and  $C_{Fluid} = 4189$  J/kg °C respectively (Incropera and DeWitt, 1996). The normal geothermal gradient  $\gamma = 0.016$  °C/m is taken as the value measured at the experimental site at boreholes without any vertical flow (Fig. 1).

The value  $r_0 = 0.053$  m provided by the caliper measurements (Le Borgne et al., 2007) was used for the modeling. Uncertainties on these parameters and their impact on flow velocities estimates are discussed in the last section of this article. Velocities estimated from the temperature profiles are found to be in very good agreement with those measured from the heat-pulse flowmeter (Fig. 6). This result indicates that for this type of geological media the temperature measurements could be used to derive borehole flow profiles.

### 4. Estimation of fracture transmissivity, hydraulic head and connectivity

In this section, we test the applicability of the method for estimating single and cross-borehole flow profiles from temperature profiles. Single-borehole flow profiles are conducted by pumping in a borehole and measuring flow below the pump (Fig. 2B). Together with ambient single-borehole flow profiles (Fig. 2A) they are used to characterize the location and hydraulic properties of fractures intersecting the borehole. Cross-borehole flow profiles are conducted by turning on a pump in an adjacent borehole, while tracking changes in vertical flow in the observation borehole (Fig. 2C). The main interest of this method is to characterize fracture connectivity and to derive the hydraulic properties of the main flow paths (Paillet, 2000; Le Borgne et al., 2007).

Here we focus on the B2 borehole at the Ploemur site, that is located 11 m away from B3 (Le Borgne et al., 2007). Both flow and temperature profiles were collected in this well under different conditions (Fig. 7): ambient, pumping at the top of well B2 (pumping rate  $Q = 125$  l/min, drawdown  $s_{B2} = 1.9$  m) and pumping in B3 (pumping rate  $Q = 145$  l/min, drawdown  $s_{B3} = 0.6$  m). As for B3 (Fig. 1), B2 is characterized by upward flow under ambient condition. Four main flow zone were detected from flowmeter profiles: B2-1 at 27 m, B2-2 at 55 m, B2-3 at 58.1 m and B2-4 at 77.8 m (vertical depth derived from a pressure sensor). Notice that these depths are slightly different from those indicated in Le Borgne et al. (2007) for which the depth was measured along the borehole (cable length). The difference is explained by deviations of the borehole axis from the vertical.

The temperature profiles are strongly affected by the pumping conditions. Under ambient condition, the temperature gradient is

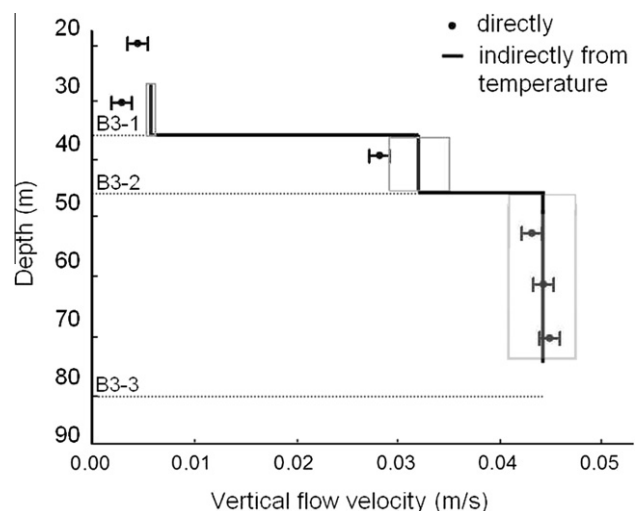


Fig. 6. Comparison between flowmeter measurements (dots, measurement errors are presented by horizontal bars) and velocity values derived from temperature measurements shown in Fig. 1D (solid line, uncertainties are presented by gray domains, see discussion on sources of uncertainties, Section 5).

approximately constant and smaller than the geothermal gradient, except for the shallowest part. This indicates an approximately constant upflow of water in the borehole. When pumping in the adjacent borehole (B3), the main change in the temperature profile is the increase of the temperature flowing from the lowest fracture and the decrease of the temperature gradient in between this fracture and the two intermediate fracture. The temperature gradient in the uppermost section is approximately parallel to the temperature gradient under ambient condition. Thus, the main effect of pumping in B3 is to increase the upflow in between B2-4 and B2-3, B2-2. When pumping in B2, the temperature gradient in all sections is reduced, which is consistent with the important increase of upflow consecutive to pumping in this well.

In order to apply the methodology presented in the previous section, we select the sections of the borehole with constant flow. Since fractures B2-2 and B2-3 are located close to each other, we group them in a single fracture zone. The estimated flow velocities are compared in Fig. 7B to flow measured by direct measurements with a flowmeter under the same hydrodynamic conditions. The changes in temperature profiles are associated with changes in flow velocities over two orders of magnitude. The agreement of flow estimated from temperature profiles with those directly measured is good for all the tested flow conditions.

The temperature profiles displayed under pumping conditions were taken after the transient regime when the temperature profile was evolving in time because of the change of pumping condition. Here, the temperature profiles were recorded 20 h after the pumping conditions were changed. Measurement of the temporal evolution of temperature in the borehole during the transient regime showed that steady-state is achieved after 4 to 5 h.

Once the single and cross-borehole temperature profiles have been converted into flow profiles, the flow profiles can be interpreted to infer fractures hydraulic properties (Le Borgne et al., 2006b). Different methods of interpretation have been proposed using different assumptions (Hess, 1986; Molz et al., 1989; Kabala,

1994). The numerical approach proposed by Paillet (1998) is used here to model flow along intervals between producing fractures. The model simulates quasisteady state flow produced by a zone for a given local transmissivity and hydraulic head at the borehole outer edge. These hydraulic heads are representative of the local hydraulic conditions of each fracture zone and represent the hydraulic heads that would be measured if the fractures were packed off. This model reproduces the flow interactions between the different fractures within the borehole, assuming that flow measured in the borehole can be modeled as the response of a series of slug tests. The superposition of slug tests is used to produce the transient head difference between the borehole and the different flow zones, which in turn drives the transient flow that is observed within the borehole. The solution used for each slug test is given by Cooper et al. (1967). In this approach, a similar storage coefficient for all flow zones is assumed. A value of  $10^{-5}$ , corresponding to fractures in a crystalline geology, is commonly assumed. Since tests are performed under quasisteady state conditions, the assumption about the storage coefficient is not critical. Uncertainties about this modeling procedure are discussed by Paillet (2000). Using this flow modeling technique, we estimate the transmissivity and hydraulic head of each flowing fractures given in Table 1.

The cross-borehole flow profile, obtained in B2 when pumping in well B3, can be used to infer hydraulic connections between the two boreholes. When pumping in B3 a large increase of upflow in the zone located between B2-4 and B2-2 fractures (about one order of magnitude) is observed compared to the ambient profile. This implies a decrease in hydraulic head in B2-2 and B2-3 fractures. As hydraulic head should change only in the flow paths connected to the pumping well we can deduce that at least one of these fractures are connected to B3. Again using the method of Paillet (2000) we estimate the hydraulic head change in B2-2 or B2-3 fractures to be  $\Delta h_{B2-2+B2-3} = -0.4$  m (Table 1). This can be compared to the hydraulic head decrease when pumping in B3

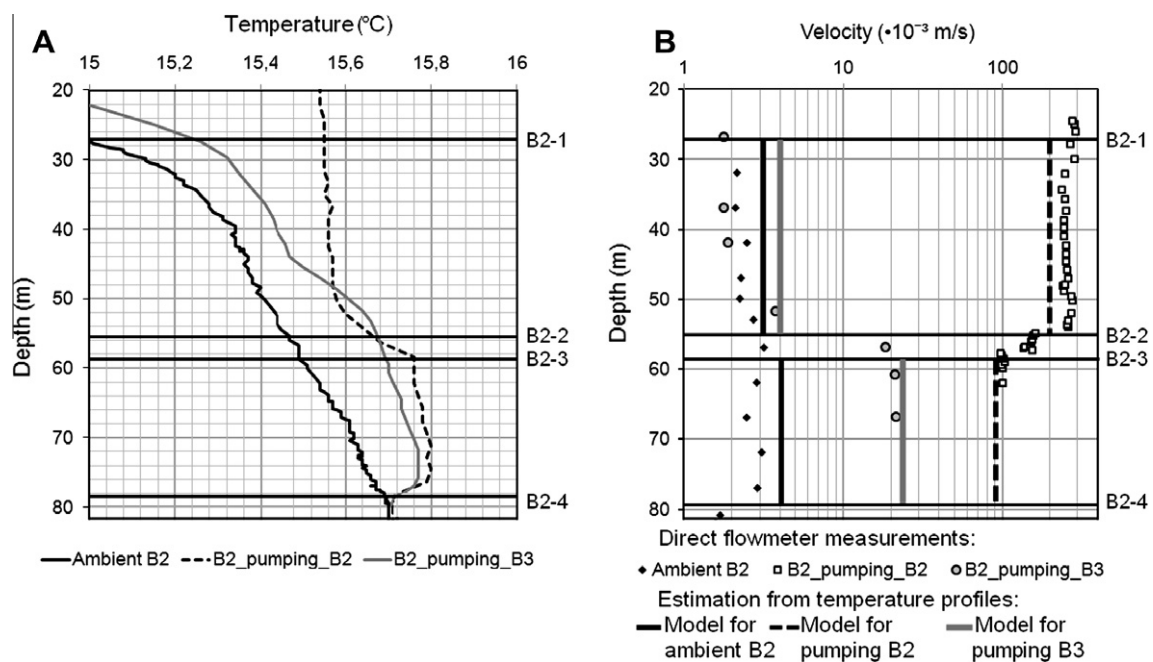


**Fig. 7.** (A) Temperature profiles in B2 measured under different flow conditions. The black solid curve presents temperature profile under ambient flow. The black dashed curve was collected while pumping with pumping at the top of B2 with a pumping rate  $Q = 125$  l/min. The gray solid curve corresponds to the cross-hole pumping test while pumping was turned on in B3 with a pumping rate  $Q = 145$  l/min. (B) Comparison of flow profiles derived from temperature measurement with flow profiles measured under the same hydrodynamic conditions with a heat-pulse flowmeter.

**Table 1**

The estimated transmissivities and hydraulic heads of flowing fractures. The reference for the head values is the sea level.

Fracture	Transmissivity (m <sup>2</sup> /s)	Hydraulic head under ambient condition (m)	Hydraulic head while pumping in B3 (m)
B2-1	$23 \times 10^{-6}$	7.57	7.57
B2-2 + B2-3	$7 \times 10^{-4}$	7.87	7.47
B2-4	$42 \times 10^{-5}$	7.95	7.95

( $s_{B3} = 0.6$  m). By repeating these experiments for the different pairs of boreholes of the site, one can obtain estimates of the hydraulic head variations in the connected zones. This can be used as an input for an inverse problem with the objective of imaging the spatial distribution of the hydraulic properties in the fracture zone in-between the borehole. Such inverse problems based on temperature profiles is the focus of a further study.

## 5. Discussion

The uncertainty about thermal diffusivity, geothermal gradient, borehole radius and temperature measurement errors imply uncertainty on the flow estimates. In this section we try to estimate the major sources of uncertainties related to the developed method. According to Jolivet et al. (1988) the thermal conductivity for Hercynian granites in Brittany can be characterized by a mean value of 2.72 W/m, with only weak regional deviations from the mean value (Jolivet et al., 1988). The geothermal gradient is estimated for the Ploemeur site by collecting temperature profiles in boreholes which are not affected by vertical flow and with suitable depth intervals  $\geq 70$  m. For the temperature profiles analyzed in this study, we found that an uncertainty of 5% in thermal conductivity or in geothermal gradient produces an uncertainty of about 3% in velocity estimation. However, it is difficult to draw general conclusions regarding this uncertainty since it depends on the local conditions of the study.

Another possible source of errors is the deviation from Poiseuille flow in the borehole. The caliper measurements Le Borgne et al. (2007) show that important borehole radius variations occur. Since these variations occur only at few localized zones, we do not expect them to introduce significant errors. Deviation from Poiseuille flow can also be related to turbulent flow. Reynolds number for flow in the borehole is given by  $Re = \frac{2r_0 v_{mean} \rho}{\mu}$ , where  $r_0 = 0.053$  m is the mean borehole radius,  $\rho = 1000$  kg/m<sup>3</sup> is the water density,  $\mu = 1.225 \times 10^{-3}$  N s/m<sup>2</sup> is the water viscosity and  $v_{mean}$  is the mean velocity in the borehole equals to the half of the maximum velocity  $v_{max}$ . Thus for the velocity range  $1 \times 10^{-4} - 2 \times 10^{-1}$  m/s, Reynolds number is in the interval [4.3–8650]. The onset of turbulence is  $Re_{critical} = 2300$ , although much larger Reynolds numbers ( $\approx 10,000$ ) are needed to achieve fully turbulent conditions (Incropera and DeWitt, 1996). Thus, turbulence is not expected to have an important effect on the flow field located in between the flowing fractures, for most of the range of velocities investigated.

A potential limitation of the method is the length of mixing zones located around flowing fractures. These are created by mixing of upflowing water with water produced by a fracture. Different processes are involved in the mixing of inflowing water with borehole water: diffusion, convection, turbulence. For the process of mixing of two jets with different temperatures and rates mixing characteristics depend strongly on the magnitude of temperature difference, flow conditions and geometric configurations (fracture aperture, fracture dip angle) (Wang et al., 2006). Furthermore, the water entering from a fracture in to the borehole is likely to create turbulent vortices which will enhance thermal mixing. From the above consideration it is difficult to estimate theoretically the length of mixing zones. In practice,

we can estimate this length from the abrupt changes of temperature around the flowing fractures which occurs at scales typically smaller than 5–10 m. These mixing zones can then be excluded from the fitting procedure.

The sources of measurement errors for the temperature profile include the logging velocity, the centering of the probe and the accuracy of the temperature sensor. The logging velocity is an important aspect because temperature probes have a finite response time. Temperature probes require a certain time to reach equilibrium with the fluid temperature. Here, the probe was lowered slowly enough to allow for sufficient equilibrium to take place (about 1 m/min). Slower logging velocities did not improve the quality of the temperature profiles.

A possible source of measurement errors in the temperature profile is related to the centering of the tool. When lowering down the thermistor it can easily deviate from the center of the borehole. This can induce bias in the temperature profile as the temperature in the center of the borehole is different from the temperature close to the borehole wall. Examples of radial numerically simulated temperature profiles are displayed in Fig. 8. The difference between the temperature at the center of the borehole and the temperature at the borehole wall may be as large as 0.15 °C. This difference increases with the vertical distances from the inflowing fracture. However, there is a part of the profile where the temperature remains approximately constant (Fig. 8). Note that the radius of this zone slightly diminishes with the distance from the inflowing fracture. For our experiment we used a centralizer for the temperature sensor to remain always in the central zone. Thus, the error related to the tool centering is small in comparison with tool accuracy.

In order to quantify the flow uncertainty induced by temperature measurement errors, we determine the range of possible flow velocities for which the difference between the simulated and measured temperature is less than the relative accuracy of the probe. Here the relative accuracy of the probe is estimated to be  $\pm 0.01$  °C (Fig. 3). Using this value we can estimate numerically error bars for the estimated flow value for each borehole section. These are shown in Fig. 6. For the conditions of our experimental data the range of velocities that could be measured is about  $1 \times 10^{-4} - 2 \times 10^{-1}$  m/s. For smaller velocities, the tool accuracy does not allow us to distinguish between the disturbed temperature profile and the geothermal gradient. For flow velocities larger than the upper range, the temperature anomaly propagates too fast to allow for measurable loss of temperature to the rock formation. Thus, the temperature profile will appear to be completely straight, and we can only say deduce the velocities are larger than this value. The method is found to be more accurate for smaller borehole flow velocities and for long impermeable sections of borehole between flowing fractures. Note that the lower limit of flow velocity estimation is obviously very sensitive to the relative precision of the temperature probe. Nevertheless, the range of velocities that could be measured depends also on the fracture spacing as well as other system parameters.

## 6. Conclusions

We demonstrate the close relationship between the borehole temperature gradient and the vertical borehole flow velocity. Using

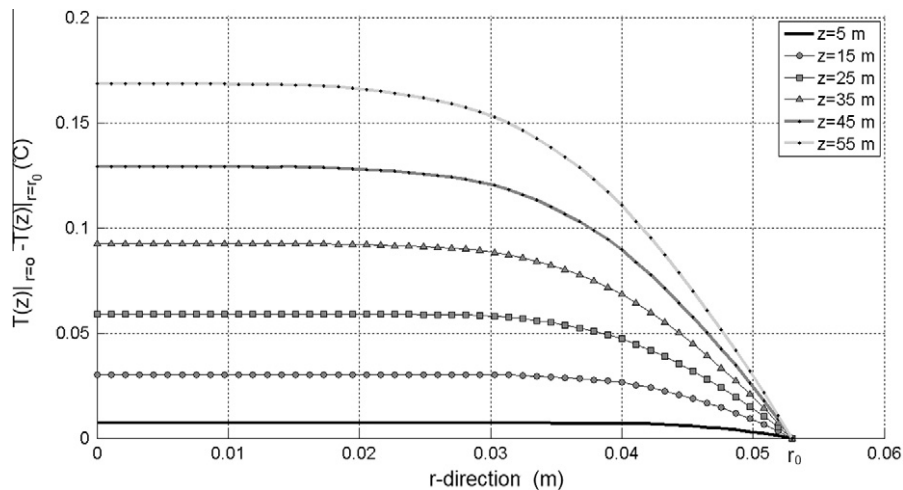


**Fig. 8.** Temperature distribution across the borehole (from  $r = 0$  (center of the borehole) to  $r = r_0$  (borehole wall)) for flow velocity  $v_{max} = 10$  mm/s when moving up away from fracture (5, 15, 25, 35, 45 and 55 m above fracture).

this finding, we have developed an experimental methodology for characterizing spatially distributed hydraulic properties based on temperature profiles under ambient, single and cross-borehole pumping conditions. The validation of the method using experimental data opens up new perspectives for using temperature profiles in inverse problems for imaging the spatial distribution of hydraulic properties. This can be a promising alternative to classical hydraulic tomography tests that requires the use of multiple packers (Li et al., 2007).

The method applied here can be compared to single and cross-borehole flowmeter tests. Temperature data are converted into vertical borehole flow estimates, which are then used to estimate local fracture transmissivity, hydraulic head and larger scale connectivities. Detecting changes in vertical borehole flow normally requires the use of a heat-pulse flowmeter and involves repeated measurements with the flowmeter positioned at different depths. Temperature profiles can be obtained more easily and continuously in space by logging in the observation borehole under different hydraulic conditions. One important aspect to be taken into account is that the transient regime for heat is longer than the transient regime for flow, since the thermal diffusivity is generally smaller than the pressure diffusivity. Thus, estimating steady state vertical borehole flows requires waiting for a longer time after pumping conditions were changed when using temperature profiles than when using local heat pulse flowmeter measurements. In the present case study, quasi-steady state temperature profiles were reached in 4 to 5 h, while quasi-steady state hydraulic heads were reached in about 10 min. Thus, in general, the proposed methodology is well adapted for the estimation of vertical borehole flows in ambient conditions or when pumping has taken place for sufficient time, such as in pumped aquifers. Note that the interpretation of transient temperature profiles could also provide interesting information, such as hydraulic and thermal diffusivities. This is the topic of further investigations.

In classical approaches for interpreting temperature profiles, the temperature of water in the borehole is generally assumed to be representative of the local aquifer temperature. Our study suggests that, in heterogeneous and fractured aquifers, the main control of borehole temperature profiles may be vertical flow in the borehole itself. Ambient vertical borehole flows are created in heterogeneous media due to differences in hydraulic heads between the different flow paths. Thus, one can expect vertical borehole flow to occur in most aquifers. Neglecting this borehole flow may lead

to significant errors in the interpretation of temperature profiles. For instance, applying the classical method of (Bredehoeft and Papadopoulos, 1965; Cartwright, 1979) to our experimental data, we found estimates of vertical velocities that are six orders of magnitude lower than those measured in the borehole.

#### Acknowledgments

This work was supported by the European Marie Curie network IMVUL (Grant Agreement 212298), by ANR project MOHINI (ANR-07-VULN-008), by the National Research Observatory H+ and by the European Interreg IV project CLIMAWAT. We especially acknowledge Simon Callais, that initiated part of this work during his master thesis at Geosciences Rennes in 2009. We thank Nicolas Lavenant for technical assistance during fieldwork, and also master students for help during temperature borehole measurements. Tanguy Le Borgne acknowledges the support of the Marie Curie ERG grant ReactiveFlows (Grant Agreement Number 230947).

#### References

- Anderson, M.P., 2005. Heat as a ground water tracer. *Ground Water* 43 (6), 951–968.
- Arriaga, M.A., Leap, D.J., 2006. Using solver to determine vertical groundwater velocities by temperature variations. *Purdue University, Indiana, USA. Hydrogeology Journal* 14 (1–2), 253–263.
- Becker, K., Davis, E.E., 2003. New evidence for age variation and scale effects of permeabilities of young oceanic crust from borehole thermal and pressure measurements. *Earth and Planetary Science Letters* 210, 499–508.
- Bense, V.F., Kooi, H., 2004. Temporal and spatial variations of shallow subsurface temperature as a record of lateral variations in groundwater flow. *Journal of Geophysical Research* 109, B04103, doi:10.1029/2003JB002782.
- Bense, V.F., Person, M.A., Chaudhary, K., You, Y., Cremer, N., Simon, S., 2008. Thermal anomalies indicate preferential flow along faults in unconsolidated sedimentary aquifers. *Geophysical Research Letters* 35 (24), L24406, doi:10.1029/2008GL036017.
- Borner, F., Berthold, S., 2009. Vertical flows in groundwater monitoring wells. *Groundwater Geophysics*, 367–389, doi:10.1007/978354088405713.
- Bredehoeft, J.H., Papadopoulos, I.S., 1965. Rates of vertical groundwater movement estimated from the Earth's thermal profile. *Water Resource Research* 1, 325–328.
- Cartwright, K., 1979. Measurement of fluid velocity using temperature profiles: experimental verification. *Journal of Hydrology* 43 (1–4), 185–194.
- Chatelier, M., Ruelleu, S., Bour, O., Porel, G., Delay, F., 2011. Combined fluid temperature and flow logging for the characterization of hydraulic structure in a fractured karst aquifer. *Journal of Hydrology* 400, 377–386.
- Chekhaluk, E.B., 1965. *Thermodynamics of Oil Reservoir*. Nedra, Moscow.
- Cooper, H.H., Bredehoeft, J.D., Papadopoulos, I.S., 1967. Response of a finite diameter well to an instantaneous charge of water. *Water Resources Research* 3 (1), 263269.

- Drury, M.J., Lewis, T.J., 1983. Water-movement within Lac-du-Bonnet botholith as revealed by detailed thermal studies of 3 closely-spaced boreholes. *Tectonophysics* 95 (3–4), 337–351.
- Fairley, J.P., Nicholson, K.N., 2006. Imaging lateral groundwater flow in the shallow subsurface using stochastic temperature fields. *Journal of Hydrology* 321 (1–4), 276–285.
- Ge, S.M., 1998. Estimation of groundwater velocity in localized fracture zones from well temperature profiles. *Journal of Volcanology and Geothermal Research* 84 (1–2), 93–101.
- Gosselin, C., Mareschal, J.C., 2003. Variations in ground surface temperature histories in the Thompson Belt, Manitoba, Canada: environment and climate changes. *Global and Planetary Change* 39 (3–4), 271–284.
- Henderson, R.D., Day-Lewis, F.D., Harvey, C.F., 2009. Investigation of aquifer-estuary interaction using wavelet analysis of fiber-optic temperature data. *Geophysical Research Letters* 36, L06403.
- Hess, A.E., 1986. Identifying hydraulically conductive fractures with a slow-velocity borehole flowmeter. *Canadian Geotechnical Journal* 23 (1), 69–78.
- Incropera, DeWitt, 1996. *Fundamentals of Heat and Mass Transfer*. fourth ed., John Wiley and Sons, NY.
- Jaupart, C., Mann, J.R., Simmons, G., 1982. A detailed study of the distribution of heat-flow and radioactivity in New-Hampshire (USA). *Science Letters* 59 (2), 267–287.
- Jolivet, J., Bienfait, G., Vignerresse, J.L., Cuney, M., 1988. Heat flow and heat production in Brittany (Western France). *Tectonophysics* 159, 61–72.
- Kabala, Z.J., 1994. Measuring distributions of hydraulic conductivity and storativity by the double flowmeter test (1994). *Water Resources Research* 30 (3), 685–690.
- Land, L.A., Paull, C.K., 2001. Thermal gradients as a tool for estimating groundwater advective rates in a coastal estuary: White Oak River, North Carolina, USA. *Journal of Hydrology* 248 (1–4), 198–215.
- Le Borgne, T., Bour, O., Paillet, F.L., Caudal, J.-P., 2006a. Assessment of preferential flow path connectivity and hydraulic properties at single-borehole and cross-borehole scales in a fractured aquifer. *Journal of Hydrology* 328, 347–359.
- Le Borgne, T., Paillet, F.L., Bour, O., Caudal, J.-P., 2006b. Cross-borehole flowmeter tests for transient heads in heterogeneous aquifers. *Ground Water* 44, doi:10.1111/j.1745-6584.2005.00150.x.
- Le Borgne, T., Bour, O., Riley, M.S., Gouze, P., Pezard, P.A., Belghoul, A., Lods, G., Le Provost, R., Gresswell, R.B., Ellis, P.A., Isakov, E., Last, B.J., 2007. Comparison of alternative methodologies for identifying and characterizing preferential flow paths in heterogeneous aquifers. *Journal of Hydrology* 345 (3–4), 134–148, doi:10.1016/j.jhydro.2007.07.007.
- Li, W., Englert, A., Cirpka, O.A., Vanderborght, J., Vereecken, H., 2007. Two dimensional characterization of hydraulic heterogeneity by multiple pumping tests. *Water Resource Research* 43, W04433, doi:10.1029/2006WR005333.
- Malard, F., Chapuis, R., 1995. Temperature logging to describe the movement of sewage-polluted surface water infiltrating into a fractured rock aquifer. *Journal of Hydrology* 173 (1–4), 191–217.
- Marechal, J.C., Perrochet, P., 2001. Theoretical relation between water flow rate in a vertical fracture and rock temperature in the surrounding massif. *Earth and Planetary Science Letters* 194, 213–219.
- Molz, F.J., Morin, R.H., Hess, A.E., Melville, J.G., Guven, O., 1989. The impeller meter for measuring aquifer permeability variations: evaluation and comparison with other tests. *Water Resources Research* 25 (7), 1677–1683.
- Paillet, F.L., 1998. Flow modeling and permeability estimation using borehole flow logs in heterogeneous fractured formations. *Water Resource Research* 34 (5), 997–1010.
- Paillet, F.L., 2000. A field technique for estimating aquifer parameters using flow log data. *Ground Water* 38 (4), 510–521.
- Pehme, P.E., Parker, B.L., Cherry, J.A., Greenhouse, J.P., 2010. Improved resolution of ambient flow through fractured rock with temperature logs. *Ground Water* 48 (2), 191–205.
- Ramey, H.J., 1962. Wellbore heat transmission. *Transactions of the Society of Petroleum Engineers of Aime* 225 (4), 427–435.
- Selker, J., van de Giesen, N., Westhoff, M., Luxemburg, W., Parlange, M.B., 2006. Fiber optics opens window on stream dynamics. *Geophysical Research Letters* 33, 24.
- Szekely, F., Galsa, A., 2006. Interpretation of transient borehole flow metering data in a fissured granite formation. *Journal of Hydrology* 327 (3–4), 462–471.
- Sorey, M.L., 1971. Measurements of vertical groundwater velocity from temperature profiles in wells. *Water Resource Research* 7 (4), 963–970, doi:10.1029/WR007i004p00963.
- Stallman, R.W., 1965. Steady one-dimensional fluid flow in a semiinfinite porous medium with sinusoidal surface temperature. *Journal of Geophysical Research* 70, 2821–2827, doi:10.1029/JZ070i012p02821.
- Wang, S.J., Devahastin, S., Mujumdar, A.S., 2006. Effect of temperature difference on flow and mixing characteristics of laminar confined opposing jets. *Applied Thermal Engineering* 26, 519–529.

### 4.3 Conclusions

Temperature anomalies at the Ploemeur fractured rock field site attain 3 degrees under and upper the natural geothermal gradient for the borehole depth 100 – 150 m. To understand and quantify this phenomena, we investigated in this chapter temperature profiles at the borehole scale. Using a flow and heat transfer numerical model, we have found that the slope of the temperature profile is related directly with vertical borehole flow velocity. Thus, we propose a method to invert temperature measurements to derive borehole flow velocities. We then demonstrated that based on single borehole and cross borehole temperature profiles, fracture hydraulic properties between and around a borehole pair can be characterized. The validation of the method from experimental data opens new perspectives for using temperature profiles in inverse problems for imaging heterogeneous fracture properties.

#### **4. USING BOREHOLE TEMPERATURE PROFILES TO ESTIMATE FRACTURE BOREHOLE FLOW VELOCITIES**

---

# Chapter 5

## Temperature tomography experiment in fractured media

### 5.1 Introduction

In order to test how well the methods developed in Chapter 2 and Chapter 4 can characterize fractured media, we present in this chapter a new experimental approach. This experiment, which we call temperature tomography, consists of sequential borehole temperature logging under cross-borehole flow conditions. To interpret temperature tomography experiments, we propose the full inverse framework, combining the two approaches proposed in the previous chapters. Finally, we apply temperature tomography approach to the Ploemeur field site.

### 5.2 Paper: Temperature tomography experiment in fractured media (Klepikova et al., in prepa- ration)

# <sup>1</sup> **Temperature tomography experiment in fractured** <sup>2</sup> **media**

Maria V. Klepikova<sup>1</sup>, Tanguy Le Borgne<sup>1</sup>, Olivier Bour<sup>1</sup>, Kerry Gallagher<sup>1</sup>,

Rebecca Hochreutener<sup>1</sup> and Nicolas Lavenant<sup>1</sup>

---

Corresponding author: M. V. Klepikova, Géosciences Rennes, OSUR, UMR CNRS 6118, University of Rennes 1, Rennes, France. (maria.klepikova@univ-rennes1.fr)

<sup>1</sup>Géosciences Rennes, OSUR, UMR CNRS  
6118, University of Rennes 1, Rennes,  
France.

**Abstract.**

Detection of flowpaths, characterization of their hydraulic properties as well as flowpath connectivity are major challenges in characterization of fractured aquifers. In this study we propose a new temperature tomography field method in which borehole temperature profiles are measured under combinations of pumping conditions by changing successively the pumping and observation borehole. We propose a framework for interpretation of these temperature-depth profiles that consists of three steps. We consider first an inverse model that allows for automatic fracture detection from borehole flowmeter profiles under pumping conditions. Then we apply the borehole-scale model to produce high resolution flowmeter profiles by inversion of temperature profiles. The third inverse problem is aimed at inferring hydraulic properties of the inter-borehole fracture connections that are compatible with the flow velocities estimated from the previous step. We test the proposed approach from field data obtained in the Ploemeur fractured rock aquifer. This inverse framework provides a means of including temperature profiles to image the spatial distribution of hydraulic properties.

## 1. Introduction

20 The accurate prediction of fluid flow in fractured media is still a challenging problem.  
21 The classical way to infer flow properties requires the identification of the flowing frac-  
22 tures followed by cross-borehole pumping tests with monitoring of the hydraulic heads in  
23 fractures isolated with packers. Recent developments [*Illman et al.*, 2009; *Sharmeen et*  
24 *al.*, 2012] significantly improve the interpretation of such tests. However, spatial resolu-  
25 tion of the inferred tomograms strongly depends on the number of observation intervals  
26 [*Sharmeen et al.*, 2012], while installation of packers is not always possible. To avoid these  
27 practical issues, other type of data, that can be more easily obtained and that are directly  
28 sensitive to ground water flow may be considered.

29 Temperature data meet these conditions as geothermal heat can be considered as a nat-  
30 ural tracer of groundwater flow [*Anderson*, 2005; *Saar*, 2011]. Furthermore, temperature  
31 profiles can be obtained easily and continuously in space by logging in the observation  
32 borehole. The use of fiber optic technology can also greatly improve the temporal and  
33 spatial coverage [*Read et al.*, 2013]. Generally, temperature-depth profiles are expected  
34 to linearly increase with depth in the absence of groundwater flow or changes in ther-  
35 mal conductivity. Even small deviations from linear, conductive temperature profile can  
36 represent significant advective heat transfer and indicate groundwater flow. Temperature  
37 data have often been used for inferring vertical or horizontal groundwater flow velocities  
38 assuming homogeneous aquifer [*Bredehoeft and Papadopulos*, 1965; *Anderson*, 2005]. Yet,  
39 relatively few methods exist for using temperature to quantify flow in fractured media.

40 In fractured rocks temperature anomalies are often observed [e.g. *Ge*, 1998; *Bense et*  
41 *al.*, 2008; *Chatelier et al.*, 2011]. In large-scale faults, groundwater temperature anomalies  
42 and velocities can be large enough to influence regional heat flux distribution [*Ge*, 1998;  
43 *Anderson*, 2005; *Garibaldi*, 2010; *Saar*, 2011]. Small-scale fractures perturb the tempera-  
44 ture profile in narrow regions due to conducted flow with either warmer or cooler origins  
45 [*Ge*, 1998]. Moreover, ambient flow in boreholes themselves, that arises due to the differ-  
46 ence in hydraulic heads between fractures intersecting the borehole, affects temperature  
47 logs collected in boreholes [*Pehme*, 2010; *Klepikova et al.*, 2011].

48 A few works have investigated borehole temperature profiles in fractured rocks under  
49 induced fluid flow conditions. Thus, *Silliman* [1989] argued that temperature anomalies  
50 produced by pumping in adjacent boreholes can be used for initial estimates of fractures  
51 connecting 'pumping-observation' borehole pair. Recently, we have demonstrated the  
52 close relationship between the borehole temperature gradients and the vertical borehole  
53 flow velocity [*Klepikova et al.*, 2011]. We showed that by applying flow and heat transfer  
54 numerical model, the slope of borehole temperature profiles under ambient, pumping and  
55 cross-pumping flow conditions can be inverted to obtain precise flowmeter profiles. Fur-  
56 thermore, we have shown in another study that using cross borehole flowmeter profiles  
57 in tomography approach, in turn, can be used for estimating inter borehole fracture hy-  
58 draulic properties as well as fracture connectivity. This approach was referred to as flow  
59 tomography (*Klepikova et al.*, submitted).

60 In the present study, we propose to couple these two approaches to a temperature to-  
61 mography experimental approach (i.e., temperature measurements during the sequential  
62 cross-borehole pumping tests). We therefore propose the full inverse framework to inter-

63 pret temperature tomography experiments. In the first part of this paper we detail the  
64 steps of our inverse approach. In the second part we present the temperature tomography  
65 experiment conducted in the fractured Ploemeur aquifer. We also discuss temperature  
66 background on the field site and interpret it in terms of aquifer flow structures. Finally,  
67 we present the results of application of our inverse approach to the Ploemeur field site.

## 2. Methodology

68 The temperature tomography approach proposed in this study consists of three main  
69 steps.

70 1. Automatic detection of fracture zones intersecting observation and pumping boreholes  
71 through the inversion of ambient and steady pumping single-borehole flowmeter profiles.

72 2. Inversion of temperature profiles under cross-borehole flow conditions to derive high  
73 resolution flowmeter profiles.

74 3. Estimation of fracture hydraulic properties and connectivity between and around  
75 borehole pair through the inversion of ambient, single and cross-borehole pumping flow  
76 profiles obtained from the previous step.

77 Note, that fractures intersecting the boreholes can be also detected through the inversion  
78 of temperature profiles. However, we found that temperature profiles are not sufficient to  
79 detect all the fractures, and flowmeter profiles are needed. The approach is systematized  
80 in Figure 1. In the following sections we detail these steps.

## 2.1. Detection of Fractures

81 The primary step in characterization of flow pattern in between a borehole pair is the  
82 detailed characterization of flow properties at the single borehole scale. Several meth-  
83 ods were proposed for fracture identification at the borehole scale. Complementary to  
84 geophysical methods, that include inspection of continuous core, caliper data, acoustic  
85 and optical televueing [*Barton and Zoback, 1992*] and electrical resistivity measurements  
86 [*Keys, 1979*], hydraulic tests, such as flowmeters [*Paillet, 1998*], straddle packers [*Quinn*  
87 *et al., 2011*], high spatial resolution temperature profiling [*Mwenifumbo, 1993; Barton et*  
88 *al., 1995*] and flexible liner profiling [*Pehme, 2010, 2013*] allow us to identify transmissive  
89 fractures.

90 In this study we consider fracture identification method based on flowmeter profiles.  
91 Ambient vertical flow from one fracture zone to another in the same borehole is commonly  
92 observed. This flow is due to differences in hydraulic heads between large-scale flow paths  
93 that connect to fractures intersecting boreholes. The transmissive fractured zones may be  
94 associated with inflow zones during the pumping test. Inflow points for each borehole can  
95 be identified by inspection of the pairs of ambient and pumping flow profiles [*Paillet, 1998*].  
96 An illustration of ambient and pumping flow profiles is given in Figure 1. In this example,  
97 abrupt changes in flow profile occur at depths where transmissive fractures intersect the  
98 borehole. However, multiple sources of error such as calibration uncertainties, changes in  
99 borehole diameter or in the velocity of troling, influence the accuracy of flow log data  
100 [*Paillet, 2004*]. The scatter of flow measurements related to these errors complicates the  
101 identification of changes in flow trends and, thus, detection of flowing fractures.

102 To facilitate the interpretation of flow logs we apply, a recently proposed transdimen-  
103 sional changepoint model [Gallagher et al., 2011]. Changepoints can be defined as abrupt  
104 changes in trends (such as the mean, gradient or any function) over depth or time. Change-  
105 point modelling is an inverse method that allows the inference of changepoints structure  
106 in noisy data series in terms of distributions for the number and location of changepoints  
107 as well as noise variance associated with each dataset. The approach is formulated in  
108 a Bayesian framework, and it uses transdimensional Markov chain Monte Carlo. The  
109 method proposed is used to quantify abrupt changes (or changepoints) in data series  
110 which are statistically significant variations in the trend over a scale of one or two mea-  
111 surements of the total dataset. Borehole flowmeter profiles in fractured media generally  
112 consist of intervals of constant flow between transmissive fractures [Paillet, 1998]. Thus,  
113 application of changepoint model to flow profiles may ideally provide inflow and outflow  
114 zones.

115 In general, identification of trends and changes in trends is directly influenced by the  
116 noise level. Thus, data with lower noise tend to produce a model with many change-  
117 points. However, the method proposed allows for unknown noise variance in each dataset  
118 and the Bayesian approach naturally balances the noise level with the complexity of the  
119 change point structure [Gallagher et al., 2011]. Furthermore, in the field example, we  
120 demonstrate that application of changepoint model to single-borehole flowmeter profiles  
121 allows for automatic fracture detection as well as estimation of uncertainties related to  
122 flow profiles. As mentioned above, in order to detect flowing fractures intersecting the  
123 borehole, we found single-borehole flowmeter profiles to be more accurate, compared to  
124 temperature profiles. This is mainly due to temperature profiles should be converted into

125 the temperature gradient over depth profiles in order to be incorporated to changepoint  
126 model. This implies loss of accuracy. However, in the cross-borehole experiment temper-  
127 ature profiles may provide a finer spatial resolution and are also less time consuming to  
128 obtain.

## 2.2. Borehole Scale Flow and Heat Inverse Modelling

129 Once the locations of fractures intersecting the boreholes had been detected, we used  
130 a numerical model of flow and heat at the borehole scale to invert temperature profiles  
131 to estimate cross-borehole flow profiles. The model included the advection of heat in the  
132 borehole with a constant vertical laminar flow and the heat dissipation in the surrounding  
133 rock matrix [Klepikova *et al.*, 2011]. We consider the cylindrical borehole (with a radius  
134 fixed to  $r_0$ ) divided into sections according to the position of flowing fractures inferred from  
135 the changepoint modeling (see previous Section). At the bottom of each borehole section  
136 we impose the borehole flow as the sum of all fractures inflows and outflows below the  
137 modeled section. The inflow temperatures (here bottom temperature for each section) are  
138 taken from the measured temperature profile. The rock temperature at the outer vertical  
139 boundary is taken as the ambient temperature in the rock. The boundary condition at the  
140 lower boundary is taken as a geothermal heat flux  $Q = -k_{Rock}\gamma$ , where  $k_{Rock}$  is a thermal  
141 conductivity of the rock and  $\gamma$  is the background geothermal gradient. The temperature  
142 at the upper boundary is taken as a surface temperature (or other constraints as the  
143 temperature of sub-horizontal fracture). A detailed description of the direct model is  
144 given in *Klepikova et al.* [2011].

In order to invert temperature profiles to high resolution flowmeter profiles we couple  
the direct model of heat and flow at the borehole scale with an optimization algorithm.

The inverse problem consists of estimating the vertical borehole flow velocities that drive the temperature profiles observed under different flow conditions. The misfit function,  $FO$ , which evaluates the difference between direct model simulations and temperature measurements, is given by

$$FO = \frac{1}{\sigma_T^2} \frac{1}{N_T} \sum_0^{N_T} (T_{obs} - T_{mod})^2 \quad (1)$$

145 where  $T_{obs}$  is the temperature measurements,  $\sigma_T$  is the noise variance associated with tem-  
 146 perature dataset,  $N_T$  is the number of temperature observations,  $T_{mod}$  is the temperature  
 147 predicted by the model. As we demonstrated further, the typical objective function for  
 148 this problem is convex and possess a global minima. Thus, the formulated optimization  
 149 problem is solved by the Nelder-Mead Simplex (NMS) algorithm employed from MAT-  
 150 LAB optimization Toolbox [*Lagarias et al.*, 2011]. The NMS algorithm is a nonlinear fast  
 151 local search method that does not need to calculate an explicit formulation of the objec-  
 152 tive function Jacobian and that is suitable for our problem. As the objective function is  
 153 normalized to the data error (Equation 1), the convergence criteria is reached when the  
 154 objective function value equals one.

### 2.3. Site Scale Flow Inverse Modeling

155 In order to estimate transmissivities of hydraulically active fractures between and  
 156 around the pumping and observation boreholes we apply the flow tomography framework  
 157 that invert single- and cross-borehole flow profiles (Klepikova et al., submitted). This  
 158 approach uses a 3-D numerical flow model (with 2-D flow in each fracture) to calibrate  
 159 measured flow profiles with simulated flow in a simplified fracture network. We use a  
 160 simplified fracture network model that attempts to reproduce basic fracture network con-

nectivity without taking the whole complexity of fracture geometry (length, orientation,  
dip) into account. In this fracture network model, the observation and pumping boreholes  
are both intersected by horizontal fractures that represent fractures identified previously  
at borehole-scale (Section 5.1). These fractures are connected by a vertical fracture equally  
distanced from both boreholes. Flow paths connectivity between boreholes are controlled  
by attributing different values of transmissivity to the different sections of this vertical  
fracture. The detailed description of the inverse modelling approach for flow tomography  
experiment is given in Klepikova et al, submitted (see Chapter 3 of this manuscript).

We first define local transmissivities of each fracture zone intersecting the observation  
and pumping boreholes through the inversion of ambient and steady pumping single-  
borehole flow profiles. The obtained results were found to be in a good agreement with the  
estimations obtained through the numerical approach proposed by *Paillet* [1998]. Then,  
the inverse approach adjusts transmissivities of different sections of the vertical fracture,  
so that the simulated profile matches the cross-borehole flow profile for all sections of  
observation well. These steps allow for identification of connectivity and transmissivities  
of simplified fracture network between and around a borehole pair.

Fracture networks often consist of several fracture connections and interpretations of  
the results are not straightforward. However, we believe that fracture connection patterns  
can be understood from the sensitivity analysis conducted for a simple fracture network  
(Klepikova et al., submitted). The main conclusions of this study can be synthesized as  
follows:

182 A. For small borehole flows, similar velocities can be produced by different combina-  
183 tions of fracture interconnection transmissivities. Thus, the uncertainty of connectivity  
184 estimation increases as borehole flow decreases.

185 B. The magnitude of the vertical borehole flow velocity increases with the difference  
186 between the direct connection transmissivities and decreases with the transmissivity of  
187 the fractures that connect the flowpaths but not the borehole.

188 C. The direction of the vertical borehole flow velocity is towards the largest connection  
189 transmissivity.

190 In the following section we apply this approach to an experimental site in fractured  
191 rocks. We further interpret the obtained results, basing on these conclusions.

### 3. Experimental Site

192 The temperature tomography experiments were carried out within a fractured rock  
193 aquifer at the test-site Stang er Brune (Ploemur, France) [*Le Borgne et al.*, 2007]. The  
194 site consists of 4 boreholes: B1 borehole (83 *m* deep), B2 and B3 boreholes (100 *m* deep)  
195 and F22 borehole (70 *m* deep). B1, B2 and B3 form a triangle within a radius of 10 *m*  
196 and F22 is 30 *m* from this triangle (Figure 2). The geology of the site is characterized  
197 by a gently dipping contact between granite and overlying micaschists. This contact  
198 zone intersects boreholes at the following depths: B1 at 38 *m*, B2 at 37 *m*, B3 at 37.5  
199 *m*, and F22 at 13 *m*. Both hydrological and borehole data [*Le Borgne et al.*, 2007]  
200 demonstrate the presence of a shallow fracture within a mica-schist formation dipping  
201 parallel to the contact zone between granite and overlying micaschists and intersecting  
202 all the boreholes at the site. Moreover, B1, B2 and B3 boreholes are intersected by

203 several permeable fractures within the granite formation [*Le Borgne et al.*, 2007; *Dorn et*  
204 *al.*, 2012]. These deep confined fractures have a higher hydraulic head than the shallow  
205 fracture leading vertical upward flow under the ambient flow conditions in these boreholes.  
206 Flow measurements demonstrated that F22 borehole is not affected by vertical flow. In  
207 the next section, we demonstrate that temperature measurements on the site are strongly  
208 influenced by these hydrogeological conditions.

### 3.1. Temperature Anomalies at the Experimental Site

209 The temperature measurements were conducted under the ambient flow conditions with  
210 a tool accuracy of  $0.005^{\circ}C$ . Figure 3B demonstrates that temperature profiles in the site  
211 are characterized by high positive anomalies. All four wells show the abrupt changes in  
212 temperature gradient at 10 – 40 *m* depth. Such a site-scale temperature field corresponds  
213 to a typical pattern of temperature profiles perturbed by a sub horizontal groundwater  
214 flow that transmits groundwater from greater depth hotter than the background rock  
215 temperature [e.g. *Ge*, 1998; *Saar*, 2011]. The illustration of corresponding flow pattern  
216 is shown in Figure 3A. For each borehole, the depth of changes in gradient, F22 at 8  
217 *m*, B1 at 24 *m*, B2 at 25 *m* and B3 at 36.5 *m*, corresponds to the depths of the first  
218 shallow fracture in mica-schists, which was firstly reported by *Le Borgne et al.* [2007].  
219 This fracture is believed to advect heat and to provide a constant temperature boundary  
220 condition. This process distorts the otherwise continuous linear geothermal profile because  
221 the fluid temperature provides a local boundary condition [*Saar*, 2011].

222 The most significant contrast in thermal gradient is in F22 well, where, in the absence  
223 of borehole flow, temperature field is dominated by the upward conductive heat transfer.  
224 Thus, F22 temperature-depth profile may be considered to represent the temperature

225 of the surrounding rock. Below the mica-schist fracture, intersecting F22 at 8 m, the  
226 temperature gradient in F22 corresponds to the background geothermal gradient  $\gamma = 0.016$   
227  $^{\circ}\text{C}/\text{m}$  measured over Hercynian granites in Brittany [Jolivet *et al.*, 1988]. Above the  
228 fracture, the temperature gradient changes to conform to the surface temperature, which  
229 is fixed by the mean annual surface temperature equal to about  $T_{surf} = 12.5 \text{ C}$ . While  
230 this large-scale phenomenon influences the whole site temperature, temperature gradients  
231 variations in granite seem to be mainly caused by local temperature anomalies.

232 In B1, B2, B3 boreholes the ambient vertical borehole flow below the shallow fracture  
233 affects the linear temperature distribution by upward advection of temperature anomalies  
234 coming from fractures intersecting the boreholes. This phenomenon causes smaller, rela-  
235 tive to the geothermal temperature, gradient in sections in between the flowing fractures  
236 [Klepikova *et al.*, 2011]. Moreover, the B3 temperature profile in Figure 3 demonstrates  
237 abrupt temperature changes at 45 m and 80 m, which correspond to depths of fractures  
238 reported by *Le Borgne et al.* [2007]. These anomalies are explained by the localized lateral  
239 advection of cold water within narrow fractures in granite intersecting the borehole [Ge,  
240 1998]. Contrary to the large-scale fracture in the mica-schist, these temperature anoma-  
241 lies seem to have much less influence on the site heat flux distribution. Thus, on this  
242 experimental site the high temperature anomalies are the result of four effects:

- 243 • upward conductive heat transfer through the rocks providing linear temperature gra-  
244 dient,
- 245 • sub horizontal groundwater flow in micaschists of warmer (deeper) origin,
- 246 • the advection of temperature anomalies by the vertical flow in the boreholes itself,
- 247 • localized lateral advective transfer of water within narrow fractures.

#### 4. Experimental Design

248 Three cross-hole pumping tests were conducted with temperature monitoring in neigh-  
249 boring boreholes: the first with pumping taking place in B1 borehole, the second in B2,  
250 and the third in B3. The ambient temperature profiles and the hydraulic heads were  
251 measured at all the boreholes before the start of pumping. The first cross-borehole pump-  
252 ing test took place in well B3 with a pumping rate of  $Q_{B3} = 154 \pm 3 \text{ l/min}$ . Prior to  
253 starting the next pumping test the pressure and temperature were allowed to recover for  
254 each experiment. Subsequently, we conducted the pumping tests in B2 well (pumping  
255 rate  $Q_{B2} = 136 \pm 14 \text{ l/min}$ ), and then in B1 well (pumping rate  $Q_{B1} = 77 \pm 2 \text{ l/min}$ ).  
256 Thus, the full data set consists of 9 hydraulic heads and 9 temperature profiles: 3 am-  
257 bient profiles and 6 profiles when pumping in the neighboring well. The temperature  
258 profiles were measured with a temperature logging device (The Idronaut CDT 302 Multi-  
259 Parameter Probe). The collected steady-state temperature-depth profile are shown in  
260 Figure 4. These temperature profiles were measured under ambient and pumping flow  
261 conditions. Figure 4 shows that these temperature measurements are sensitive to changes  
262 in pumping conditions.

263 For the temperature tomography study, the temperature profiles need to be measured  
264 after pumping took place for a sufficient time to reach steady state. To monitor this, a  
265 set of 7 thermistors was installed permanently in each well. The number of transducers  
266 was chosen to be able to control all borehole sections between the flowing fractures. The  
267 acquisition time of 20 s was appropriate to collect temperature transients for the chosen  
268 depths. An example of temporal evolution of temperature is given in Figure 4D. These  
269 data show that thermal steady state for each particular depth and well couple was reached

270 in 1 – 2 hours after switching on the pumping, depending on the pumping and observation  
271 points. The temperature transients were not used in the subsequent analysis for this study.  
272 However, the interpretation of transient data could also provide interesting information,  
273 such as thermal diffusivity values.

## 5. Results

274 In this section, we present the results of the application of the developed inverse mod-  
275 elling framework at Stang er Brune field site. We firstly detect the flowing fractures  
276 intersecting the boreholes by applying changepoint modelling to single-borehole flowme-  
277 ter profiles. Then, we assess inter-borehole connections properties by applying our inverse  
278 modeling to temperature tomography data set. Finally, we discuss corresponding uncer-  
279 tainty estimates.

### 5.1. Detection of Fractures

280 In order to detect flowing fractures intersecting the boreholes, we apply changepoint  
281 modelling [Gallagher et al., 2011] to vertical flow data measured using a heat-pulse flowme-  
282 ter under both ambient and pumping flow conditions. Figure 5 presents one of the mea-  
283 sured flow profiles (B1 borehole) and the inferred changepoints. In this example the flow  
284 profile represents the difference between the pumping (pump placed at the top of the  
285 well  $Q = 82 \text{ l/min}$ ) and the ambient flow profiles. The inferred changepoint structure is  
286 shown by red line. The locations of the inferred changepoints,  $z = 44.3, 50.9, 60.9$  and  
287  $78.7 \text{ m}$ , correspond well to fracture locations in B1, identified previously by *Le Borgne*  
288 *et al.* [2007] and *Dorn et al.* [2012]. Due to the low transmissivity and casing vicinity,  
289 the B1-2 fracture, located at  $24 \text{ m}$  depth, can not be detected from the flowmeter pro-

file under pumping conditions. However, this fracture can be clearly identified from the  
ambient flow profile (see Chapter 2). For the flow log data presented here, the mean of  
the noise (variance) distribution is  $\pm 0.01$  m/s. This example demonstrates the suitability  
of changepoint modelling applied to flowmeter profiles to detect automatically transmiss-  
ive fractures. While for fracture detection we use single-borehole flow profiles, in the  
subsequent section the temperature tomography data set is analyzed.

## 5.2. Borehole-Scale Flow and Temperature Inverse Modelling

In this section we invert temperature tomography data to flowmeter profiles by applying  
borehole-scale model of heat and flow. Once the flowing fractures have been detected,  
we simulate flow and temperature propagation for each borehole from the first bottom  
transmissive fracture up to the shallowest transmissive fracture. The rock temperature at  
the outer boundary is taken as temperature profile measured in F22 as it is not affected  
by borehole flow. The thermal properties of the rock matrix were chosen to be equal to  
the mean thermal properties measured in laboratory on samples from B1 borehole (see  
Chapter 3 of the manuscript). Thus, the rock thermal conductivity is given by  $k_{Rock} = 3.31$   
 $W/mC$ , the heat capacity of the granite is given by  $C_{Rock} = 738$  J/kgC. The values for  
water properties are given by  $k_{Fluid} = 0.59$  W/mC and  $C_{Fluid} = 4189$  J/kgC respectively  
[Incropera and DeWitt, 1996].

An illustration of the objective function versus the vertical borehole flow velocity is  
presented in Figure 6. In this figure the optimal flow velocity and its uncertainty are  
presented for the part of temperature profile measured in B1 borehole (at the depth  
60.9 – 78.7 m) while pumping in B2. The objective function becomes less sensitive for  
larger flow velocity. For this example the objective function is no more sensitive to the

312 changes in flow starting from  $v = 2 \cdot 10^{-2} \text{ m/s}$ . For flow velocities larger than this upper  
313 limit, the temperature anomaly propagates too fast to allow for measurable temperature  
314 change by heat loss to the rock formation and the temperature profile becomes vertical.  
315 This is a typical example of model calibration, and the objective function was found to  
316 be convex and to possess a global minima.

317 Inversion results show that vertical borehole flow occurs in all boreholes in ambient  
318 conditions. In order to check the accuracy of the estimated flow profiles, we measured flow  
319 profiles directly with heat-pulse flowmeter for some hydrodynamic conditions (ambient  
320 and during pumping in B2 borehole). The flow velocities obtained from temperature  
321 measurements are compared in Figure 7 to flow measured directly with a flowmeter under  
322 the same hydrodynamic conditions. Heat pulse flowmeter can measure flow as small as  
323  $0.05 \text{ l/min}$  in laboratory flow columns [Paillet, 2004]. The uncertainty about velocity  
324 values obtained from temperature profiles are individual and depends on the length of  
325 the borehole flowing sections, temperature tool precision and flow velocity [Klepikova et  
326 al., 2011]. The agreement of flow estimated from temperature profiles with those directly  
327 measured is relatively good for all the tested flow conditions over two orders of magnitude.  
328 Thus, the inversion of all measured temperature profiles allows obtaining a complete and  
329 continuous data set for flow tomography.

### 5.3. Site Scale Flow Inverse Modelling

330 Once temperature profiles under cross-borehole flow conditions have been inverted to  
331 high resolution flow profiles, we invert cross-borehole flow profiles to estimate the trans-  
332 missivities of hydraulically active fractures between each borehole pair. To model flow  
333 between boreholes the fracture network geometry have been simplified as follows in agree-

334 ment with procedure explained in Section 3. Transmissive fractures intersecting the bore-  
335 holes, that were identified in Section 5.1, are represented through horizontal fractures,  
336 and a vertical fracture equally distanced from both boreholes is introduced to control  
337 inter-fracture connectivity. In order to estimate transmissivities of fracture connections,  
338 we perform a joint inversion of two pumping tests where pumping and observation bore-  
339 holes are inversed. Observations for each pumping test consists of the observation well  
340 drawdown and values of vertical velocities in between all fractures intersecting observation  
341 borehole. A set of 20 starting points is generated for each boreholes pair to search for a  
342 minimum of the objective functions. The obtained parameter estimates provide good fit to  
343 the data (Table 1). However, we admit the possibility that obtained solutions correspond  
344 to local minima of the objective function, and parameter estimations can be improved by  
345 increasing the number of the starting points. The resulting parameter estimates providing  
346 the minimum of the objective functions are shown in Figures 8, 9 and 10. Nevertheless,  
347 the presented solutions are not unique and we discuss further another parameter estimates  
348 that provide a good fit to the data.

349 For all solutions providing a good fit to the data from the B1-B2 borehole pair, including  
350 the best one shown in Figure 8, deep fractures, B1-4 and B2-4, were found to be poorly  
351 connected ( $\log T_5 \leq -5.3$ ). This result could be explained from borehole flow velocities,  
352 that inverse model attempts to fit to (Table 1). For B1-B2 borehole pair borehole, we found  
353 upward flow for all the sections of both boreholes. As the direction of the vertical borehole  
354 flow velocity is towards the largest connection transmissivity (Section 2.3, conclusion C),  
355 then it implies that overall transmissivities of fractures connecting the B1-B2 borehole  
356 pair should decrease with depth. Moreover, since the deep fractures themselves are very

357 transmissive,  $\log T_{B1-4} = -3.8$  and  $\log T_{B2-4} = -3.2$ , it provides a strong limitation for  
358 the transmissivity of their interconnection  $T_5$ .

359 Further, large flow velocities in deep borehole sections (Table 1) provide a strong con-  
360 straint for  $T_3$  and  $T_4$  fracture connections. To maximize the difference in hydraulic heads  
361 drawing these velocities, the transmissivity of the  $T_3$  fracture connection should be max-  
362 imized, while the transmissivity of the  $T_4$  fracture connection should be minimized (ac-  
363 cording to conclusion B, Section 2.3). Flow velocities in shallow borehole sections was  
364 found to be close to zero that implies that  $T_2$  and  $T_3$  parameter estimation are rather  
365 uncertain (conclusion A, Section 2.3).

366 Similarly, for B1-B3 borehole pair, upward flow in both boreholes (Table 1) implies  
367 good fracture connections for the shallow fracture, while minimizes the transmissivity of  
368 deep fracture interconnection  $T_6$ . For fracture network connecting B2-B3 borehole pair,  
369 small flow velocities in both wells (Table 1), do not provide a strong constraint for the  
370 interconnection fracture transmissivities ( $T_2$ ,  $T_3$  and  $T_4$ ). Consequently, the uncertainty  
371 of connectivity estimations increase and the estimations of  $T_2$ ,  $T_3$  and  $T_4$  vary within  
372 two orders of magnitude. However, upward flow in the deep section of B2 provides an  
373 estimation for the  $T_5$  transmissivity.

374 The most transmissive fracture connections at the site can be synthesized through:

- 375 •  $B1 - B2$  borehole pair is mainly connected through  $B1 - 2$  and  $B2 - 2$
- 376 •  $B1 - B3$  borehole pair is mainly connected through the cluster that consists of  $B3 - 1$ ,  
377  $B3 - 2$ ,  $B1 - 1$  and  $B1 - 2$  fractures

378 •  $B2 - B3$  borehole pair is mainly connected through 2 independent clusters. The first  
379 one consists of  $B2 - 2$ ,  $B3 - 1$  and  $B3 - 2$ , and the second one consists of  $B2 - 4$  and  
380  $B3 - 3$ .

381 In the next section we test the relevance of these estimation by comparison of our results  
382 with results of studies, based on other types of measurements.

## 6. Discussion

383 The analysis of fracture connections on Stang er Brun field site have been also conducted  
384 by *Le Borgne et al.* [2007] and *Dorn et al.* [2012]. *Le Borgne et al.* [2007] used televiwer  
385 data together with cross-borehole single packer testing and cross-borehole flowmeter test-  
386 ing at the site to characterize fracture hydraulic connections. Using a combination of  
387 these data, the main connected flow zones were identified for each borehole pair at the  
388 site. Comparison of our results demonstrates that temperature based approach provides  
389 relatively consistent results with few exceptions. The main difference concerns to the  
390 connection in between B2-4 and B1-4 fractures. Thus, *Le Borgne et al.* [2007] found that  
391  $B2 - 4$  and  $B1 - 2$  fractures are connected. Further, *Dorn et al.* [2012] used tracer test data  
392 combined with single-hole ground-penetrating radar (GPR) data to characterize fracture  
393 pattern in between B1 and B2 wells. The obtained images confirmed the existence of  
394 connected multifracture network including B2-4 and B1-4 fractures. This issue illustrates  
395 the difficulty of characterizing connectivity in multifracture networks. The cause of the  
396 inconsistency could be the using of simplified fracture network geometry. A limitation  
397 of our conceptual approach is that fractures at different depths can not be connected  
398 independently. A possible solution would be the use of more realistic fracture geometry  
399 provided through geophysical data [*Dorn et al.*, 2012].

## 7. Conclusions

400 The temperature tomography approach (i.e. sequential borehole temperature logging  
401 under cross-borehole flow conditions) is proposed to characterize the connectivity and  
402 transmissivity of preferential permeable flow paths in fractured aquifers. An inverse model  
403 approach is developed to estimate log-transformed transmissivity values of hydraulically  
404 active fractures between the pumping and observation wells by inverting temperature  
405 profiles under cross-borehole flow conditions, single-borehole flowmeter data and borehole  
406 drawdowns. The proposed approach appears to be a promising approach for identification  
407 of general connectivity patterns and transmissivities of the main flowpaths.

408 The results of application of the proposed approach to Ploemeur field site can be syn-  
409 thesized as follows:

- 410 • A general flow pattern for the experimental site is proposed based on the analysis of  
411 borehole temperature profiles under ambient flow conditions.
- 412 • The inversion of single-borehole flow and cross-borehole temperature data is shown  
413 to allow the detection of the main fractures at the site and to image their hydraulic  
414 properties.
- 415 • In some cases of multifracture connections it could be difficult to propose a simple  
416 conceptual model of flow and connectivity.

417 Although some difficulties, this work represents a promising strategy. In future, tracer  
418 experiments and geophysical surveys [*Dorn et al.*, 2012] may be additional approaches to  
419 assess fracture network geometry and its hydraulic properties. Furthermore, a possible  
420 extension of this inverse approach consists in simultaneous joint inversion of multiple  
421 pumping tests to identify and characterize a connected fracture cluster all over the site.

422 **Acknowledgments.** This work was supported by the European Marie Curie network  
423 IMVUL (Grant Agreement 212298), by the National Research Observatory H+ and by  
424 the European Interreg IV project CLIMAWAT.

## References

- 425 Anderson, M. P. (2005), Heat as a ground water tracer, *Ground Water*, 43(6), 951–968.
- 426 Barton, C. A. and Zoback, M. D. and Moos, D. (1995), Fluid flow along potentially active  
427 faults in crystalline rock, *Geology*, 23(8).
- 428 Barton, C. A. and M. D. Zoback (1992), Self-Similar Distribution and Properties of  
429 Macroscopic Fractures at Depth in Crystalline Rock in the Cajon Pass Scientific Drill  
430 Hole, *Journal of Geophysical Research*, 97(B4), 5181–5200.
- 431 Bense, V. F., Person, M. A., Chaudhary, K., You, Y., Cremer, N., and S. Simon (2008),  
432 Thermal anomalies indicate preferential flow along faults in unconsolidated sedimentary  
433 aquifers, *Geoph. Res. Lett.*, 35(24), L24406, doi:10.1029/2008GL036017.
- 434 Bredehoeft, J. H., and I. S. Papadopoulos (1965), Rates of vertical groundwater movement  
435 estimated from the Earth’s thermal profile, *Water Resour. Res.*, 1, 325–328.
- 436 Chatelier, M., S. Ruelleu, O. Bour, G. Porel, and F. Delay (2011), Combined fluid tem-  
437 perature and flow logging for the characterization of hydraulic structure in a fractured  
438 karst aquifer, *Journal of Hydrology*, 400, 377-386.
- 439 Dorn C., N. Linde, T. Le Borgne, O. Bour, and M. Klepikova (2012), Inferring trans-  
440 port characteristics in a fractured rock aquifer by combining single-hole GPR reflection  
441 monitoring and tracer test data, *Water Resour. Res.*, .
- 442 Gallagher, K., Bodin, T., Sambridge, M., Weiss, D., Kylander, M., Large, D.  
443 (2011), Inference of abrupt changes in noisy geochemical records using transdimen-

- 444 sional changepoint models, *Earth and Planetary Science Letters*, 311(1), 182–194,  
445 doi10.1016/j.epsl.2011.09.015.
- 446 Garibaldi, C., Guillou-Frottier, L., Lardeaux, J. M., Bonte, D., Lopez, S., Bouchot, V. and  
447 Ledru, P. (2010), Thermal anomalies and geological structures in the Provence basin:  
448 Implications for hydrothermal circulations at depth, *Bulletin de la societe geologique de*  
449 *France*, 181(4), 363-376
- 450 Ge, S. M. (1998), Estimation of groundwater velocity in localized fracture zones from well  
451 temperature profiles, *Journal of Volcanology and geothermal research*, 84(1–2), 93-101.
- 452 Hess, A. E. (1986), Identifying hydraulically conductive fractures with a slow velocity  
453 borehole flowmeter, *Can. Geotechn.*, 23, 69–78.
- 454 Illman, W. A., X. Liu, S. Takeuchi, T.-C. J. Yeh, K. Ando, and H. Saegusa (2009), Hy-  
455 draulic tomography in fractured granite: Mizunami Underground Research site, Japan,  
456 *Water Resour. Res.*, 45, W01406, doi10.1029/2007WR006715.
- 457 Incropera and DeWitt (1996), Fundamentals of heat and mass transfer.
- 458 Klepikova, M., T. Le Borgne., O. Bour, P. Davy (2011), A methodology for using  
459 temperature-depth profiles under ambient, single and cross-borehole pumping condi-  
460 tions to estimate fracture hydraulic properties, *Journal of Hydrology*, 407(1-4), 145–152,  
461 doi10.1016/j.jhydrol.2011.07.018.
- 462 Keys, W. S. (1979), Borehole geophysics in igneous and metamorphic rocks, *Trans. SP-*  
463 *WLA Annu. Logging Syrup.*, 20th, 407, 1-26.
- 464 Lagarias, J.C., J. A. Reeds, M. H. Wright, and P. E. Wright (1998), Convergence Prop-  
465 erties of the Nelder-Mead Simplex Method in Low Dimensions, *SIAM Journal of Opti-*  
466 *mization*, 9(1), 112–147.

- 467 Jolivet, J., G. Bienfait, J. L. Vignerresse, and M. Cuney (1988), Heat flow and heat  
468 production in Brittany (Western France), *Tectonophysics*, 159, 61-72.
- 469 Le Borgne, T., Paillet, F.L., Bour, O., Caudal, J.-P. (2006), Cross-borehole flowmeter tests  
470 for transient heads in heterogeneous aquifers, *Ground Water*, 44, doi10.1111/j.1745-  
471 6584.2005.00150.x.
- 472 Le Borgne, T., O. Bour, M.S. Riley, P. Gouze, P.A. Pezard, A. Belghoul, G. Lods,  
473 R. Le Provost, R. B. Gresswell, P. A. Ellis, E. Isakov, and B. J. Last (2007),  
474 Comparison of alternative methodologies for identifying and characterizing preferen-  
475 tial flow paths in heterogeneous aquifers, *Journal of Hydrology*, 345(3-4), 134-148,  
476 doi10.1016/j.jhydro1.2007.07.007.
- 477 Mwenifumbo, C. J. (1993), Temperature logging in mineral exploration, *J. Appl. Geo-*  
478 *phys*,30, 297-313.
- 479 Paillet, F. L. (1998), Flow modeling and permeability estimation using borehole flow logs  
480 in heterogeneous fractured formations *Water Resource Research*,34(5), 997-1010.
- 481 Paillet, F. L. (2000), A field technique for estimating aquifer parameters using flow log  
482 data, *Ground Water*, 38(4), 510-521.
- 483 Paillet, F. L. (2004), Borehole flowmeter applications in irregular and large-diameter  
484 boreholes, *Journal of Applied Geophysics*, 55, 39-59.
- 485 Paillet, F. L., J. H. Williams, J. Urik, J. Lukes, M. Kobr and S. Mares (2012), Cross-  
486 borehole flow analysis to characterize fracture connections in the Melechov Granite,  
487 Bohemian-Moravian Highland, Czech Republic, *Hydrogeology Journal*, 20(1), 143-154,  
488 doi10.1007/s10040-011-0787-1.

- 489 Pehme, P.E., B.L. Parker, J.A. Cherry, and J.P. Greenhouse (2010), Improved resolution  
490 of ambient flow through fractured rock with temperature logs, *Ground Water*, 48(2),  
491 191-205.
- 492 P.E. Pehme and B.L. Parker and J.A. Cherry and J.W. Molson and J.P. Greenhouse  
493 (2013), Enhanced detection of hydraulically active fractures by temperature profiling in  
494 lined heated bedrock boreholes, *Journal of Hydrology*, 48(0), 1–15.
- 495 Quinn, P.M., J.A. Cherry, B.L. Parker (2011), Quantification of non-Darcian flow ob-  
496 served during packer testing in fractured rock, *Water Resour. Res.*, 47(9), W09533 ,  
497 doi10.1029/2010WR009681.
- 498 Read, T., O. Bour, V. F. Bense, T. Le Borgne, P. Goderniaux, M. Klepikova, R.  
499 Hochreutener. N. Lavenant and V. Boscherio (2013), Characterizing groundwater flow  
500 and heat transport in fractured rock using fiber-optic distributed temperature sensing,  
501 *GRL*, accepted.
- 502 Saar, M. O. (2011), Review: Geothermal heat as a tracer of large-scale groundwater flow  
503 and as a means to determine permeability field, *Hydrogeology Journal*, 19, 31–52.
- 504 Sawdey, J.R., and A.S. Reeve (2012), Automated inverse computer modeling of borehole  
505 flow data in heterogeneous aquifers, *Computers and Geosciences*, 46, 219–228.
- 506 Silliman, S. and Robinson, R. (1989), Identifying Fracture Interconnections Between Bore-  
507 holes Using Natural Temperature Profiling: I. Conceptual Basis, *Ground Water*, 27,  
508 393402, doi10.1111/j.1745-6584.1989.tb00463.x.
- 509 Sharmeen, R., W. A. Illman, S. J. Berg, T.-C. J. Yeh, Y.-J. Park, E. A. Sudicky, and  
510 K. Ando (2012), Transient hydraulic tomography in a fractured dolostone: Laboratory  
511 rock block experiments, *Water Resour. Res.*, 48, W10532, doi10.1029/2012WR012216.

512 Tarantola, A. (2004), Inverse Problem Theory and Model Parameter Estimation, *SIAM*.

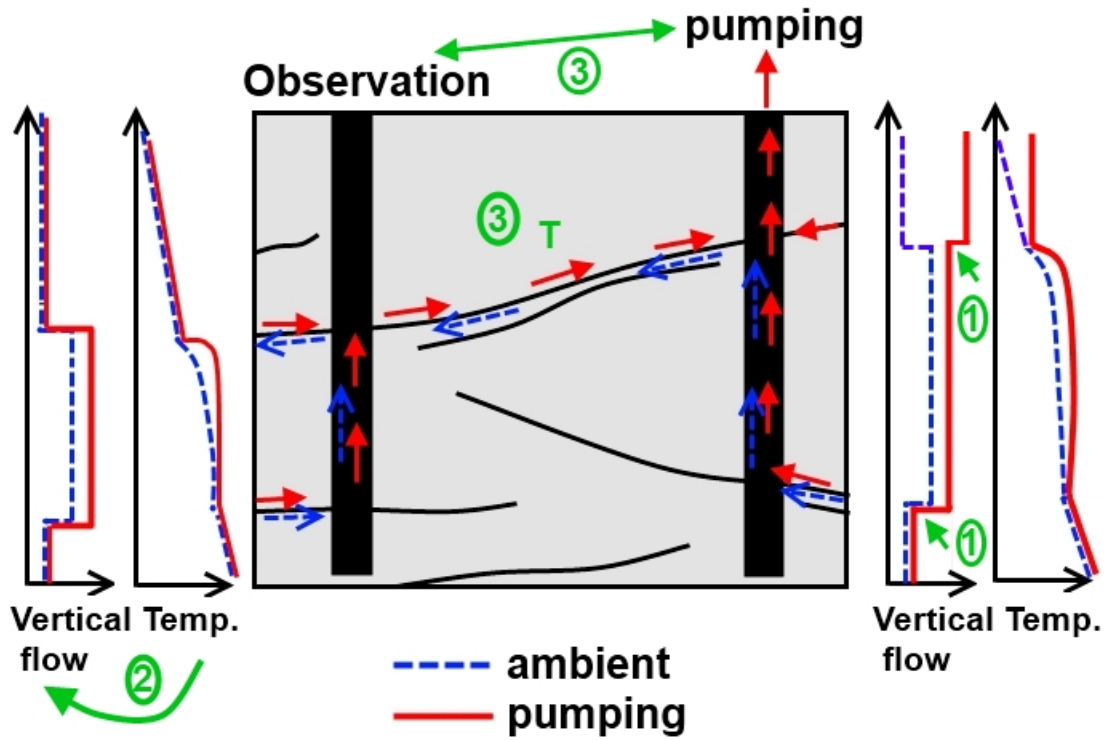


**Figure 1.** Flow pattern, flowmeter and temperature profiles for a pair of pumping and observation boreholes connected by one main flowpath under ambient (blue dotted line) and pumping (red line) flow conditions. Different steps of the proposed inverse framework are shown.

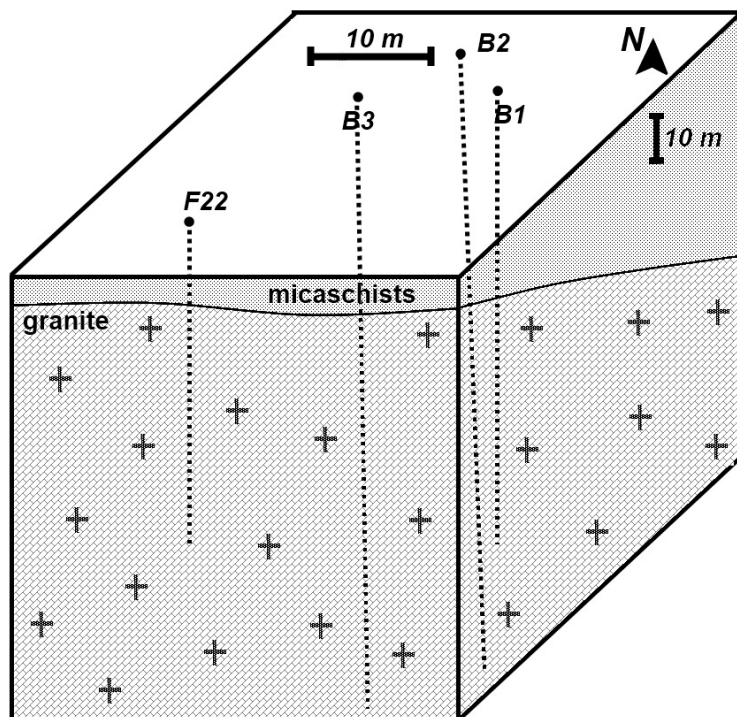


**Figure 2.** Experimental site. Boreholes array configuration and geology of the site.

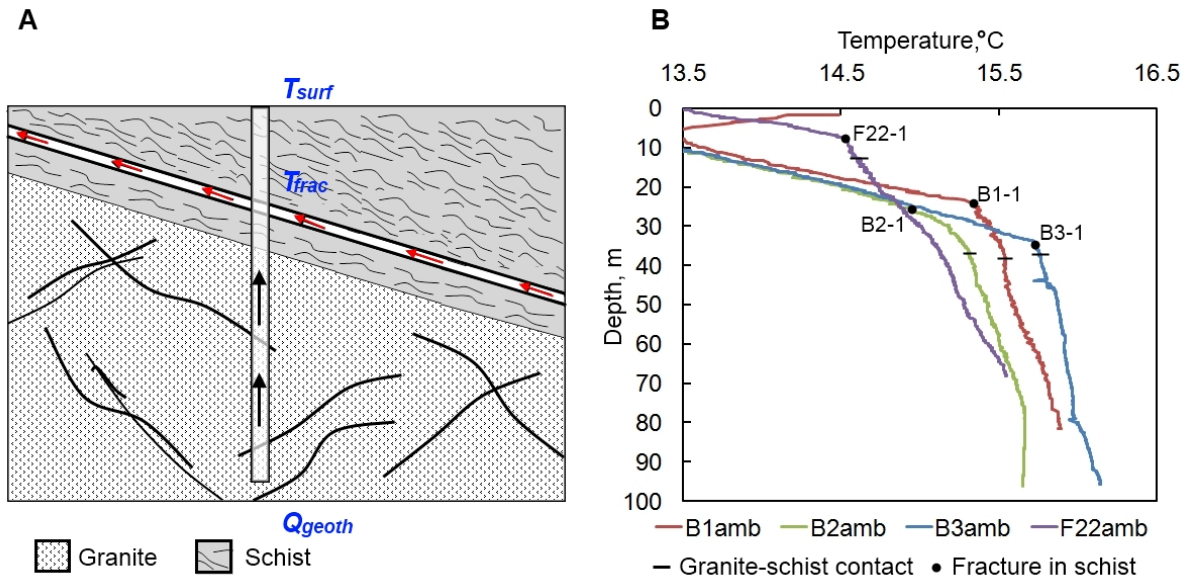


**Figure 3.** A. Conceptual hydrothermal setting: temperature profile affected by groundwater flow of warmer origin, by localized flow of warmer or cooler origin in narrow fractures and by vertical flow in the borehole itself. B. Temperature profiles measured at the site under the ambient flow conditions.

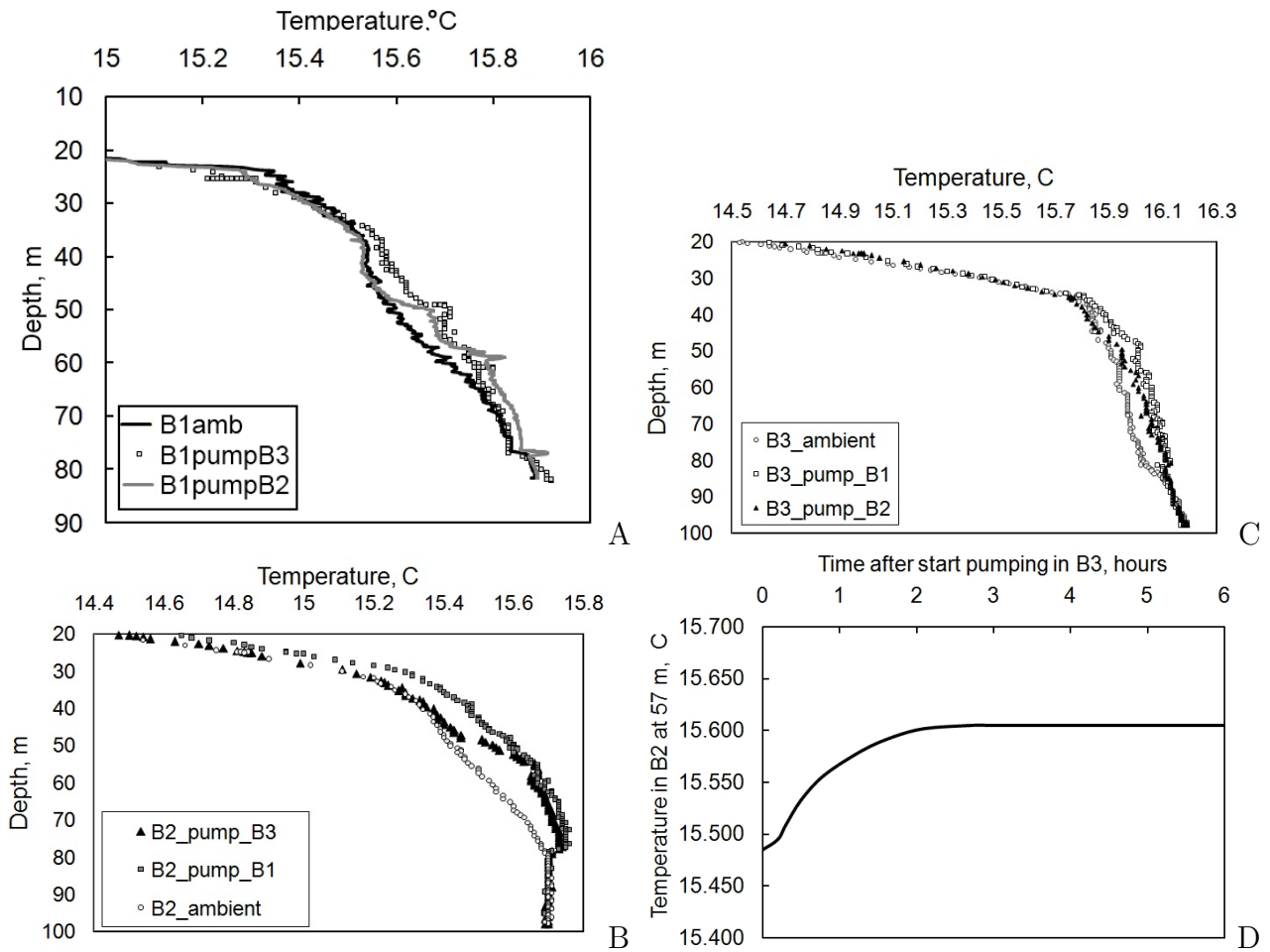


**Figure 4.** Temperature tomography experiment. Steady-state temperature profiles measured in B1 well when pumping in B2 and B3 wells (A). Steady-state temperature profiles measured in B2 well when pumping in B1 and B3 wells (B). Steady-state temperature profiles measured in B3 well when pumping in B1 and B2 wells (C). Example of temporal evolution of temperature in B2 at 57 m depth (D).

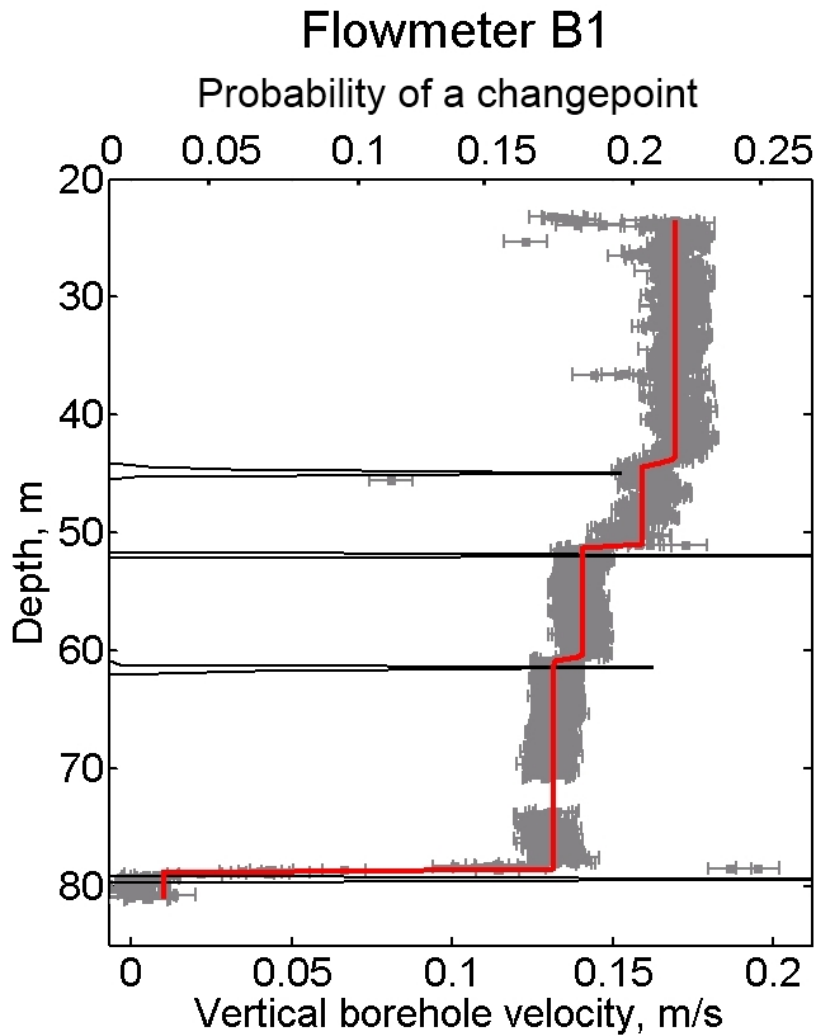


**Figure 5.** Inferred changepoint model for the flowmeter profile under pumping conditions for B1 borehole. The solid red line is the inferred function (relative to the down axis), and the solid black line represents the probability of a changepoint (relative to the upper axis). The error bars are drawn using the mean value of the noise variances for each data set (relative to the down axis).

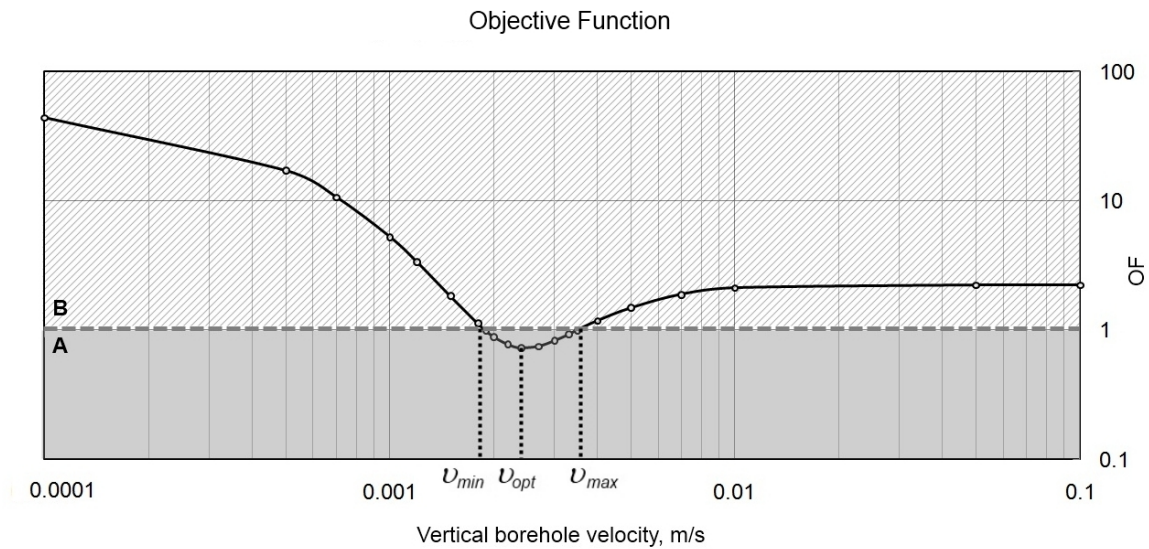


Figure 6. Example of the objective function and determination of the uncertainty.

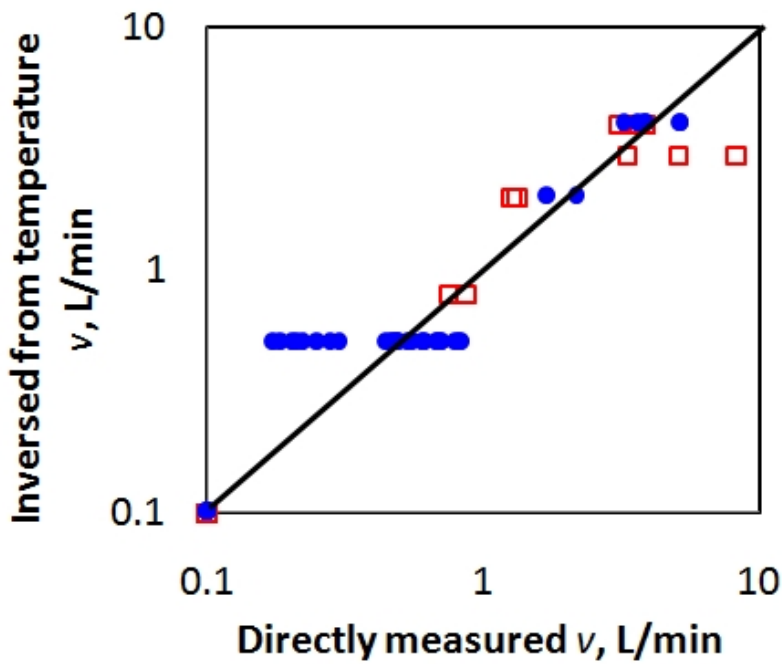
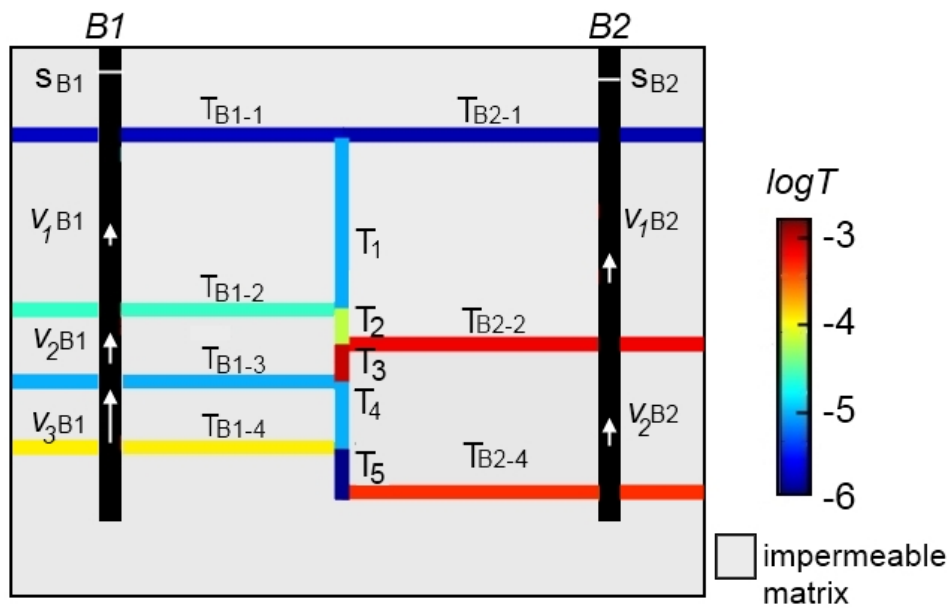


Figure 7. Comparison between flowmeter measurements and velocity values inversed from temperature measurements. Blue markers correspond to ambient flow conditions, while red markers correspond to cross-borehole pumping conditions.

**Table 1.** Comparison of flow tomography data (inverted from temperature) with results of numerical inverse modelling (the 'best' solution is presented).

Borehole pair	Observation	From T data	Model results
	$s_{B1}, cm$	34	29
	$s_{B2}, cm$	15	15
	$v_{1B1}, mm/s$	0	0
B1-B2	$v_{2B1}, mm/s$	1	1
	$v_{3B1}, mm/s$	3	1.3
	$v_{1B2}, mm/s$	1.1	0.5
	$v_{2B2}, mm/s$	1.1	1.3
	$s_{B1}, cm$	19	16
	$s_{B3}, cm$	2	7
	$v_{1B1}, mm/s$	1.4	0
B1-B3	$v_{2B1}, mm/s$	1.4	0
	$v_{3B1}, mm/s$	1.4	0.5
	$v_{1B3}, mm/s$	2.8	0.5
	$v_{2B3}, mm/s$	2.8	3.4
	$s_{B2}, cm$	14	14.9
	$s_{B3}, cm$	18	16
B2-B3	$v_{1B2}, mm/s$	-0.8	0
	$v_{2B2}, mm/s$	1.4	1
	$v_{1B3}, mm/s$	0	-1
	$v_{2B3}, mm/s$	0	0



**Figure 8.** Inferred pattern of fracture hydraulic properties and connectivities between and around B1-B2 borehole pair.

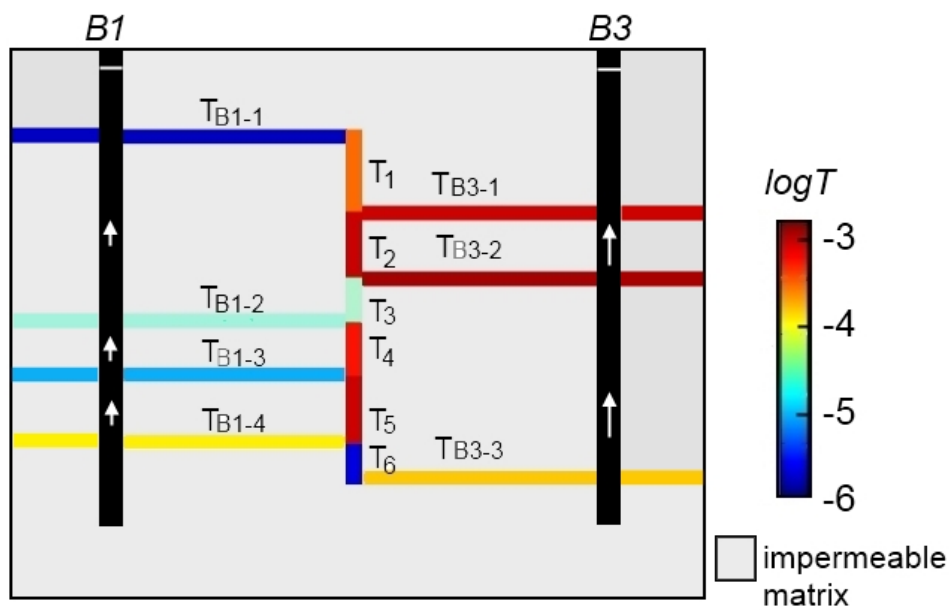


**Figure 9.** Inferred pattern of fracture hydraulic properties and connectivities between and around B3-B1 borehole pair.

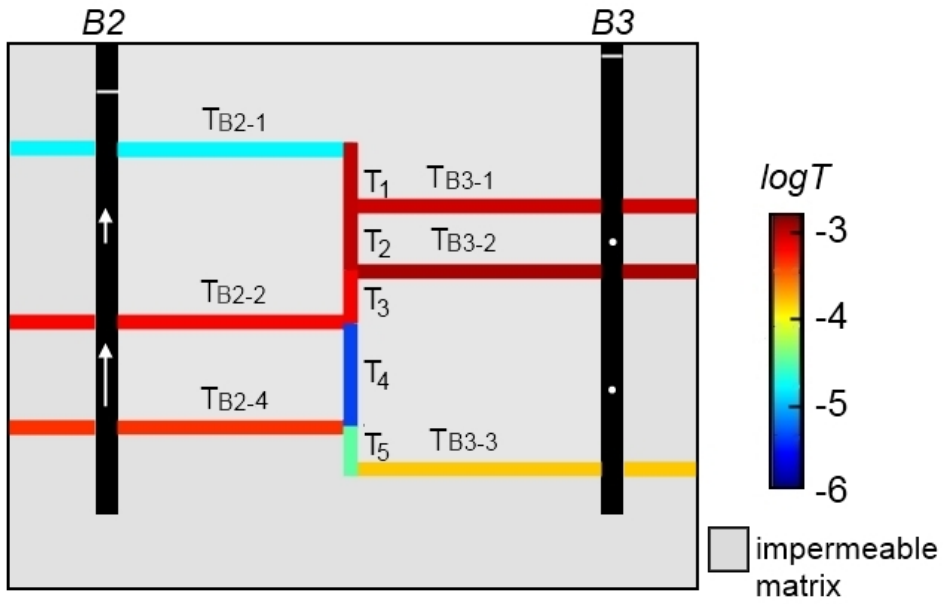


**Figure 10.** Inferred pattern of fracture hydraulic properties and connectivities between and around B2-B3 borehole pair.

### 5.3 Conclusions

The temperature tomography approach (i.e. sequential borehole temperature logging under cross-borehole flow conditions) is proposed to characterize the connectivity and transmissivity of preferential permeable flow paths in fractured aquifers. We present an inverse model approach to invert the temperature tomography data set to estimate log-transformed transmissivity values of hydraulically active fractures between the pumping and observation wells. The temperature tomography approach was applied to the Ploemeur field site. Application results show that borehole temperature profiles make it possible to image spatial distribution of hydraulic properties.

The framework proposed in this study is an analog to the flow tomography approach (Klepikova et al., submitted). The advantage of temperature based tomography is that temperature can be obtained more easily and continuously compared to direct flow measurements. However, the transient regime for heat is longer than the transient regime for flow and one can need up to several hours to reach steady-state. The advantage of both methods, flow tomography (Chapter 2) and temperature tomography (Chapter 4), is that they don't require fractures to be isolated with packers. However, the capacity of these approaches are limited when cross-borehole pumping induces similar hydraulic head variations within flowpaths connecting borehole pair. In this case, resulting velocity in the concerned section of observation borehole is close to zero and uncertainty about corresponding parameter drastically increases. Packer hydraulic tests don't have this limitation, and packer test data can be useful to properly characterize fracture hydraulic properties within these specific intervals.

## 5. TEMPERATURE TOMOGRAPHY EXPERIMENT IN FRACTURED MEDIA

---

# Chapter 6

## Heat and solute transport in fractured media

### 6.1 Introduction

As discussed in Chapter 1, the characterization of flow and transport patterns from tracer migration tests is, in general, subject to a high uncertainty, as different mechanisms can influence breakthrough curves in a similar way [e.g. Dentz et al., 2011; Haggerty et al., 2000]. In particular, matrix diffusion is known to produce an extended breakthrough tailing [e.g. Haggerty et al., 2001]. When this process is dominant, late time breakthrough data exhibit a slope of approximately  $-3/2$  when plotted on a log-log scale. However, breakthrough curves measured in the field often show different log log slopes [Becker and Shapiro, 2003; Haggerty et al., 2000]. Furthermore, several experimental studies observed an apparent increase of matrix diffusion with tracer travel distance [e.g. Liu et al., 2007; Shapiro, 2001]. These results gave rise to the idea, that this scale effect results from different advective processes [Becker and Shapiro, 2000; Liu et al., 2007]. For instance, mass transfer within a fracture network with a broad hydraulic conductivity can produce an extended tailing of the tracer breakthrough [Becker and Shapiro, 2000]. Similar effects can be induced by hydrodynamic dispersion in the fracture plane due to fracture aperture variability. Tailing may also be due to advective exchange between immobile and mobile fluids along rough fractures. Hence, the

## 6. HEAT AND SOLUTE TRANSPORT

---

highly heterogeneous spatial and temporal nature of solute transport in fractured media makes it difficult to separate the influence of different processes. One way to constrain the system, is to conduct tracer tests under different configurations or by using different tracers. For example, to investigate matrix diffusion, tracers of different diffusivity can be used [Becker and Shapiro, 2000]. In such context, the idea of using heat as a tracer was proposed by several researchers [e.g. Anderson, 2005; Jung and Pruess, 2012].

Heat tracer tests are of interest in themselves for two main reasons: the current important development of geothermal applications [e.g. Genter et al., 2003; Kocabas, 2005] and the use of heat to quantify subsurface flows and, in particular, surface-groundwater exchanges in rivers [e.g. Vogt et al., 2010]. The fundamental difference between solute and heat transport is that heat diffusion in rocks is large compared to molecular diffusion, implying that fracture-matrix exchange is more significant for heat than for solute tracers. Consequently, thermal breakthrough curves are strongly controlled by matrix diffusion, thus bringing information on diffusive transport processes [Becker and Shapiro, 2003]. The main objective of this chapter is to investigate which type of information can be obtained from heat tracer tests and what test configuration should be chosen to extract relevant information. This raises questions regarding the influence of heterogeneities and scale of investigation on transport processes. An important issue concerns the role of fracture-scale heterogeneity in transport processes. For instance, Neuville et al. [2010] showed that fracture-matrix thermal exchange is highly affected by the fracture wall roughness. Another related question, is the effect of network-scale heterogeneities, including effects of multiple fractures and fracture density.

Several analytical studies of heat injection in fractured aquifers were conducted [e.g. Gringarten and Sauty, 1975; Jung and Pruess, 2012; Kocabas and Horne, 1990; Lauwerier, 1955; Pruess and Doughty, 2010]. Heat diffusion is known to result in significant retardation of the heat breakthrough compared to the solute breakthrough. Field heat tracer test data were also reported, including data from geothermal fields [e.g. Bjornsson et al., 1994; Malate and O'Sullivan, 1991]. Flynn [1985] conducted cross-borehole temperature tracer tests in order to identify fracture interconnections between boreholes. Hence, due to significant heat losses to the matrix, inter borehole heat tracer tests can demonstrate weak and

slow breakthrough. Single-borehole push-pull tracer tests were proposed as an alternative to inter-borehole tracer test [e.g. Jung and Pruess, 2012; Kocabas, 2005; Neretnieks, 2007; Pruess and Doughty, 2010]. Vandenbohede et al. [2009] presented push-pull heat and solute tracer tests in porous media to study the effect of thermal dispersivity. To our knowledge, no push-pull tests have been presented in fractured media.

Push-pull test usually involves tracer injection and subsequent recovery from the same location with continuous monitoring of tracer temperature and/or concentration. Variants of the test can be conceived e.g. intermediate back pumping, or waiting period, or pushing with fresh water (Dirac-type or pulse injection). During push-pull tracer tests, the tracer follows approximately the same streamlines during the injection and during the backflow. This implies that, compared to cross-borehole tests, measurements may be much less affected by heterogeneities of flow and mostly sensitive to irreversible diffusive processes. Thus, while for cross-borehole solute tracer the tests peak arrival time provides a mean fracture aperture, for a push-pull test this is not the case as the mean arrival time is determined by the push and pull time and equals to  $t_{peak} = t_{push} + t_{pull}$ . The use of push-pull heat tracer test in fractured media was recently investigated by the analytical study of Jung and Pruess [2012]. The conclusions of this study was rather negative, as they did not find that these tests were sensitive to flow rate and fracture apertures. They found that flow rate does affect the temperature distribution in the push phase but that this effect compensated exactly in the pull phase. Furthermore, sensitivity of push pull thermal breakthrough curves to the fracture aperture was found to be negligible, due to fast and overwhelming heat transfer from the rock matrix. This lack of sensitivity may be partly due to the fact that this study considered continuous injections, which is equivalent to a superimposition of Dirac-type injection.

In this study we further investigate the interest of push-pull heat tracer test with pulse injection and varying the scale of investigation. For this purpose we explore the sensitivity of push pull heat tracer tests to a range of transport parameters. Furthermore, we perform a series of push-pull thermal and solute tracer tests at the fractured aquifer of Ploemeur. Varying the push time allows us to investigate the scale effects on heat transport. Based on these experimental

## 6. HEAT AND SOLUTE TRANSPORT

---

data, the relevance of single homogeneous fracture model is investigated. We compare transport parameters estimated from heat and transport tracer tests. In the following section we present the numerical model of flow and heat transport. Then, we present the experimental results and their interpretation.

### 6.2 Heat transport: numerical modeling

In order to study heat transport in fractured media and in particular the interest of push pull thermal tests, we develop a simple numerical model. We consider horizontal fracture with 2D radial flow with a parabolic velocity transverse to the flow direction, surrounded by an impermeable rock matrix. This model is a simplification as it does not consider fracture heterogeneities. The influence of fracture wall roughness on flow and heat transport have been studied by Neuville et al. [2010]. It was found that compared to flat fractures, fracture matrix heat exchange is less efficient in rough fractures. This is due to the reduction of effective exchange area, related to flow channeling. Here we do not investigate this effect in details. However, the comparison of the push-pull thermal response in 2D with that in 1D case (which corresponds to a case of extreme flow channeling) gives some insights about possible effects. To model heat transport, we consider heat conduction in the matrix and in the fracture, and heat advection in the fracture. We assume, that the effects of thermal dispersion are negligible compared to conduction [Bear, 1972; Vandenbohede et al., 2009]. The validity of this assumption is examined through numerical simulations, which indicate that this simplification has only a minor effect on thermal push pull breakthrough curves.

The governing equation for thermal transport within a fracture can be written as [Molson et al., 2007]

$$(\rho C_p)_{eq} \frac{\partial T}{\partial t} + \rho C_p u \cdot \nabla T = \nabla \cdot (\lambda_{eq} \nabla T) \quad (6.1)$$

where  $(\rho C_p)_{eq} = \phi(\rho C_p)_f + (1 - \phi)(\rho C_p)_s$  is the equivalent volumetric heat capacity of the matrix,  $u$  is the fluid velocity field,  $\lambda_{eq} = \phi\lambda_f + (1 - \phi)\lambda_s$  is the equivalent thermal conductivity and  $\phi$  is the porosity. For our case  $\phi = 0$  in the matrix and  $\phi = 1$  in the fracture.

The geometry example is shown in Figure 6.1. The thermal tracer is injected through the fracture inlet at the axis of the symmetry of the system  $T|_{t=0} = T_{inj}$  during the time of injection  $t_{inj}$ . Afterwards, the tracer is pushed with water at ambient temperature  $T|_{t=t_{inj}} = T_{zero}$ . The push time is taken equal to the injection time  $t_{push} = t_{inj}$ . The fracture flow is given by  $u$  and the ambient (initial) temperature is  $T_{zero}$ . The system is bounded at radial distance  $r = R$ . This distance is chosen far enough not to influence thermal breakthrough curves. The boundary condition at fracture outlet is taken as  $T|_{r=R} = T_{zero}$ . For the example of Figure 6.1 the fracture aperture is  $b = 2 \text{ mm}$ , the thickness of the rock matrix layer is  $D = 3 \text{ m}$ , the matrix and fracture thermal conductivity is  $\lambda_r = 3 \text{ W/mK}$  and  $\lambda_f = 0.59 \text{ W/mK}$ , the heat capacity is  $C_{pr} = 2500 \text{ J/kgK}$  (we used thermal properties corresponding to the mean values measured for granites) and  $C_{pf} = 4200 \text{ J/kgK}$  and the density is  $\rho_r = 2600 \text{ kg/m}^3$  and  $\rho_f = 1000 \text{ kg/m}^3$  for rock and water respectively [Incropera and DeWitt, 1996].

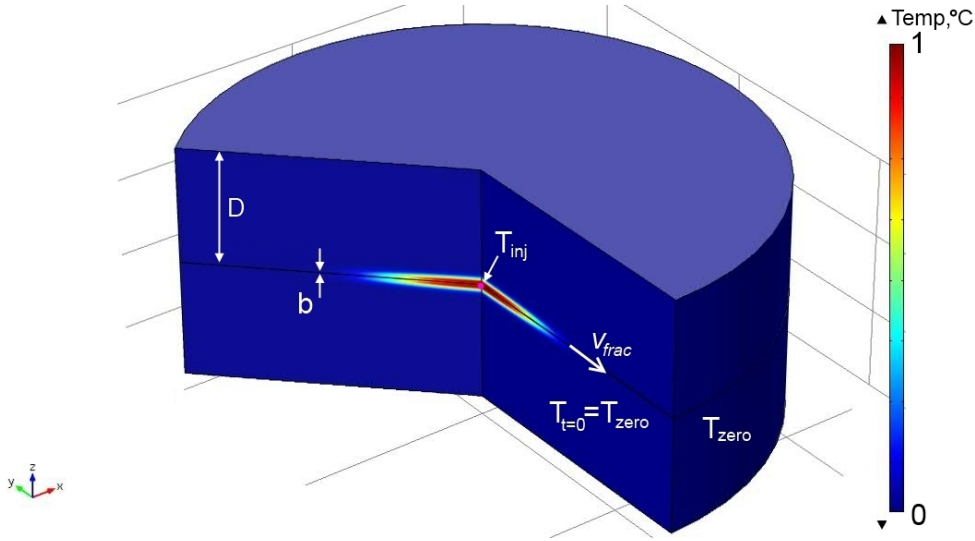


Figure 6.1: Temperature field for an example of model geometry with a fracture with  $2 \text{ mm}$  aperture.

The numerical model was developed in COMSOL Multiphysics and validated by comparison of numerical results against the analytical model for heat transport in a single horizontal fracture presented in Molson et al. [2007]. This analytical solution considers hot water injection in a  $1D$  single fracture within a porous

## 6. HEAT AND SOLUTE TRANSPORT

---

matrix. The considered tracer test configuration is presented on Figure 6.2A. The velocity in the fracture is  $u = 0.005 \text{ m/s}$ , the fracture aperture is  $b = 1 \text{ mm}$ , the rock thermal properties are  $\lambda = 2.0 \text{ W/mK}$ ,  $c = 860 \text{ J/kg/K}$ , the density is  $\rho = 2630 \text{ kg/m}^3$  and the rock matrix is impermeable [Molson et al., 2007]. The simulated longitudinal thermal profiles within the fracture, displayed in Figure 6.2B, shows a good agreement between the numerical model and the analytical solution. In the subsequent sections we use this numerical model to test the sensitivity of temperature recovery during push-pull tracer test to the fracture aperture, injection/withdrawal flow rates, push time and scale of investigation.

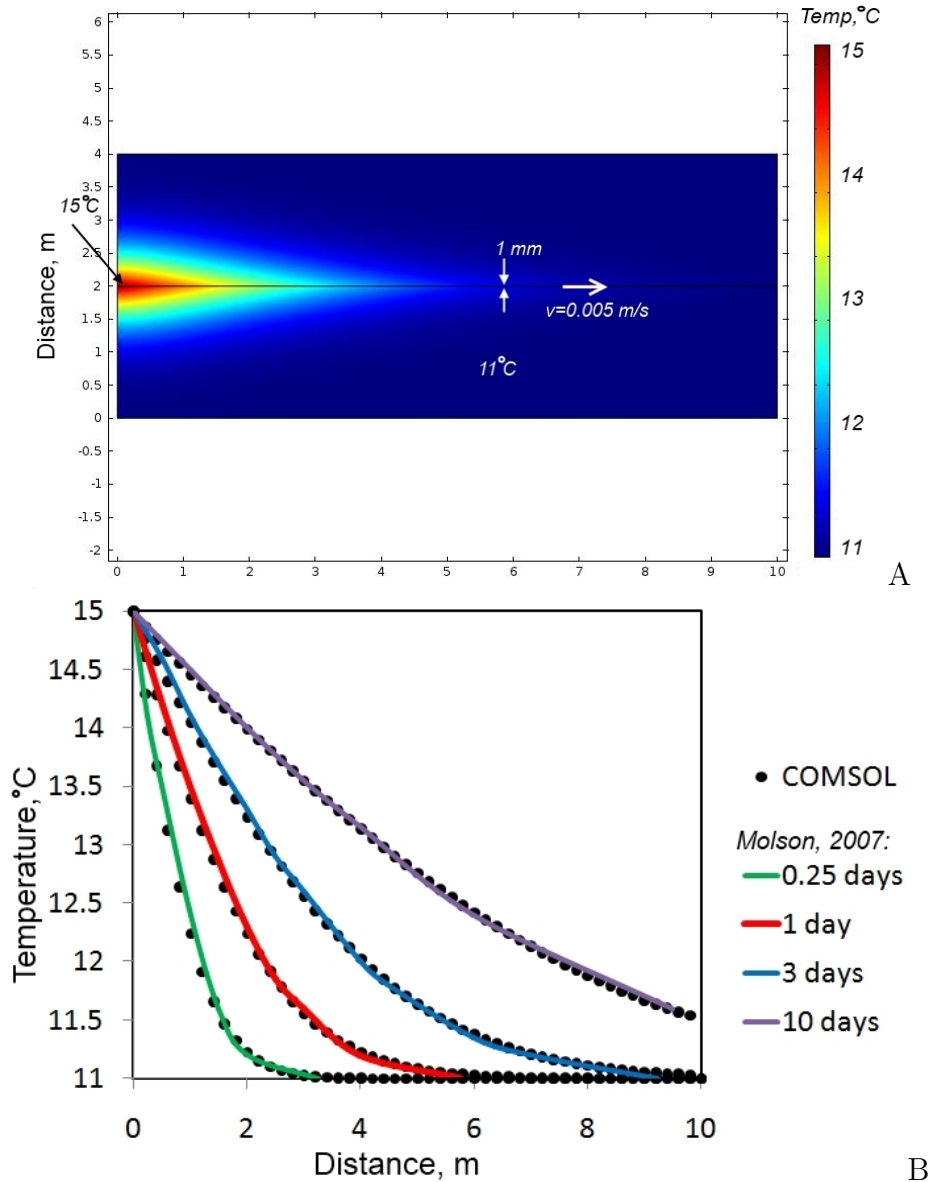


Figure 6.2: A. Model geometry and parameters used for model validation. Two dimensional, single planar fracture system, numerical temperature solution shown at 3 days (compare to Molson et al. [2007]). B. Comparison of the numerical model (COMSOL) against the analytical model (SFRAC-H, Molson et al. [2007]) for a single fracture system (A).

## 6. HEAT AND SOLUTE TRANSPORT

---

### 6.2.1 Sensitivity analysis

In this section we use the developed numerical model to investigate the interest of thermal push-pull test with Dirac-type injection for characterizing fracture transport parameters. Interpretation of several recently published field tracer tests demonstrated a possible scale effect of matrix diffusion [Neretnieks, 2007]. As for heat transport matrix diffusion is expected to be the dominant mechanism, the question of scale dependency is therefore addressed in this study. Furthermore, we investigate the effect of fracture-matrix interaction surface area. This parameter is controlled by the volume of injected tracer. The sensitivity of the push-pull thermal response to flow rate and flow geometry is a subject of the second section. Lastly, we discuss the sensitivity of temperature recovery to the fracture aperture.

#### 6.2.1.1 Sensitivity of temperature recovery to push time

In this section we examine the relationship between the push time and the shape of the thermal breakthrough curve. As the thermal tracer is pushed in the fracture, the heat which has diffused in the matrix diffuses away from the fracture. An increase of push time increases the distance between the fracture and the 'heat plume' in the matrix. During the backflow, heat is transferred back from the matrix into the fracture, the further the matrix 'heat plume' has diffused during the push phase, the lower is the back thermal flux expected to be during the pull phase. Consequently, an increase of push time yields lower rates of fracture-matrix heat transfer during the pull period. We, then, expect lower temperatures of the push pull breakthrough curves.

We conducted a numerical experiment in which the duration of push period was changed. For this scenario, the flow rate is set to  $Q = 3.5 \text{ L/min}$ , the fracture aperture is  $b = 15 \text{ mm}$  and the tracer injection time is  $t_{inj} = 1000 \text{ s}$ , while push time varies as follows  $t_{push} = 500, 1000, 10000 \text{ s}$ . The temperature distributions during push period are shown in Figure 6.3 at different times. This figure shows the vertical conduction of heat from injected fluid into the rock matrix. During the push phase the injection of ambient temperature water results in the cooling down of the system in the vicinity of the injection point.

The simulation results, presented in Figure 6.4, show that this is indeed the case: when the tracer is pushed to a larger distance, the temperature of the peak decreases. Here and further in the text, temperature is expressed through the dimensionless temperature given by  $T_D = (T - T_{zero}) / (T_{inj} - T_{zero})$ . It is interesting to note, that the simulated breakthrough tail at late times has a straight line power law slope of  $-1.5$ , which is typical of matrix diffusion [Becker and Shapiro, 2000; Haggerty et al., 2000]. However, we observe an early time regime, with an apparent power law decay of slope  $-1$ . A power law trend line passing through the peaks of the breakthrough curves has also a slope of  $-1$  on a log-log plot.

## 6. HEAT AND SOLUTE TRANSPORT

---

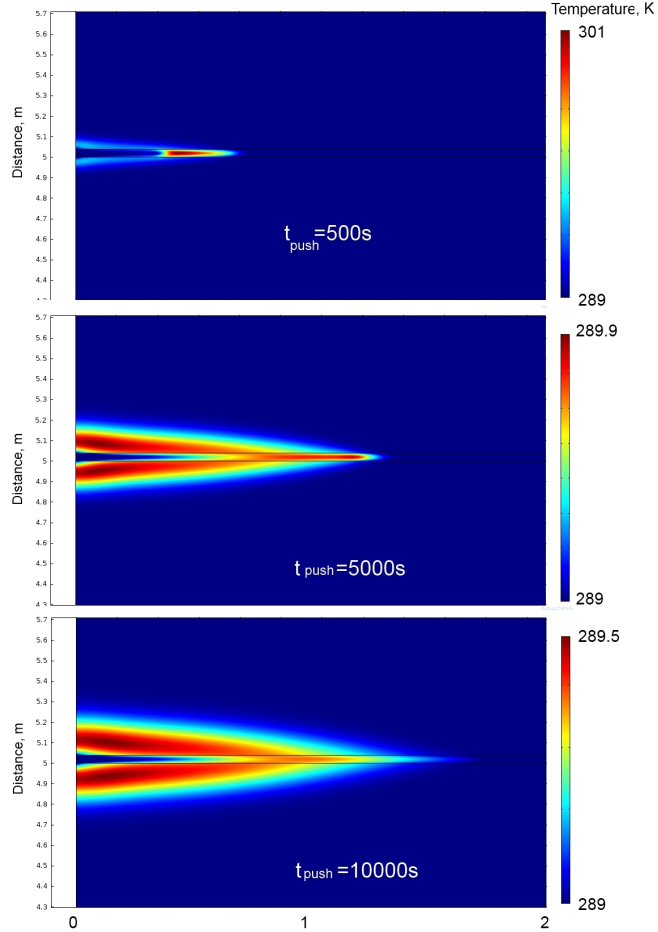


Figure 6.3: Simulated temperature distribution during pulse tracer injection in a single fracture with aperture fixed to  $b = 15 \text{ mm}$  for injection with the rate  $Q = 3.5 \text{ L/min}$  and during the fixed time  $t_{inj} = 1000 \text{ s}$ . The tracer is the pushed with water of the ambient temperature. The temperature is given at different times  $t = 1500, 6000, 11000 \text{ s}$ .

### 6.2.1.2 Sensitivity of temperature recovery to flow rate and geometry

In this section we investigate the sensitivity of push pull thermal breakthrough curves to flow rate and flow geometry (1D versus 2D). As discussed, the flow rate is an important parameter as it directly related to the effect of multiple fractures. Jung and Pruess [2012] argued that pumping (injection) flow rate do have an influence on the temperature distribution in the push phase, but that

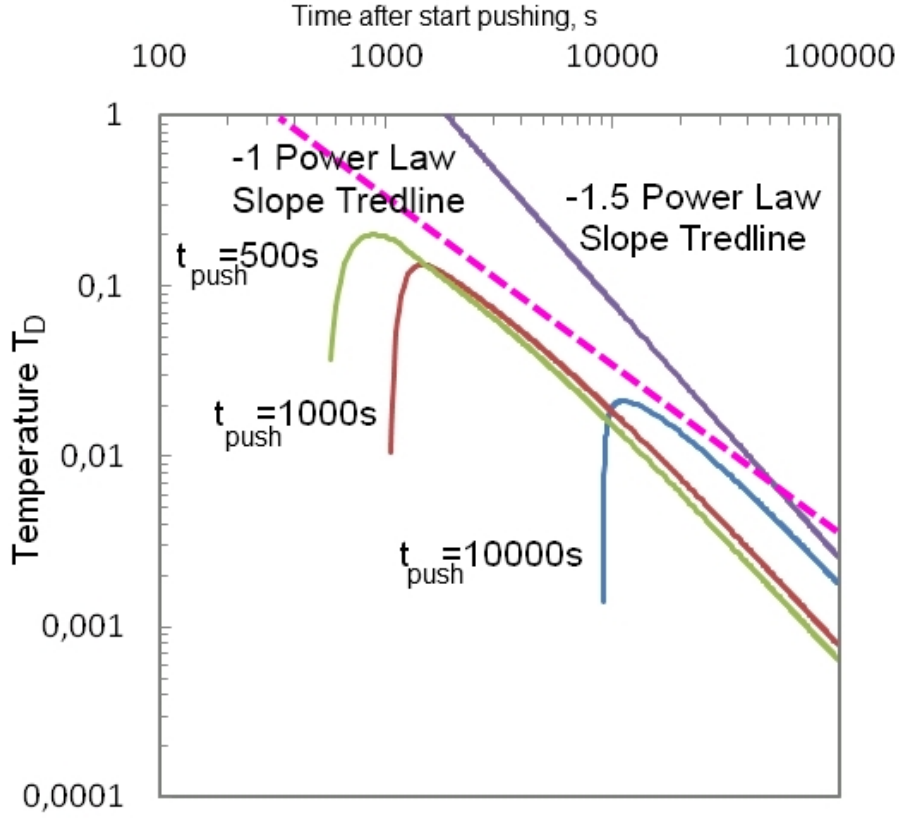


Figure 6.4: Simulated heat breakthrough curves during push-pull tracer test in a single fracture with aperture fixed to  $b = 15 \text{ mm}$  for injection with the fixed pumping rate  $Q = 3.5 \text{ L/min}$  and during the fixed time  $t_{inj} = 1000 \text{ s}$ , while pushing time is varied as  $t_{push} = 500, 1000, 10000 \text{ s}$ .

these effects are compensated in the pull phase. In order to demonstrate this, dimensionless parameters introduced by Bodvarsson and Tsang [1982] can be used:

$$\xi = \frac{\lambda_s \pi r^2 (2 + \theta)}{\rho_f C_{pf} Q D}, \quad (6.2)$$

$$\tau = \frac{\lambda_s t}{\rho_s C_{ps} D^2}, \quad (6.3)$$

## 6. HEAT AND SOLUTE TRANSPORT

---

$$\nu = \frac{z}{D}, \quad (6.4)$$

where  $r$  is the location of the thermal front at given,  $z$  is the vertical coordinate ( $z = 0$  at the fracture center) time  $t$  and  $\theta = \rho_f C_{pf} b / \rho_s C_{ps} D$ . Using this parameters, the governing equation 6.1 can be written as:

Fracture

$$(2 + \theta) \frac{\partial T_{Df}}{\partial \xi} + \theta \frac{\partial T_{Df}}{\partial \tau} - 2 \frac{\partial T_{Df}}{\partial \nu} = 0 \quad (6.5)$$

Rock

$$\frac{\partial^2 T_{Dr}}{\partial \nu^2} = \frac{\partial T_{Dr}}{\partial \tau} \quad (6.6)$$

where infinite vertical thermal conductivity is considered in the fracture and diffusion in the matrix is assumed to occur only in the  $z$  direction [Bodvarsson and Tsang, 1982]. The governing equations for the withdrawal phase are similar to those for the injection phase. The only change is the negative sign for the convective heat transfer term (first term in the equation above) due to the reversed flow direction during the withdrawal phase [Jung and Pruess, 2012]. In these equations the flow rate term  $Q$  only appears in the dimensionless squared distance  $\xi$ . Thus the effect of changing the flow is only to rescale the temperature field in the longitudinal direction, proportionally to the square root of flow. Then, at the injection point ( $r = \xi = 0$ ) the time dependence of temperature recovery is insensitive to the applied flow rate.

We verify the sensitivity of thermal push pull breakthrough curves to changes in flow rate, by considering a scenario of a single fracture with a fixed fracture aperture  $b = 15 \text{ mm}$ , and a fixed injection and push times  $t_{inj} = t_{push} = 1000 \text{ s}$ , while the pumping (injection) rate is varied between the tests  $Q = 3.5, 35, 70 \text{ L/min}$ . Results, presented on Figure 6.5, show that temperature recovery is insensitive to changes in pumping rate, as expected Jung and Pruess [2012].

In order to investigate the effect of flow channeling to the thermal response, we also consider the push-pull in 1D geometry. This case corresponds to the extreme flow channeling. The thermal push pull breakthrough curves were found

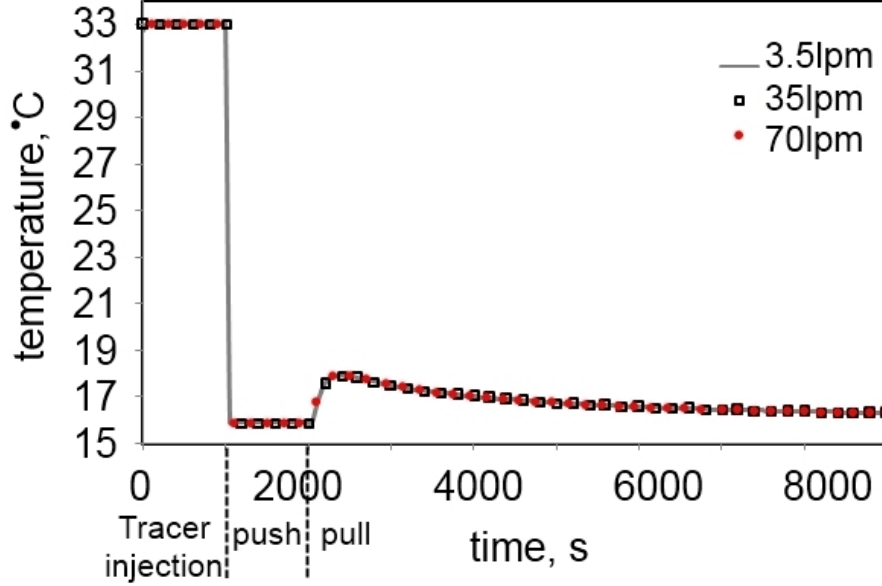


Figure 6.5: Simulated heat breakthrough curves during push-pull tracer test in a single fracture aperture  $b = 15 \text{ mm}$  and various pumping rate ( $Q = 3.5, 35$  and  $70 \text{ L/min}$ ). The injection time  $t_{inj} = t_{push} = 1000 \text{ s}$ . The temperature of injected water is constant  $T_{inj} = 33^\circ\text{C}$

to be absolutely identical to those in 2D case. This results can also be explained by noting that the flow geometry only affects the dependence of  $\xi$  on the distance  $r$  (linear instead of quadratic). Thus, it has no effect at  $r = 0$  ( $\xi = 0$ ). This result suggests a general insensitivity of thermal push-pull tests to advective mechanisms.

### 6.2.1.3 Sensitivity of temperature recovery to the fracture aperture

In order to study the influence of fracture aperture on temperature recovery, a series of numerical experiments was conducted. For these experiments fracture aperture was varied from  $1 \cdot 10^{-3} \text{ m}$  up to  $5 \cdot 10^{-2} \text{ m}$ , while for all experiments the flow rate was fixed to  $Q = 3.5 \text{ L/min}$  and the injection and push times were fixed to  $t_{inj} = t_{push} = 1000 \text{ s}$ .

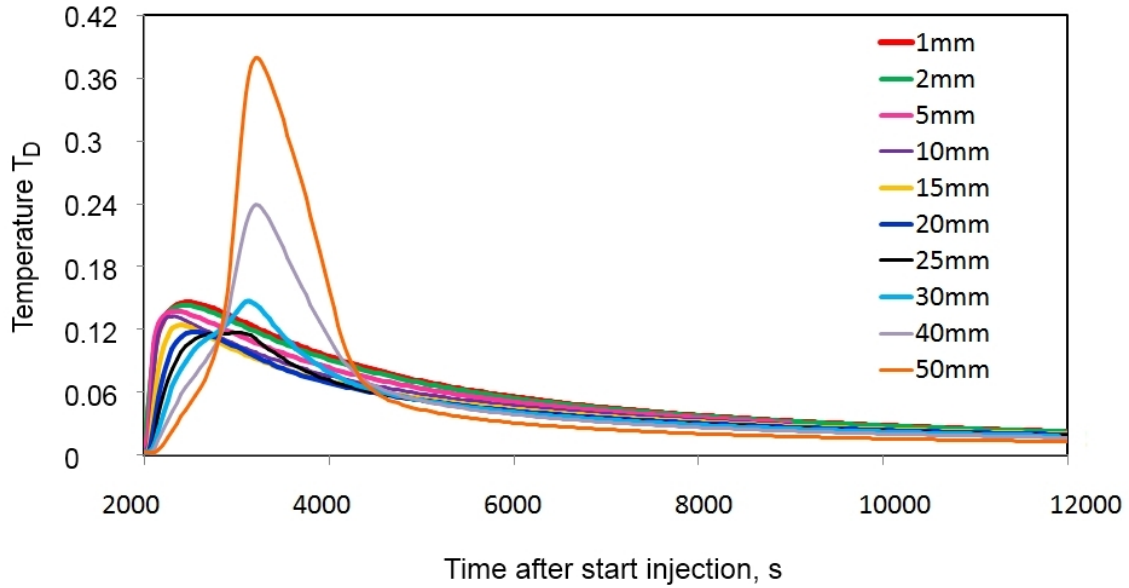
Temperature breakthrough curves are presented in Figure 6.6A for different fracture apertures. The temperature of the peak as a function of fracture aper-

## 6. HEAT AND SOLUTE TRANSPORT

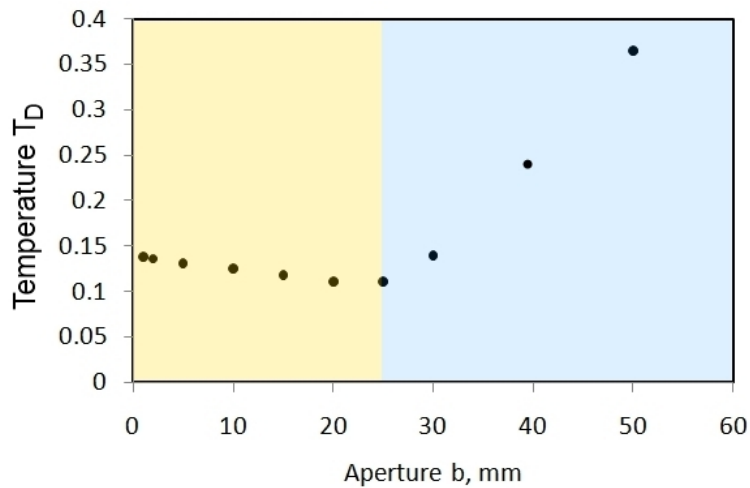
---

ture, provided in Figure 6.6B, shows two regimes. The first regime corresponds to the relatively large fracture apertures varying from 20  $mm$  and larger. In this aperture range the temperature recovery peak decreases when fracture aperture decreases. On the other hand, for the smaller apertures, the temperature peak increases when fracture aperture decreases. The transition between the two regimes occurs at a fracture aperture of about  $b_D = 25 \cdot 10^{-3} m$ . This aperture roughly corresponds to the distance at which heat diffuses during the experiment time for the considered parameters ( $r = \sqrt{Dt} = \sqrt{1.4 \cdot 10^{-7} \cdot 3000} = 21 \cdot 10^{-3} m$ ).

For the large aperture range ( $b > b_D$ ), fractures are large and heat has no time to diffuse across the fracture aperture. Consequently, larger fracture apertures imply less heat losses to the matrix. For smaller fracture apertures,  $b \leq b_D m$ , in contrast to the study of Jung and Pruess [2012], we found temperature recovery to be also sensitive to changes in fracture aperture. The temperature peak increase for decreasing apertures is explained in the following.



A



B

Figure 6.6: Simulated temperature breakthrough curves during push-pull tracer test. Fracture aperture varies from  $1 \cdot 10^{-3} m$  up to  $50 \cdot 10^{-3} m$ , flow rate  $Q$  is given by  $3.5 L/min$  and for all experiments injection time is given by  $17 min$ . Here  $T_D = (T - T_{zero}) / (T_{inj} - T_{zero})$

In order to explain the temperature peak increase with decreasing fracture aperture (for  $1 \cdot 10^{-3} m \leq b \leq 25 \cdot 10^{-3} m$  fracture aperture range), we consider spatial temperature profiles for different fracture apertures. Figure 6.7 shows spatial temperature profiles for  $b_1 = 5$  (blue markers) and  $b_2 = 15 mm$  (red markers)

## 6. HEAT AND SOLUTE TRANSPORT

at the end of the injection period  $t = t_{inj}$ . To highlight the effect of matrix diffusion, we present also spatial profiles for conservative tracer not affected by the matrix. Figure 6.7 shows that in the absence of matrix diffusion tracer advances more rapidly in the thinner fracture, as expected since the fracture velocity is inversely proportional to its aperture. As also expected, heat conduction in the matrix retards the advancement of the tracer. However, contrary to the solute transport case, the advancement of the front is less for the smaller aperture fracture (Figure 6.7), which may explain why the temperature recovery is improved in this case. To understand this phenomenon, we have investigated in more details the rate of the thermal front advancement along the fracture in dimensionless coordinates.

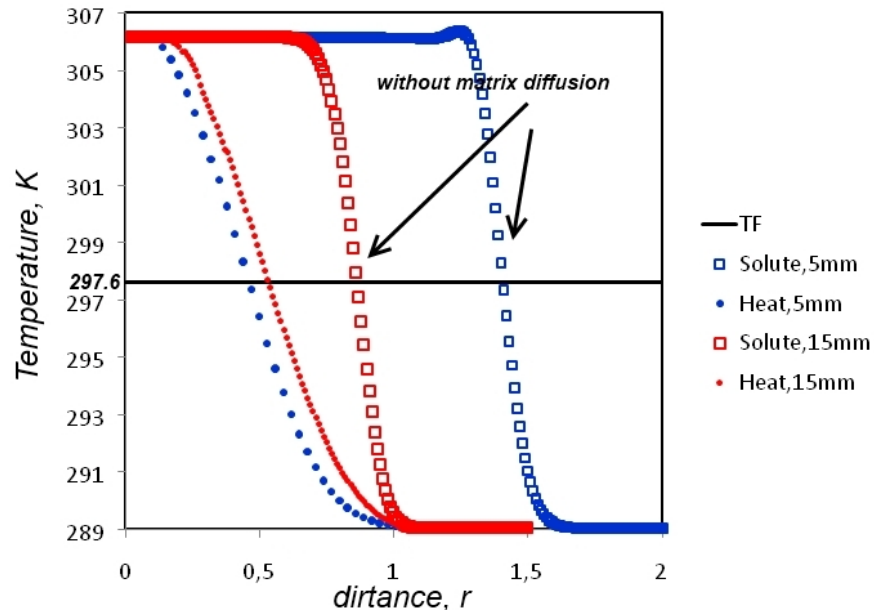


Figure 6.7: Spatial profiles of temperature and concentration of a conservative tracer at the end of injection period ( $t = 1000$  s). Position of thermal front is shown by black line.

To compare the advancement of tracer for different apertures we follow the displacement of the thermal front defined as an average of the initial rock temperature and the injection temperature  $T_{TF} = (T_{inj} + T_{zero})/2$  [Bodvarsson and Tsang, 1982]. We plot in Figure 6.8 the advancement of the thermal front away from the injection point along both fractures ( $b = 5 \text{ mm}$  and  $b = 15 \text{ mm}$ ) in terms of the dimensionless parameters (Equations 6.2, 6.3). For comparison, the analytical solution developed by Bodvarsson and Tsang [1982] is also presented (dashed line). Figure 6.8 shows that two regimes of thermal front propagation exist. At early times, advection dominates over diffusion and the thermal front advances as fast as the solute front would. Later, as the available surface area for fracture-matrix heat transfer increases, diffusion slows down the thermal front.

Figure 6.8 shows a quite good agreement between the numerical simulation results (dotted line) and the analytical solution of Bodvarsson and Tsang [1982]. However, the transition time between the two regimes is found to be larger. Furthermore, the dimensionless distance shows an apparent 'overshoot' before converging to the analytical solution. A possible reason for this discrepancy can be that analytical solution of Bodvarsson and Tsang [1982] neglects heat conduction within the fracture, as instantaneous thermal equilibrium in the fracture is assumed. The consequence of this assumption is that the transition time between the advective and diffusive regimes occurs before the characteristic diffusion time over the fracture aperture. In our numerical model we do consider heat conduction in the fracture, which implies that during injection period the fracture has higher temperatures in the middle. We find that the transition time between the two regimes is equal to the diffusion time over the fracture aperture. The longer duration of the advective regime also explains the temperature 'overshoot' of our simulations compared to the analytical solution as heat losses are smaller in the first regime. At late times, thermal equilibrium is reached, and the analytical solution and our simulations give close results.

## 6. HEAT AND SOLUTE TRANSPORT

---

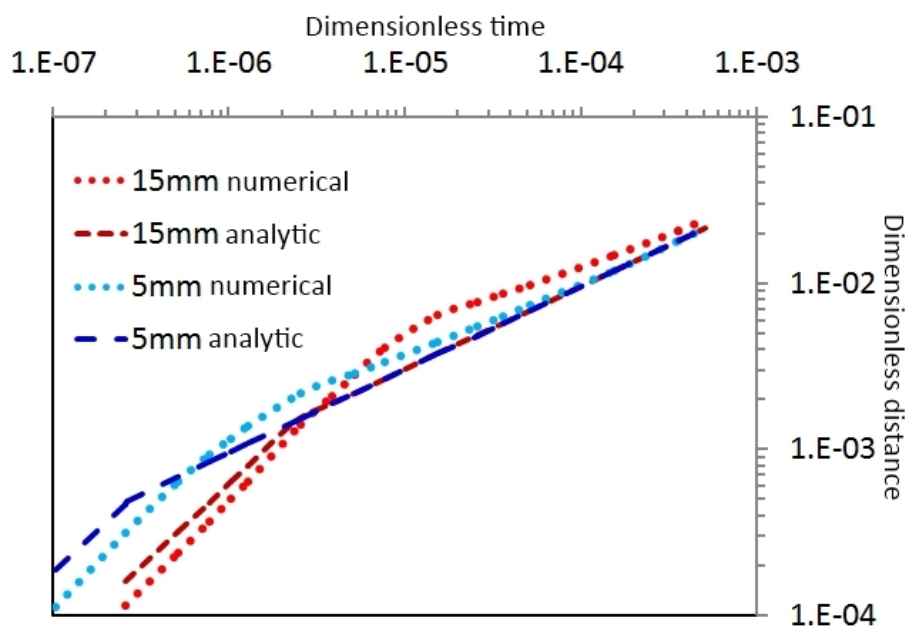


Figure 6.8: Movement of the thermal front in the fracture for  $b = 5 \text{ mm}$  and  $b = 15 \text{ mm}$  fracture apertures, shown on a log-log plot

Figure 6.8 confirms that the thermal tracer penetration increases with fracture aperture in the small aperture regime. Note that this was also the case when increasing the flow rate. However, the non dimensional analysis showed that varying the flow rate does not affect the temperature field in dimensionless coordinates, which explained the insensitivity of the push pull thermal response to flow rate. Conversely, the fact that the aperture influences the temperature field in dimensionless coordinates explains the observed impact on temperature breakthrough curves. In particular, increasing the fracture apertures leads to a larger penetration length in dimensionless coordinates and thus to enhanced heat losses. Note, that the fracture aperture is also found to influence the peak time (Figure 6.6). Thus, while for push pull solute tracer tests the peak time has no particular physical meaning, we find that for push pull thermal tests the retardation of the thermal peak time with respect to the solute peak time bears information on the effective fracture aperture. In the following section we explore the potential of thermal push-pull tests at the field.

### 6.3 Heat transport: push-pull heat tracer tests

In this section we present the experimental results of field push-pull heat tracer tests, that were conducted at the Stang er Brune experimental site in June 2011. The main objectives of this campaign were to test the possibility of the heat tracer test conduction, and to bring new experimental data. Furthermore, we aimed to explore possible scale effects on the thermal response and to investigate the relevance of a single homogeneous fracture model. In particular, as our modelling results demonstrate the sensitivity of temperature return to fracture aperture, we use this finding to assess the fracture aperture.

A series of heat push-pull tracer test with Dirac-type injection was conducted during the same field campaign as thermal tracer tests described by Read et al. (Appendix 2). The schema of the experiment is presented in Figure 6.9. The experiments have been conducted in B1-2 fracture, intersecting the B1 borehole at 50.9 *m* depth [Dorn et al., 2012; Le Borgne et al., 2007]. For each experiment, hot water was injected during the  $t_{inj}$  time interval at a controlled rate into the B1-2 fracture, isolated from the rest of the injection borehole by a double-packer system. The water was injected from a water tank at the surface, where a water heater was installed in order to maintain the temperature of injection at about 30°C. After the injection, we continued to push the tracer with fresh groundwater at approximately the same rate during the same time  $t_{push} = t_{inj}$ . Temperature and conductivity were monitored in the middle of the double-packer system, where B1-2 fracture intersects B1 borehole. Table 6.1 provides the experimental details of the tracer tests, referred to as Test1, Test2 and Test3.

Table 6.1: Experimental setup of the three tracer migration experiments in B1–2.

Experimental parameters	Experiment		
	Test1	Test2	Test3
Injection rate, <i>L/min</i>	7	7	7.3
Duration of injection, <i>min</i>	10	17	147
Maximum injection temperature, °C	33	34	27
Tracer conductivity, $\mu S/cm$	670	4000	670

## 6. HEAT AND SOLUTE TRANSPORT

---

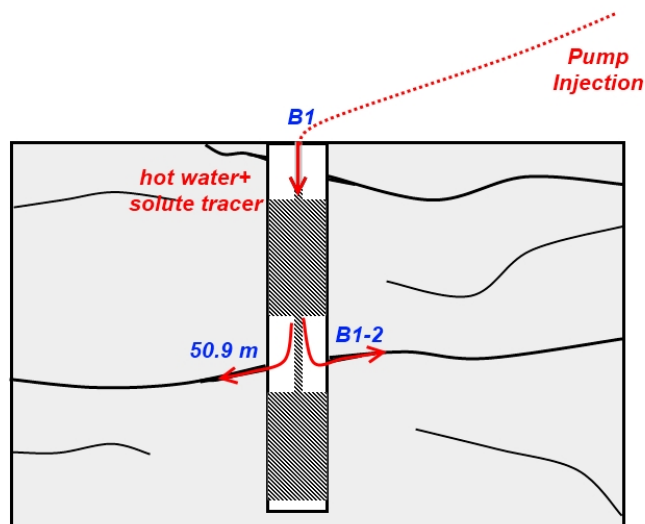


Figure 6.9: Tracer test experimental schema. Push-pull tracer in B1-2 fracture isolated with packers.

During the Test 2 experiment, salt, as a conservative tracer, was added during injection. The temperature and concentration breakthrough curves for Test 2 are presented in Figure 6.10. For Test 2, we injected the tracer during  $t_{inj} = 20$  min. Once we started to push with fresh water ( $t = t_{push}$ ), the temperature and concentration drops down to their initial values (Figure 6.10). Then, in the recovery time we observe an increase of concentration and a slight increase of temperature. Their comparison shows that temperature recovery peak arrives earlier than concentration peak as expected. Moreover, the peak is significantly smaller for temperature recovery which is again due to thermal loss to the rock matrix. In order to explore the scale dependence of the thermal response, we performed additional experiments for different injection and push times (Table 6.1). The temperature recoveries for all the conducted tests are shown in Figure 6.11.

In order to explore the scale effects, measured temperature backflow profiles were presented in log-log (Figure 6.12, data is shown by blue). To do so, we normalized thermal breakthrough so that its integral, over injection and pushing

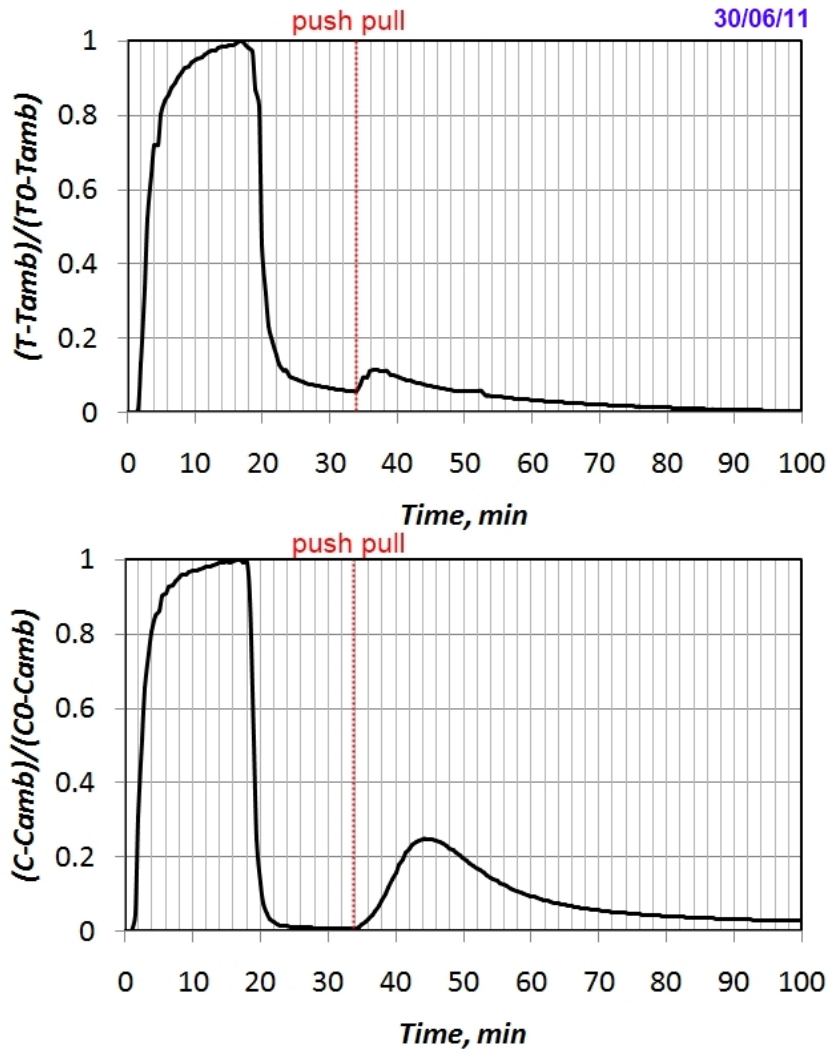


Figure 6.10: Temperature and concentration breakthrough curves measured in between packers for Test 2.

time, is 1. As expected, backflow temperatures decrease with scale of investigation. Note that, as observed in the numerical simulations, power law trend of approximately  $-1$  on a log-log pass through all the breakthrough peaks (Figure 6.12). We do not have an explanation to this effect, but this result may be interesting in particular for geothermal application, where the temperature recovery as a function of the scale of the thermal plume is a key element. Moreover, for

## 6. HEAT AND SOLUTE TRANSPORT

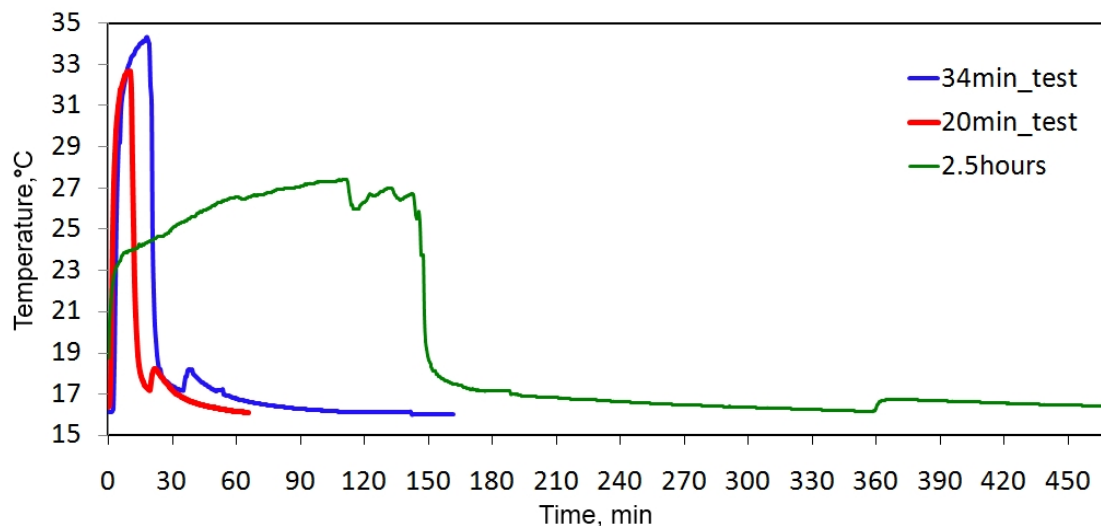


Figure 6.11: Temperature breakthrough curves for push-pull heat tracer tests in  $B1 - 2$  fracture.

late breakthrough times we observe a similar slope for all tests. However, durations of the experiments are not sufficient to analyze breakthrough tail power law slopes in details.

Measured temperature breakthrough curves were fitted with the numerical model by varying manually the fracture aperture. Figure 6.12, representing two fits for different fracture apertures:  $b = 5 \text{ mm}$  (Figure 6.12A) and  $b = 10 \text{ mm}$  (Figure 6.12B), shows the sensitivity of temperature breakthrough to changes in fracture aperture. A good agreement between the measured and modelled breakthrough curves is obtained for a fracture aperture  $b = 10 \text{ mm}$ . The relatively small peak temperature for Test 3 suggests that fracture aperture may increase with distance from the injection point. However, this feature can also result from heterogeneity effects at fracture scale [Neuville et al., 2010].

The B1-2 fracture aperture was also assessed independently using the results of a radially convergent solute tracer test, conducted in between B1-2 fracture and B2 borehole. The breakthrough curve, measured in B2 well (7 m away from B1 well) is shown in Figure 6.13. Using our numerical model, we fit the mean arrival time to derive the fracture aperture. Our best fit, presented in Figure 6.13, provides the value of 27 mm for B1-2 fracture, which is significantly larger

than the fracture aperture estimated from thermal tests. Note however, that the scales of investigation of the push pull and cross borehole tracer tests are different. Hence, this discrepancy may be consistent with an increase of effective fracture aperture with scale.

## 6. HEAT AND SOLUTE TRANSPORT

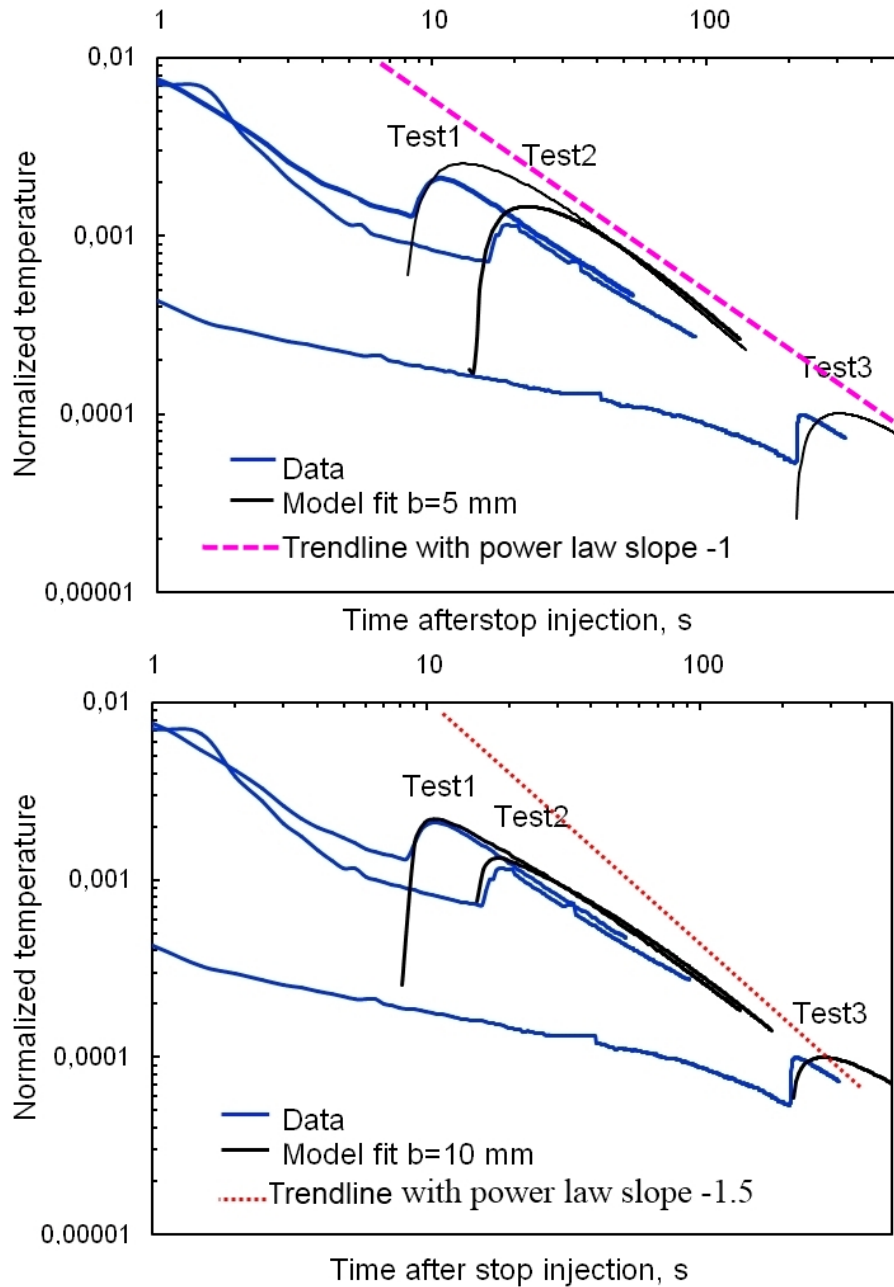


Figure 6.12: Breakthrough curves for push-pull heat tracer tests in  $B1-2$  fracture. Here temperature is normalized so that its integral, over injection and pushing time, is 1.

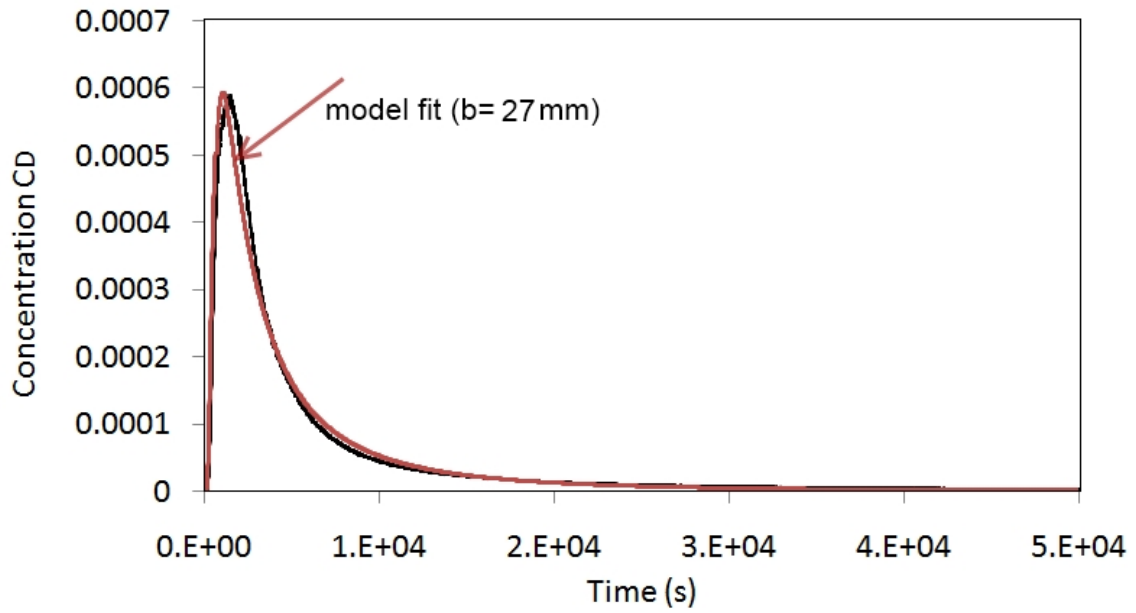


Figure 6.13: Measured breakthrough curves and model fit (fracture aperture  $b = 27 \text{ mm}$ ) for radial convergent tracer tests between  $B1 - 2$  fracture and B2 borehole.

### 6.4 Discussion and Conclusions

In this study the interest of using push-pull thermal tracer tests was investigated through numerical modelling and field experiments. We also study the influence of scale on heat transport. In agreement with previously developed analytical solutions [Jung and Pruess, 2012; Pruess and Doughty, 2010], we found that for practically relevant fracture apertures, the shape of the push-pull thermal breakthrough is mainly controlled by matrix diffusion. In terms of parameter estimation, we found that thermal signal is insensitive to flow rate, and, consequently, to the fracture-matrix interaction surface. Moreover, temperature backflow during push-pull tests was found insensitive when 2D push-pull was compared with to 1D case (which corresponds to an extreme flow channeling). This suggests the insensitivity of thermal push-pull tests to flow heterogeneities, which remains however to be confirmed. Investigations of the scale effect show that the recovered peak temperature decreases with scale. We also found that power law trend line passing through the peaks of the breakthrough curves has a slope of  $-1$  on a log-log plot. Finally, we found that the thermal response for push-pull tests with pulse injections is sensitive to the fracture aperture even for small apertures, which is in contrast with previous findings [Jung and Pruess, 2012].

Push-pull heat tracer tests were conducted at the Stang er Brune field site. When compared to the solute tracer, the temperature recovery peak is significantly smaller and demonstrates earlier arrival time than concentration peak. Our measurements also confirm that breakthrough temperatures decrease with scale of investigation. Based on our numerical model, we were able to estimate the aperture of B1-2 fracture ( $b_{est} = 10 \text{ mm}$ ). However, the experimental results also suggest that the effective fracture aperture may increase with scale in the present case.

In terms of modelling, an open question is whether heterogeneities influence thermal response during push-pull tests. At fracture scale, fracture-matrix thermal exchange is highly affected by the fracture wall roughness [Neuville et al., 2010]. This has two main implications: channeling effect and variability in fracture aperture. Our modelling results suggest that in push-pull configuration thermal response may be insensitive to advective effects. The second effect is re-

lated to local changes in fracture aperture, that, according to our results, should affect thermal breakthrough. At the network scale, once multiple flowing fractures exist, the tracer will then be distributed between them, reducing flow in each fracture. As we have shown, the decrease of flow rate, consecutive to flow division in several fractures, does not influence temperature recovery (Figure 6.5). Nevertheless, if several fractures are located close to each other, heat diffusion profiles from each fracture superimpose each other. An example of temperature recovery for push-pull in two 20 *mm* aperture fractures separated by 20 *mm* is shown in Figure 6.14A. For this example the cooling rate in each fracture is found to be approximately two times lower than for the single-fracture case, as heat losses occur mostly only through one the sides of the fracture. This figure illustrates fracture density effect on the push pull heat recovery. In this case, thermal breakthrough should be affected by the number of flowing fractures as well as distance in between them. The influence of these parameters on thermal breakthrough curves will be the topic of a subsequent study.

## 6. HEAT AND SOLUTE TRANSPORT

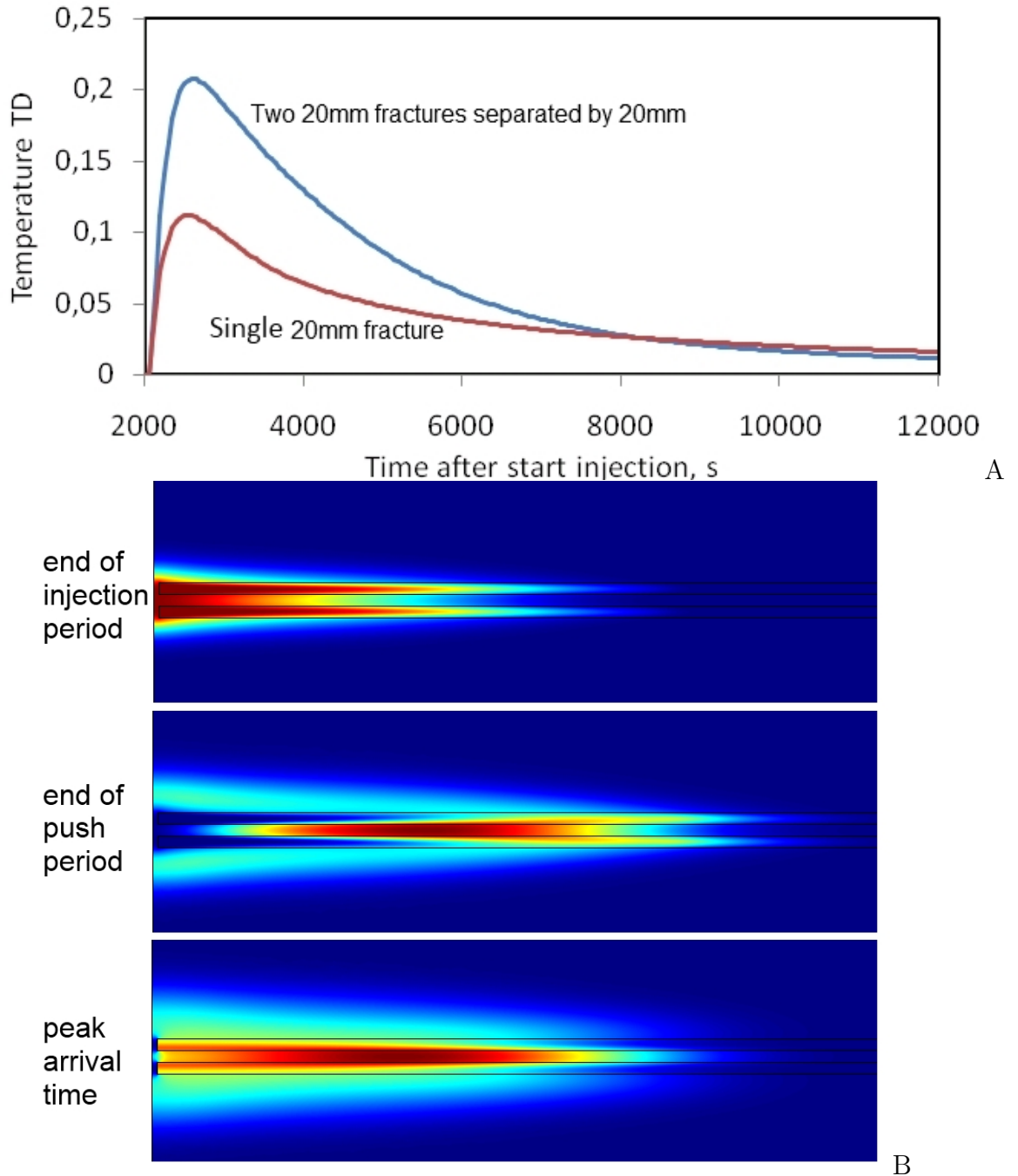


Figure 6.14: (A) Temperature breakthrough curves for a single 20 mm aperture fracture (red line) and for two 20 mm aperture fractures separated by 20 mm distance. The total flow rate for both experiments  $Q$  is given by 3.5 L/min (for the case with two fractures the flow rate in each fracture is reduced to half the rate that was seen for the single-fracture case  $Q_1 = Q_2 = 1.75$  L/min) and for all experiments injection time is given by 17 min. (B) Temperature distribution for two 20 mm aperture fractures separated by 20 mm distance at different times.

# Chapter 7

## Conclusions and perspectives

In this chapter, the thesis conclusions and suggestions for future studies are presented. The chapter starts by summarizing significant thesis contributions. Thereafter, the relevance of the obtained results and the research perspectives, including extension of the thesis work and promising applications of the developed approaches, are discussed.

### 7.1 Conclusions

The overall aim of the thesis was to develop new inverse approaches specifically for imaging the hydraulic and transport properties in fractured media at the field-scale. Four complementary approaches that concern new field measurements as well as new inverse modelling frameworks were developed. The ensemble of the methods proposed in the thesis is synthesized in Figure 7.1.

In Chapter 2, we proposed an inverse model approach for inverting flow tomography (i.e., sequential cross-borehole flowmeter tests) data set to infer fracture connectivity and transmissivities. The developed inverse modelling framework uses a simplified discrete fracture network model that highlights connectivity structures. We have explored the potential of this approach for different simplified synthetic fracture networks. Flow tomography appears to be a promising method for providing detailed characterization of fracture network hydraulic properties without the necessity of using packers. The key finding was that the tomographic approach reduces significantly the uncertainty on the inference of con-

## 7. CONCLUSIONS AND PERSPECTIVES

---

nectivity patterns and hydraulic parameters, compared to classical cross-borehole flowmeter tests. Another finding was that flow tomography is more effective if cross-borehole pumping induces large changes in vertical borehole velocities. The approach was shown to provide a good estimation of connectivity patterns and transmissivities of main flowpaths, while estimations of transmissivity of fractures that connect the main flowpath but not the boreholes are generally more uncertain, in agreement with Paillet [1998].

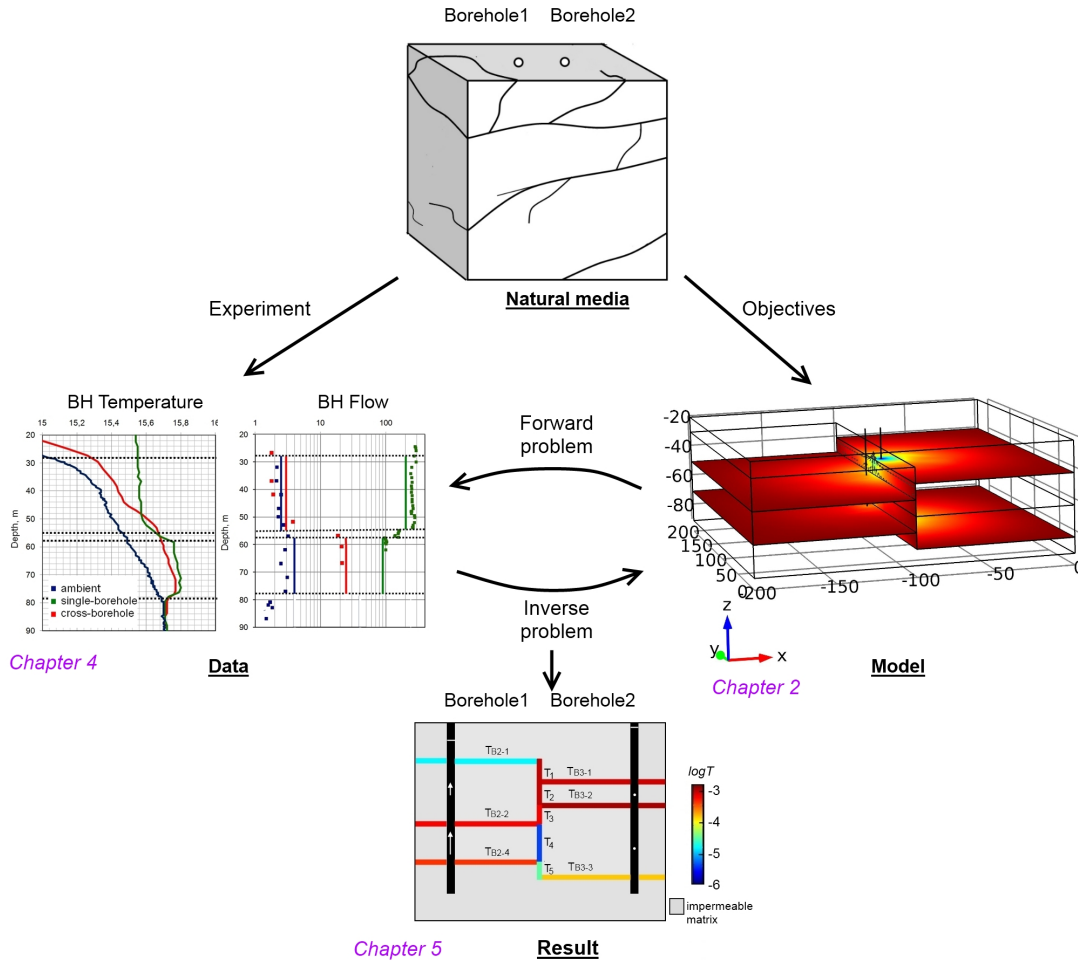


Figure 7.1: Illustration of the inverse modelling methods for imaging of fracture hydraulic properties developed during the thesis. In Chapter 2, we propose an inverse model approach for inverting flow tomography data. In Chapter 4, we propose a framework to invert temperature measurements to derive borehole flow velocities. In Chapter 5, we couple the approaches developed in the two previous chapters to interpret experimental data set to image fracture hydraulic properties at the site scale.

The second objective of the thesis was to include temperature data in an inverse framework for estimating hydraulic fracture properties (Figure 7.1). The advantage of using temperature data is that temperature profiles can be obtained more easily and continuously in space, compared to flowmeter profiles. Moreover, as shown in Read et al. (Appendix 2), the use of fiber optic technology can also

## 7. CONCLUSIONS AND PERSPECTIVES

---

greatly improve the temporal and spatial monitoring of temperature measurements. In Chapter 4, the close relationship between the borehole temperature gradient and the vertical borehole flow velocity was demonstrated. Using a numerical model of flow and heat transfer at the borehole scale, a method to invert temperature measurements to derive borehole flow velocities was proposed.

The third objective consisted of validating of the developed approaches using experimental data. In Chapter 5, we coupled the two approaches developed in the two previous chapters in a new experimental approach which we call temperature tomography. This experiment consists of sequential borehole temperature logging under cross-borehole flow conditions. The full inverse framework, combining the two previously proposed methods, is then presented to interpret temperature tomography experiments. Application of the temperature tomography approach to Stang er Brune field site succeed in identification of general connectivity patterns and transmissivities of the main flowpaths. However, the results suggest that for multifracture connections it is difficult to propose a simple conceptual model of flow and connectivity.

In the last chapter the interest of using push-pull thermal tracer tests was investigated through numerical modelling and field experiments. We also studied the influence of scale on heat transport. In agreement with previously developed analytical solutions, we found that for practically relevant fracture apertures, the shape of the push-pull thermal breakthrough is mainly controlled by matrix diffusion. In terms of parameter estimation, we found that thermal signal is insensitive to flow rate, and, consequently, to the fracture-matrix interaction surface. Moreover, our results suggest insensitivity of thermal push-pull tests to flow heterogeneities, which remains however to be confirmed. Investigations of the scale effect show that the recovered peak temperature decreases with scale. Finally, we found that the thermal response for push-pull tests with pulse injections is sensitive to the fracture aperture even for small apertures, which is in contrast with previous findings [Jung and Pruess, 2012]. Based on this finding, we were able to estimate the aperture of the fracture at the field.

The achievement of all these objectives opens new perspectives for future studies that we discuss in the next section.

## 7.2 Perspectives

In this section we discuss possible improvements and applications of the methods proposed in the thesis.

### 7.2.1 Tomography approaches

The results from the temperature tomography study are encouraging in that the method was able to image transmissivities of the main flowpaths connecting borehole pairs. However, we believe that several modifications can significantly improve this approach. For instance, the simplified conceptual model of fracture network connectivity fail to capture the spatial organization for some multiconnected fractures (Figure 7.2). Future developments could focus on improving conceptual model of flow and fracture connectivity.

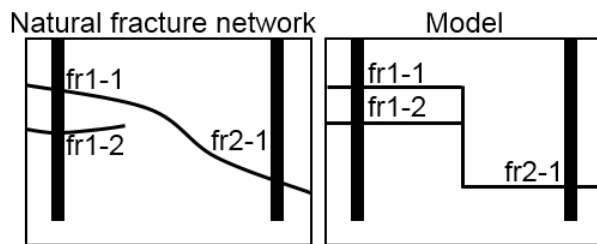


Figure 7.2: An example of fracture network and its conceptualization with a model. For this fracture network, model simplicity does not allow to represent fr1-2 as an independent flowpath.

In order to improve the representation of the fracture network geometry one may need additional data. The combination of tracer and time lapse geophysical data, which has been tested in the same site, is particularly promising [Dorn et al., 2012] (Appendix 1). The joint interpretation of these data together with flow tomography data should improve the estimation of fracture hydraulic properties. Additional geophysical surveys may help us to image 3D fracture network geometry. This would be particularly important for characterizing spatial distribution of hydraulic properties for the overall cluster of connected fractures in the site.

## 7. CONCLUSIONS AND PERSPECTIVES

---

Another possible extension of this inverse approach consists of using transient flow data to estimate both transmissivities and specific storage of the main flowing fractures.

### 7.2.2 Temperature and flow heterogeneity

A possible extension of the approach proposed for using temperature measurements to assess flow heterogeneity is the study of temperature anomalies at large scale. In order to study this question, temperature profiles were collected in Guidel field site, situated 5 km away from Ploemeur in similar geological conditions, under two different flow conditions: during a 2-months pumping test and under ambient conditions. Measured temperature profiles are presented in Figure 7.3. Temperature profiles are generally characterized by relatively high anomalies (up to  $3^{\circ}C$  per 130  $m$ ). Some temperature profiles (PSR5 well) were found to be changed depending on pumping conditions, while the others (PSR1 well) remain undisturbed. These data along with site-scale flow and heat transfer model could be considered to investigate large scale circulation patterns (recharge, discharge, flow cells).

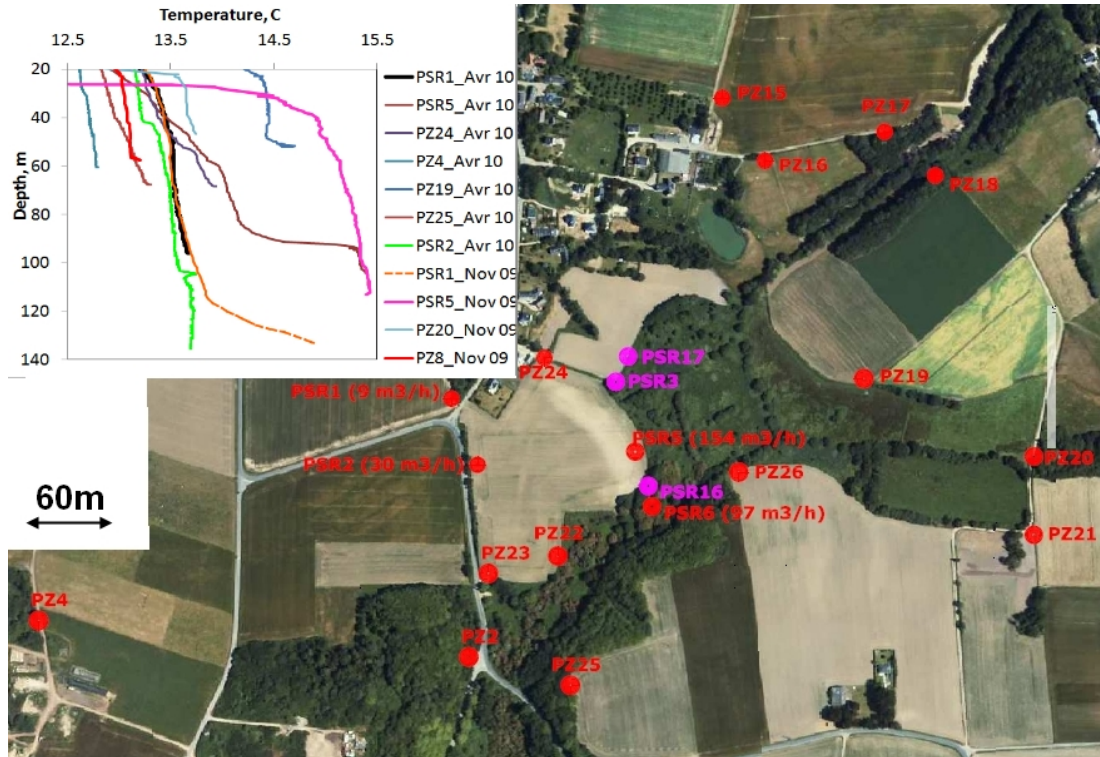


Figure 7.3: Temperature anomalies at large scale. In November 2009, pumping took place in PSR3 borehole and in April 2010 temperature was measured under ambient flow conditions.

### 7.2.3 Heat as a tracer

Another promising perspective concerns using heat as a tracer under various hydraulic configurations. Thermal tracer tests were performed by injecting continuously 50 degrees Celsius water in a fracture located at 50 meters depth [Read et al.] (Appendix 2). The breakthrough curves measured in an adjacent borehole show a significant time lag between the thermal and solute breakthrough due to the large coefficient of heat diffusion compared to molecular diffusion. Moreover, the breakthrough locations of heat and solute was found to be different [Dorn et al., 2012; Read et al.]. This indicates that heat and solute transport are not sensitive to the same characteristics of the flow heterogeneity, thus, these tracer tests carry complementary information on transport patterns in fractured media. As discussed in Read et al., the possible reasons for these different behaviors

## 7. CONCLUSIONS AND PERSPECTIVES

---

could be related to density effects [Bouquain et al., 2011] or to the influence of fracture wall roughness [Neuville et al., 2010]. In order to understand the reason of these differences we are planning to develop a model allowing to interpret cross-borehole heat tracer tests. This model is computationally more demanding than the push-pull model since the axial symmetric conditions cannot be used.

Furthermore, investigation of heat transport in fractured-porous media can be addressed in future. Numerical simulations of heat transfer in fractured porous domains demonstrate that at high matrix permeabilities advection in the matrix dominates over diffusion, resulting in more heterogeneous temperature distributions in the matrix blocks [Geiger and Emmanuel, 2010]. The possible research question of this study will be on discussing how advective flow in porous rock will influence heat transport behavior.

Appendix 1. Paper: Inferring transport characteristics in a fractured rock aquifer by combining single-hole ground-penetrating radar reflection monitoring and tracer test data (Dorn et al., Water Resources Research, 2012)

# Inferring transport characteristics in a fractured rock aquifer by combining single-hole ground-penetrating radar reflection monitoring and tracer test data

Caroline Dorn,<sup>1</sup> Niklas Linde,<sup>1</sup> Tanguy Le Borgne,<sup>2</sup> Olivier Bour,<sup>2</sup> and Maria Klepikova<sup>2</sup>

Received 12 December 2011; revised 19 September 2012; accepted 2 October 2012; published 15 November 2012.

[1] Investigations of solute transport in fractured rock aquifers often rely on tracer test data acquired at a limited number of observation points. Such data do not, by themselves, allow detailed assessments of the spreading of the injected tracer plume. To better understand the transport behavior in a granitic aquifer, we combine tracer test data with single-hole ground-penetrating radar (GPR) reflection monitoring data. Five successful tracer tests were performed under various experimental conditions between two boreholes 6 m apart. For each experiment, saline tracer was injected into a previously identified packed-off transmissive fracture while repeatedly acquiring single-hole GPR reflection profiles together with electrical conductivity logs in the pumping borehole. By analyzing depth-migrated GPR difference images together with tracer breakthrough curves and associated simplified flow and transport modeling, we estimate (1) the number, the connectivity, and the geometry of fractures that contribute to tracer transport, (2) the velocity and the mass of tracer that was carried along each flow path, and (3) the effective transport parameters of the identified flow paths. We find a qualitative agreement when comparing the time evolution of GPR reflectivity strengths at strategic locations in the formation with those arising from simulated transport. The discrepancies are on the same order as those between observed and simulated breakthrough curves at the outflow locations. The rather subtle and repeatable GPR signals provide useful and complementary information to tracer test data acquired at the outflow locations and may help us to characterize transport phenomena in fractured rock aquifers.

**Citation:** Dorn, C., N. Linde, T. Le Borgne, O. Bour, and M. Klepikova (2012), Inferring transport characteristics in a fractured rock aquifer by combining single-hole ground-penetrating radar reflection monitoring and tracer test data, *Water Resour. Res.*, 48, W11521, doi:10.1029/2011WR011739.

## 1. Introduction

[2] Security concerns about waste disposals (nuclear, toxic waste, CO<sub>2</sub>) and the need for efficient and sustainable extractions of natural resources (water, oil, gas, heat) in fractured rock formations require both process understanding and characterization of transport properties in fractured media. This implies a need for reliable monitoring technology for tracking temporal changes in the subsurface, in particular those related to contaminant transport. The limited accessibility to fractured rock systems contrasts with hydrological properties that are typically extremely heterogeneous at all scales [e.g., Bonnet *et al.*, 2001; Long *et al.*, 1996; Paillet, 1998].

Generally, the data available for constraining fractured rock models have rather low information content with respect to the complexity of the system. For example, breakthrough curve data can be explained by a relatively small number of model parameters, while a very complex structure might have given rise to the observed data [e.g., Becker and Shapiro, 2000, 2003].

[3] Models of conservative solute transport in fractured media typically combine advective and dispersive transport mechanisms within fractures with possibly matrix diffusion and sorption [Maloszewski and Zuber, 1985; Hadermann and Heer, 1996; Lapcevic *et al.*, 1999]. While these basic mechanisms are well known, a major challenge for modeling a system is the adequate description of heterogeneity at different scales. At the scale of the fracture, heterogeneous advection or “flow channeling” has been shown to be very common. Flow channeling, which is a phenomenon that increases in importance with the statistical variability in fracture aperture, refers to the situation in which the flow within discrete pathways make up a very large fraction of the total flow [Tsang and Neretnieks, 1998; Moreno and Tsang, 1994]. Highly localized fluxes and diffusion into stagnant interchannel spaces within fracture planes are typically not

<sup>1</sup>Centre de recherche en l'environnement terrestre, Université de Lausanne, Lausanne, Switzerland.

<sup>2</sup>OSUR, Géosciences Rennes, Université Rennes 1-CNRS, Rennes, France.

Corresponding author: C. Dorn, Centre de recherche en l'environnement terrestre, Université de Lausanne, CH-1015 Lausanne, Switzerland. (caroline.dorn@unil.ch)

taken into account in classical dispersion theories and the testing of alternative transport models requires detailed experimental investigations and imaging at the fracture scale [Becker and Shapiro, 2000].

[4] Stochastic continuum methods can provide equivalent distributed models explaining observed state variables (e.g., temperature, pressure, tracer concentration, etc.) [Neuman and Di Federico, 2003]. The applicability of such models at the local field scale (1–100 m) is questionable in fractured rock systems as it is uncertain if a representative elementary volume (REV) exists as fractures often prevail at all scales [Long et al., 1982; de Dreuzy et al., 2001, 2002; Neuman, 2005]. Alternative representations based on discrete fracture networks (DFN) [e.g., Darcel et al., 2003] are relatively difficult to condition and calibrate even with detailed measurements of aperture in boreholes or in situ flow properties [Neuman, 2005]. Instead of building complex distributed models of heterogeneity, it is possible to account for unresolved heterogeneity and processes using effective models, for example, using concepts of multirate mass transfer [Haggerty and Gorelick, 1995; Cvetkovic and Haggerty, 2002], continuous time random walk [Berkowitz et al., 2006], or multiple flow channels [Becker and Shapiro, 2000]. However, it is often difficult to assess which interpretive framework is the relevant considering typically available breakthrough data (or other hydrological data) [Haggerty et al., 2000, 2001; Harvey and Gorelick, 2000; Le Borgne and Gouze, 2008]. Obtaining spatially distributed images related to tracer movement within the formation can therefore be of key importance for defining appropriate effective models for transport in fractured media.

[5] When analyzing breakthrough curves alone, it is generally not possible to uniquely (1) determine if transport occurs through one or several fractures and if multiple arrivals are caused by fracture heterogeneity (aperture variations) or by multiple flow paths involving different fractures or (2) infer what may be the cause of low mass recovery (e.g., through flow paths driven by density effects or ambient flow; storage close to the injection point, in the fractures taking part in the tracer transport or through mass exchange with the rock matrix).

[6] Geophysical imaging may provide information about subsurface structure and dynamics in between the injection and extraction points, that is, at locations where hydrological data are generally not available [e.g., Rubin and Hubbard, 2005]. One of the most suitable geophysical methods in fractured rock investigations at the 1–100 m scale is ground-penetrating radar (GPR). This method allows detecting millimeter aperture fractures and resolving temporal changes away from the observation points [Olsson et al., 1992; Lane et al., 1996, 1998; Becker and Tsofiias, 2010; Dorn et al., 2011]. Surface GPR is useful to study transport in shallow subhorizontal fractures [Talley et al., 2005; Becker and Tsofiias, 2010]. For larger depths, cross-hole difference-attenuation radar tomography [e.g., Liu et al., 1998; Day-Lewis et al., 2003] can image tracer movement through fracture zones, but the resolution of the resulting tomograms is insufficient for imaging transport in individual millimeter aperture fractures.

[7] Dorn et al. [2011] showed that time-lapse single-hole GPR data acquired during and after saline tracer injection tests allow imaging tracer movement through a network of

connected fractures. The recovered images are relatively subtle despite extensive processing and many different time lapses are necessary to make robust interpretations concerning transport pathways. Nevertheless, the resulting information about tracer transport and storage cannot be obtained by any other field technique that we are aware of, which warrants further study with this type of data. Herein, we build on the work by Dorn et al. [2011] by analyzing five tracer experiments (one of them being the experiment presented in our previous study) that were acquired under different injection and pumping conditions in a granitic rock aquifer. The objectives of this work are to show that time-lapse single-hole GPR reflection data acquired during saline tracer injection experiments make it possible (1) to obtain repeatable results, (2) to identify transport pathways over tens of meters through connected individual fractures, (3) to identify main transport mechanisms and causes of incomplete mass recovery at a site, and (4) to provide geometrical constraints for the estimation of effective transport properties, namely hydraulic conductivities and dispersion coefficients. It is our hope that this contribution will motivate further research in how time-lapse GPR data can be used in fractured rock hydrology for (1) model validation, (2) model calibration, and (3) inversion purposes. A simplified flow and transport model calibrated to the breakthrough data is used to highlight some of these possibilities and associated challenges.

## 2. Methods

### 2.1. The Single-Hole Ground-Penetrating Radar Reflection Method

[8] GPR is an electromagnetic imaging method of the subsurface that is presented by Annan [2005], while Balanis [1989] describes the underlying physics of radar wave propagation. A GPR transmitter sends a source signal out into the medium, while a GPR receiver collects the resulting signals arising from signal transmission, reflections, and scattering at electromagnetic boundaries. The single-hole GPR configuration refers to the case in which the transmitter and receiver are both located in the same borehole at a known separation (see Figure 1). In single-hole reflection mode, imaged reflectors can arise from fractures located in all directions from the borehole as illustrated in Figure 1; planar reflectors that intersect the borehole are imaged as V-shaped reflections. Data processing of the acquired data allows determining the distances to the reflectors and their associated dips, but not their azimuth. Reflectors are predominantly related to variations in electrical permittivity  $\epsilon$ , but also in electrical conductivity  $\sigma$ , and in magnetic permeability  $\mu$ . The attenuation of the signal propagating in the medium is proportional to  $\sigma$ . The data recorded by a receiver located at a given distance from the transmitter is traditionally used to image boundaries that in fractured media correspond to fracture surfaces [e.g., Olsson et al., 1992; Liu and Sato, 2006]. When saline tracer arrives at a fracture, the locally elevated conductivity leads to increases in the reflectivity of the fracture and thus a higher-amplitude GPR reflection. [Tsofiias and Becker, 2008]. An unwanted effect associated with measurements in boreholes following tracer injection tests is that temporal variations in fluid conductivity within the pumping borehole changes the radiation

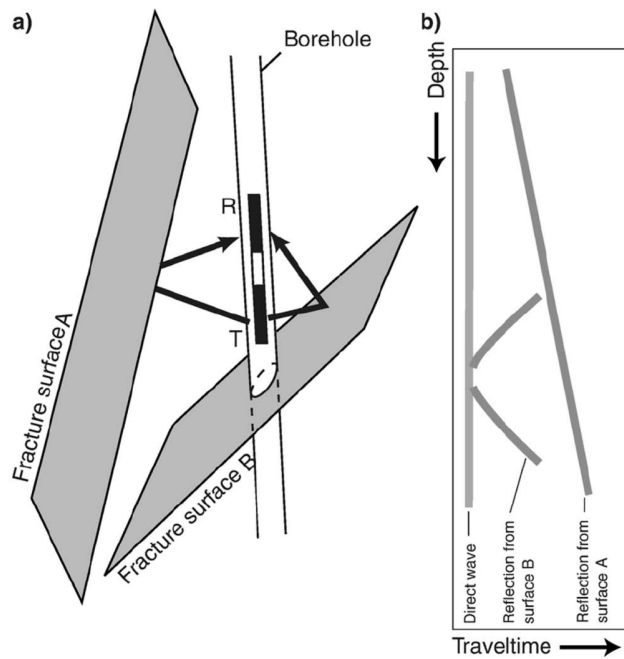


**Figure 1.** (a) Principle of the single-hole GPR reflection method, in which a transmitter T sends out a signal that is reflected and subsequently collected by a receiver R located in the same borehole as the transmitter. (b) Schematic reflection section illustrating typical reflection patterns arising from intersecting and nonintersecting fractures. From *Spillmann et al.* [2007].

characteristics of the antenna [Ernst *et al.*, 2006] and therefore the effective source wavelet, which complicates the subsequent data processing.

[9] Beside the medium constitutive parameters, the recorded reflection amplitude from a fracture depends on a number of factors. (1) The fracture aperture and signal wavelength, closely spaced reflections from the upper and lower fracture surfaces interfere with each other [see *Tsoflias and Becker*, 2008; *Widess*, 1973]. (2) The dip of the fracture, as the reflection coefficient of a dipping interface (or fracture) is a function of the signal angle of incidence and signal polarization [Bradford and Deeds, 2006; *Tsoflias and Hoch*, 2006], and subvertical dipping features have higher reflection amplitudes than subhorizontal fractures when using GPR in vertical boreholes ( $0\text{--}30^\circ$  dipping fractures are not directly detectable). (3) The distance between a fracture and the antennas, due to signal attenuation fractures are detectable up to roughly  $r = \sim 15$  m radial distance in granitic formations using a central signal frequency of 140 MHz. (4) The spatial extent of a fracture, as a reflection is an integration over an area of about the first Fresnel zone (e.g., for a central frequency of 140 MHz, the Fresnel radius is 0.6 m at a radial distance  $r = 2$  m and is 2 m at  $r = 20$  m). (5) The azimuth of a fracture, as reflections from a plane fracture can only be observed if a normal vector to the reflector crosses the borehole. (6) The roughness of the fracture that creates diffractions that might allow imaging of fractures with unfavorable orientations.

## 2.2. Field Site

[10] The experiments presented herein were carried out within a fractured rock aquifer that constitutes the main water supply for the town of Ploemeur, France (Figure 2), with an average extraction rate of  $2000 \text{ L min}^{-1}$  [Le Borgne *et al.*, 2006]. Our tracer tests were conducted  $\sim 3$  km away from the water extraction site at the test site Stang-er-Brune [Le Borgne *et al.*, 2007]. The experiments were carried out between two  $\sim 6$  m spaced boreholes B1 (83 m deep) and B2 (100 m deep). The boreholes reach a contact zone at a depth  $z = \sim 40$  m ( $z = 0$  m corresponds to the top of the B1 borehole casing) between highly deformed mica schists and underlying saturated granite. Within the granite (at  $z = 40\text{--}80$  m), the strongly deviated B2 is located  $40\text{--}100^\circ\text{N}$  relative to B1. The granite formation has the most permeable fractures [Le Borgne *et al.*, 2007] and is therefore the area of primary interest in this study (Figure 2).

[11] *Le Borgne et al.* [2007] used televiewer data together with hydraulic testing (notably single-hole and cross-hole flowmeter tests) at the site to characterize fractures that intersect the boreholes and identify those that are hydraulically connected. The formation is highly transmissive with overall hydraulic transmissivities on the order of  $10^{-3} \text{ m}^2 \text{ s}^{-1}$  over the length of each borehole. *Le Borgne et al.* [2007] reported an ambient vertical upward flow in the boreholes of about  $1.5 \text{ L min}^{-1}$ . This ambient vertical flow is the result of a 50 cm hydraulic head difference between the deepest fractures at  $z = 100$  m and the upper mica schist. This regional upward flow that appears in all permeable boreholes is also expected to affect the well-connected fractures. The transmissive fracture network at the site is dominated by a relatively limited number of well-connected fractures (i.e., only 3–5 such fractures intersect a borehole over its entire length). These fractures have a dip in the range of  $30\text{--}80^\circ$  and an azimuth in the range of  $190\text{--}270^\circ$ . The dips and azimuths of the boreholes suggest that there is no single fracture that intersects both boreholes B1 and B2 [Le Borgne *et al.*, 2007].

[12] *Dorn et al.* [2012] acquired 100 MHz and 250 MHz multifold single- and cross-hole GPR reflection data to constrain the geometry of the main fractures within the granite formation. Using the single-hole 250 MHz data, it was possible to obtain high-resolution images of the main fractures in the granite at radial distances  $r = 2\text{--}13$  m away from B1 and B2 [Dorn *et al.*, 2012] including those that were identified as being transmissive by *Le Borgne et al.* [2007].

## 2.3. Experimental Setup

[13] Table 1 provides the experimental details of the tracer tests (referred to as experiments Ia, Ib, II, IIIa, and IIIb in the following) that were performed between B1 and B2 in June 2010. Figure 2c is a sketch of the experimental setup for the case in which B1 is the injection and B2 the pumping borehole. All logging takes place in the pumping borehole. Note that our naming convention is different than the one used by *Le Borgne et al.* [2007] in that we name each fracture according to the borehole name and the depth at which it intersects. For example, a fracture intersecting borehole B1 between  $44.0 \text{ m} \leq z < 45.0 \text{ m}$  is named B1-44.

[14] For each experiment, a saline solution of  $\sim 90$  L was injected during a short time interval (10–30 min) at a controlled rate into a transmissive fracture (experiments Ia and

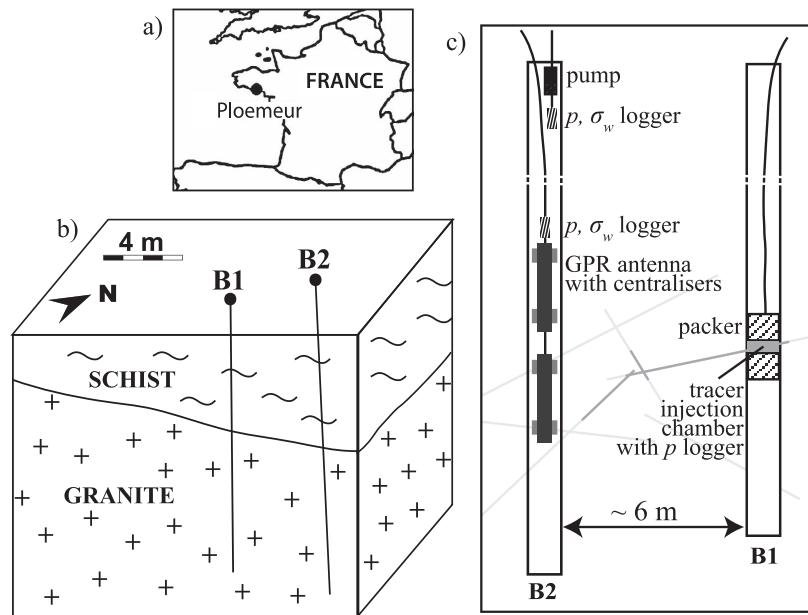


**Figure 2.** (a) Location of the Stang-er-Brune study site in the vicinity of Ploemeur, France. (b) Geological model of the field site with a  $30^\circ$  dipping contact between mica schist and underlying granite. (c) Schematic of the data acquisition setup, in which  $p$  and  $\sigma_w$  logger refer to hydraulic pressure and groundwater conductivity loggers, respectively.

Ib in B1–78, experiment II in B1–50, and experiments IIIa and IIIb in B2–55) that was isolated from the rest of the injection borehole by a double-packer system. The initial tracer salinity was  $\sim 30$  times higher than the background salinity of the groundwater. After the injection, we continued in four of the five experiments to push the tracer with fresh groundwater at approximately the same rate. For experiment Ib, no further injection of fresh groundwater was pursued after the end of the tracer injection. To pull the tracer solution toward the pumping borehole, we pumped water in the upper cased section of the pumping

borehole. Salt concentrations were monitored below the pump at  $z = 10$  m using an electrical conductivity logger. Although the mean transfer time between the two boreholes was about 1 to 3 h depending on the experiments, pumping lasted for at least 12 h to remove most of the tracer from the rock formation. Along the observation depth interval in the pumping borehole, we repeatedly acquired single-hole GPR data while measuring the borehole fluid electrical conductivity  $\sigma_w$  and hydraulic pressure  $p$  (one CTD logger was attached to the GPR antenna cable just above the upper antenna; Figure 2c). We used 250 MHz GPR antennas

**Table 1.** Experimental Setup of the Five Tracer Experiments<sup>a</sup>

Experimental Parameters	Experiment				
	Ia	Ib	II	IIIa	IIIb
		<i>Injection Well</i>			
Fracture of injection	B1–78	B1–78	B1–50	B2–55	B2–55
Depth of injection	78.7 m	78.7 m	50.9 m	55.6 m	55.6 m
Injection rate	2–3 L min <sup>-1</sup>	2.3–3.5 L min <sup>-1</sup>	2.3–2.7 L min <sup>-1</sup>	8–10 L min <sup>-1</sup>	7–9 L min <sup>-1</sup>
Amount of tracer	87 L	90 L	92 L	93.5 L	92.5 L
Injected amount of salt	3.5 kg	4.7 kg	3.7 kg	4.7 kg	4.6 kg
Tracer conductivity	5 S m <sup>-1</sup>	5.5 S m <sup>-1</sup>	5 S m <sup>-1</sup>	5.5 S m <sup>-1</sup>	5.5 S m <sup>-1</sup>
Pushing tracer with fresh water	yes	no	yes	yes	yes
		<i>Observation Well</i>			
Borehole	B2	B2	B2	B1	B1
Number of time steps $N$	16	21	29	31	33
Observation interval	35–95 m	35–90 m	35–85 m	35–80 m	35–75 m
Range of pumping rates	$\sim 30$ L min <sup>-1</sup>	5–30 L min <sup>-1</sup>	13–25 L min <sup>-1</sup>	1–10 L min <sup>-1</sup>	5–6 L min <sup>-1</sup>
Mean pumping rate	30 L min <sup>-1</sup>	16 L min <sup>-1</sup>	16 L min <sup>-1</sup>	6 L min <sup>-1</sup>	5.5 L min <sup>-1</sup>
Mean time step	10 min	10 min	10 min	10 min	5 min
		<i>Mass Recovery</i>			
Recovered amount of salt	24%	15%	32%	19%	32%

<sup>a</sup>The listed pumping rates refer to the time periods of GPR monitoring.

(MALÅ borehole antennas with center frequencies around 140 MHz; antenna separation of 4 m) to obtain a high spatial resolution.

[15] The different raw GPR sections  $\mathbf{D}_i^{\text{raw}}$  (depth sampling of  $\Delta z = 0.1$  m) and corresponding  $\sigma_w$  borehole logs (depth sampling of  $\Delta z < 0.2$  m) were acquired over observation intervals of tens of meters. Each time lapse  $i$  is associated with an observation time  $t_i^{\text{obs}}$  relative to the start of the saline tracer injection. For each experiment, a reference GPR section  $\mathbf{D}_1^{\text{raw}}$  was acquired just before the injection, and the following sections  $\mathbf{D}_i^{\text{raw}}$  were acquired every 5–10 min (the acquisition of one GPR section takes approximately 5 min), except for the last section  $\mathbf{D}_N^{\text{raw}}$  that was acquired the following day after overnight pumping. Repeatability in the vertical positioning between the radar sections of a few centimeters were obtained by using a calibrated digital measuring wheel and by marking the start and end points on the cables. Two plastic centralizers attached to each GPR antenna assured that the lateral positions within the boreholes were similar between acquisitions (Figure 2c).

[16] The whole suite of experiments (Table 1) allowed us to investigate under different conditions to what extent saline tracer transport in fractured media can be imaged with single-hole GPR reflection monitoring. The chosen injection points largely determine the fractures that take part in the tracer transport, but also variations in the injection and pumping rates will have a strong influence on the spreading of the tracer (especially at this site exhibiting significant ambient upward flow ( $\sim 1.5$  L  $\text{min}^{-1}$ ) in the boreholes [Le Borgne et al., 2007]). The main differences between experiments Ia and Ib were (as mentioned above) that no pushing of the injected tracer with groundwater was performed in experiment Ib and that the pumping rate was higher ( $\sim 30$  L  $\text{min}^{-1}$ ) in experiment Ia than in experiment Ib ( $\sim 16$  L  $\text{min}^{-1}$ ). The injection in experiment II was carried out in a fracture for which prior hydrological investigations indicate that the flow paths toward B2 are rather subhorizontal. This is a challenging setup for single-hole GPR as subhorizontal fractures cannot directly be detected due to the high angle of incidence (tangential to the fracture) resulting in no reflected signal returning to the receiver antenna. Experiments IIIa and IIIb differ with respect to the previous surveys in terms of the higher injection rate (8–10 and 7–9 L  $\text{min}^{-1}$ ); the pumping throughout experiment IIIa was unstable, whereas the pumping rate during experiment IIIb ranged between 5 and 6 L  $\text{min}^{-1}$  (see Table 1). Dorn et al. [2012] presented the GPR results from experiment IIIa and processing of experiment IIIb reveals similar results. The processing employed was slightly different than what is proposed below, but the overall tendencies were very similar. The results from the GPR processing presented herein therefore only consider experiments Ia, Ib, and II, while the results of experiments IIIa and IIIb are included in the interpretation.

#### 2.4. GPR Data Processing

[17] The most important aspect of successful GPR difference imaging is repeatability. Processing of high-frequency single-hole GPR reflection monitoring data is very challenging and a quite extensive testing of alternative processing strategies was necessary to assure that the difference

amplitudes are comparable between acquisitions and to assure smooth transitions in the retrieved patterns between time lapses. Indeed, positioning accuracy of sources and receivers is most important when imaging subhorizontally dipping fractures. Apart from standard GPR processing, we therefore had to account for (1) vertical positioning uncertainties on the centimeter scale due to cable twisting during the data acquisition, (2) temporal variations in the effective GPR source signals caused by variations in the borehole fluid conductivity, and (3) significant direct wave energy and ringing signals caused by poor dielectric coupling that severely contaminate the individual raw sections  $\mathbf{D}_i^{\text{raw}}$  to  $\mathbf{D}_N^{\text{raw}}$  for traveltimes  $t < 90$  ns (the direct wave is a wave traveling along the borehole wall). Generally, the raw data have high signal-to-noise ratios for  $t < 160$  ns.

[18] Figure 3 summarizes the main processing steps of the GPR data. We accounted for time-zero drifts of the transmitter initialization time before correcting the residual misalignments of the direct wave between individual sections. An initial geometrical scaling of the signal was applied assuming spherical divergence of the source amplitude followed by a wide band pass filter in the frequency domain (linearly tapered with corner frequencies 0–20–300–380 MHz) that removes low- and high-frequency noise.

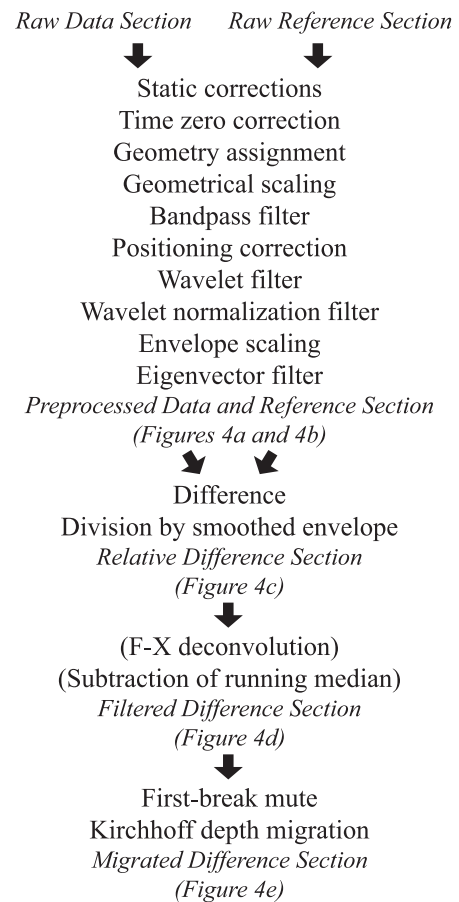


**Figure 3.** Flowchart of the GPR processing steps with reference to figures showing intermediate results. Processing steps in parentheses only apply to experiments Ia and Ib.

[19] To minimize vertical positioning errors, we calculated depth corrections (Figure 3) using the processed data up to this point. To calculate the corrections, we aligned first-arrival energy, restricted the data to a time window after the first arrivals for times with a high signal-to-noise ratio, applied a dip filter to suppress signals parallel to the direct wave, and narrowed the frequency spectrum of the data (60–70–190–210 MHz). We then calculated zero-crossing patterns of all data traces (1 for a zero crossing before a maximum,  $-1$  before a minimum and 0 otherwise). The vertical corrections were determined iteratively by searching, for each data trace, a correction that maximized the correlation between the zero-crossing patterns of an individual data trace and the corresponding stacked traces of all time-lapse data. The corrections were then used to construct a new stacked data section on which this process was repeated until the proposed correction from one iteration to the next was smaller than 3 cm on average. These corrections were applied to the widely band-pass-filtered data (Figure 3).

[20] To correct for temporal changes of the effective source signal due to salinity variations in the observation borehole, we followed *Dorn et al.* [2011] by applying a continuous wavelet transform and analyzing the wavelet power spectra of the data using the Morlet wavelet [*Torrence and Compo*, 1997]. In a first step, we removed wavelet scales with center frequencies outside the 20–160 MHz range. In a second step, we defined wavelet-scale-dependent factors  $F_i$  as the ratios of the wavelet power of the direct wave of the processed data  $D_i^{\text{proc}}$  with respect to the direct wave of the reference  $D_1^{\text{proc}}$  ( $=R_1^{\text{proc}}$ ). We then used the factors  $F_i$  to rescale  $R_1^{\text{proc}}$  in the wavelet domain into new reference sections  $R_i^{\text{proc}}$ . The underlying assumption for this correction of the reference conditions is that the increased electrical conductivity of the borehole fluid affects the later arriving signals similarly as the direct wave, such that any remaining differences between time lapses after this correction only reflect changes occurring within the rock formation. The reason for rescaling  $R_1^{\text{proc}}$  instead of  $D_i^{\text{proc}}$  is the higher bandwidth of  $R_1^{\text{proc}}$  as high frequencies are strongly attenuated at later acquisition times due to the increasing borehole fluid conductivity.

[21] To remove ringing signals caused by poor dielectric coupling, we applied an eigenvector filter that decomposes the data into eigenimages in a time window around the direct wave ( $t < 90$  ns) using Karunen-Loeve theory. Then we excluded eigenimages representing ringing signals identified as those being parallel to the direct wave before reconstructing the data. After this preprocessing of the GPR data, the amplitudes are comparable and minimally affected by noise and signals other than reflections. As an example, the data at  $t^{\text{obs}} = 45$  min and its reference section of experiment Ib are shown in Figures 4a and 4b. It is important to note that the reflections corresponding to fractures (or changes in salinity within the fractures during the time-lapse experiments) are seen over a relatively wide time window (e.g., the strong top reflector between  $z = 40$ – $50$  m) and do not represent direct images of the fractures. In fact, the recorded GPR signal is a convolution of a finite source signal ( $\sim 30$  ns corresponding to  $\sim 3$  m) with a rather discrete reflectivity distribution arising from the millimeter

aperture fractures. The time or distance to a given reflector corresponds to the first-arriving energy in these wave trains.

[22] To facilitate the comparison of difference magnitudes, we calculated relative differences  $M_i$  (Figure 4c) over time by multiplying the differences  $D_i^{\text{proc}} - R_i^{\text{proc}}$  with the inverse envelope (reflection strength) sections of  $R_i^{\text{proc}}$ . To avoid overinterpreting energy differences in low-reflectivity regions, we defined a minimum amplitude threshold for the envelope sections of  $R_i^{\text{proc}}$ . Generally, the relative difference magnitudes vary smoothly between time lapses. The largest changes occur during the first few time lapses following the tracer injection and the signal generally returns toward zero at the end of the experiment (not shown). For experiments Ia and Ib it was necessary to further reduce the ambient noise level prior to migration (mapping data from time to distance from borehole) by applying a conservative f-x deconvolution (prediction filter in distance for each frequency) and subtracting a running median trace (Figure 4d; processing steps in brackets in Figure 3).

[23] Prestack Kirchhoff depth migration based on the 1-D velocity function of *Dorn et al.* [2012] made it possible to migrate  $M_i$  with minimal smearing or other artifacts (Figure 4e). Migration of difference sections is possible due to the linearity of migration with respect to the input wavefield term, which makes the final migrated sections comparable to migrated GPR sections [*Dorn et al.*, 2011]. The unmigrated difference sections  $M_i$  (Figure 4c) contain significant ambient noise at  $t > 130$  ns, but the destructive superposition of ambient noise energy during migration significantly decreases the presence of incoherent events in the migrated images.

### 3. Results

#### 3.1. Tracer Test Data

[24] Figure 5 shows the measured electrical conductivities in the pumping borehole during the course of each experiment (interpolated from data logs with a depth sampling of  $\Delta z < 0.2$  m and a time sampling  $\Delta t \approx 10$  min,  $\Delta t \approx 5$  min for experiment IIIb). The columns shown to the right of each plot are the electrical conductivities acquired following overnight pumping. The flow and associated transport in the boreholes are directed upward partly due to the natural upward gradient, but mainly because we pump at the top (except for experiment IIIa when the overnight pumping became weak and eventually stopped resulting in tracer accumulation at the bottom of the borehole).

[25] The variations of electrical conductivity in time and space can be used to identify tracer and freshwater outflow zones by identifying those locations in which the electrical conductivity varies sharply in the vertical direction over extended time periods. These zones highlighted in Figure 5 correspond to open fracture locations in the optical logs; most of them identified by *Le Borgne et al.* [2007]: (1) B1–44, B1–50, B1–60, and B1–78 and (2) B2–49, B2–52, B2–55, B2–58, and B2–79. In experiments IIIa and IIIb, the location of the tracer outflow zone at the lower boundary of the observed depth interval (B1–78; see Figures 5d and 5e) is inferred from flowmeter data, as this is the only permeable zone below the observation interval. In order to

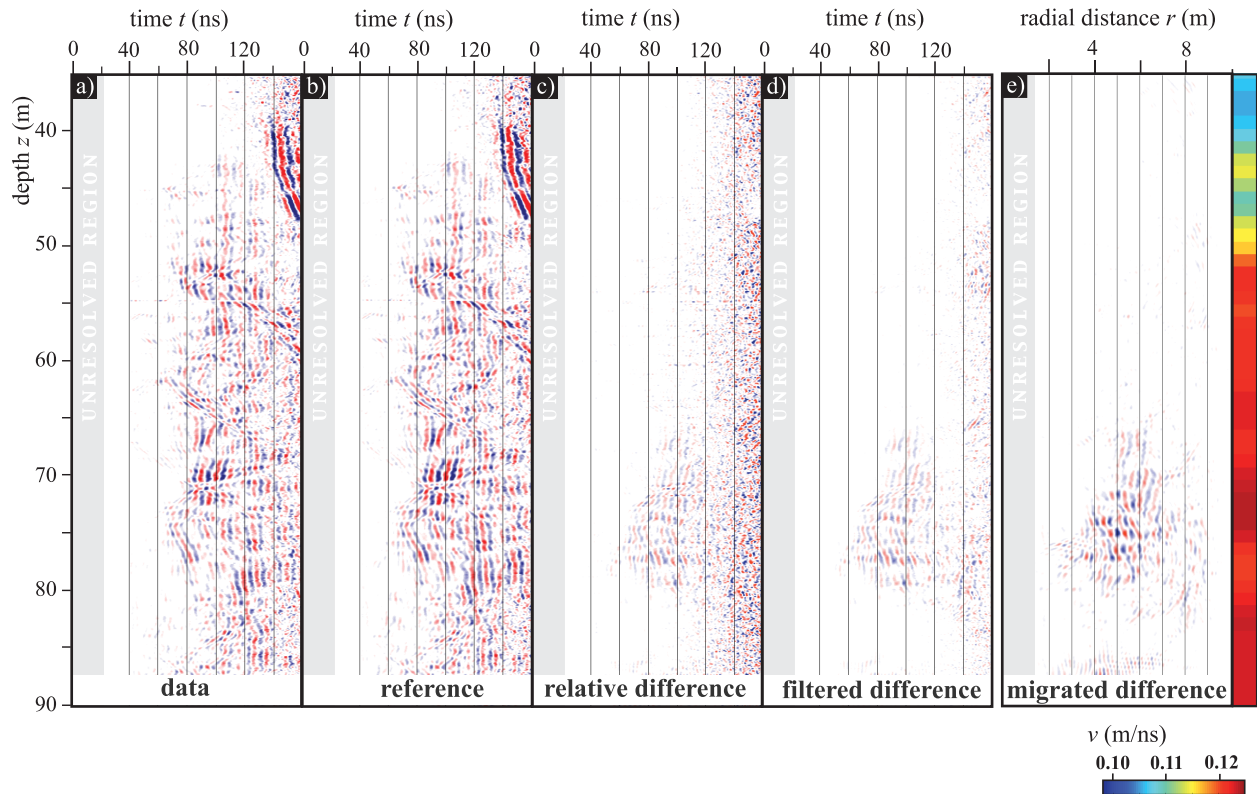


**Figure 4.** Results of data processing applied to a single-hole GPR data section of experiment Ib acquired after saline tracer injection at  $z = 78.7$  m ( $t^{obs} = 45$  min, 4 m antenna offset). (a) Data and (b) reference section after preprocessing. (c) Relative difference between Figures 4a and 4b normalized by the envelopes of Figure 4b. (d) As in Figure 4c, but after f-x deconvolution to remove noise. (e) As in Figure 4d, but after depth migration using the velocity model shown to the right of the migrated difference. The axis aspect ratio  $r:z$  is 2:1.

identify the actual fractures through which tracer outflow occurs, we normalized the electrical conductivities (Figure 5) by the vertical flow distribution (Figure 6) of the fractures. In fact, some outflow zones do not carry significant amounts of tracer (see fractures B2–49 and B2–52 in Figures 5a and 5b, B2–58 and B2–79 in Figure 5c, and B1–44 and B1–52 in Figures 5d and 5e) and the tracer outflow zones B2–49 and B2–52 (experiment II) were not detected in the flowmeter data analysis of *Le Borgne et al.* [2007].

[26] The peak electrical conductivities in the pumping borehole reach  $\sim 5\%$  of the injected tracer conductivity, except for experiment II where we observe only  $\sim 2.5\%$ . Such low percentages are due to (1) dispersion of the solute within the fractured media, (2) the pumping of fresh water that mixes with the saline water within the pumping borehole and (3) the influence of the ambient flow regime that may lead to tracer mass loss.

[27] To estimate the curves of mass recovered at each individual fracture, we subtracted the estimated mass flux in the borehole below the fracture from the estimated mass flux above. When converting concentrations to mass rates, we accounted for the monitored, but rather unstable pumping rates (see Table 1), and available flowmeter data (Figure 6) that provide the relative contribution to flow of each outflow zone. To obtain the local mass recovery

estimates, we then integrated the fracture-specific solute fluxes during the course of the GPR monitoring. The local mass recoveries should be analyzed with some caution as (1) the pumping rates and flow partitions between fractures are not perfectly known and (2) electrical conductivity logs acquired within the first 3–5 h following the tracer injections do not capture the whole tail of the tracer breakthrough.

[28] The derived fracture-specific curves of solute fluxes show very different characteristics for each type of tracer experiment (Figure 7):

[29] 1. For experiments Ia and Ib (Figures 7a and 7b), the tracer injected in B1–78 arrives after 20 min in B2–79. Additional tracer arrival occurs after 30 min in B2–55 and B2–58 (subtle increase of salinity). Nearly half of the recovered mass comes from B2–79, while  $\sim 40\%$  of the recovered mass arrives at B2–55. After the main peak at  $t^{obs} = \sim 45$  min at B2–79, there is a second peak in the solute flux curve after  $\sim 90$  min. At the end of the experiment, the total mass recovery is  $\sim 25\%$  for both experiments.

[30] 2. For experiment II (Figure 7c), the tracer injection in B1–50 gives after 30 min rise to tracer breakthrough in B2 at B2–49 and B2–52. Additional tracer arrival occurs after 60 min in B2–55 and a very small amount of tracer arrives after 2.5 h in B2–58. The fracture B2–49 contributes

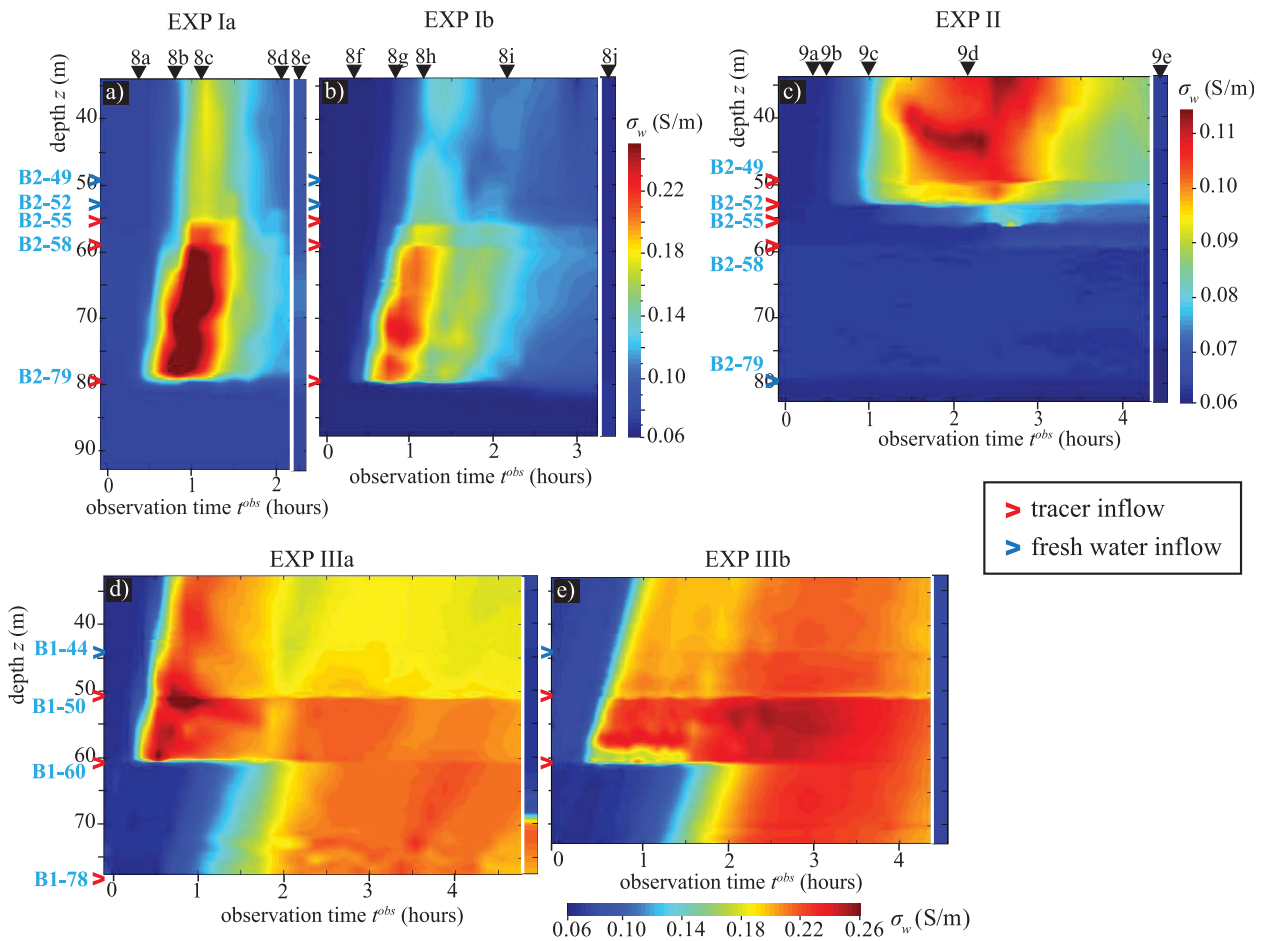


**Figure 5.** Electrical conductivity  $\sigma_w$  in the pumping borehole during experiments (a) Ia, (b) Ib, (c) II, (d) IIIa, and (e) IIIb. The values of  $\sigma_w$  the day after saline injections are shown in separate columns to the right of the plots. Black triangles mark the acquisition times of the conductivity profiles shown in Figures 8 and 9. The red arrowheads indicate locations with interpreted tracer inflow, while the blue arrowheads indicate inflow locations that are unaffected by the saline injections.

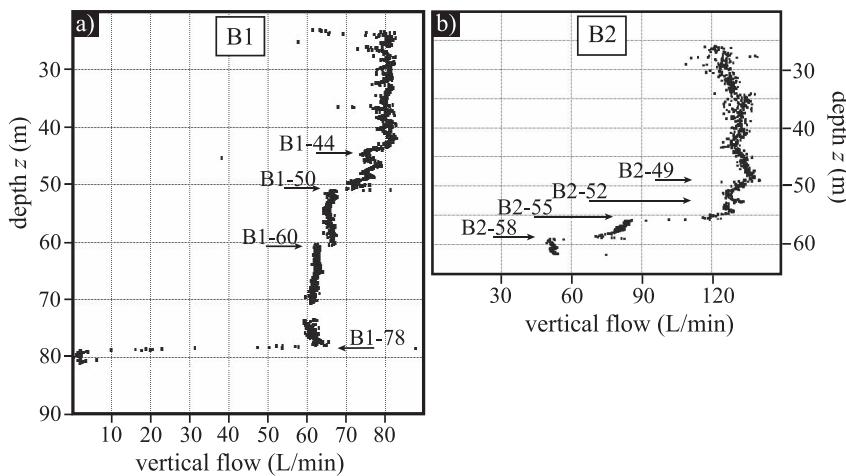


**Figure 6.** Induced vertical flow due to pumping in (a) B1 with  $82 \text{ L min}^{-1}$  and in (b) B2 with  $138 \text{ L min}^{-1}$  measured with an impeller flowmeter. All flow below  $z = 60 \text{ m}$  in B2 stems from fracture B2-79 at  $z = 79.3 \text{ m}$ . Arrows indicate the locations of interpreted permeable fractures.

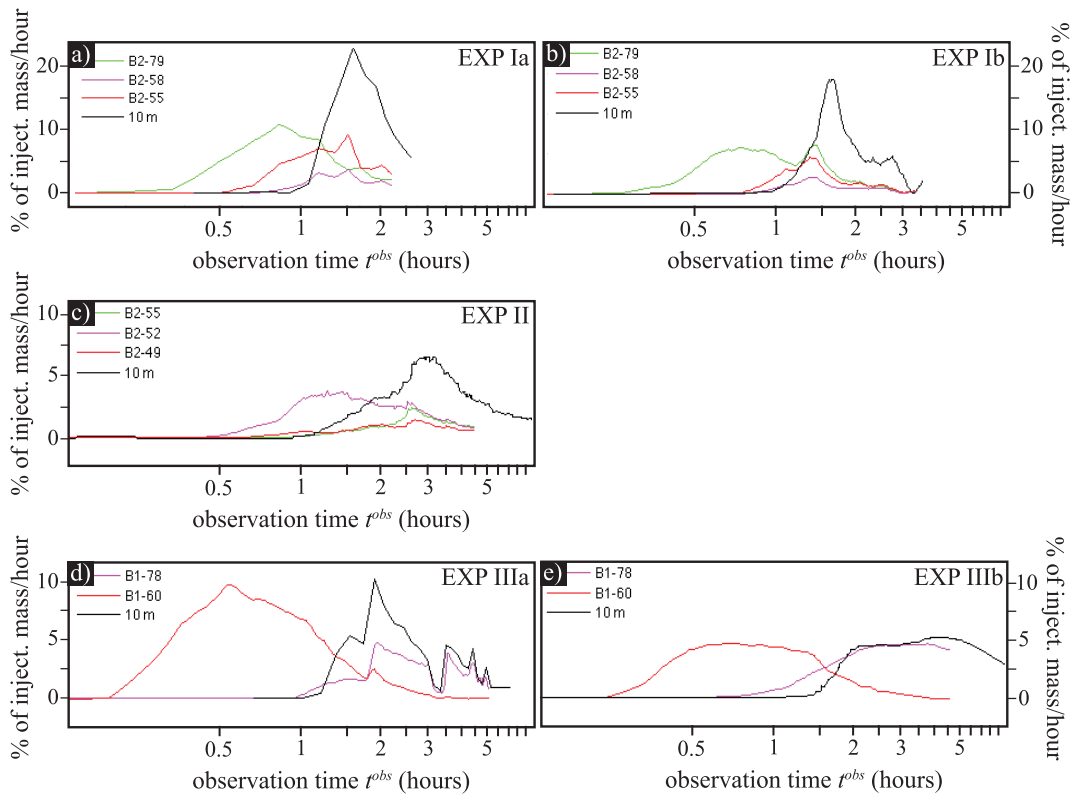


**Figure 7.** Local salt solute flux curves estimated at depth locations with significant tracer arrival (colored lines) and below the pump ( $z = 10$  m, black line) normalized by the injected amount of tracer mass for experiments (a) Ia, (b) Ib, (c) II, (d) IIIa, and (e) IIIb.

with  $\sim 20\%$  of the recovered mass, the largest contribution to the total mass ( $\sim 50\%$ ) comes from B2–52. None of these two fractures were detected by *Le Borgne et al.* [2007]. About  $\sim 20\%$  of the recovered mass arrives at B2–55. The estimated total mass recovery of salt after overnight pumping is  $\sim 30\%$ .

[31] 3. For experiments IIIa and IIIb (Figure 7d and 7e), the tracer injection in B2–55 gives after only 10 min rise to tracer breakthrough in B1–60. Within the first 2 h,  $\sim 40\%$  of the recovered tracer mass arrives at this fracture. After 1 h, tracer arrival occurs in B1–78, where  $\sim 60\%$  of the total mass is recovered. The total mass recovery at the end of the GPR acquisition experiment is  $\sim 20\%$  for experiment IIIa and after overnight pumping  $\sim 30\%$  for experiment IIIb.

[32] In summary, (1) the estimated solute fluxes from the outflow zones in the pumping borehole are the result of several different fractures or pathways; (2) the mass recoveries are generally relatively low, which we attribute to the ambient flow regime, density effects and the injection conditions.

### 3.2. Single-Hole GPR Data and Difference Imaging

[33] Figures 8 and 9 show, for each of the experiments Ia, Ib, and II, five migrated GPR relative-difference sections acquired at different times plotted on top of the migrated GPR sections of *Dorn et al.* [2012]. These images represent changes in reflection amplitudes in a 2-D projection around the borehole (i.e., depth  $z$  and radial distance  $r$ ) with respect to background conditions. Note that the GPR

difference images have a large imprint of the finite source signal. This implies that the fractures in which salinity changes occur are located where the first arriving energy of the reflection wave trains are observed. Figure 10 highlights the reflections in the background images that correlate to the high-magnitude patterns in the difference sections (Figures 8 and 9).

[34] Patterns of high magnitudes have predominantly subhorizontal to vertical dips ranging from  $30^\circ$  to  $90^\circ$  (relative to the surface) covering radial distances  $r = 2$ – $10$  m from the pumping borehole. It is not possible to resolve features for  $r < 2$  m due to the very high direct wave amplitudes in the corresponding time interval that completely mask the much smaller reflection amplitudes. Subhorizontal patterns show overall weaker amplitudes than subvertical patterns, which can be attributed to the high angle of incidence to the fracture surface. Difference patterns close to the injection point are predominantly imaged with high magnitudes at early times  $t^{\text{obs}}$  (Figures 8a, 8f, and 9a). At depths different than the injection point, patterns with typically weaker amplitudes appear at later  $t^{\text{obs}}$  and are generally visible for longer time periods. Patterns of evolving difference magnitudes can generally be traced from the injection points through depth intervals ranging over some tens of meters. The GPR difference images in Figures 8 and 9 are discussed in detail below together with some of the trends observed at the many intermediate observation times that are not shown (see Table 1).

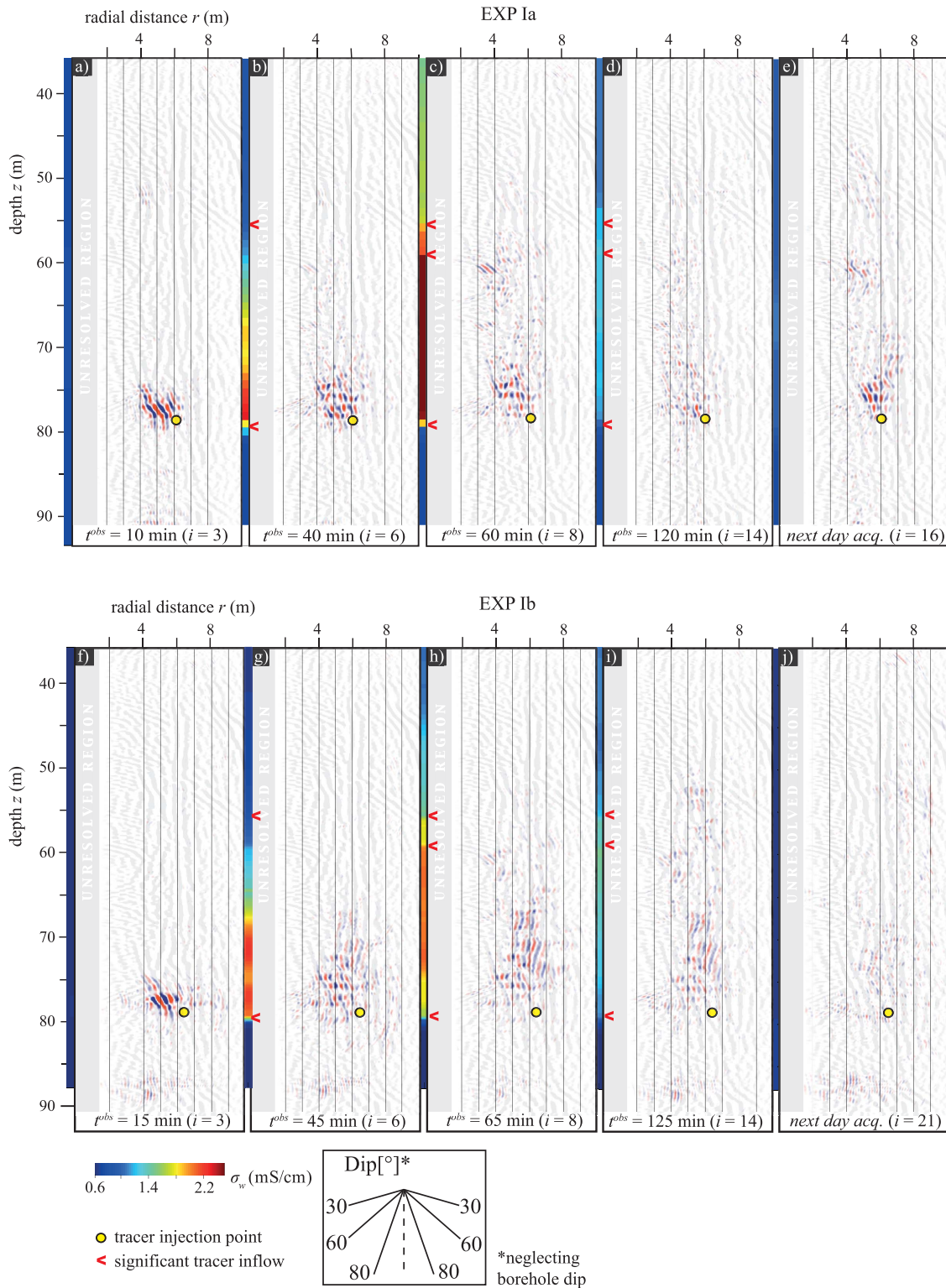


**Figure 8.** Migrated relative difference GPR sections acquired in B2 during (a–e) experiment Ia and (f–j) experiment Ib at different observation times  $t^{obs}$ , superimposed on the gray opaque migrated GPR section acquired under natural flow conditions [Dorn et al., 2012]. High-difference patterns originate from increased salinity in fractures located at the front of each such pattern (i.e., the smallest radial distance  $r$  for each depth  $z$ ). Note that we do not image any features at  $r < 1.5$  m (gray region) because of the dominance of the direct wave at early times and its subsequent removal, which tends to remove superimposed reflections at early times. The corresponding electrical conductivities  $\sigma_w$  of the borehole fluid in B2 are shown in the color profile at  $r = 0$  m.

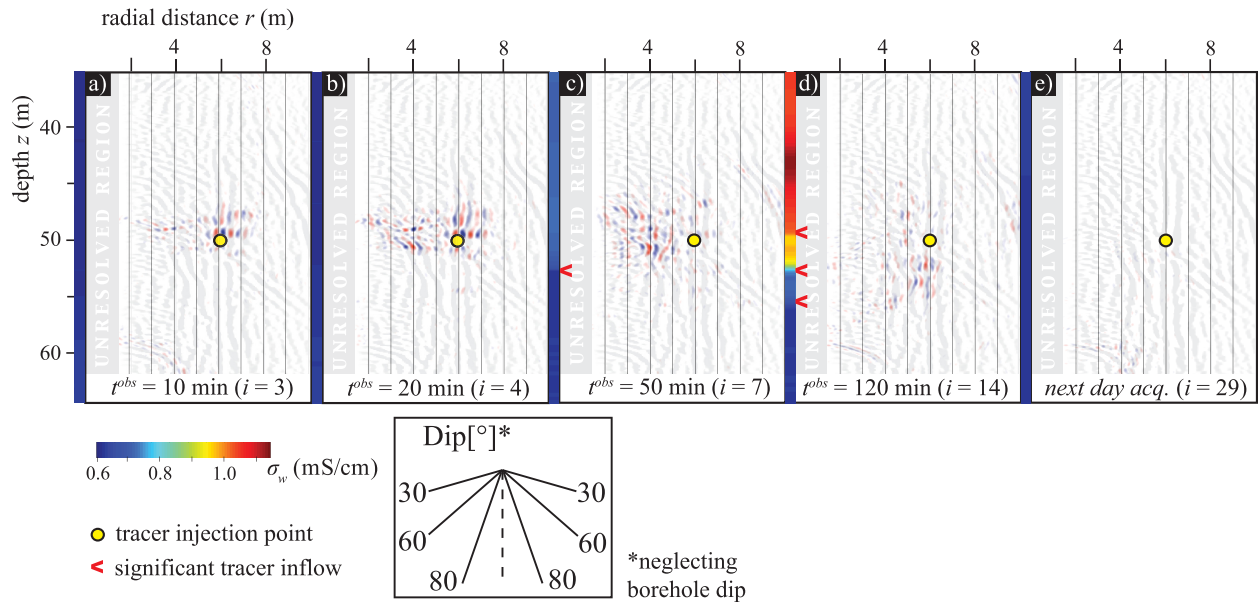


**Figure 9.** Migrated relative difference GPR sections acquired in B2 during experiment II at different observation times  $t^{\text{obs}}$ , superimposed on the gray opaque migrated GPR section acquired under natural flow conditions [Dorn *et al.*, 2012]. The corresponding electrical conductivities  $\sigma_w$  of the borehole fluid in B2 are shown in the color profile at  $r = 0$  m.

### 3.2.1. Experiments Ia and Ib

[35] The main difference in experimental design between experiments Ia and Ib is that we did not push the injected tracer with groundwater in experiment Ib after the end of the tracer injection. During tracer injection, pumping conditions were similar for both experiments. We expect significant differences for the tail of the solute flux curves if we push the tracer with groundwater or not, but less for the mean arrival times that are similar for the two experiments (Figures 7a and 7b). The spatial distributions of the GPR magnitude patterns and their evolution over time are similar for the two experiments (Figure 8; the difference amplitudes are plotted with the same scale in all plots). At early times (Ia:  $t^{\text{obs}} = 10$  min, Ib:  $t^{\text{obs}} = 15$  min; Figures 8a and 8f), a single high-magnitude pattern is visible at  $z = 75$ – $80$  m indicating an upward movement of the tracer from the injection point toward the pumping borehole. At later  $t^{\text{obs}}$  (Figures 8b, 8c, 8g, and 8h), new magnitude patterns with dips between  $40^\circ$  and  $80^\circ$  show up in this depth region. The magnitudes get weaker with time and patterns start to appear at shallower depths (up to  $\sim 50$  m depth). Two hours after injection, magnitude patterns for experiment Ia appear patchy and weak (Figure 8d), while for experiment Ib they are continuous and moderate in amplitude (Figure 8i). The next day acquisition for experiment Ia (Figure 8e) does not show weak and random amplitudes as experiment Ib (Figure 8j), but a region of moderate amplitudes above the injection point. These remaining amplitudes are partly attributed to unstable overnight pumping.

[36] By overlaying the difference images on the migrated GPR sections of Dorn *et al.* [2012], we find at least 9 fractures through which the tracer solution likely moved (highlighted fractures in Figure 10a). Close to the injection point there are three prominent fractures through which the tracer

moves upward (dipping  $70^\circ$ ,  $75^\circ$  and  $80^\circ$  between  $r = 3.5$  and 7 m). The imaged magnitude pattern close to the pumping borehole at  $r = 2$ – $4$  m and  $z = 76$  m, which is dipping  $40^\circ$  is most likely related to the fracture through which the tracer flows into the pumping borehole in B2–79 (Figures 7a, 7b, and 8a). Between  $z = 50$  and 70 m, the tracer solution moves through at least 4 more fractures, but the connections between these fractures are not always clearly imaged. Most probably, fractures outside of the detection range (with respect to dip and azimuth) carry some of the tracer. Even though tracer arrival at  $z = 79.3$  m has been imaged, it is clear from the difference images that the tracer mainly moves upward through a network of connected fractures. This upward movement corresponds well with the later arriving tracer in B2–55 and B2–58 as shown in Figures 5a and 5b. The fractures carrying the tracer into the borehole in this depth interval are probably not imaged because of the low dips. In fact, optical logs indicate dips of  $33^\circ$  and  $31^\circ$  for these fractures.

[37] We attribute the less patchy and stronger relative difference magnitudes in experiment Ib to the tracer solution being spatially more contained compared with experiment Ia. The pushing of the tracer in experiment Ia might have partially pushed the tracer in other directions than the pumping borehole B2, and therefore increased the spreading of the tracer. The overall similarity of the two sets of difference images representing experiment Ia (Figures 8a–8e) and experiment Ib (Figures 8f–8j) makes us confident (considering experimental differences) that the experiments are generally repeatable and the processing scheme can handle the majority of the experimental uncertainties. Furthermore, the dips and locations of the patterns correlate well with previously imaged fractures using multioffset single-hole data [Dorn *et al.*, 2012] and hydrogeological studies

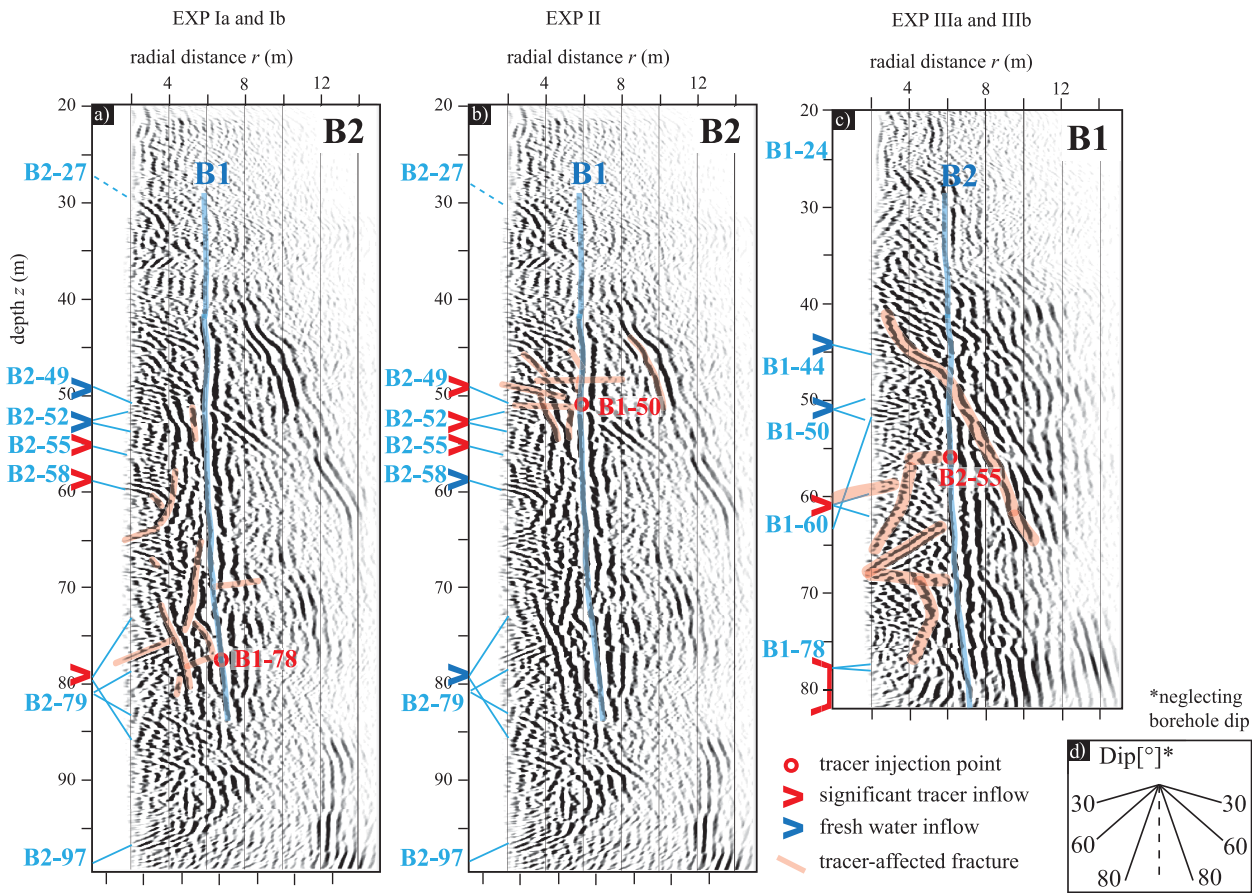


**Figure 10.** Extracts of the migrated multi-offset single-hole GPR sections of B1 and B2 from *Dorn et al.* [2012] with superimposed interpretations of tracer pathways for experiments (a) Ia and Ib, (b) II, and (c) IIIa and IIIb. Red circles indicate the tracer injection points, while red and blue arrowheads locate saline and unaffected groundwater inflow into the pumping borehole, respectively. Light red regions highlight fractures through which the injected tracer is interpreted to move, whereas blue regions highlight reflections from other boreholes. Light blue letters refer to transmissive fractures identified in the boreholes using optical logs and flowmeter tests with corresponding blue lines indicating their corresponding dips [Le Borgne *et al.*, 2007]. (d) Dip angles corresponding to the axis aspect ratio  $r:z$  of 2:1.

[Le Borgne *et al.*, 2007]. It appears thus that we can identify the main tracer-occupied fractures by superimposing migrated relative difference sections on the migrated multi-offset single-hole GPR data. Nevertheless, the interpretation must consider many intermediate acquisition times to assure that interpreted features are not related to processing artifacts. The interpretation shown in Figure 10a is based on careful analysis of the 16–21 difference images obtained for each experiment (see Table 1).

### 3.2.2. Experiment II

[38] The migrated difference images from experiment II (Figure 9) show complex magnitude patterns of superimposed reflections that are limited to the depth range of  $z = 45\text{--}60$  m. The superposition of different signal contributions and the shallow dips of the fractures through which the tracer appears to move make it very difficult to trace magnitude patterns related to individual fractures. One well-resolved feature is the spatially compact high-amplitude pattern above and behind the injection point that is visible at

early times  $t^{\text{obs}} < 50$  min ( $z = 47\text{--}50$  m and  $r = 5.5\text{--}7.5$  m in Figures 9a and 9b). Polarity changes are found at successive observation times at  $z = 49$  m (Figures 9a and 9b), which appear to cut horizontally through this subvertical reflectivity pattern. Rather complex weak-to-high magnitude patterns at smaller radial distances are also seen in Figures 9a–9c. At  $t^{\text{obs}} > 50$  min, weak magnitudes appear at  $r = 9\text{--}10$  m in the depth range  $z = 45\text{--}48$  m. After 2 h, the magnitude patterns between the injection and pumping boreholes in the depth range  $z = 45\text{--}52$  m have weakened considerably and the remaining magnitudes are mostly concentrated in a region below the injection point (Figure 9d). The data acquired on the following day does not show any significant remaining relative difference magnitude patterns, thereby indicating that most of the tracer has left the observable region.

[39] The small differences between the tracer injection depth in B1 ( $z = 50.9$  m) and the outflow depths in B2 ( $z = 49\text{--}58.9$  m) makes the GPR interpretation difficult as it suggests that flow paths are rather subhorizontal. We find that

the difference patterns are largely limited to a region in between the injection and pumping borehole covering a similar depth interval as the outflow locations. The pattern that is imaged close to the pumping borehole (dipping  $30^\circ$ ) around  $z = 48$  m is likely related to B2–49 at which the tracer arrives in the borehole. The polarity changes discussed above are also observed in the migrated GPR sections of *Dorn et al.* [2012]. They might originate from nearly horizontal reflection boundaries in between the boreholes. We have been conservative in interpreting these polarity changes in the difference images as possible tracer transport paths and only indicated one where we could correlate it to the GPR sections by *Dorn et al.* [2012] (see Figure 10b). A possible explanation for the low mass recovery of this experiment is that this horizontal fracture at  $z = 48$  m that can be traced over  $r = 4$ –10 m carried the tracer away from the injection point to a larger subvertical fracture zone located at larger radial distance ( $r = 9$ –10 m) at  $z = 45$ –50 m.

### 3.2.3. Experiments IIIa and IIIb

[40] Experiments IIIa [*Dorn et al.*, 2011] and IIIb (not shown due to strong similarity with the results of experiment IIIa) indicate a strong influence of the natural gradient. By interpreting the overlaid images, we observe at least 6 tracer-occupied fractures (Figure 10c), including a large fracture zone covering a wide depth interval of  $z = 40$ –65 m [cf. *Dorn et al.*, 2011]. The saline tracer quickly moves down through two fractures dipping  $50^\circ$  and  $75^\circ$ . The tracer arrives in the pumping borehole through fracture B1–60. Tracer arrivals at greater depths cannot be inferred by our difference images alone as the tracer outflow occurs close to the bottom of the pumping borehole. It is likely that fracture B1–78 carries the tracer to the borehole. This fracture appears to be directly connected to the fractures we observe at  $z > 70$  m in experiments Ia and Ib (Figure 10a).

[41] The results in this section clearly demonstrate that the GPR difference patterns are related to transport within connected fractures. Evidence for this is given by the gradual spreading of the GPR difference patterns away from the injection point (Figures 8 and 9 and *Dorn et al.* [2011, Figure 1]), the similarity of the inferred patterns for repeat experiments that include the same injection fracture (experiments Ia and Ib in Figure 8; experiments IIIa and IIIb (not shown)), and an overall agreement between the timing of the depth intervals experiencing temporal changes in the GPR images (Figures 8 and 9 and Figure 1 of *Dorn et al.* [2011]) and the arrival of saline tracer at the outflow locations (Figure 7).

## 4. Comparison of GPR Reflection Sections With Tracer Transport Modeling

[42] In this section, we investigate in a more quantitative manner the agreement between tracer transport and the GPR difference sections. To do so, we calibrate a fracture model representing experiment Ib using a simplified three-fracture model that only models the main features of the observed mass flux curve in Figure 7b. This 3-D model (with 2-D flow in each fracture) is simplistic in that it (1) ignores the azimuths of the fractures, (2) it merges several connected fractures in one large fracture, (3) no heterogeneities of the fractures are considered except for classical dispersion parameters, (4) no density effects are considered,

and (5) the natural gradient is ignored. This presented model is clearly very simplified, but it is useful to assess if changes in the difference sections at chosen locations are consistent with the simulated tracer distributions. We investigate below if discrepancies between the inferred curves are similar to those observed for the simulated and observed solute transport at the outflow locations. If this is the case, we argue that the resulting GPR-inferred reflectivity changes can be used to derive semiquantitative breakthrough curves at locations between the boreholes.

[43] The map of interpreted tracer pathways (Figure 11a) for experiment Ib is used as a basis to define continuous transport pathways between injection and outflow locations (Figure 11b). The model in Figure 11c combines the three transport pathways in Figure 11b into three fractures. The distances between outflow and injection locations are inferred from Figure 11b. The sketched 3-D fracture planes in Figure 11c are modeled with an aperture of 1 mm and an extension of  $\pm 100$  m in the out-of-plane dimension. We modeled flow and transport using COMSOL Multiphysics 3.5 using a finite element mesh with 6200 elements. We solve Darcy's law with the observed time-varying head boundaries in the pumping well for the tracer arrival locations (Figure 11e) and use mixed boundary conditions at the injection location (the observed fixed head during the injection period and zero flow conditions afterward). The edges of the fractures are modeled as zero head boundaries. Using the calculated velocity field, we solve the advection-dispersion equation assuming a constant concentration at the injection location during the injection period. The free fitting parameters are hydraulic conductivities, dispersivity and the concentration as a fraction of the actual injected concentration. The latter allows us to partly consider mass loss and to fit the magnitudes of the observed solute fluxes.

[44] The effective parameters for the three fractures were obtained by manual calibration aiming at fitting the first arrival times and the peak solute fluxes at  $t^{\text{obs}} \sim 1.4$  h. An automatic calibration procedure based on a Levenberg-Marquardt algorithm was also used, but did not provide significantly better results. It is clear that the simulated curves in Figure 11d (dotted lines) only represent some of the main characteristics of the measured curves (solid lines), which makes the estimated transport properties rather approximate. The derived effective hydraulic conductivities are  $K_1 = 0.6 \text{ m s}^{-1}$ ,  $K_2 = 2.3 \text{ m s}^{-1}$  and  $K_3 = 0.2 \text{ m s}^{-1}$  and the dispersivities are  $\alpha_1 = 0.6 \text{ m}$ ,  $\alpha_2 = 0.3 \text{ m}$  and  $\alpha_3 = 0.2 \text{ m}$ . The fitted curves underestimate mass fluxes at early arrival times and overestimate them after peak arrivals. Fluctuations in the pressure conditions significantly influence the shape of the modeled flux curves, for example, by reproducing observed peaks at  $t^{\text{obs}} \sim 1.4$  and 2.3 h (Figure 11e).

[45] The resulting concentration fields were used to calculate how the simulated tracer distributions affect GPR reflectivity. This analysis is based on local tracer concentrations that correspond to the three locations highlighted in Figure 11b (green highlighted letters). The concentrations are mapped into  $\sigma_w$  values that we relate to variations of reflection coefficients of thin-layer reflectors using the expression of *Deparis and Garambois* [2009] under the assumption of a normal incidence wave.

[46] Reflectivity strengths from the GPR difference sections are retrieved at each depth location by picking the

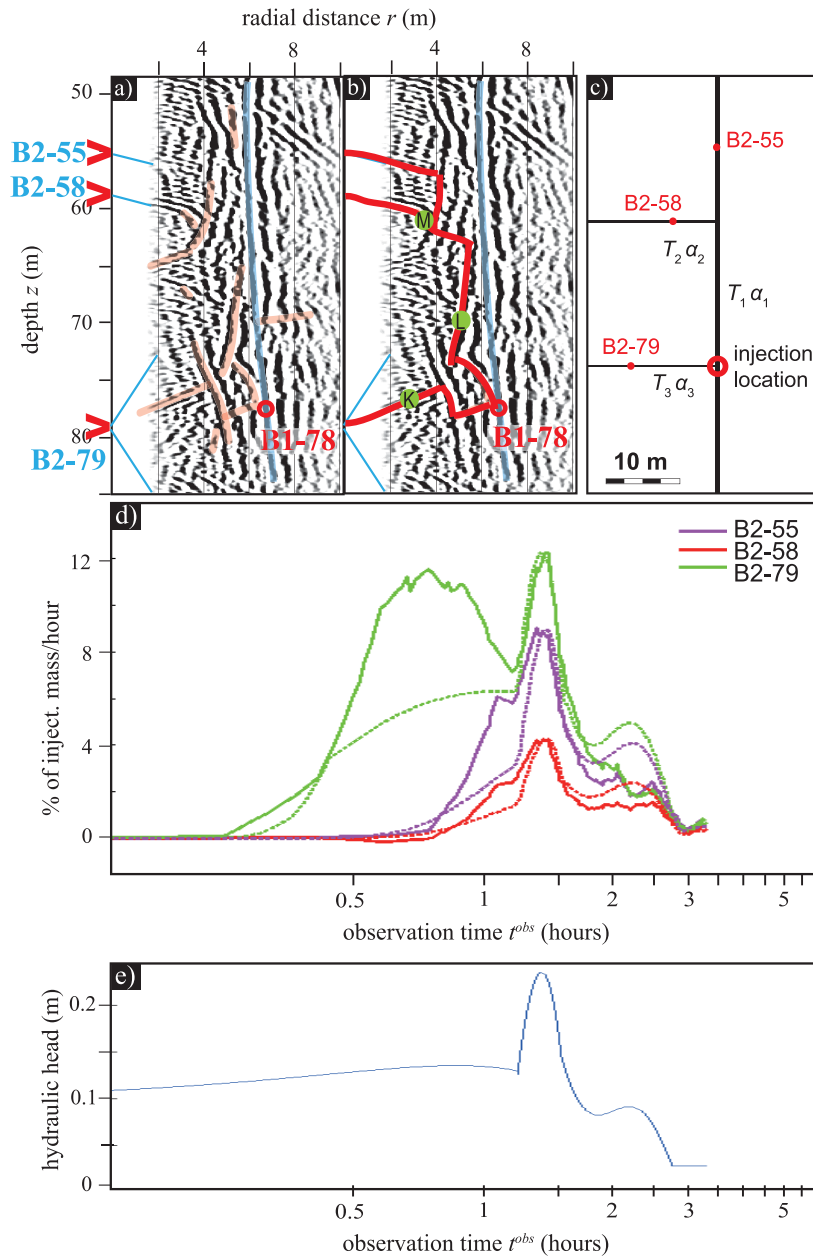


**Figure 11.** Transport model and modeling results for experiment Ib based on a simplified 3-D fracture model with three intersecting rectangular fracture planes with an aperture of 1 mm. (a) Extract of Figure 10a, on which we assign (b) three continuous transport pathways between injection and outflow locations. Letters K-M in Figure 10b refer to the positions considered in Figure 12. (c) Graph representing a simplified representation of the pathways in Figure 10b used in the transport model to estimate effective hydraulic conductivities  $K$  and dispersivities  $\alpha$ . (d) Observed (solid lines) and simulated (dashed lines) local salt flux curves at outflow locations B2-55, B2-58, and B2-79. The derived transport parameters are  $K_1 = 0.6 \text{ m s}^{-1}$ ,  $K_2 = 2.3 \text{ m s}^{-1}$ ,  $K_3 = 0.2 \text{ m s}^{-1}$ ,  $\alpha_1 = 0.6 \text{ m}$ ,  $\alpha_2 = 0.3 \text{ m}$ , and  $\alpha_3 = 0.2 \text{ m}$ . (e) Hydraulic head used for the boundary conditions at the three outflow locations.

maximum value around the chosen location (marked by letters K-M in Figure 11b). Figure 12 plots the time evolution of these picked reflectivity strengths (asterisks, normalized to the maximum of its fitted second order polynomial) and the estimated reflection coefficients from the simulated concentrations (solid line, normalized to the maximum

value). Note that both estimates have been averaged over a 1 m large zone at each location.

[47] Figure 12 illustrates that the times at which reflection strengths rise are overall similar for the two estimates. The earliest rise of the reflection strengths are observed for region K (6 m away from the injection point), which is

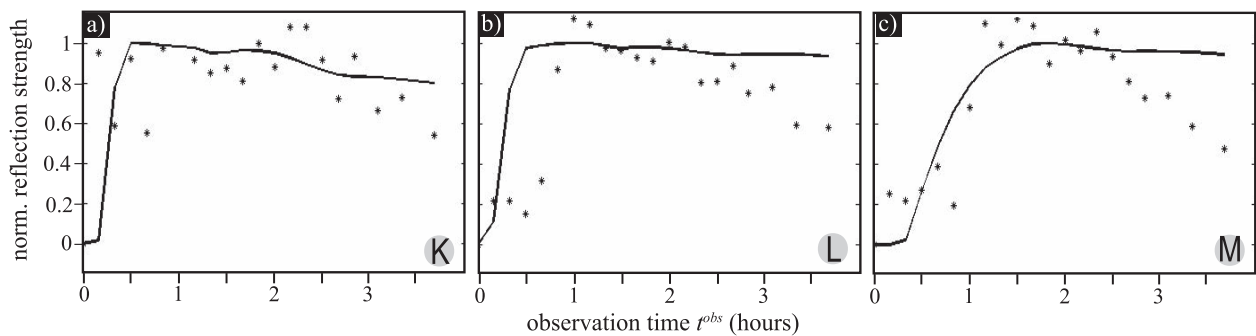


**Figure 12.** Time evolution of normalized reflectivity changes with respect to reference conditions observed in the GPR difference images (asterisks) and calculated from simulated tracer distributions (solid line) corresponding to locations (a) K, (b) L, and (c) M in Figure 11b. At each location, we average the data over 1 m, but there is no smoothing over time.

consistent with the observed breakthrough data in that the first arriving mass is found along this flow path. Reflection strengths are found to rise earlier in region L than in region M, which is consistent with their distance to the injection location (L is 8 m and M is 19 m away from the injection location). The main discrepancy between the curves is that the picked reflection strengths from the GPR difference images start to go down after  $\sim 1$ – $2$  h, which is not seen in the simulated reflectivity coefficients based on transport modeling, except for position K (Figure 12a). This is consistent with the discrepancy evoked earlier between the simulated and observed solute fluxes in Figure 11d. Indeed, the simulated tracer concentration stay relatively high at the end of the simulations, while both the GPR data and the estimated solute fluxes at the outflow locations indicate that the tracer concentration goes down significantly after the peak arrival.

[48] The results in Figure 12 provide evidence that the amplitude changes in the GPR data are directly related to concentration changes within the fractures, which implies that we can obtain relative breakthrough curves for locations between the observation boreholes. Absolute breakthrough curves would require more precise knowledge of the GPR source signal or alternatively a calibration of the radar reflected amplitudes to controlled tracer concentrations as done by *Becker and Tsofiias* [2010]. Another striking aspect of Figure 12 is that the picked reflectivity strengths vary relatively smoothly over time. The fact that there is no smoothing applied to the GPR-inferred reflectivity changes over time gives confidence that the GPR data provide information about solute transport at locations within the formation.

## 5. Discussion

[49] The GPR difference amplitude images presented in this work (Figures 8 and 9) and by *Dorn et al.* [2012] provide useful complementary information to classical breakthrough data. Although each method has its limitations, we argue that their combination have a high potential to improve characterization and lead to new insights about tracer transport in fractured media. The main limitations are as follows: (1) breakthrough data provide integrated responses between injection and observation points, (2) the

GPR data do not provide information about the region in the intermediate vicinity of the pumping borehole, and (3) the GPR data are only 2-D projections imaging those parts of the local fracture planes that have a favorable orientation with respect to the acquisition geometry, and they do not provide information on the azimuth of fractures.

[50] For all tracer injection experiments, we find that multiple transport paths carry the tracer between the injection point and the pumping borehole. This is seen already by considering the distribution of mass rates along the borehole (Figure 7), but the GPR difference images offer a more complete view of fracture connections and transport pathways between the two boreholes (Figures 8 and 9 and *Dorn et al.* [2011, Figure 1]). In all experiments, we find that the depth intervals and the timing of the GPR magnitude patterns agree well with the calculated mass rates. We see similarly located magnitude patterns in experiments Ia and Ib (Figure 8), as well as in experiments IIIa and IIIb (not shown). The patterns appear at slightly different times due to differences in the experimental setup (e.g., in terms of the pumping and injection rates). The similarities of the two sets of difference images obtained from repeat tests using the same fracture for injection make us confident that the experiments are repeatable and the processing scheme is robust. Our results suggest that it is possible to identify the main tracer-occupied fractures over time by superimposing migrated relative difference sections on the migrated GPR sections from B1 and B2 acquired under natural flow conditions [*Dorn et al.*, 2012]. When comparing these images, it seems that the most prominent fractures imaged by *Dorn et al.* [2012] also carry tracer in the saline tracer experiments. The GPR difference images provide us with a plausible explanation about where the unaccounted mass went. For the experiments presented herein, it seems that most of the missing mass was transported from the injection point in a direction away from the pumping boreholes and the observable region, while some storage or delay in less mobile zones may have occurred.

[51] When interpreting these results, it is important to consider that the GPR relative difference images provide an incomplete description of tracer movement as the fracture azimuth is unresolved, but also because certain fractures that carry tracer will not be imaged. These include small-scale fractures (i.e., with a fracture surface smaller

than about the first Fresnel zone (0.6 m at  $r = 2$  m and 2 m at  $r = 20$  m)), fractures with subhorizontal dips, fractures with an unsuitable azimuth, and fractures located close to the boreholes. We observe dips of fractures at all detectable angles (considering that only dips between  $30^\circ$ – $90^\circ$  are detectable), the most common dip being around  $30^\circ$ . The recorded GPR difference amplitudes are surface-averaged measures (over the first Fresnel zone) of electromagnetic contrasts, which imply that the difference images have a limited sensitivity to tracer dispersion within a single fracture. Still, in fractures that are imaged in the difference sections it is very likely that spreading within the fractures occur at least on the meter scale.

[52] Differences in the experimental setup lead to observable differences in the temporal and spatial dynamics of the tracer transport. First of all, the pathways but also the ratios between the imposed heads and the upward natural gradient differ: In experiments Ia and Ib with an injection rate on the order of the natural gradient, the tracer moves upward and spreads over tens of meters (Figures 8 and 10a), in experiment II with again an injection rate on the order of the natural gradient, the tracer moves subhorizontally (Figures 9 and 10b); and in experiments IIIa and IIIb where the injection head is roughly three times stronger than the natural gradient, the tracer moves partly downward and spreads over tens of meters (Dorn *et al.* [2011, Figure 1] and Figure 10c). We observe multiple peaks in the solute flux inferred at different fracture locations (e.g., in B2–79 at  $z = 79.3$  m for experiments Ia and Ib, Figures 5a and 5b) that are attributed to variations in the pumping rates as we see similar behavior in the simulated breakthrough curves of experiment Ib (Figure 11d).

[53] For our experimental setup we have to note that the relative contributions to flow and mass of a given fracture depend on overall connectivity with the permeable fracture network, whereas the mass contribution depends on the local connections with the injection fracture. In experiment II, most of the mass arrives through a fracture that does not contribute significantly to flow (in B2 at  $z = 52.7$  m). In fact, this fracture was not even identified by *Le Borgne et al.* [2007] when analyzing flowmeter data from the site. In experiments IIIa and IIIb, the recovered mass is arriving nearly in equal parts at two fractures located 22 m apart, one contributing with 80% and the other <5% to flow.

[54] The mass recovery is low (<30%) in all experiments. The tracer might move out into fractures that carry the tracer away from the pumping borehole either due to the ambient flow field, by density effects or by the injection pressure. The pushing of the tracer by continued water injection in experiments Ia, II, IIIa and IIIb likely pushed some of the tracer away from the pumping borehole. In these cases, the pumping might only weakly affect the tracer and its subsequent movement. The regional upward gradient that is manifested by a  $\sim 1.5$  L  $\text{min}^{-1}$  flow in the boreholes [*Le Borgne et al.*, 2007] seems to influence the tracer movement for some of the experiments, for which we observe significant upward movement of the tracer into larger fracture zones (experiments Ia, Ib, IIIa, and IIIb).

[55] Tracer transport between the two  $\sim 6$  m distant boreholes is fast for the experiments presented here. Tracer breakthrough occurs during the first hour in all experiments and peak concentrations in the borehole fluid are observed

after 30 min (Figures 5a and 5b (experiments Ia and Ib)) to 3 h (Figure 5c (experiment II)). Correspondingly, the GPR difference images evolve quickly in time during early observation times. The corresponding apparent tracer velocities considering the length of the 2-D projected pathway between injection and outflow locations in Figure 10 and the minimal tracer travel time give estimates in the range of  $0.2$ – $1.3$  m  $\text{min}^{-1}$ . These velocities of the first arriving tracer are likely higher as the actual travel path length in 3-D is larger.

[56] A comparison between picked GPR reflectivity changes at specific locations over time with those inferred from flow and transport modeling (Figure 12) show a good agreement at early times and discrepancies at late times, indicating that a more complex flow and transport model could be constrained with these data. The discrepancies are on the same order as those between observed and simulated solute fluxes at the outflow locations using the same flow and transport model. The time series of GPR reflectivity changes have a high signal-to-noise ratio and indicate not only the arrival time of the saline tracer at a specific location, but also how the tracer concentration decreases over time. Forced tracer tests examine only the fractures that are involved in tracer transport and does not represent natural conditions. To better understand and build models for predicting flow and transport under natural conditions one must carry out experiments under natural flow conditions. Using single-hole GPR difference imaging as presented here offer the possibility to image transport under such conditions even in the case of no or very limited tracer arrival in the boreholes.

[57] The resulting GPR difference sections are a result of a rather extensive processing workflow. Research is warranted to better understand under what conditions this type of data can provide reliable information about transport within specific fractures and how to best use such data to constrain realistic 3-D fracture network models that honor not only borehole information, but also transport pathways, effects of natural flow gradients, and storage changes imaged by the GPR data. To facilitate the interpretation of the difference-migrated images, it would be most fruitful to test and further develop suitable deconvolution algorithms that remove the imprint of the GPR source signal [*Schmelzbach et al.*, 2011].

## 6. Conclusions

[58] We find that time-lapse single-hole GPR data acquired during saline tracer injection tests provide insights about the temporal evolution of tracer plume geometry that is complementary to information derived from classical hydrological characterization of fractured aquifers. The GPR data make it possible to derive a length scale of the fractures involved in the tracer transport and to infer the connectivity and geometry of these fractures. Furthermore, the data help to better understand where the tracer that did not arrive in the pumping boreholes went. For five tracer experiments in a fractured granite, we find that the GPR data acquired with 250 MHz antennas provide subtle but reliable images of the evolution of tracer plumes through time at radial distances  $r = 2$ – $10$  m from the boreholes (Figures 8 and 9). Hydrological data and migrated relative

difference amplitude images derived from the GPR experiments are consistent with each other and indicate similar tracer transport characteristics for the experiments that involved the same injection fracture. For all experiments, we find that multiple pathways involving several fractures connect the injection fracture with the pumping borehole and that the total vertical spread of the tracer is in the range of tens of meters despite that the two boreholes are only located six meters apart. The vertical ambient pressure gradient at the site seems to carry most of the injected tracer upward through fractures that do not intersect the pumping boreholes, while some storage of tracer mass appears to occur in less mobile zones within the interborehole region. We find that 2-D geometrical information about pathway lengths and connections help to constrain breakthrough analyses. We demonstrate also for one of the experiments using a simplified fracture model how GPR reflectivity time series at chosen locations may be used to test and provide further constraints to transport models.

[59] **Acknowledgments.** We thank the field crew, which included Ludovic Baron, Nicolas Lavenant, and Vincent Boschero. We are thankful to Alan Green at ETH Zurich for making his GPR equipment available. This research was supported by the Swiss National Science Foundation under grant 200021-124571, the French National Observatory H+, the European ITN network IMVUL (grant agreement 212298), and the European Interreg IV project CLIMAWAT. Many useful comments from three anonymous reviewers and the AE Frederick Day-Lewis helped to improve the paper.

## References

- Annan, A. P. (2005), GPR methods for hydrogeological studies, in *Hydrogeophysics*, edited by Y. Rubin and S. S. Hubbard, chap. 7, pp. 185–214, Springer, New York.
- Balanis, C. (1989), *Advanced Engineering Electromagnetics*, John Wiley, New York.
- Becker, M. W., and A. M. Shapiro (2000), Tracer transport in fractured crystalline rock: Evidence of nondiffusive breakthrough tailing, *Water Resour. Res.*, *36*, 1677–1686, doi:10.1029/2000WR900080.
- Becker, M. W., and A. M. Shapiro (2003), Interpreting tracer breakthrough tailing from different forced-gradient tracer experiment configurations in fractured bedrock, *Water Resour. Res.*, *39*(1), 1024, doi:10.1029/2001WR001190.
- Becker, M. W., and G. P. Tsofilias (2010), Comparing flux-averaged and resident concentration in a fractured bedrock using ground penetrating radar data, *Water Resour. Res.*, *46*, W09518, doi:10.1029/2009WR008260.
- Berkowitz, B., A. Cortis, M. Dentz, and H. Scher (2006), Modeling non-Fickian transport in geological formations as a continuous time random walk, *Rev. Geophys.*, *44*, RG2003, doi:10.1029/2005RG000178.
- Bonnet, E., O. Bour, N. E. Odling, P. Davy, I. Main, P. Cowie, and B. Berkowitz (2001), Scaling of fracture systems in geologic media, *Rev. Geophys.*, *39*(3), 347–383, doi:10.1029/1999RG000074.
- Bradford, J. H., and J. C. Deeds (2006), Ground-penetrating radar theory and application of thin-bed offset-dependent reflectivity, *Geophysics*, *71*(3), K47–K57, doi:10.1190/1.2194524.
- Cvetkovic, V., and R. Haggerty (2002), Transport with multiple-rate exchange in disordered media, *Phys. Rev.*, *65*(5), 051308, doi:10.1103/PhysRevE.65.051308.
- Darcel, C., O. Bour, and P. Davy (2003), Stereological analysis of fractal fracture networks, *J. Geophys. Res.*, *108*(B9), 2451, doi:10.1029/2002JB002091.
- Day-Lewis, F. D., J. W. Lane, J. M. Harris, and S. M. Gorelick (2003), Time-lapse imaging of saline-tracer transport in a fractured rock using difference-attenuation radar tomography, *Water Resour. Res.*, *39*(10), 1290, doi:10.1029/2002WR001722.
- de Dreuzy, J. R., P. Davy, and O. Bour (2001), Hydraulic properties of two-dimensional random fracture networks following a power law length distribution: 2. Permeability of networks based on log-normal distribution of apertures, *Water Resour. Res.*, *37*(8), 2079–2096, doi:10.1029/2001WR900011.
- de Dreuzy, J. R., P. Davy, and O. Bour (2002), Hydraulic properties of two-dimensional random fracture networks following power law distributions of length and aperture, *Water Resour. Res.*, *38*(12), 1276, doi:10.1029/2001WR001009.
- Deparis, J., and S. Garambois (2009), On the use of dispersive APVO GPR curves for thin-bed properties estimation: Theory and application to fracture characterization, *Geophysics*, *74*(1), J1–J12, doi:10.1190/1.3008545.
- Dorn, C., N. Linde, T. Le Borgne, O. Bour, and L. Baron (2011), Single-hole GPR reflection imaging of solute transport in a granitic aquifer, *Geophys. Res. Lett.*, *38*, L08401, doi:10.1029/2011GL047152.
- Dorn, C., N. Linde, J. Doetsch, T. Le Borgne, and O. Bour (2012), Fracture imaging within a granitic rock aquifer using multiple-offset single-hole and cross-hole GPR reflection data, *J. Appl. Geophys.*, *78*, 123–132, doi:10.1016/j.jappgeo.2011.01.010.
- Ernst, J. R., K. Holliger, H. Maurer, and A. G. Green (2006), Realistic FDTD modeling of borehole georadar antenna radiation: Methodology and application, *Near Surf. Geophys.*, *4*, 19–30.
- Hadermann, J., and W. Heer (1996), The Grimsel (Switzerland) migration experiment: Integrating field experiments, laboratory investigations and modelling, *J. Contam. Hydrol.*, *21*, 87–100, doi:10.1016/0169-7722(95)00035-6.
- Haggerty, R. S., and S. M. Gorelick (1995), Multiple-rate mass transfer for modeling diffusion and surface reactions in media with pore-scale heterogeneity, *Water Resour. Res.*, *31*(10), 2383–2400.
- Haggerty, R. S., S. A. McKenna, and L. C. Meigs (2000), On the late-time behavior of tracer test breakthrough curves, *Water Resour. Res.*, *36*(12), 3467–3480, doi:10.1029/2000WR900214.
- Haggerty, R. S., S. W. Fleming, L. C. Meigs, and S. A. McKenna (2001), Tracer tests in a fractured dolomite: 2. Analysis of mass transfer in single-well injection-withdrawal tests, *Water Resour. Res.*, *37*(5), 1129–1142, doi:10.1029/2000WR900334.
- Harvey, C. F., and S. M. Gorelick (2000), Rate-limited mass transfer or macrodispersion: Which dominates the plume evolution at the Macrodispersion Experiment (MADE) site?, *Water Resour. Res.*, *36*(3), 637–650, doi:10.1029/1999WR900247.
- Lane, J. W., F. P. Haeni, G. Placzek, and D. L. Wright (1996), Use of borehole-radar methods to detect a saline tracer in fractured crystalline bedrock at Mirror Lake, Grafton County, New Hampshire, USA, in *Proceedings, 6th International Conference on Ground-Penetrating Radar (GPR'96)*, Sendai, Japan, pp. 185–190.
- Lane, J. W., Jr., F. P. Haeni, and R. Versteeg (1998), Use of multi-offset borehole-radar reflection method in fractured crystalline bedrock at Mirror Lake, Grafton County, New Hampshire, in *Proceedings of the Symposium on the Application of Geophysics to Engineering and Environmental Problems, March 22–26, 1998, Chicago, Illinois*, pp. 359–368, Environ. and Eng. Geophys. Soc., Wheat Ridge, Colo.
- Lapevic, P. A., K. S. Novakowski, and E. A. Sudicky (1999), The interpretation of a tracer experiment conducted in a single fracture under conditions of natural groundwater flow, *Water Resour. Res.*, *35*, 2301–2312, doi:10.1029/1999WR900143.
- Le Borgne, T., and P. Gouze (2008), Non-Fickian dispersion in porous media: 2. Model validation from measurements at different scales, *Water Resour. Res.*, *44*, W06427, doi:10.1029/2007WR006279.
- Le Borgne, T., O. Bour, F. L. Paillet, and J. P. Caudal (2006), Assessment of preferential flow path connectivity and hydraulic properties at single-borehole and cross-borehole scales in a fractured aquifer, *J. Hydrol.*, *328*(1–2), 347–359.
- Le Borgne, T., et al. (2007), Comparison of alternative methodologies for identifying and characterizing preferential flow paths in heterogeneous aquifers, *J. Hydrol.*, *345*(3–4), 134–148, doi:10.1016/j.jhydrol.2007.07.007.
- Liu, L., J. W. Lane, and Y. Quan (1998), Radar attenuation tomography using the centroid frequency downshift method, *J. Appl. Geophys.*, *40*(1–3), 105–116.
- Liu, S., and M. Sato (2006), Subsurface water-filled fracture detection by borehole radar: A case history, *J. Environ. Eng. Geophys.*, *11*(2), 95–101, doi:10.2113/JEEG11.2.95.
- Long, J., J. S. Remer, C. R. Wilson, and P. A. Witherspoon (1982), Porous media equivalents for networks of discontinuous fractures, *Water Resour. Res.*, *18*, 645–658, doi:10.1029/WR018i003p00645.
- Long, J., et al. (1996), *Rock Fractures and Fluid Flow: Contemporary Understanding and Applications*, Natl. Acad. Press, Washington, D. C.
- Maloszewski, P., and A. Zuber (1985), On the theory of tracer experiments in fissured rocks with a porous matrix, *J. Hydrol.*, *79*(3–4), 333–358, doi:10.1016/0022-1694(85)90064-2.

- Moreno, L., and C. F. Tsang (1994), Flow channeling in strongly heterogeneous porous media: A numerical study, *Water Resour. Res.*, *30*(5), 1421–1430, doi:10.1029/93WR02978.
- Neuman, S. P. (2005), Trends, prospects and challenges in quantifying flow and transport through fractured rocks, *Hydrogeol. J.*, *13*, 124–147.
- Neuman, S. P., and V. Di Federico (2003), Multifaceted nature of hydrogeologic scaling and its interpretation, *Rev. Geophys.*, *41*(3), 1014, doi:10.1029/2003RG000130.
- Olsson, O., L. Falk, O. Forslund, L. Lundmark, and E. Sandberg (1992), Borehole radar applied to the characterization of hydraulically conductive fracture zones in crystalline rock, *Geophys. Prospect.*, *40*, 109–142.
- Paillet, F. L. (1998), Flow modeling and permeability estimation using borehole flow logs in heterogeneous fractured formations, *Water Resour. Res.*, *34*, 997–1010.
- Rubin, Y., and S. S. Hubbard (Eds.) (2005), *Hydrogeophysics*, Springer, New York.
- Schmelzbach, C., F. Scherbaum, J. Tronicke, and P. Dietrich (2011), Bayesian frequency-domain blind deconvolution of ground-penetrating radar data, *J. Appl. Geophys.*, *75*, 615–630, doi:10.1016/j.jappgeo.2011.08.010.
- Spillmann, T., H. Maurer, H. Willenberg, K. F. Evans, B. Heincke, and A. G. Green (2007), Characterization of an unstable rock mass based on borehole logs and diverse borehole radar data, *J. Appl. Geophys.*, *61*, 16–38.
- Talley, J., G. S. Baker, M. W. Becker, and N. Beyrle (2005), Four dimensional mapping of tracer channelization in subhorizontal bedrock fractures using surface ground penetrating radar, *Geophys. Res. Lett.*, *32*, L04401, doi:10.1029/2004GL021974.
- Torrence, C., and G. P. Compo (1997), A practical guide to wavelet analysis, *Bull. Am. Meteorol. Soc.*, *79*(1), 61–78.
- Tsang, C. F., and I. Neretnieks (1998), Flow channeling in heterogeneous fractured rocks, *Rev. Geophys.*, *36*, 275–298.
- Tsoflias, G. P., and M. W. Becker (2008), Ground-penetrating-radar response to fracture-fluid salinity: Why lower frequencies are favorable for resolving salinity changes, *Geophysics*, *73*(5), J25–J30, doi:10.1190/1.2957893.
- Tsoflias, G. P., and A. Hoch (2006), Investigating multi-polarization GPR wave transmission through thin layers: Implications for vertical fracture characterization, *Geophys. Res. Lett.*, *33*, L20401, doi:10.1029/2006GL027788.
- Widess, M. B. (1973), How thin is a thin bed?, *Geophysics*, *38*, 1176, doi:10.1190/1.1440403.

**. APPENDIX 1. PAPER: INFERRING TRANSPORT  
CHARACTERISTICS IN A FRACTURED ROCK AQUIFER BY  
COMBINING SINGLE-HOLE GROUND-PENETRATING RADAR  
REFLECTION MONITORING AND TRACER TEST DATA  
(DORN ET AL., WATER RESOURCES RESEARCH, 2012)**

---

**Appendix 2. Paper:**  
**Characterizing groundwater flow  
and heat transport in fractured  
rock using Fiber-Optic  
Distributed Temperature Sensing  
(Read et al., Geophysical  
Research Letters, accepted)**

**1 Characterizing groundwater flow and heat transport**  
**2 in fractured rock using Fiber-Optic Distributed**  
**3 Temperature Sensing**

T. Read<sup>1</sup>, O. Bour<sup>2</sup>, V. Bense<sup>1</sup>, T. Le Borgne<sup>2</sup>, P. Goderniaux<sup>2</sup>, M.V.

Klepikova<sup>2</sup>, R. Hochreutener<sup>2</sup>, N. Lavenant<sup>2</sup>, and V. Boschero<sup>2</sup>

---

T. Read and V. Bense, School of Environmental Sciences, University of East Anglia, Norwich, UK. (tom.read@uea.ac.uk)

T. Le Borgne, O. Bour, P. Goderniaux, M.V. Klepikova, R. Hochreutener, N. Lavenant, and V. Boschero, Geosciences Rennes, UMR 6118, CNRS, University of Rennes 1, Rennes, France.

<sup>1</sup>School of Environmental Sciences,  
University of East Anglia, Norwich, UK.

<sup>2</sup>Geosciences Rennes, UMR 6118, CNRS,  
University of Rennes 1, Rennes, France.

4 We show how fully distributed space - time measurements with Fiber-Optic  
5 Distributed Temperature Sensing (FO-DTS) can be used to investigate ground-  
6 water flow and heat transport in fractured media. Heat injection experiments  
7 are combined with temperature measurements along fiber optic cables in-  
8 stalled in boreholes. Thermal dilution tests are shown to enable detection  
9 of cross - flowing fractures and quantification of the cross flow rate. A cross  
10 borehole thermal tracer test is then analyzed to identify fracture zones that  
11 are in hydraulic connection between boreholes and to estimate spatially dis-  
12 tributed temperature breakthrough in each fracture zone. This provides a  
13 significant improvement compared to classical tracer tests, for which concen-  
14 tration data are usually integrated over the whole abstraction borehole. How-  
15 ever, despite providing some complementary results, we find that the main  
16 contributive fracture for heat transport is different to that for a solute tracer.

## 1. Introduction

17 Heterogeneous aquifers, such as fractured rocks, often require detailed characteriza-  
18 tion for water resources assessment and for the prediction of potential contaminant path-  
19 ways [Neuman, 2005]. Such characterization may consist of simply identifying the most  
20 transmissive fractures, to the formulation of a statistical model of the solute transport  
21 properties of the fracture network such as permeability and dispersivity. This is usu-  
22 ally carried out in situ through cross-flowmeter tests or hydraulic response tests [Paillet,  
23 1998; Illman *et al.*, 2009], or with tracer experiments using solutes. In between two or  
24 more boreholes, tracer tests allow the advective velocity and dispersion of solutes to be  
25 quantified [e.g., Becker and Shapiro, 2003]. While these well-established aquifer character-  
26 ization techniques successfully yield results in terms of flow through the fracture network,  
27 the requirement for frequent sampling and subsequent analysis may be time consuming  
28 and expensive. Only with sophisticated multi-depth sampling [Riley *et al.*, 2011], multi-  
29 packer systems [Delouvrier and Delay, 2004], or repetitive continuous logging [Dorn *et al.*,  
30 2012], can a more continuous log along the borehole be obtained. This, as opposed to  
31 a time series recorded at a single depth which incorporates the response of all transmis-  
32 sive features intersecting the borehole, is required for analysis of the transport properties  
33 through individual fracture zones or permeable units. There is, therefore, a great need  
34 for new sensors capable of providing continuous measurements in space and time.

35 The availability of fully distributed fiber-optic temperature sensors (FO-DTS) allows  
36 such continuous measurements for temperature [Selker *et al.*, 2006; Tyler *et al.*, 2009].  
37 It is long-established that heat can be used as a tracer to estimate groundwater flow in

38 a range of hydrogeological settings [Anderson, 2005; Saar, 2011]. In fractured aquifers,  
39 heat advection along fractures from regions of higher or lower temperature can cause  
40 anomalies in temperature-depth profiles [Barton et al., 1995; Ge, 1998; Pehme et al., 2010].  
41 Moreover, vertical flow in boreholes, driven by head gradients in fractures at different  
42 depths, can be quantified through analysis of temperature-depth profiles [Klepikova et al.,  
43 2011]. Heat is more diffuse than solutes by several orders of magnitude, but in some  
44 settings, it has been shown to be a reasonable proxy for solute tracers and hence can  
45 be used to calibrate models of hydraulic conductivity distribution [Ma et al., 2012]. In  
46 fractured media, heat may be expected to bring different and complementary information  
47 compared to solute tracers, since it is more much sensitive to matrix diffusion processes  
48 [Geiger and Emmanuel, 2010].

49 The application of FO-DTS has been demonstrated in boreholes for thermal conduc-  
50 tivity estimation and surface temperature reconstruction [Freifeld et al., 2008]. FO-DTS  
51 was also used to infer fluid flow rates inside boreholes as an alternative for a directly  
52 measured flow log [Leaf et al., 2012]. In the application of aquifer characterization as  
53 described above, FO-DTS deployments have been limited to only a few case studies [Hur-  
54 tig et al., 1994; Macfarlane et al., 2002], and there have been significant advances in the  
55 measurement precision of FO-DTS systems in the intervening time. Here, we demonstrate  
56 the potential for FO-DTS monitoring of heat dilution and tracer tests in heterogeneous  
57 systems such as fractured rock aquifers. We show how cross flow rates from fracture  
58 zones and temperature breakthrough curves for individual fractures can be calculated,

59 and find that FO-DTS offers some significant advantages over point temperature loggers  
60 for monitoring such tests and for characterizing flow and heat transport in fractured rocks.

## 2. Methodology

61 Thermal test data were collected at Ploemeur, Brittany, north west France, in four  
62 boreholes (B1, B2, B3 and F22), separated by a distance of 6 to 30 m and ranging from  
63 70 to 100 m deep (Figure 1). The geology of the site consists of mica-schist, underlain by an  
64 intrusive granite, the contact of which provides a locally significant groundwater resource  
65 [*Le Borgne et al.*, 2004; *Ruelleu et al.*, 2010]. The site is considered a typical fractured  
66 crystalline basement aquifer, and has been subject to numerous hydraulic - [*Le Borgne*  
67 *et al.*, 2004, 2007; *Klepikova et al.*, 2011], and geophysical tests [*Dorn et al.*, 2011, 2012].  
68 Interference tests have suggested that fluid flow and associated tracer transport between  
69 boreholes is concentrated in only a few transmissive fracture zones [*Le Borgne et al.*,  
70 2007]. Solute dispersion is dominated by fracture network connectivity showing that few  
71 interconnecting fractures contribute to solute transport at the scale of several meters by  
72 which the boreholes are separated [*Dorn et al.*, 2012].

73 For the FO-DTS experiments discussed here, a single BruSteel (Brugg Cables, Switzer-  
74 land) steel armored fibre optic cable of 1 km in length was installed in all four boreholes  
75 for the continuous monitoring of temperature. Additionally, two coiled sections of cable  
76 were placed in a calibration bath consisting of water wetted ice and monitored with a  
77 submersible temperature logger. We deploy the widely used Oryx-DTS unit (Sensornet  
78 Ltd., UK, Herts), configured to take single-ended temperature measurements with a spa-  
79 tial sampling interval of 1.01 m along the cable and an integration time of 2 minutes.

80 To convert the laser backscatter detected by the instrument to a temperature, we post-  
81 processed the raw backscatter data to further improve the instrument accuracy using the  
82 dynamic calibration procedure outlined by *Hausner et al.* [2011]. However, this was not  
83 possible for the thermal dilution tests due to warming of the ice baths, so here we rely on  
84 the inbuilt calibration software of the device.

## 2.1. Thermal Dilution Test set-up

85 Thermal dilution tests were conducted in borehole B3. The method we employ is  
86 similar to a borehole dilution test using solutes [e.g., *Novakowski et al.*, 2006; *Brouyère*  
87 *et al.*, 2008], also referred to as hydro-physical logging in the literature [e.g., *Doughty*  
88 *et al.*, 2005], but here using heat instead. A similar method has been applied in lined  
89 boreholes using the Active Line Source technique [*Pehme et al.*, 2007]. Since we are  
90 interested in cross flowing fractures, an inflatable packer was installed at a depth of 44  
91 m to prevent ambient vertical flow in between fractures tapping into the borehole which  
92 otherwise occurs in most boreholes at the site. We injected water, heated to 50 °C using  
93 a mobile heating system, just above the packer at 43 m. The borehole was pumped at the  
94 same rate at shallow depth in order to draw the warm injected water upwards. During the  
95 experiment, the hydraulic head in the borehole was monitored to verify that any changes  
96 were small enough to ensure no net flow in or out of the borehole taking into account  
97 effects of temperature on fluid density. The thermal dilution test was carried out under  
98 ambient conditions and then under cross pumping conditions, with B2 at a distance of 10  
99 m away pumped at 140 L min<sup>-1</sup>.

## 2.2. Thermal Tracer Test set-up

100 For the thermal tracer test, we concentrate on B1, the injection well, and B2, the  
101 abstraction well, separated by approximately 6 m. Two inflatable packers were used to  
102 hydraulically isolate a known fracture at a depth of 78.7 m in B1 (B1-79). Water was  
103 injected into a one-meter interval across this fracture at a constant rate and temperature  
104 of  $35 \text{ L min}^{-1}$  and  $50 \text{ }^\circ\text{C}$ . Simultaneously, B2 was pumped at a constant rate of  $140 \text{ L}$   
105  $\text{min}^{-1}$ . The injection of heated water in B1 continued for approximately 11 hours, and  
106 was followed by a 'push' of water at ambient groundwater temperature for 5 hours to test  
107 the heat recovery under similar hydraulic conditions. Subsequently, the injection at B1  
108 ceased but pumping in the abstraction well, B2, continued. In addition to monitoring  
109 by FO-DTS, temperature in the abstraction well was recorded continuously using three  
110 temperature loggers located at set depths of 40, 60 and 72 m respectively.

## 3. Results

### 3.1. Thermal Dilution Tests

111 FO-DTS data for the thermal dilution tests carried out in B3, including both the in-  
112 jection and cooling phases, are shown in Figure 2a and Figure 2c for ambient and cross  
113 pumping conditions respectively. In both cases  $t = 0 \text{ h}$  corresponds to when the in-  
114 jection stopped. By the time the injection ceases, the fluid between the point of injection  
115 and abstraction is replaced with water approximately  $25$  to  $40 \text{ }^\circ\text{C}$  warmer than ambient  
116 temperatures. During the cooling phase, the absolute temperature values are clearly in-  
117 fluenced by the initial conditions at  $0 \text{ h}$  which were not entirely isothermal. To correct  
118 for the influence of the initial non-isothermal distribution of heat in the borehole on the

119 depth-variant cooling rates observed later, the Relative Temperature Anomaly (*RTA*)  
120 was calculated according to:

$$121 \quad RTA(z, t) = \frac{T(z, t) - T_{ambient}(z)}{T_{initial}(z) - T_{ambient}(z)} \quad (1)$$

122 where  $T_{ambient}$  is the temperature prior to the start of the injection and  $T_{initial}$  is the  
123 temperature when the injection ceased. This scales the initial temperature anomaly to  
124 unity at all depths, with a value of zero representing a full return to pre-testing ambient  
125 temperature conditions. The cased section cools more slowly than the open section below,  
126 which can be explained by the larger borehole diameter and low thermal conductivity  
127 casing material. From the end of the casing to 36 m, the cooling is relatively uniform,  
128 which corresponds well with core data and flow logs that suggest there are no significant  
129 transmissive fractures intersecting the borehole along this depth interval (Figure 2b and  
130 d). A zone of enhanced cooling beneath 36 m can be readily distinguished in ambient and  
131 cross pumping conditions. The top of this zone coincides with two transmissive fractures  
132 located just above the transition from micaschist to granite identified by *Le Borgne et al.*  
133 [2007], and continues to 42 m.

134 The fast cooling below 36 m is potentially due to both advective flow in the fracture  
135 zone, but also partly to the higher thermal diffusivity of granite compared to micaschist  
136 ( $1.8 \times 10^{-6}$  and  $1.4 \times 10^{-6} \text{ m}^2\text{s}^{-1}$  respectively). Nevertheless, during the injection phase, in  
137 particular during cross-pumping (Figure 2c), the injected water is cooled significantly as it  
138 passes the fracture zone. During this time the contrast in temperature across the fracture  
139 zone would not be explained by the contrast in thermal diffusivity between granite and

140 mica-schist. In the following, we assume that during the injection phase, this step-like  
141 change in temperature across the fracture zone is due solely to an advective effect.

142 To estimate the cross-flow rate  $Q_f$  [ $\text{L min}^{-1}$ ] through the fracture zone, we use a mixing  
143 equation applicable during the injection phase:

$$144 \quad Q_f = \left( \frac{T_{below} - T_{above}}{T_{above} - T_f} \right) Q_{inject} \quad (2)$$

145 in which  $Q_{inject}$  [ $\text{L min}^{-1}$ ] is the rate of injection, and  $T_{above}$  and  $T_{below}$  are the temperatures  
146 above and below the fracture zone of interest respectively, and  $T_f$  is the temperature of  
147 groundwater flowing through the fracture zone, which is assumed to be constant with  
148 time. This mixing equation assumes that water from the cross flowing fracture enters the  
149 borehole and becomes fully mixed before being advected upwards or leaving the borehole.  
150 Application of equation (2) using the FO-DTS data for B3 and a  $T_f$  of 15 °C results  
151 in a calculated cross flow of 3.4  $\text{L min}^{-1}$  for the fracture zone at 36 m. When the  
152 thermal dilution test was repeated, but under cross pumping conditions, the calculated  
153 flow through this zone increases to 3.9  $\text{L min}^{-1}$ , a slight but measurable change. Hence,  
154 using FO-DTS to monitor thermal dilution tests allowed us to measure significant ambient  
155 flow through the identified fracture. The ambient flow measured through the fracture is  
156 quantitatively comparable with the vertical ambient flows measured by precise borehole  
157 flowmeters [*Le Borgne et al.*, 2007]. Such ambient flows are explained by the location of  
158 the site in a discharge area of the catchment. The effect of pumping in an adjacent well,  
159 although small, apparently produces a temperature effect strong enough to be detected.

160 Note that at the start of the monitoring period after the borehole volume was replaced  
161 with heated water, the thermal gradients near the top of the borehole are large enough  
162 to potentially result in variable-density driven free-convection in the borehole [*Sammel*,  
163 1968]. However, this was not observed as free-convection would lead to very different  
164 cooling patterns (more irregular and faster) than we eventually observe during later time  
165 data.

### 3.2. Thermal Tracer Tests

166 Time series of temperature data from the temperature loggers and corresponding post-  
167 processed FO-DTS measurements at these depths during the thermal tracer test are shown  
168 in Figure 3a. The data show good agreement, with the FO-DTS data having high temporal  
169 repeatability characterized by a standard deviation of 0.03 °C. Thus, the FO-DTS appears  
170 to be an excellent tool for detecting and monitoring temperature change during thermal  
171 tracer tests.

172 FO-DTS data for all depths in the abstraction well are shown in Figure 3b in terms of a  
173 temperature breakthrough, calculated as the difference between the measured temperature  
174 and the mean of the 10 temperature-depth profiles obtained prior to the injection of  
175 heated water. Based on visual inspection of the temperature data alone, there are three  
176 readily identifiable fractures contributing to the upflow in the borehole to the pump. At  
177 approximately 79 and then 67 m there are sources of warmer water which must therefore  
178 be fracture zones that are in connection with the fracture zone B1-79 in the injection well.  
179 Between 57 and 59 m there appears to be a wider zone of fracture inflows that results in

180 the cooling of the upflowing borehole water and therefore appear to be disconnected from  
 181 B1-79. From this point upwards there appear to be no thermal breakthroughs.

182 In the following we estimate the contribution of each fracture to the transport of heat  
 183 during the thermal tracer test and compare it to other tracer tests. Under the assumptions  
 184 that the temperature change above and below the fracture zone is larger than the precision  
 185 of the FO-DTS instrument, the water inside the borehole is laterally fully mixed, and  
 186 that heat loss from the borehole by conduction can be neglected over the depth interval  
 187 of interest, the heat balance of flux weighted temperatures across the fracture zone can  
 188 be written as:

$$189 \quad Q_{above}T_{above} = Q_{below}T_{below} + Q_fT_f \quad (3)$$

190 where  $Q_f$  is now considered to produce a net gain to the vertical flow in the borehole.

191 The DTS measured temperature in the borehole was combined with flowmeter data to  
 192 calculate the temperature response in the different fracture zones B2-55, B2-58, B2-66  
 193 and B2-79 identified in the borehole log and flow log (Figure 3c). Assuming that all of  
 194 the difference in the flow above and below the fracture zone originates from the fracture,  
 195 equation (3) can be rearranged to give:

$$196 \quad T_f = \frac{Q_{above}T_{above} - Q_{below}T_{below}}{Q_{above} - Q_{below}} \quad (4)$$

197 allowing the temperature of groundwater from the inflowing fracture zone of interest to  
 198 be determined. For this calculation, we first removed the high frequency noise in the  
 199 FO-DTS measured temperature which would otherwise be amplified (approximately 0.1  
 200 °C), by fitting a 2nd degree polynomial using a weighted linear least-squares regression to  
 201 each of the thermal breakthrough curves along the borehole length. The flow log indicated

202 that there was no detectable inflow at 66 m where the largest step change in temperature  
203 was observed, whereas two closely spaced fractures can be seen in an optical borehole  
204 log in this zone. For the purpose of the thermal breakthrough calculation, we assume  
205 that the fractures contribute  $5 \text{ L min}^{-1}$  as this is approximately the detection limit of the  
206 impeller flowmeter for the borehole diameter. The true temperature breakthrough from  
207 this fracture zone is potentially much higher than calculated in the following, as the flow  
208 from this fracture is potentially much less than this.

209 Using equation (4), Figure 4 provides the calculated temperature of the inflow to B2  
210 from each fracture zone. The largest temperature response ( $4.0 \text{ }^\circ\text{C}$ ) is from fracture B2-  
211 66. This breakthrough is very rapid, and continues for approximately 1 hour after the  
212 injection switched to a cold water push. In comparison B2-79 responds more slowly and  
213 rises to a lower temperature ( $0.8 \text{ }^\circ\text{C}$ ). The calculated responses for fracture zones B2-58  
214 and B2-55 confirms the initial observation that no heat was recovered from these fractures  
215 during the duration of the experiment.

216 Compared to solute tracer tests, performed at the same location, the main differences  
217 observed are the time, amplitude, and spatial distribution of the breakthrough. For  
218 instance, with a slug injection of the fluorescent dye uranine, the peak arrives at B2 after  
219 around 20 minutes, but only very slight changes are observed at these times using heat  
220 as a tracer (Figure 4). Thus, the thermal breakthrough is significantly attenuated due  
221 to fracture-matrix heat exchange. Some remarkable differences are also observed when  
222 investigating the fractures contributing to transport. *Dorn et al.* [2012] carried out a  
223 solute tracer test between B2 and B1 by injecting a saline tracer into the same fracture

224 and pumping B2 at a rate of  $30 \text{ L min}^{-1}$ . During their test, the main contributing  
225 fracture in B2 was B2-79 (see Figures 5 and 7 in *Dorn et al.* [2012]). Fracture B2-66 was  
226 detected in the GPR time-lapse images (Figure 10a in *Dorn et al.* [2012]) but did not  
227 contribute significantly to conductivity variations in the borehole. For the duration of our  
228 thermal test, the main contributive fracture was B2-66. These differences are significant  
229 as they confirm that thermal and solute tracer tests do not provide the same information  
230 on the transport pathways, even at the scale of a few meters. Different elements may  
231 explain these differences. Density effects may drive the saline tracer downwards and  
232 heat upwards. Furthermore, heat transfer is much more sensitive to the fracture-matrix  
233 exchanges compared to solute transfer. The effect of flow channeling may also control the  
234 heat exchanges [*Newville et al.*, 2010], since it may reduce the fracture-matrix exchange  
235 area. Thus, heat and solute transfer may respond very differently to flow channeling. In  
236 the present case, fracture B2-66 may be of a small aperture, with strongly channelized flow,  
237 which would explain a negligible flow contribution and only small solute tracer recovery  
238 but an important temperature breakthrough as we observe.

#### 4. Conclusions

239 We find that FO-DTS is a significant advance over traditional point temperature sensors  
240 in the borehole environment which enables thermal dilution or thermal tracer tests to be  
241 monitored accurately and efficiently in both time and space. Such thermal experiments  
242 offer new insights in the characterization of fractured media, as they provide complemen-  
243 tary information with respect to solute tracer experiments. In particular, the thermal  
244 dilution test was shown to be an efficient method to estimate cross flowing groundwater

245 through a fracture zone. To control the heat input, some improvements may be obtained  
246 by combining electrical heating elements in fiber optic cables, as is starting to be done  
247 [*Liu et al.*, 2013].

248 FO-DTS was also found very useful to provide a detailed characterization of heat trans-  
249 port through a fracture network. The thermal breakthrough curve is strongly attenuated  
250 due to fracture-matrix interactions, and the relative contribution of the different fractures  
251 is found to be strikingly different than for solute transport potentially due to channeling  
252 and density effects. The main advantages of FO-DTS is to avoid the risk of disturbing  
253 the fluid column by raising and lowering a probe, and to generate a synchronous data  
254 set with measurements distributed over the entire borehole. Hence, we anticipate that  
255 DTS combined with heating experiments will become a more commonplace geophysical  
256 method for aquifer characterization.

257 **Acknowledgments.** Funding for this work was provided by the INTERREG IV  
258 project CLIMAWAT, Marie Curie ITN project IMVUL, the national network of hydro-  
259 geological sites H+, and a Natural Environment Research Council (NERC) studentship  
260 (NE/J500069/1) to Tom Read. The authors thank Alain Dassargues and S. Brouyère from  
261 the Université de Liège for generously lending the portable water heater. We would also  
262 like to thank Niklas Linde and an anonymous reviewer for their constructive comments.

## References

263 Anderson, M. P., Heat as a ground water tracer., *Ground water*, 43(6), 951–68, doi:  
264 10.1111/j.1745-6584.2005.00052.x, 2005.

- 265 Barton, C. A., M. D. Zoback, and D. Moos, Fluid flow along potentially active faults in  
266 crystalline rock, *Geology*, *23*, 683–686, doi:10.1130/0091-7613(1995)023;0683, 1995.
- 267 Becker, M. W., and A. M. Shapiro, Interpreting tracer breakthrough tailing from different  
268 forced-gradient tracer experiment configurations in fractured bedrock, *Water Resources*  
269 *Research*, *39*(1), 1024, doi:10.1029/2001WR001190, 2003.
- 270 Brouyère, S., J. Batlle-Aguilar, P. Goderniaux, and A. Dassargues, A new tracer technique  
271 for monitoring groundwater fluxes: the Finite Volume Point Dilution Method., *Journal*  
272 *of Contaminant Hydrology*, *95*(3-4), 121–40, doi:10.1016/j.jconhyd.2007.09.001, 2008.
- 273 Delouvrier, J., and J. Delay, *Engineering Geology for Infrastructure Planning in Europe*,  
274 chap. Multi-level Groundwater Pressure Monitoring at the Meuse/Haute Marne Under-  
275 ground Research Laboratory, France, pp. 377–384, Springer, 2004.
- 276 Dorn, C., N. Linde, T. L. Borgne, O. Bour, and L. Baron, Single-hole GPR reflection  
277 imaging of solute transport in a granitic aquifer, *Geophysical Research Letters*, *38*, 1–5,  
278 doi:10.1029/2011GL047152, 2011.
- 279 Dorn, C., N. Linde, T. L. Borgne, O. Bour, and M. Klepikova, Inferring transport charac-  
280 teristics in a fractured rock aquifer by combining single-hole ground-penetrating radar  
281 reflection monitoring and tracer test data, *Water Resources Research*, *48*, 1–18, doi:  
282 10.1029/2011WR011739, 2012.
- 283 Doughty, C., S. Takeuchi, K. Amano, M. Shimo, and C.-F. Tsang, Application of multirate  
284 flowing fluid electric conductivity logging method to well DH-2, Tono Site, Japan, *Water*  
285 *Resources Research*, *41*(10), W10,401, doi:10.1029/2004WR003708, 2005.

- 286 Freifeld, B. M., S. Finsterle, T. C. Onstott, P. Toole, and L. M. Pratt, Ground surface  
287 temperature reconstructions: Using in situ estimates for thermal conductivity acquired  
288 with a fiber-optic distributed thermal perturbation sensor, *Geophysical Research Letters*,  
289 *35*(14), 3–7, doi:10.1029/2008GL034762, 2008.
- 290 Ge, S., Estimation of groundwater velocity in localized fracture zones from well temper-  
291 ature profiles, *Journal of Volcanology and Geothermal Research*, *84*, 93–101, 1998.
- 292 Geiger, S., and S. Emmanuel, Non Fourier thermal transport in fractured geological media,  
293 *Water Resources Research*, *46*, 1–13, doi:10.1029/2009WR008671, 2010.
- 294 Hausner, M. B., F. Suárez, K. E. Glander, N. V. D. Giesen, J. S. Selker, and S. W. Tyler,  
295 Calibrating Single-Ended Fiber-Optic Raman Spectra Distributed Temperature Sensing  
296 Data, *Sensors*, *11*(11), 10,859–10,879, doi:10.3390/s111110859, 2011.
- 297 Hurtig, E., S. Growig, M. Jobmann, K. Kuhn, and P. Marschall, Fibre-Optic Tempera-  
298 ture Measurements in Shallow Boreholes: Experimental Application for Fluid Logging,  
299 *Geothermics*, *23*(4), 355–364, 1994.
- 300 Illman, W. A., X. Liu, S. Takeuchi, T.-C. J. Yeh, K. Ando, and H. Saegusa, Hydraulic  
301 tomography in fractured granite : Mizunami Underground Research site , Japan, *Water*  
302 *Resources Research*, *45*, 1–18, doi:10.1029/2007WR006715, 2009.
- 303 Klepikova, M. V., T. L. Borgne, O. Bour, and P. Davy, A methodology for using  
304 temperature-depth profiles under ambient, single and cross-borehole pumping condi-  
305 tions to estimate fracture hydraulic properties, *Journal of Hydrology*, *407*, 145–152,  
306 doi:DOI: 10.1016/j.jhydrol.2011.07.018, 2011.

- 307 Le Borgne, T., O. Bour, J. R. de Dreuzy, P. Davy, and F. Touchard, Equivalent mean  
308 flow models for fractured aquifers: Insights from a pumping tests scaling interpretation,  
309 *Water Resources Research*, *40*(3), 1–12, doi:10.1029/2003WR002436, 2004.
- 310 Le Borgne, T., et al., Comparison of alternative methodologies for identifying and charac-  
311 terizing preferential flow paths in heterogeneous aquifers, *Journal of Hydrology*, *345*(3-  
312 4), 134–148, doi:10.1016/j.jhydrol.2007.07.007, 2007.
- 313 Leaf, A. T., D. J. Hart, and J. M. Bahr, Active Thermal Tracer Tests for Improved  
314 Hydrostratigraphic Characterization, *Ground Water*, pp. 1–10, doi:10.1111/j.1745-  
315 6584.2012.00913.x, 2012.
- 316 Liu, G., S. Knobbe, and J. Butler, Resolving centimeter-scale flows in aquifers and  
317 their hydrostratigraphic controls, *Geophysical Research Letters*, pp. n/a–n/a, doi:  
318 10.1002/grl.50282, 2013.
- 319 Ma, R., C. Zheng, J. M. Zachara, and M. Tonkin, Utility of bromide and heat tracers for  
320 aquifer characterization affected by highly transient flow conditions, *Water Resources*  
321 *Research*, *48*(June), doi:10.1029/2011WR011281, 2012.
- 322 Macfarlane, A., A. Förster, D. Merriam, J. Schrötter, and J. Healey, Monitoring arti-  
323 ficially stimulated fluid movement in the Cretaceous Dakota aquifer, western Kansas,  
324 *Hydrogeology Journal*, *10*(6), 662–673, 2002.
- 325 Neuman, S. P., Trends, prospects and challenges in quantifying flow and transport through  
326 fractured rocks, *Hydrogeology Journal*, *13*, 124–147, doi:10.1007/s10040-004-0397-2,  
327 2005.

- 328 Neuville, A., R. Toussaint, and J. Schmittbuhl, Hydrothermal coupling in a self-affine  
329 rough fracture, *Physical Review E*, *82*, 1–14, doi:10.1103/PhysRevE.82.036317, 2010.
- 330 Novakowski, K., G. Bickerton, P. Lapcevic, J. Voralek, and N. Ross, Measurements of  
331 groundwater velocity in discrete rock fractures., *Journal of contaminant hydrology*, *82*(1-  
332 2), 44–60, doi:10.1016/j.jconhyd.2005.09.001, 2006.
- 333 Paillet, F. L., Flow modeling and permeability estimation using borehole flow logs  
334 in heterogeneous fractured formations, *Water Resources Research*, *34*(5), 997, doi:  
335 10.1029/98WR00268, 1998.
- 336 Pehme, P. E., J. P. Greenhouse, and B. L. Parker, The Active Line Source Temperature  
337 Logging Technique and Its Application in Fractured Rock Hydrogeology, *Journal of*  
338 *Environmental & Engineering Geophysics*, *12*(4), 307–322, doi:10.2113/JEEG12.4.307,  
339 2007.
- 340 Pehme, P. E., B. L. Parker, J. Cherry, and J. P. Greenhouse, Improved resolution of  
341 ambient flow through fractured rock with temperature logs., *Ground water*, *48*(2), 191–  
342 205, doi:10.1111/j.1745-6584.2009.00639.x, 2010.
- 343 Riley, M. S., J. H. Tellam, R. B. Greswell, V. Durand, and M. F. Aller, Convergent tracer  
344 tests in multilayered aquifers : The importance of vertical flow in the injection borehole,  
345 *Water Resources Research*, *47*, 1–14, doi:10.1029/2010WR009838, 2011.
- 346 Ruelleu, S., F. Moreau, O. Bour, D. Gapais, and G. Martelet, Impact of gen-  
347 tly dipping discontinuities on basement aquifer recharge: An example from Ploe-  
348 meur (Brittany, France), *Journal of Applied Geophysics*, *70*(2), 161–168, doi:  
349 10.1016/j.jappgeo.2009.12.007, 2010.

- 350 Saar, M. O., Review : Geothermal heat as a tracer of large-scale groundwater flow and  
351 as a means to determine permeability fields, *Hydrogeology Journal*, pp. 31–52, doi:  
352 10.1007/s10040-010-0657-2, 2011.
- 353 Sammel, E., Convective Flow and Its Effect on Temperature Logging in Small Diameter  
354 Wells, *Geophysics*, 33(6), 1004–1012, doi:10.1190/1.1439977, 1968.
- 355 Selker, J. S., et al., Distributed fiber-optic temperature sensing for hydrologic systems,  
356 *Water Resources Research*, 42(12), 2006.
- 357 Tyler, S. W., J. S. Selker, M. B. Hausner, C. E. Hatch, T. Torgersen, C. E. Thodal,  
358 and S. G. Schladow, Environmental temperature sensing using Raman spectra DTS  
359 fiber-optic methods, *Water Resources Research*, 45, 1–11, doi:10.1029/2008WR007052,  
360 2009.

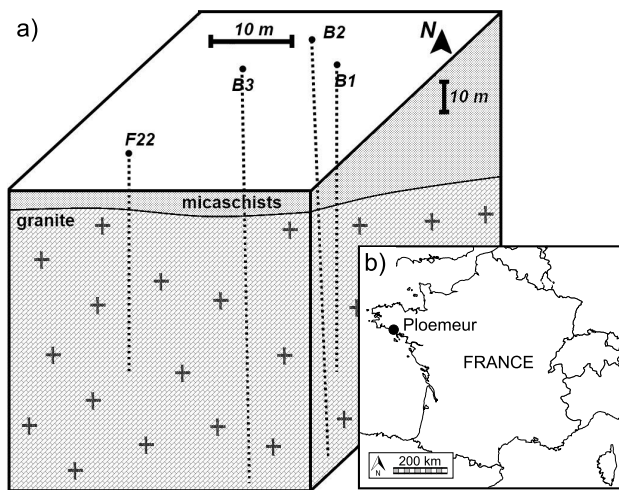


**Figure 1.** (a) Borehole array configuration, (b) location of the site

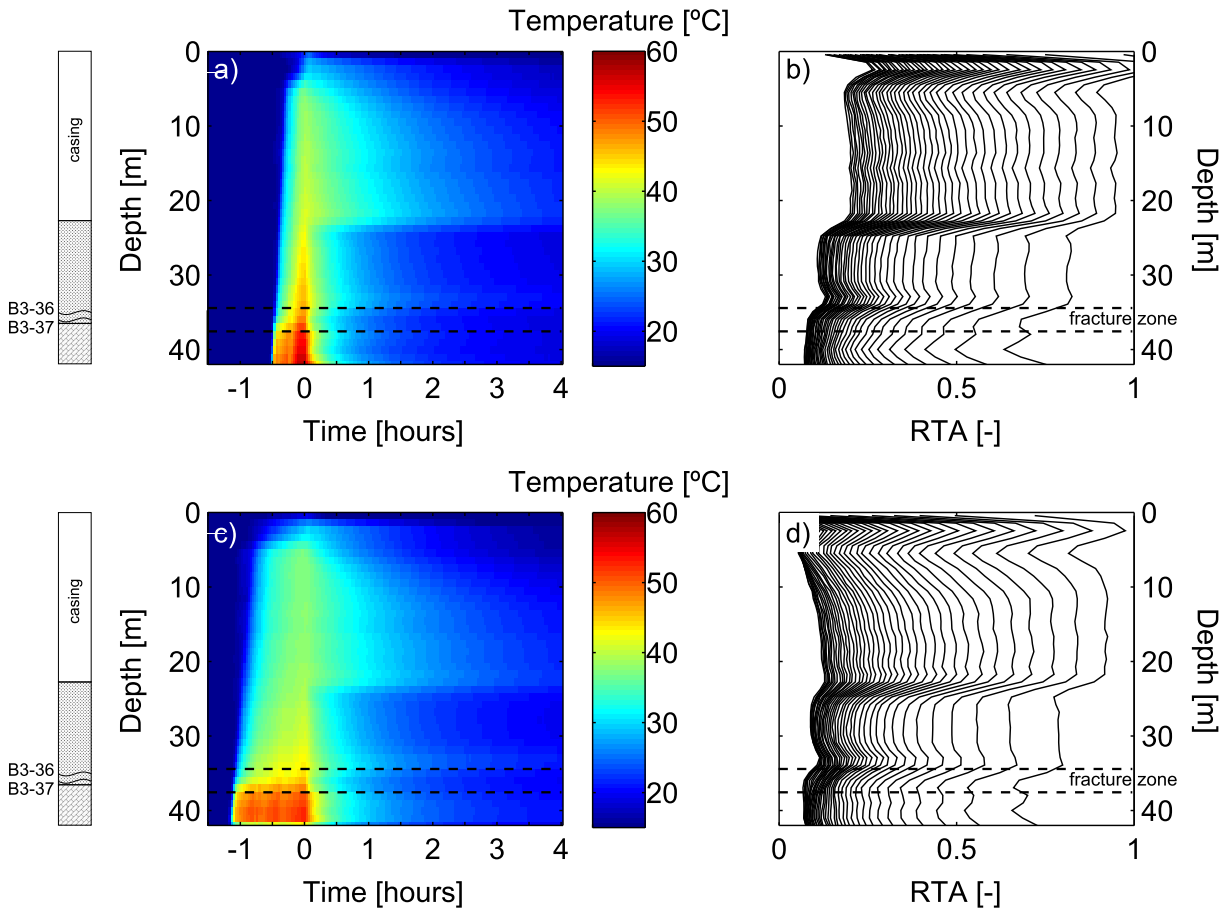


**Figure 2.** Temperature in B3 during the thermal dilution test under ambient conditions (a) and while pumping B2 (c), and corresponding Relative Temperature Anomaly (b) and (d) at normalized times of 0.2 to 8 [-] (right to left). The time was normalized to account for the different injection durations, with 1 hour taken as the standard injection length

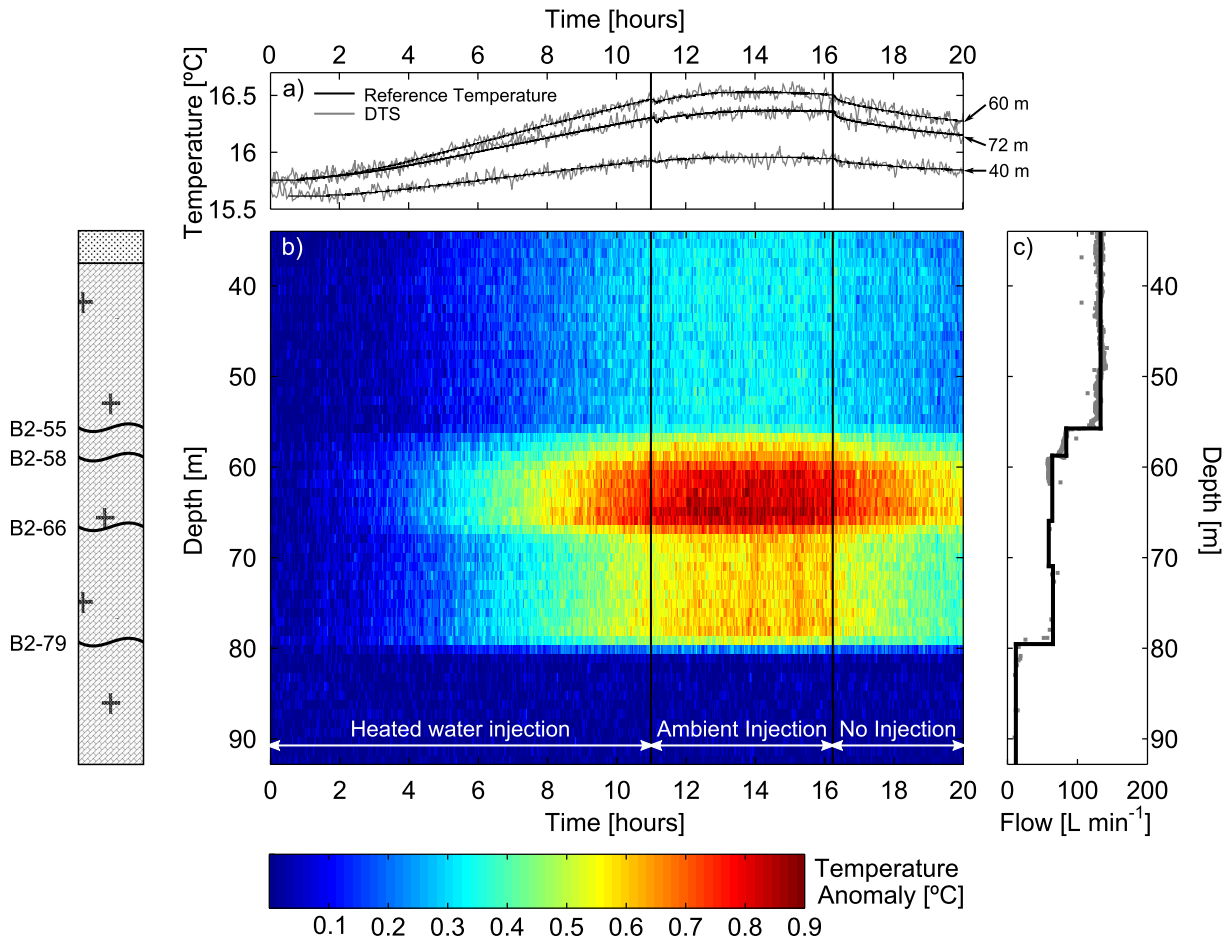


**Figure 3.** a) Temperature logger and DTS measured temperature at the corresponding depths during the thermal tracer test from B1 to B2, b) DTS measured temperature anomaly for all depths, c) measured flow in B2 for a pumping rate of 140 L min<sup>-1</sup> with solid line to indicate the flow profile assumed for the application of Equation 4

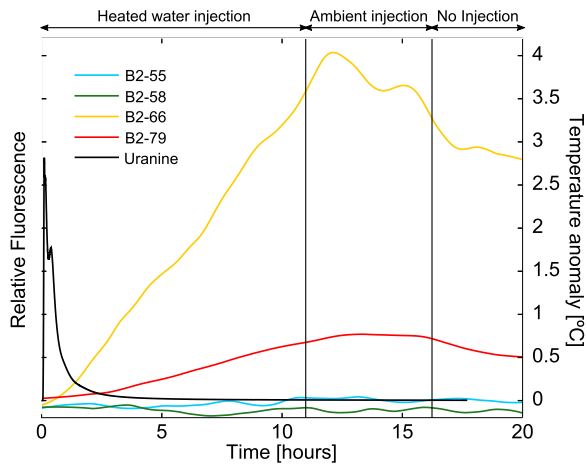


**Figure 4.** Uranine breakthrough, and calculated temperature anomaly of the inflowing fractures B2-55, B2-58, B2-66 and B2-79 during the thermal tracer test

# References

- M. P. Anderson. Heat as a ground water tracer. *Ground Water*, 43(6):951–968, 2005. [xvi](#), [22](#), [23](#), [83](#), [134](#)
- K. Ando, A. Kostner, and S. P. Neuman. Stochastic continuum modeling of flow and transport in a crystalline rock mass: Fanay-augeres, france, revisited. *Hydrogeology Journal*, 11:521–535, 2003. [13](#)
- J. Bear. *Dynamics of Fluids in Porous Media*. American Elsevier Publishing Company Inc., New York, 1972. [136](#)
- M. W. Becker and A. M. Shapiro. Tracer transport in fractured crystalline rock: evidence of nondiffusive breakthrough tailing. *Water Resources Research*, 36(7):1677–1686, 2000. [12](#), [133](#), [134](#), [141](#)
- M. W. Becker and A. M. Shapiro. Interpreting tracer breakthrough tailing from different forcedgradient tracer experiment configurations in fractured bedrock. *Water Resources Research*, 39(1):1024, 2003. [xvi](#), [10](#), [11](#), [12](#), [133](#), [134](#)
- B. Berkowitz. Characterizing flow and transport in fractured geological media: A review. *Advances in Water Resources*, 25:861–884, 2002. [4](#), [7](#), [8](#), [13](#)
- B. Berkowitz, O. Bour, P. Davy, and N. Odling. Scaling of fracture connectivity in geological formations. *Geoph. Res. Letters*, 27:2061–2064, 2000. [7](#), [8](#)
- G. Bjornsson, G. Axelsson, and Flovenz. Thelamork low-temperature system in n-iceland. *Reservoir Engineering, Stanford University, Stanford*, pages 5–13, 1994. [134](#)

## REFERENCES

---

- J. Bodin, F. Delay, and G. de Marsily. Solute transport in fissured aquifers: 1. fundamental mechanisms. *Hydrogeol Journal*, 11:418–433, 2003a. [10](#), [11](#)
- J. Bodin, F. Delay, and G. de Marsily. Solute transport in a single fracture with negligible matrix permeability: 2. mathematical formalism. *Hydrogeol Journal*, 11:434–454, 2003b. [11](#)
- G. S. Bodvarsson and C. F. Tsang. Injection and thermal breakthrough in fractured geothermal reservoirs. *Journal of Geophysical Research*, 87(B2):1031–1048, 1982. [26](#), [143](#), [144](#), [149](#)
- J. Bouquain, Y. Meheust, and P. Davy. Horizontal pre-asymptotic solute transport in a plane fracture with significant density contrasts. *JOURNAL OF CONTAMINANT HYDROLOGY*, 120-21(SI):184–197, 2011. [168](#)
- O. Bour and P. Davy. Connectivity of random fault networks following a power law fault length distribution. *33(7):1567–1583*, 1997. [xv](#), [7](#), [8](#), [9](#)
- O. Bour and P. Davy. On the connectivity of three-dimensional fault networks. *Water Resources Research*, 34(10):2611–2622, 1998. [7](#), [8](#)
- J. H. Bredehoeft and I. S. S. Papadopoulos. Rates of vertical groundwater movement estimated from the earth’s thermal profile. *Water Resource Research*, 1:325–328, 1965. [23](#)
- J. J. Butler, C. D. McElwee, and G.C. Bohling. Pumping tests in networks of multilevel sampling wells: Motivation and methodology. *Water Resources Research*, 35(11):3553–3560, 1999. [xvi](#), [16](#), [17](#)
- M. C. Cacas, E. Ledoux, G. De Marsily, and B. Tillie. Modeling fracture flow with a stochastic discrete fracture network: Calibration and validation 1. the flow model. *Water Resources Research*, 26(3):479–489, 1990. [14](#), [15](#)
- K. Cartwright. Measurement of fluid velocity using temperature profiles: experimental verification. *Journal of Hydrology*, 43(1-4):185–194, 1979. [23](#)
- L. Clark. The analysis and planning of step drawdown test. *J1 Engng Geol.*, 10: 125–143, 1977. [75](#)

## REFERENCES

---

- C. Clauser. Permeability of crystalline rocks. *Am. Geophys. Union*, 73:233, 1992. [5](#), [70](#), [72](#), [82](#)
- C. Darcel, O. Bour, P. Davy, and J.-R. de Dreuzy. Connectivity properties of two-dimensional fracture networks with stochastic fractal correlation. *Water Resources Research*, 39(10):1272, 2003. [7](#), [8](#)
- F. D. Day-Lewis, P. A. Hsieh, and S. M. Gorelick. Identifying fracture-zone geometry using simulated annealing and hydraulic-connection data. *Water Resources Research*, 36(7):1707–1721, 2000. [xv](#), [6](#), [17](#)
- J.-R. de Dreuzy. *Analyse des propriétés hydrauliques des réseaux de fractures. Discussion des modeles compatibles avec les principales propriétés géométriques*. Université de Rennes 1, 1999. [13](#), [14](#)
- J.-R. de Dreuzy, P. Davy, and O. Bour. Hydraulic properties of two-dimensional random fracture networks following a power law length distribution 1. effective connectivity. *Water Resources Research*, 37(8):2065–2078, 2001. [7](#)
- M. Dentz, T. Le Borgne, A. Englert, and B. Bijeljic. Mixing, spreading and reaction in heterogeneous media : A brief review. *Journal of Contaminant Hydrology*, 120-121:1–17, 2011. [133](#)
- R. L. Detwiler, H. Rajaram, and R. J. Glass. Solute transport in variable-aperture fractures: an investigation of the relative importance of Taylor dispersion and macrodispersion. *Water Resources Research*, 36(7):1611–1625, 2000. [11](#)
- C. Dorn, N. Linde, T. Le Borgne, O. Bour, and M. Klepikova. Inferring transport characteristics in a fractured rock aquifer by combining single-hole gpr reflection monitoring and tracer test data. *Water Resour. Res.*, 48(W11521), 2012. [xix](#), [16](#), [69](#), [78](#), [79](#), [151](#), [165](#), [167](#)
- M. J. Drury and T. J. Lewis. Water-movement within lac-du-bonnet botholith as revealed by detailed thermal studies of 3 closely-spaced boreholes. *Tectonophysics*, 95(3-4):337–351, 1983. [24](#)
- G. Ferguson. Perturbation of ground surface temperature reconstructions by groundwater flow. *Geophys. Res. Lett.*, 33, 2006. [xvi](#), [22](#), [23](#), [24](#)

## REFERENCES

---

- T. Flynn. *Water temperature as a groundwater tracer in fractured rock*. Univ. of Arizona, Tucson, 1985. [134](#)
- A. Frampton and V. Cvetkovic. Inference of field-scale fracture transmissivities in crystalline rock using flow log measurements. *Water Resources Research*, 46: W11502, 2010. [xvi](#), [14](#), [15](#)
- B. M. Freifeld, S. Finsterle, T. C. Onstott, P. Toole, and L. M. Pratt. Ground surface temperature reconstructions: Using in situ estimates for thermal conductivity acquired with a fiber-optic distributed thermal perturbation sensor. *Geoph. Res. Lett.*, 35(14), 2008. [22](#)
- S. M. Ge. Estimation of groundwater velocity in localized fracture zones from well temperature profiles. *Journal of Volcanology and Geothermal Research*, 84 (1-2):93–101, 1998. [xvii](#), [23](#), [24](#), [25](#)
- S. Geiger and S. Emmanuel. Non-fourier thermal transport in fractured geological media. *Water Resources Research*, 46, 2010. [xvii](#), [26](#), [27](#), [168](#)
- L. W. Gelhar and C. Welty. A critical review of data on field-scale dispersion in aquifers. *Water Resources Research*, 28(7):1955–1974, 1992. [10](#)
- A. Genter, L. Guillou-Frottier, J.-L. Feybesse, N. Nicol, C. Dezayes, and S. Schwartz. Typology of potential hot fractured rock resources in europe. *Geothermics*, 32:701–710, 2003. [134](#)
- C. Gosselin and J. C. Mareschal. Variations in ground surface temperature histories in the thompson belt, manitoba, canada: environment and climate changes. *Global and Planetary Change*, 39(3-4):271–284, 2003. [22](#)
- A. C. Gringarten and J. P. Sauty. A theoretical study of heat extraction from aquifers with uniform regional flow. *JOURNAL OF GEOPHYSICAL RESEARCH*, 80(35), 1975. [134](#)
- R. Haggerty, S. A. McKenna, and L. C. Meigs. On the late-time behavior of tracer test breakthrough curves. *Water Resour. Res.*, 36(12):3467–3479, 2000. [133](#), [141](#)

## REFERENCES

---

- R. Haggerty, S. Fleming, L. C. Meigs, and S. A. McKenna. Tracer tests in a fractured dolomite 2. analysis of mass transfer in single-well injection-withdrawal tests. *WATER RESOURCES RESEARCH*, 37:1129–1142, 2001. [xvi](#), [12](#), [133](#)
- Y. T.-C. Hao, J. Yeh, J. Xiang, W. Illman, K. Ando, K.-C. Hsu, and C.-H. Lee. Hydraulic tomography for detecting fracture zone connectivity. *Ground Water*, 46(2):183–192, 2008. [13](#), [15](#), [17](#)
- R. D. Henderson, F. D. Day-Lewis, and C. F. Harvey. Investigation of aquifer-estuary interaction using wavelet analysis of fiber-optic temperature data. *Geophys. Res. Lett.*, 36(6), 2009. [22](#)
- A. E. Hess. Identifying hydraulically conductive fractures with a slow velocity borehole flowmeter. *Canadian Geotechnical Journal*, 23:69–78, 1986. [20](#)
- P. A. Hsieh, editor. *Scale Effects in Fluid Flow through Fractured Geologic Media, in Scale dependence and scale invariance in hydrology*, volume 14 of *Encyclopaedia of Mathematical Sciences*. edited by G. Sposito, Cambridge University Press, Cambridge, 1998. [xv](#), [5](#), [6](#), [70](#), [82](#)
- W. A. Illman. Strong field evidence of directional permeability scale effect in fractured rock. *J. of Hydrol.*, 319:227–236, 2006. [xv](#), [5](#), [6](#)
- W. A. Illman, A. J. Craig, and X. Liu. Practical issues in imaging hydraulic conductivity through hydraulic tomography. *Ground Water*, 46(1):120–132, 2008. [17](#)
- W. A. Illman, X. Liu, S. Takeuchi, T.-C. Yeh, K. Ando, and H. Saegusa. Hydraulic tomography in fractured granite: Mizunami underground research site, japan. *Water Resources Research*, 45, 2009. [xvi](#), [13](#), [14](#), [15](#), [17](#), [18](#)
- Incropera and DeWitt. *Fundamentals of heat and mass transfer*. 1996. [137](#)
- A. Jardani and A. Revil. Stochastic joint inversion of temperature and self-potential data. *Geophys. J. Int.*, 179:640–654, 2009. [22](#)

## REFERENCES

---

- C. Jaupart, J. R. Mann, and G. Simmons. A detailed study of the distribution of heat-flow and radioactivity in new-hampshire (usa). *Science Letters*, 59(2): 267–287, 2009. [22](#)
- Y. Jung and K. Pruess. A closed-form analytical solution for thermal single-well injection-withdrawal tests. *Water Resources Research*, 48(W03504), 2012. [26](#), [134](#), [135](#), [142](#), [144](#), [146](#), [158](#), [164](#)
- Y. Jung and K. Pruess. Reply to comment by maier and kocabas on a closed-form analytical solution for thermal single-well injection-withdrawal tests. *Water Resource Research*, 49, 2013. [28](#)
- I. Kocabas. Geothermal reservoir characterization via thermal injection backflow and interwell tracer testing. *Geothermics*, 34:27–46, 2005. [26](#), [134](#), [135](#)
- I. Kocabas and R. N. Horne. A new method of forecasting the thermal breakthrough time during reinjection in geothermal reservoirs. *Proceedings 15th Workshop on Geothermal Engineering, Stanford University, Stanford, CA*, pages 179–186, 1990. [26](#), [134](#)
- O. Kolditz. Modelling flow and heat transfer in fractured rocks: Dimensional effect of matrix heat diffusion. *Geothermics*, 24:421–437, 1995. [26](#)
- H. A. Lauwerier. The transport of heat in an oil layer caused by the injection of hot fluid. *Appl. Sci. Res.*, 5, 1955. [26](#), [134](#)
- T. Le Borgne, O. Bour, F.L. Paillet, and J.-P Caudal. Assessment of preferential flow path connectivity and hydraulic properties at single-borehole and cross-borehole scales in a fractured aquifer. *Journal of Hydrology*, 328:347–359, 2006a. [20](#), [31](#), [69](#), [71](#), [72](#)
- T. Le Borgne, F.L. Paillet, O. Bour, and J.-P Caudal. Cross-borehole flowmeter tests for transient heads in heterogeneous aquifers. *Ground Water*, 44, 2006b. [13](#), [20](#), [31](#), [71](#), [72](#)
- T. Le Borgne, O. Bour, M.S. Riley, P. Gouze, P.A. Pezard, A. Belghoul, G. Lods, R. Le Provost, R.B. Greswell, P.A. Ellis, E. Isakov, and B.J. Last. Comparison

## REFERENCES

---

- of alternative methodologies for identifying and characterizing preferential flow paths in heterogeneous aquifers. *Journal of Hydrology*, 345:134–148, 2007. [xviii](#), [xix](#), [20](#), [21](#), [22](#), [31](#), [69](#), [72](#), [73](#), [74](#), [75](#), [79](#), [80](#), [151](#)
- R. Le Goc, J.-R. de Dreuzy, and P. Davy. An inverse problem methodology to identify flow channels in fractured media using synthetic steady-state head and geometrical data. *Advances in water resources*, 33:782–800, 2010. [xv](#), [7](#), [14](#), [16](#)
- S. Leray, J.-R. de Dreuzy, O. Bour, T. Labasque, and L. Aquilina. Contribution of age data to the characterization of complex aquifers. *JOURNAL OF HYDROLOGY*, 464:54–68, 2012. [69](#), [71](#)
- S. Leray, J.-R. de Dreuzy, O. Bour, and E. Bresciani. Numerical modeling of the productivity of vertical to shallowly dipping fractured zones in crystalline rocks. *JOURNAL OF HYDROLOGY*, 481:64–75, 2013. [74](#)
- M. Levy and B. Berkowitz. Measurement and analysis of non-fickian dispersion in heterogeneous porous media. *Journal of Contaminant Hydrology*, 64:203–226, 2003. [xvi](#), [10](#)
- H. H. Liu, Y. Zhang, Q. Zhou, and Q. Molz. An interpretation of potential scale dependence of the effective matrix diffusion coefficient. *Journal of Contaminant Hydrology*, 90:41–57, 2007. [133](#)
- J. C. S. Long, J. S. Remer, C. R. Wilson, and P. A. Witherspoon. Porous media equivalents for networks of discontinuous fractures. *Water Resources Research*, 18(3):645–658, 1982. [13](#)
- R. C. M. Malate and M. J. O’Sullivan. Mathematical modelling of silica deposition. *Proc. 10th New Zealand Geothermal Workshop, University of Auckland, Auckland*, pages 257–262, 1991. [134](#)
- J. C. Marechal and P. K. Perrochet. Theoretical relation between water flow rate in a vertical fracture and rock temperature in the surrounding massif. *Planetary Science Letters*, 194:213–219, 2001. [23](#)

## REFERENCES

---

- G. Margolin, B. Berkowitz, and H. Scher. Structure, flow, and generalized conductivity scaling in fracture networks. *Water Resour. Res.*, 34(9):2103–2121, 1998. [7](#)
- Y. Meheust and J. Schmittbuhl. Geometrical heterogeneities and permeability anisotropy of rough fractures. *J Geophys Res*, 106(B2):2089, 2001. [4](#)
- J. Molson, P.E. Pehme, J. Cherry, and B. Parker. Numerical analysis of heat transport within fractured sedimentary rock: Implications for temperature probes. *NGWA/U.S. EPA Fractured Rock Conference: State of the Science and Measuring Success in Remediation, Portland, Maine*, 2007. [xix](#), [26](#), [136](#), [137](#), [138](#), [139](#)
- F. J. Molz, R. H. Morin, A. E. Hess, J. G. Melville, and O. G. Aijven. The impeller meter for measuring aquifer permeability variations: evaluation and comparison with other tests. *Water Resources Research*, 25:1677–1683, 1989. [20](#)
- L. Moreno and I. Neretnieks. Fluid flow and solute transport in a network of channels. *J Contam Hydrol*, 14(3-4):163–192, 1993. [11](#)
- L. Moreno, Y. W. Tsang, C. F. Tsang, F. V. Hale, and I. Neretnieks. A stochastic model and its relation to some field observations. *WATER RESOURCES RESEARCH*, 24(12):2033–2048, 1988. [4](#)
- L. Moreno, Y. W. Tsang, C.-F. Tsang, F. V. Hale, and I. Neretnieks. Some anomalous features of flow and solute transport arising from fracture aperture variability. *Water Resour. Res.*, 26:2377–2391, 1990. [4](#)
- I. Neretnieks. Diffusion in the rock matrix: An important factor in radionuclide retardation? *J. Geophys. Res.*, 85(B8):4379–4397, 1980. [11](#)
- I. Neretnieks. Single well injection withdrawal tests (swiw) in fractured rock: some aspects on interpretation. *SKB Rapport R-07-54, Department of Chemical Engineering and Technology Royal Institute of Technology*, 2007. [135](#), [140](#)
- S. P. Neuman. Trends, prospects and challenges in quantifying flow and transport through fractured rocks. *Hydrogeology Journal*, 13:124–147, 2005. [16](#)

## REFERENCES

---

- A. Neuville, R. Toussaint, and J. Schmittbuhl. Hydrothermal coupling in a self-affine rough fracture. *PHYSICAL REVIEW E*, 82:036317, 2010. [xv](#), [4](#), [26](#), [134](#), [136](#), [154](#), [158](#), [168](#)
- K. S. Novakowski and P. A. Lapcevic. Field measurement of radial solute transport in fractured rock. *Water Resour. Res.*, 30(1):27–44, 1994. [11](#)
- O. Olsson. *Site characterization and validation. Final Report, Stripa Project 92-22*. Conterra AB, Uppsala, Sweden, 1992. [xv](#), [5](#)
- F. Paillet. Borehole flowmeter applications in irregular and large-diameter boreholes. *Journal of Applied Geophysics*, 55:39–59, 2004. [20](#), [75](#)
- F. L. Paillet. Flow modeling and permeability estimation using borehole flow logs in heterogeneous fractured formations. *Water Resour. Res.*, 34:997–1010, 1998. [20](#), [21](#), [31](#), [162](#)
- F. L. Paillet. A field technique for estimating aquifer parameters using flow log data. *Ground Water*, 38:510–521, 2000. [20](#), [31](#)
- F. L. Paillet, J. H. Williams, J. Urik, J. Lukes, M. Kobr, and S. Mares. Cross-borehole flow analysis to characterize fracture connections in the melechov granite, bohemian-moravian highland, czech republic. *Hydrogeology Journal*, 20(1):143–154, 2012. [21](#), [31](#)
- C. K. Park, T. T. Vandergraaf, D. J. Drew, and P. S. Hahn. Analysis of the migration of nonsorbing tracers in a natural fracture in granite using a variable aperture channel model. *J Contam Hydrol*, 26(1-4):97–108, 1997. [11](#)
- P.E. Pehme, B.L. Parker, J.A. Cherry, and J.P. Greenhouse. Improved resolution of ambient flow through fractured rock with temperature logs. *Ground Water*, 48(2):191–205, 2010. [xvii](#), [24](#), [25](#)
- K. Pruess and C. Doughty. Thermal single-well injection-withdrawal tracer tests for determining fracture-matrix heat transfer area. *Thirty-Fifth Workshop on Geothermal Reservoir Engineering, Stanford Univ., Stanford, Calif*, 2010. [26](#), [134](#), [135](#), [158](#)

## REFERENCES

---

- T. Read, O. Bour, V. F. Bense, T. Le Borgne, P. Goderniaux, M. Klepikova, R. Hochreutener, N. Lavenant, and V. Boschero. Characterizing groundwater flow and heat transport in fractured rock using fiber-optic distributed temperature sensing. *GRL*, in press. [69](#), [79](#), [151](#), [163](#), [167](#)
- F. Rolandone, J. C. Mareschal, and C. Jaupart. Temperatures at the base of the laurentide ice sheet inferred from borehole temperature data. *Geoph. Res. Lett.*, 30, 2003. [22](#)
- Y. Rubin and S. S. Hubbard. *Hydrogeophysics*. Springer, New York, 2005. [16](#)
- S. Ruelleu, F. Moreau, O. Bour, D. Gapais, and G. Martelet. Impact of gently dipping discontinuities on basement aquifer recharge: An example from ploemeur (brittany, france). *Journal of Applied Geophysics*, 70:161–168, 2010. [xvii](#), [xviii](#), [69](#), [71](#), [72](#), [73](#), [74](#)
- M. O. Saar. Review: Geothermal heat as a tracer of large-scale groundwater flow and as a means to determine permeability field. *Hydrogeology Journal*, 19: 31–52, 2011. [xvii](#), [22](#), [25](#)
- X. Sanchez-Vila and J. Carrera. On the striking similarity between the moments of breakthrough curves for a heterogeneous medium and a homogeneous medium with a matrix diffusion term. *Journal of Hydrology*, 294:164–175, 2004. [12](#)
- J. Selker, N. van de Giesen, M. Westhoff, W. Luxemburg, and M. B. Parlange. Fiber optics opens window on stream dynamics. *Geophys. Res. Lett.*, page 3324, 2006. [22](#)
- A. M. Shapiro. Effective matrix diffusion in kilometer-scale transport in fractured crystalline rock. *Water Resources Research*, 37(3):507–522, 2001. [133](#)
- R. Sharmeen, W. A. Illman, S. J. Berg, T.-C. J. Yeh, Y.-J. Park, E. A. Sudicky, and K. Ando. Transient hydraulic tomography in a fractured dolostone: Laboratory rock block experiments. *Water Resour. Res.*, 48(W10532), 2012. [xvi](#), [18](#), [19](#)

## REFERENCES

---

- J.A.T. Smellie and F. Karlsson. The use of natural analogues to assess radionuclide transport. *Eng Geol*, (52), 1999. [11](#)
- M.L. Sorey. Measurements of vertical groundwater velocity from temperature profiles in wells. *Water Resource Research*, 7(4):963–970, 1971. [23](#)
- D. Stauffer and A. Aharony. *Introduction to Percolation Theory*. Taylor & Francis, London, 1985. [8](#)
- F. Touchard. *Caractérisation hydrologique d'un aquifère en socle fracturé*. Université de Rennes 1, 1999. [69](#), [72](#)
- C.-F. Tsang and I. Neretnieks. Flow channeling in heterogeneous fractured rocks. *Reviews of Geophysics*, 36:257–298, 1998. [4](#), [5](#)
- A. Vandenbohede, A. Louwyck, and L. Lebbe. Conservative solute versus heat transport in porous media during push-pull tests. *Transp Porous Med*, 76:265–287, 2009. [135](#), [136](#)
- T. Vogt, P. Schneider, L. Hahn-Woernle, and O. A. Cirpka. Estimation of seepage rates in a losing stream by means of fiber-optic high-resolution vertical temperature profiling. *Journal of Hydrology*, 380(1-2):154–164, 2010. [134](#)
- J. H. Williams and F. L. Paillet. Using flowmeter pulse tests to define hydraulic connections in the subsurface: a fractured shale example. *J. of Hydrol.*, 265(8/30):100–117, 2002. [21](#)
- T. C. Jim Yeh and S. Liu. Hydraulic tomography: Development of a new aquifer test method. *Water Resources Research*, 36(8):2095–2105, 2000. [16](#), [17](#)
- Y.W.Tsang, C.F. Tsang, F.V. Hale, and B. Dverstop. Tracer transport in a stochastic continuum model of fractured media. *Water Resour. Res.*, 32(10):3077–3092, 1996. [13](#)
- J. Zhu and T.-C. J. Yeh. Characterization of aquifer heterogeneity using transient hydraulic tomography. *Water Resources Research*, 41(7):1–10, 2005. [17](#)